Variable Supply Pressure Electrohydraulic System for Efficient Multi-axis Motion Control

Du, Can

Award date:
2014

Awarding institution:
University of Bath

Variable Supply Pressure Electrohydraulic System for Efficient Multi-axis Motion Control

Can Du

A thesis submitted for the degree of Doctor of Philosophy

University of Bath

Department of Mechanical Engineering

November 2014

Abstract

The conventional fixed supply pressure valve-controlled (FPVC) hydraulic actuation method is a simple way to obtain motion control of a multi-axis system. The energy dissipated by the relief valve and the control valves is the main cause of the low energy-efficiency (and consequent oil heating) in the system. To overcome this problem, some approaches have been investigated such as load sensing, separate meter-in-and-meter-out, switching control and electro-hydrostatic actuation. In this thesis, a load-prediction based energy-efficient electrohydraulic actuation system – variable supply pressure valve-controlled (VPVC) actuation is described and implemented. A two-axis robotic arm is used as an example plant.

In this research, the VPVC hydraulic actuation system is implemented by a fixed capacity pump driven by a brushless servo-motor. The feed forward part of the VPVC controller predicts the minimum required supply pressure for the demanded motion to each joint of the robotic arm by assuming its control valve is fully open. It is based on the prediction of the required piston force for a given motion demand, by applying Lagrange's equations of the-second-kind. The supply pressure for the whole system is the higher one of the two load branches; the other one is controlled by the common valve throttling. The supply flow is varied by controlling the speed of the servomotor. The feedback control of the VPVC is simple PI control for the valves and P control for the motor speed. Although the VPVC method is demonstrated for a two axis system, it is applicable to systems with any number of axes.

By using the variable minimum required supply pressure together with the maximum valve opening (and hence minimum throttling losses), the hydraulic

energy-efficiency is improved compared with a fixed supply pressure valve-controlled (FPVC) system. Moreover, due to the feed forward control, the response has much less phase lag hence the dynamic error is much smaller than a conventional FPVC system with proportional integral position feedback control. Applied to a known plant, especially enough load information, VPVC provides a higher energy-efficiency and a higher accuracy of motion control.

The simulation and experimental results have validated the advantages of the VPVC over the FPVC. The hydraulic power consumption comparison between VPVC and FPVC with the same sine wave motion demand showed that up to 70% saving was achieved by VPVC experimentally. If the energy loss via relief valve in FPVC is taken into account, the saving can be increased greatly. The experiment also showed that the VPVC brought a very quiet operating due to the minimum flow throttling and variable motor speed, whereas serious flow throttling and constant high speed of motor in FPVC. Very low noise is another significant benefit of VPVC over FPVC. All the dynamic errors in VPVC tests were smaller than in FPVC. They were within 6% of the total motion range, compared to 14% for FPVC. And the average dynamic errors of VPVC tests were within 1.5% of the total motion range.

Acknowledgement

I would like to show my gratitude to my supervisors Prof. Andrew Plummer, Dr. Nigel Johnston and Dr. Andy Hillis, for their guidance, encouragement and valuable advice. Thanks are also to the technical staff of the 4E and 8E laboratories for assisting in experiments.

Many thanks to all the staff of the Centre for Power Transmission and Motion Control (CPTMC) at the University of Bath who assisted in making this thesis a reality.

Many thanks go out to my friends in Bath, for their accompanying, understanding and listening to my occasional rants. Also to those who hurt me. Thank you for forcing me to this final achievement.

Special thanks to my parents, for their love and support.

Contents

Nomenclature

Variables

Symbol	Description
A_p	Area of the piston side in the cylinder
A_r	Area of the rod side in the cylinder
B	Bulk modulus of the oil in GPa
C	Viscous coefficient for pump in Nm/(rad/sec)
$c(\theta)$	Actuator length (body and piston)
D_P	Pump displacement
F	Hydraulic actuation force
$F_c\ F_f$	Cushion force, viscous friction force in the actuator
$l(\theta)$	Force arm
$I_0\ I_1\ I_2\ I_3$	Inertial of torso, upper arm including the elbow actuator, forearm and hand; with respect to their own gravity centres, around y-axis
J	Inertial of motor, pump and flexible coupling
K	Effective stiffness of the oil inside the supply galleries
K_f	Coefficient for viscous friction force inside the actuator in N/(m/s)
$K_P\ K_I$	Proportional gain, Integral gain
K_t	Torque constant of servomotor
K_V	Valve constant obtained from rated data

$M_0\ M_1\ M_2\ M_3$	Mass of torso, upper arm including the elbow actuator, forearm and hand
P_A	Pressure in the piston side chamber
P_B	Pressure in the rod side chamber
P_r	Return line pressure
P_{SO}	Predicted supply pressure when control valve fully open
P_{SC}	Predicted supply pressure when achieving critical value for no cavitation in the thrust chamber
P_{th}	Threshold value for no cavitation in the chamber
Q_a	Flow rate to/from the piston side of actuator
Q_b	Flow rate to/from the rod side of actuator
T	Torque of motor
V_{cp}	Internal volume of piston side chamber when mid-stroke
V_{cr}	Internal volume of rod side chamber when mid-stroke
V_{ps}	Volume of the supply hoses
V_p	Internal volume of one micro pipe
$V_1\ V_2\ V_3\ V_4$	Path volume in the steel manifold block. V_1: to rod side chamber of shoulder actuator V_2: to piston side chamber of shoulder actuator V_3: to piston side chamber of elbow actuator V_4: to rod side chamber of elbow actuator
x	Valve opening (from +100% to -100%)
x_{SO}	Valve opening when fully open (+100% or -100%)
x_{SC}	Valve opening when achieving critical value for no cavitation in thrust chamber
y	Linear position of the actuator

Greek Symbols

Symbol	Description
ω	Angular speed of servomotor
θ	Angular position of joint
v	Linear velocity of the actuator
α	Area ratio A_p/A_r
η_v	Volumetric efficiency of pump
ω_V ζ_V	Natural frequency of valve, damping ratio of valve

Accents

Symbol	Description
Circumflex ($\hat{}$)	Signal out of feed forward part of VPVC controller
Tlide ($\tilde{}$)	Final signal out of the overall VPVC controller

Subscripts

Symbol	Description
1, 2	Shoulder joint and elbow joint
d	Demand/command
a	Actual measured signal
m	servomotor
SO	Control valve fully open
SC	Critical condition of no cavitation in thrust chamber

Abbreviations

Symbol	Description
FPVC	Fixed supply pressure valve-controlled
VPVC	Variable supply pressure valve-controlled
P I D	Proportional, Integral and Derivative
VPVHA	Variable pressure valve-controlled hydraulic actuation
MA	Master actuator

Operator

Symbol	Description
sgn	Output the sign of the input

Chapter 1

1 Introduction

In many hydraulic actuation applications, energy efficiency is becoming an important consideration. For a multi-axis system, the general requirement is to generate the minimum power from the pump. In this research, a load prediction-based energy-efficient hydraulic actuation system is proposed. The system aims to reduce energy loss by generating a variable supply pressure. A two-axis robotic arm is used to demonstrate the control approach in this project. The proposed control method, load prediction-based variable supply pressure valve-control (VPVC), is designed to provide higher energy efficiency compared with a conventional fixed supply pressure valve-controlled (FPVC) hydraulic system, while achieving an at least similar dynamic response.

This chapter has 3 sections. The structure is as follows:

- Motivation
- Aims and objectives
- Structure of the thesis

1.1 Motivation

Hydraulic power is a widely used method for power transmission. It offers superior advantages like high power density and mechanical robustness. Hydraulic actuation delivers linear and rotary motion with high force and torque within a smaller, lighter package than other forms of power transmission like electrical drives.

Some traditional hydraulic applications like machine tools, fatigue test machines, aircraft and nuclear power engineering, require reliable control regardless of energy considerations. Fixed supply pressure systems are suitable for these kinds of applications. Usually, the fixed supply pressure hydraulic actuation system offers simple and reliable control of speed, force and torque by throttling the flow via control valves. But with the advent of energy saving requirements, energy efficiency improvement plays an important role to maintain the dominance of hydraulic actuation in many of these applications.

As described above, conventional control of an industrial multi-axis system (such as a hydraulic robot or a structural test rig) is achieved using fixed supply pressure valve-controlled (FPVC) hydraulic actuation, which has to throttle the flow by the valve to reduce the pressure; hence it brings an energy loss across the valve. For the sizing and cost consideration, usually one single pump is used to distribute the flow to more than one actuator. It is obvious that in FPVC system, the supply pressure should be set high enough for all the actuators requirements and all duty cycles.

Generally, the energy efficiency of an industrial multi-axis system can be increased by the following ways (Murrenhoff, et al., 2014):

- Reducing throttling losses over the valves.
- Avoiding inefficient component operating points.

- Recovering potential energy.

Many possible high energy-efficient hydraulic actuation methods have been investigated and realised in real applications. Load sensing (LS) system is a most common concept. It maintains a constant pressure drop over the control valves by the pump control device and the load sensing valves, which to decrease the pressure loss over the control valves compared with the fixed supply pressure valve-control system. However, the dynamic response of the load sensing systems is not as good as fixed supply pressure systems, as both pump displacement control and (usually) electric motor speed control, is significantly slower than conventional fixed supply pressure valve control method.

In this project, a load prediction-based variable supply pressure valve-controlled (VPVC) hydraulic actuation system is put forward and investigated. VPVC aims to reduce throttling losses over the control valves by generating a variable supply pressure. The variable pressure is produced by a servo motor and a fixed capacity pump according the changing load requirements. VPVC has some similarity to load sensing systems but it does not use any actual pressure signals for control. The VPVC controller predicts the minimum supply pressure P_S required in advance, with the aim of achieving a good dynamic response while achieving high energy efficiency.

VPVC computes the dynamic force required from the given motion demand to the actuators and then assumes a maximum valve opening of the highest load branch, which then enables a minimum supply pressure P_S to be estimated.

From the previous description of VPVC and FPVC, it is suggested that the potential advantages of VPVC are:

- Good efficiency due to variable supply pressure.
- Lighter weight than traditional load sensing system due to the usage of a fixed capacity pump and an electronic controller.
- Good dynamic response due to load prediction in advance.

Hence VPVC is targeted at future mobile robots applications where efficiency and weight are crucial. In this project, the benefits of the VPVC control algorithm will be evaluated by simulated and experimental tests on a two-axis robotic arm system (see Figure 1.1).

Figure 1.1 The two-axis robotic arm

1.2 Aims and objectives

The aim of the research is to develop and investigate an energy-efficient control method for hydraulic actuation systems: load prediction-based variable supply pressure valve-controlled (VPVC). VPVC is expected to be able to save a significant amount of energy compared with conventional fixed supply pressure valve-controlled hydraulic actuation (FPVC); in addition, VPVC should have a similar or better dynamic response, and should not increase the system weight.

The detailed objectives are as follows:

- Review of energy-efficient hydraulic actuation methods and qualitative comparison with VPVC concept.
- VPVC control algorithm derivation.
- System modelling including FPVC controller and VPVC controller, hydraulic domain and mechanical domain.
- Simulation tests. Analyse and compare the simulation results of FPVC and VPVC.
- Experimental tests. Analyse and compare the experimental results of FPVC and VPVC.

1.3 Structure of the thesis

Chapter 1 presents the introduction of the project. An overview of the proposed control method, the problem it addresses and objectives are shown.

Chapter 2 presents a literature review of traditional fixed supply pressure hydraulic actuation, and several efficient control methods for multi-axis hydraulic actuation. Furthermore, a brief review of the motion control of robots is presented.

Chapter 3 presents the theoretical derivation of the VPVC control algorithm. It includes the concept introduction; VPVC feed forward control description and VPVC feedback control description.

Chapter 4 presents the detailed description of the two-axis robotic arm system developed in this project. It includes the overall test rig schematic and components selection.

Chapter 5 presents the modelling of the two-axis robotic arm system. It consists of the VPVC controller modelling, hydraulic systems modelling and mechanical domain modelling. Also, the modelling of the FPVC controller is introduced briefly.

Chapter 6 presents the simulated results of FPVC and VPVC. For FPVC, the performance of square wave motion and sine wave motion are shown and discussed. For VPVC, the performance of filtered square wave motion and sine wave motion are shown and discussed. The comparison of power consumption and dynamic response are carried out between FPVC simulated results and VPVC simulated results.

Chapter 7 presents the experimental validation of FPVC and VPVC. All the simulated tests in Chapter 6 are implemented experimentally. The differences between the simulated results and the experimental results are discussed and explained. The comparison of power consumption and dynamic response are carried out between FPVC and VPVC experimental results. The merits of VPVC are shown experimentally.

Chapter 8 presents the conclusions of the research from the results and discussions. Recommendations for future work are also included.

Chapter 2

2 Literature Review

The aim of this chapter is to critically review literature relevant to the research of energy-efficient hydraulic actuation for multi-axis systems, with particular focus on robotics. The first section gives an overview of hydraulic actuation and its applications. The second section is about hydraulic actuated robots including a review of this application development and an investigation of robot motion control methods. The next section is a review of several current approaches to energy-efficient hydraulic actuation. The last section is a conclusion.

2.1 Background

Hydraulic actuation systems have been playing a very important role in diverse applications due to their high power density and good durability. Hydraulics is one of the oldest forms of power transmission. Despite the rapid growth of the electric power transmission, hydraulics keeps its inherent advantages. Besides the high power-to-weight ratio, hydraulic power transmission can achieve linear motion easily and stepless speed control without the limitations of conventional gears and driveshafts (Chapple, 2003).

Figure 2.1 Hydraulic workshop press HSP-60M from Baileigh Industrial company (Baileigh industrial, 2014)

One of the major customers for the hydraulics is the machine tool industry. For implementing linear motion tasks like lifting and tipping, hydraulic actuation is unbeatable. Hydraulics applied to machine tools can bring an extremely smooth movement under infinitely variable speed control, which would be very difficult to be achieved with a standard motor without the complication of complex electronics (Hunt & Vaughan, 1996). Injection moulding machinery is one of the most demanding types hydraulic machinery. The full process has to be completed by hydraulic cylinder in a repeated cycle of only a few seconds: mold-closing, injection, maintaining pressure and mold-opening. The individual parameter setting for each step is strictly controlled (Gotz, 1984). Hydraulic presses are predominant in repetitive industrial machinery with a wide range of pressure forces. Figure 2.1 shows a hydraulic press model HSP-60M from Baileigh Industrial. This hydraulic press is designed to have 2-speed mode with automatic cylinder return.

Hydraulic systems were used on aircraft from the early 1930s when the retractable undercarriage was introduced (Moir & Seabridge, 2008). Hydraulics occupies a very special position in the aircraft industry, with its high power and high stiffness. Hence it is ideal for the operation of the primary flight controls like ailerons and elevator. For utility systems, landing gear extension/retraction, steering and brake are common applications of hydraulics on aircraft (see Figure 2.2). Not only are many flight controls of aircraft operated hydraulically, but also ground support like mobile test stands and test equipment and rigs like flushing rigs depend heavily on hydraulic transmissions. Flight simulator is a most useful device in pilot training. And it is also facilitated by hydraulic actuation to achieve any combination of movements.

Figure 2.2 Left outboard leg of the main landing gear of Boeing 747-8 (Wikimedia Commons , 2011)

Hydraulics in marine applications makes its appearance on steering, mooring, hatch covers, etc. For steering, through proportional closed loop control, a hydraulic transmission provides reliable and accurate positioning. Automatic mooring winches usually adopt radial hydraulic motors and can be rendered in almost any size and capacity in a neat and compact solution. Hydraulically operated hatch covers are used by many cargo ships because of their considerable time-saving compared with manual labour (Hunt & Vaughan, 1996). Offshore and subsea operations take place in extreme and hazardous environments from not only the corrosive nature of the sea water but also the storm forces and the high pressure below sea level. Hydraulics, suitably designed are involved in a variety of operations including oil and gas rig platform construction, drilling, offshore and subsea cranes, subsea clamp and grab systems, etc. The control mechanism on a remotely operated vehicle consists of a drive unit for the thrusters and the manipulators as well as the camera and the tilting function, and the actuators used subsea are nearly always of the hydraulic type (Albers, 2010).

Figure 2.3 The EHS-B 12m³ electro-hydraulic grab used for ship unloading from ORTS Maschinenfabrik (ORTS, 2014)

For machines which are operating with heavy-duty load or in some extreme conditions, such as mining machinery, hydraulic power transmission is the best and almost exclusive solution (Shi, et al., 2013). Hydraulics also supplies lifting applications and load handling facilities with safety and reliability very much in mind for nuclear engineering. For transport and disposal of hazardous waste from the hospital, the container is lifted by a hydraulically operated telescopic arm with four diagonally connected suction cups. Hydraulic patient hoist is a good example for hydraulic applications in medicine due to the unrivalled power/weight ratio possibilities. The hydraulic hoist in Figure 2.4 is suitable for a heavy patient up to 180kg.

Figure 2.4 Oxford Midi 180 hydraulic patient hoist (Oxfordhoists, 2014)

Mobile hydraulics is often adopted in the construction industry and agricultural industries. Hydraulic forklifts are used to lift and move materials short distances. Excavators may either be tracked or wheeled but both have very similar hydraulic actuation principles (see Figure 2.5). Many mobile cranes are hydraulically actuated because hydraulics can provide infinitely variable speed actuation at least as effectively as any other forms of power transmission. Agricultural tractors and harvesters usually complete ploughing, traction and harvesting movements by the use of hydraulic rams.

Figure 2.5 Tracked excavator (left) and wheeled excavator (right) (JCB, 2014)

Some robots also use hydraulic actuation. Hydraulically actuated robots have rapid responses and high power-to-weight ratios which make them suitable for many industrial requirements (Sirouspour & Salcudean, 2001). For the mobile robots in future, they require low-cost and energy-efficiency as well as good control precision (Guizzo & Deyle, 2012). Roller-Walker as a leg–wheel hybrid mobile robot using a passive wheel was investigated to find the relationship between the leg trajectory and the energy efficiency of propulsion using a dynamic simulator (Gen & Shigeo, 2012).

Many of the traditional hydraulic applications mentioned above adopt fixed supply pressure actuation along with valve-control due to its simplicity of implementation and good dynamic response. Usually, for multi-axis systems, only one hydraulic power source is used because of cost and size considerations. Thus the throttle valves are required to regulate the motion of the actuators by restricting the flow. The pressure reduction across the throttling valve is often the major part of the energy loss of the whole hydraulic system. Conventional systems also require a powerful cooling system to remove the wasted energy (heat) in the system.

As a summary of this section, hydraulic power transmission occupies an important role in a wide range of applications. Conventional fixed supply pressure valve-controlled actuation is simple with excellent dynamic performance but inefficient. As a fast growing industry, hydraulic robots attract more and more attention. High energy-efficiency along with good control ability will be one of the main interests in future research, both in hydraulic actuated robots and other hydraulic applications.

2.2 Hydraulically actuated robots

2.2.1 Hydraulic robot applications

With the improvement of sensors and control accuracy, lots of robots could be created to do jobs in the manufacturing industry, military, space exploration and medical applications etc. Robots are used to complement human behaviour in applications where it is either difficult or impossible to use human operators (Atherton & Irwin, 1996). Hydraulic robots can perform mechanical tasks repeatedly and achieve utmost accuracy in a dangerous working environment like subsea work and nuclear engineering (see Figure 2.6). The manipulator is one typical hydraulic robot widely used in manufacturing industry, construction industry and other industries with difficult working conditions and heavy load requirements (Ranch, 2014) (see Figure 2.7).

Figure 2.6 Schilling Robotics - TITAN 4 Manipulator (FMC technologies, 2014)

Figure 2.7 Brokk-100 hydraulic demolition machine (Brokk, 2014)

Mobile robots are another kind of robot that could be hydraulically actuated. Legged robots are mechanical structures with legs that they have several links connected by prismatic or rotational joints which make them adapt to irregular terrains easily (Silva & Tenreiro Machado, 2007). They could be applied successfully in nuclear power plants or places with high radiation (Konaka, 1991). The General Electric Walking Truck or Cybernetic Anthropomorphous machine is an early development in legged robots with a hydraulic drive system (see Figure 2.8). A human operator in the truck used both arms and legs to interface with force-feedback control devices (GE, 2012).

Big Dog is the most famous hydraulically actuated quadruped mobile robot developed by Boston Dynamics (see Figure 2.9). Its power source is an internal combustion engine driving a variable displacement pump. Four hydraulic actuators for each leg drive the complex motion of the joints (Boston Dynamics, 2008). Mobile robots could benefit substantially from increased energy-efficiency, in the meantime even 'Big Dog' suffers from reduced payload and range due to high power consumption (Bhatti & Plummer, 2011).

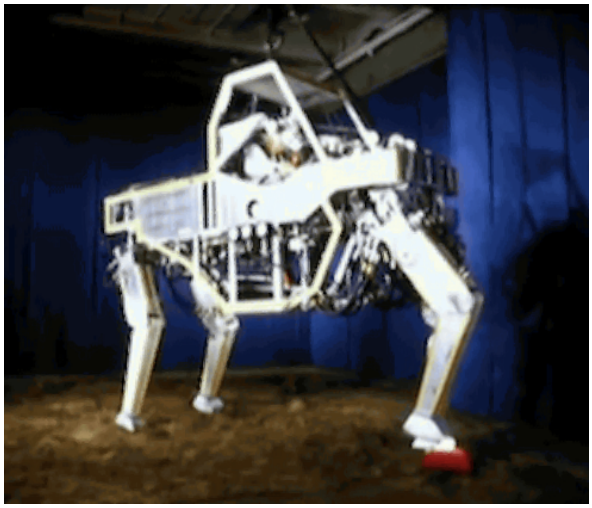

Figure 2.8 General Electric Walking Truck (GE, 2012)

As a typical application of a multi-axis hydraulic system, a mobile robot requires sufficient power to be supplied to many independently controlled actuators, whilst minimising weight and size. A fixed pressure hydraulic power supply with flexible hoses connecting to the valves is the conventional hydraulic actuation circuit for robots (Habibi & Goldenberg, 1994). However the conventional fixed supply pressure valve-controlled hydraulic system can't achieve good energy-efficiency. Low efficiency requires a larger power source and more heating thus a bigger cooling system. Energy-efficient multi-axis hydraulic actuation systems should be a worthwhile research area for mobile robots.

Figure 2.9 BigDog on snow (Boston Dynamics, 2014)

2.2.2 Motion control of multi-body robots

The motion control of robots can be divided into two main areas: kinematic control and dynamic control (Boddy, et al., 1996). Kinematic control is to deal with the motion of rigid bodies without reference to their masses or forces producing the motion. Dynamic control is to use the effects of the forces following the commanded motion (positions/velocities) (Koivo, 1989). Dynamic analysis, i.e. the relationship between actuation forces/torques and motion, is important for the mechanical design, the motion control and simulation of robots. It can help the robot controller predict the forces/torques to a command motion, which improves the dynamic response of the robot motion (Siciliano, 2008).

Figure 2.10 shows a classic design of robot dynamics control. A primary controller is an inverse dynamic model which computes the command signals under ideal circumstances. A secondary controller is designed as a corrector to compensating for the effects caused by inaccuracies in the inverse model and disturbance acting on the system.

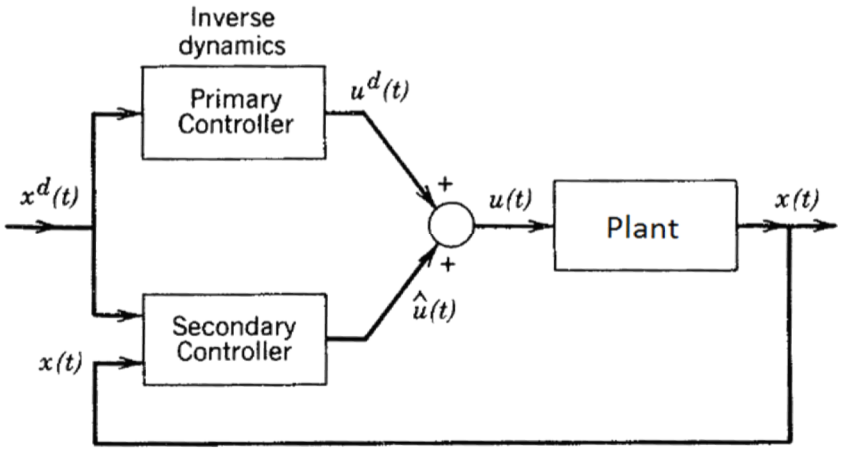

Figure 2.10 Robot control system with primary and secondary controllers

For a known objective, computed-torque method (also known as inverse dynamics) is one effective model-based control, which has potentially higher tracking accuracy and lower required feedback gains required (Sciavicco & Siciliano , 2000). In the computed-torque method, the robot nonlinear dynamics is compensated through feedback linearization.

Normally, the dynamical equations of motion for a multi-joint robot can be calculated by the Lagrange energy function (Ortega & Spong, 1989). Another approach is using Newton-Euler's formulation, considering each link as a free body. Lagrange energy function is a dynamical model for the whole robotic system. Hence, the interactions between the variables and the coupling influence between dynamical equations of the joints are quite apparent (Koivo, 1989). Therefore, for a research of multi-body mechanisms (e.g. a multi-joint robotic arm) with distributed masses, Lagrangian dynamics provide a sufficient simple method to construct the equations of motion (Niku, 2011). Generally, the dynamic equations figured out can be expressed as follows:

$$M(q)\ddot{q} + C(q,\dot{q})\dot{q} + G(q) = \tau \qquad (2.1)$$

where $q, \dot{q}, \ddot{q}$ are the joint position, velocity and acceleration vectors, respectively, *M(q)* is the inertia matrix, $C(q,\dot{q})$ is the centripetal and Coriolis matrix, $G(q)$ is the gravity vector and τ is the required torque. But in most practical cases, the plant is not exactly known. The Equation 2.1 has to be written as:

$$\check{M}(q)(\ddot{q}_d + K_v\dot{e} + K_p e) + \check{C}(q,\dot{q})\dot{q} + \check{G}(q) = \tau \qquad (2.2)$$

where $\check{M}(q), \check{C}(q,\dot{q})$ and $\check{G}(q)$ are the estimations of $M(q), C(q,\dot{q})$ and $G(q)$ respectively, K_v and K_p are symmetrical positive definite gain matrices; q_d is the desired joint position; $e = q_d - q$ is the tracking error vector. So this equation includes motion feedback to complete the commanded torque from each actuator, and fits the structure shown in Figure 2.10.

The uncertainties in the robot dynamic model make the estimated computed-torque control lack robustness in actual performance (Chen, et al., 2012). Some adaptive control methods had been proposed and validated. An adaptive Jacobian controller for robot tracking control with uncertain kinematics and dynamics was proposed (Cheah, et al., 2006). It was validated experimentally that the end-effector was able to track a desired trajectory with the uncertain kinematics and dynamics parameters being updated online using feedback of the end-effector position. A decentralized adaptive robust controller for trajectory tracking of robot manipulators was illustrated (Yang, et al., 2012). A disturbance observer (DOB) was used for compensating the low-passed coupled uncertainties, and an adaptive sliding mode control term was used for handling the fast changing components of the uncertainties beyond the pass-band of the DOB.

For a simple robotic system with typical control accuracy requirements, classic computed-torque control with simple PD or PID linear feedback can provide excellent tracking performance by considering nonlinear compensation with a precise dynamic model (Yang, et al., 2008).

As a conclusion of this section, hydraulic robots can increase productivity dramatically while avoiding risk to human operators. The power source available to feed the robot should be compact to reduce the weight and size of the whole system. As mentioned in last section, the energy-efficiency of hydraulic robots is becoming more and more important in a world concerned with energy consumption; and the conventional fixed supply pressure valve-controlled method is inefficient. For the motion control of a robot manipulator, the computed-torque control is a classical and effective method to meet the typical requirements of control accuracy. Next section is a review of several hydraulic actuation solutions which have higher energy-efficiency than conventional fixed supply pressure valve-controlled system.

2.3 Energy-efficient solutions for hydraulic actuation systems

2.3.1 Hydro-mechanical load sensing systems

To avoid the excess pressure drop over the control valve in fixed supply pressure hydraulic actuation, load sensing is one common concept which means a type of pump control according to the sensed load information.

The conventional hydro-mechanical load sensing (HM-LS) system detects the load pressure P_L, and then set the outlet pressure of the pump P_S higher by a certain amount ΔP than P_L by the pump regulator. Hence, there is a constant pressure drop ΔP over the control valve. Usually, this pressure drop is normally 15 to 25 bar (Jing, 2010).

To implement this constant pressure drop for multi-axis systems, pressure compensators are required to work with the control valves. When the individual compensator is located between the pump and individual control valve, the pre-setting of the spring in the pressure compensator maintains a constant pressure drop over the control valve. As a result, the flow rate of this load branch (the linear velocity of this cylinder) depends on the opening of the individual control valve, independent of the load pressure. Unfortunately, if the pump flow is insufficient, the control of the pressure compensator fails; as a consequence, the highest load branch has to slow down (see Figure 2.11 Left). Another design is to locate the individual pressure compensator between its control valve and the cylinder (see Figure 2.11 Right). The highest load pressure detected controls the pump and two individual pressure compensators. The division of flow is proportional to the opening of the two control valves. If the pump flow is insufficient, the cylinders will be slowed down proportionally.

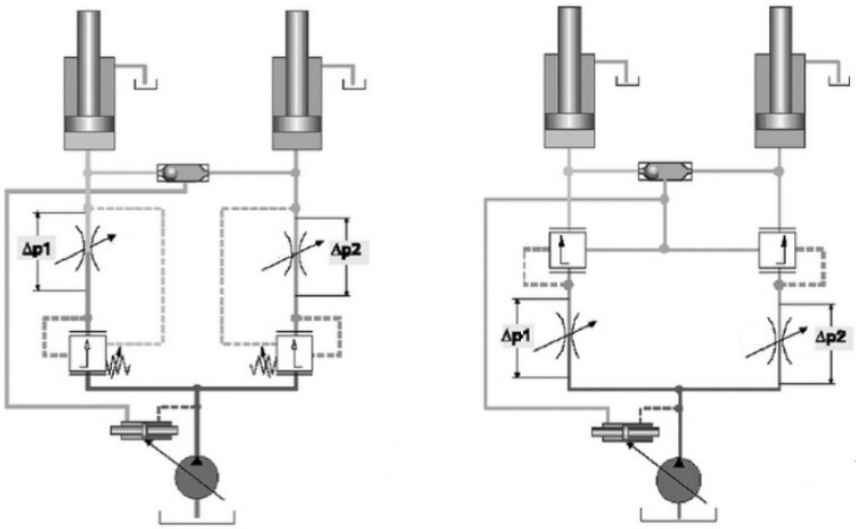

Figure 2.11 Two solutions for HM-LS (Jing, 2010)

The constant pressure drop ΔP in the HM-LS system is excessive for some operating points. Moreover, the load pressure signal sensed is transmitted to the pump controller by the hydraulic circuit, and the pump adjustment may not respond quickly to the load variations. This hydraulic circuit is easily influenced by the interaction of the pressure compensator and the controller of the variable capacity pump, so pressure oscillation can occur. For example, HM-LS gave a poor performance after a disturbance because of poor damping of the control in pump (Lantto, 1994). These drawbacks reveal that HM-LS systems have to be improved in terms of system response and further reduction of energy consumption (Finzel & Helduser, 2008). The electro-hydraulic load sensing (EH-LS or ELS) systems have been developed with the advantages of further energy saving, good handling quality and user friendliness. A review of electro-hydraulic load sensing systems is performed in the next subsection.

2.3.2 Electro-hydraulic load sensing systems

With the necessary electrical equipment's decreasing costs, reliability, and user friendliness, electro-hydraulic load sensing (EH-LS) is becoming widely used with a lot of advantages compared with the hydro-mechanical load sensing system. EH-LS system provides important features such as improved energy-efficiency, ease of controller parameterization and ease of monitoring etc.

A generalised structure of an electro-hydraulic load sensing system is shown in Figure 2.12. Djurovic & Helduser proposed a concept for general EH-LS: flow matching. It means that the flow generated by pump should meet the demand from the actuators exactly; and the individual flow rates are controlled by individual control valves. The pump flow is adjusted by the variation of pump capacity and/or motor speed (Djurovic & Helduser, 2004). They investigated three solutions: flow control without feedback (FC-M/ECV), position control of the individual pressure compensator (PC-IPC) and position control of the 3-way pressure compensator (PC-3WPC) (Djurovic & Helduser, 2004).

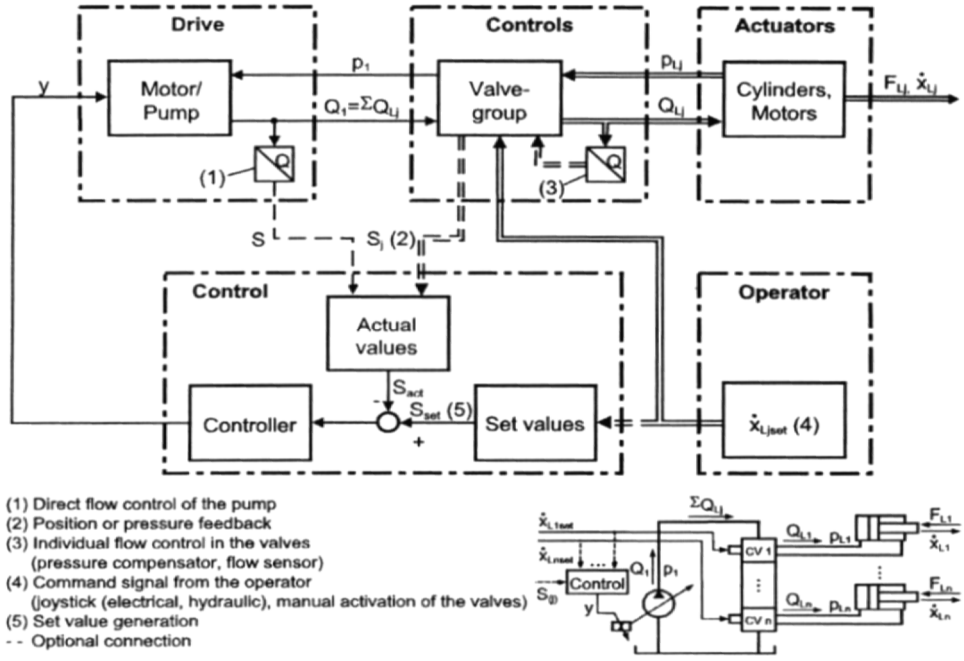

Figure 2.12 Generalised structure of an electro-hydraulic load sensing system (Djurovic & Helduser, 2004)

FC-M (E)/CV is the simplest design (see Figure 2.13). The pressure compensator keeps the pressure drop over the control valve constant, and the commands for the control valve opening are sent from the controller. This idea was presented firstly in 1994 (Harms, 1994).

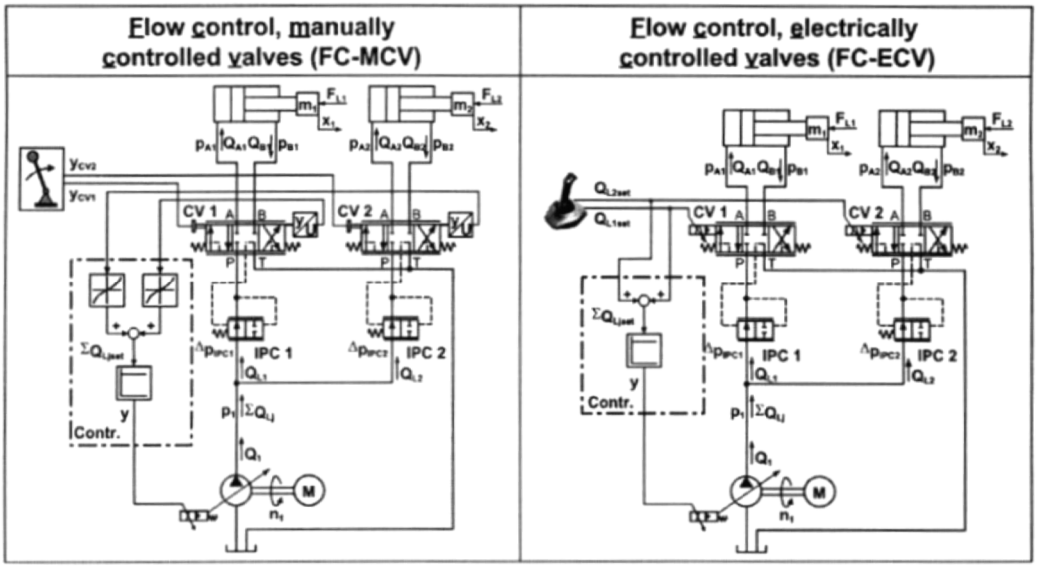

Figure 2.13 EH-LS system with primary pressure compensators and flow control without feedback (Djurovic & Helduser, 2004)

PC-IPC uses the maximum value of the measured positions of pressure compensators to be the feedback signal (see Figure 2.14 left). The PC in the highest load branch is the most open one, which is used for the adjustment of the pump flow. But this method can't be applied on a secondary pressure compensator system. PC-3WPC measures the error of a 3-way pressure compensator (3WPC), which maintains the pressure drop over PC and CV of the highest load branch and throttles the excessive pump flow to the reservoir.

Djurovic and Helduser's investigation consisted of the controller design, steady state behaviour comparison and dynamic behaviour comparison of the experimental results for loads consisting of a torque-controlled hydraulic motor and pressure-drop controlled throttle valves. The HM-LS with a LS margin of 20 bar was used for comparison. The comparison of steady state behaviour revealed that EH-LS systems achieved a reduction of the pressure excess of 10-12 bar. The comparison of dynamic behaviour proved that EH-LS had higher damping and shorter settling time than HM-LS. The static accuracy of an open loop flow control system (FC-M/ECV) is limited by the linearity characteristics of the pump controller and the volumetric efficiency of the pump. Hence the feedback control methods (PC-IPC and PC-3WPC) which use several sensors can provide better performance (Mettälä, et al., 2007).

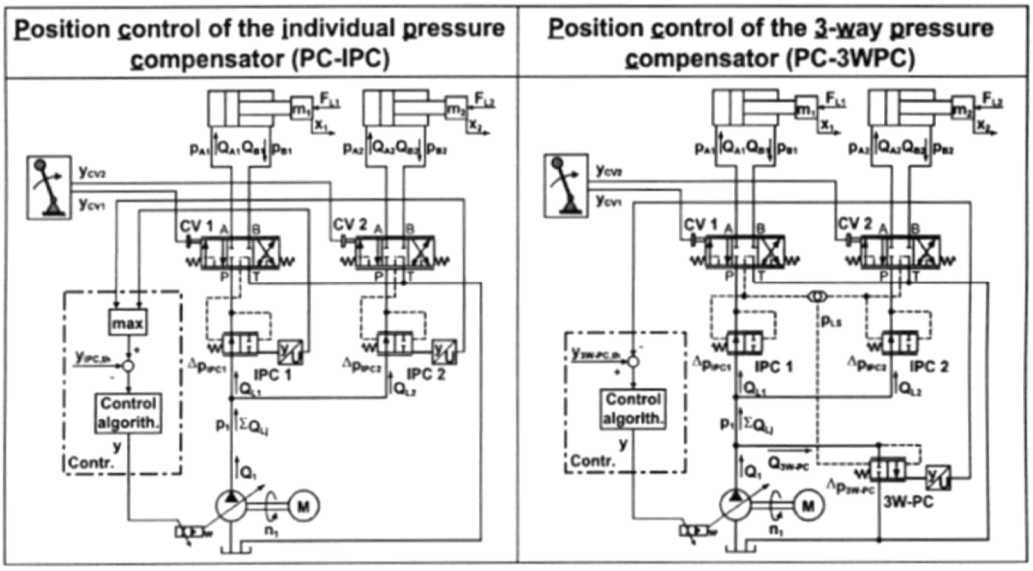

Figure 2.14 EH-LS systems with position control feedback (Djurovic & Helduser, 2004)

An investigation into excavators using typical load cycles was carried out to present the potential advantage of EH-LS flow matching (Finzel, et al., 2009). The results indicated that the EH-LS flow matching method reduced the energy consumption by about 11%. The enlargement to dual circuit systems increased the savings (see Figure 2.15). Axin analysed the dynamic advantages of the flow matching concept (Axin, et al., 2011). Furthermore, Axin presented a novel way to optimize the damping by controlling the opening of the directional valve.

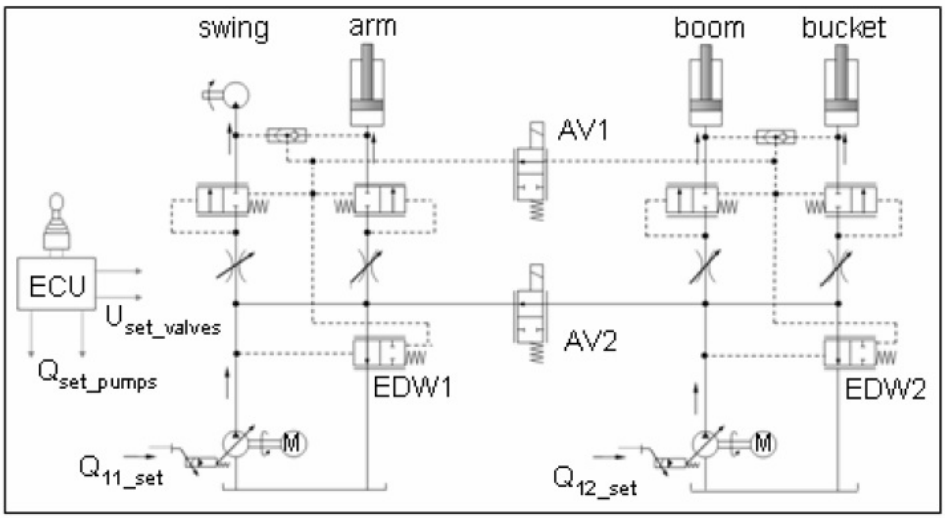

Figure 2.15 New EH-LS dual circuit system (Finzel, et al., 2009)

The working pressure was used as a feedback signal in simulation research on a mini evacuator (Cheng, et al., 2014). Cheng modified the common flow matching system with usage of load pressure feedback and adaptive valve opening regulation. The simulated results showed the improved flow matching system had reduced the energy consumption compared with the original open-loop flow matching system: the system pressure had been reduced up to 2.8 MPa and the system efficiency could be improved up to 23.3%. Meanwhile, the dynamic response was also satisfactory. The experimental test on a bench was expected to validate the advantages of this new strategy (see Figure 2.16). It should be noted that the low pass filtering to the pressure signal is required to reduce the noise in load pressure feedback methods, Cheng pointed out.

Figure 2.16 The photograph of the test stand for the energy-efficient flow matching concept (Cheng, et al., 2014)

Using a variable-speed fixed-capacity pump as an alternative to a variable displacement pump is also possible. Some early applications of speed control pumps have been studied to validate the efficiency improvement (Helduser, 2003). Lovrec, Kastrevc and Ulaga investigated the performance of an EH-LS system with a speed-controlled induction motor and a constant-displacement internal gear pump (Lovrec, et al., 2008). The comparison of the experimental results between a variable capacity mechanically controlled axial-piston pump and a speed-controlled fixed capacity pump were presented: the speed-controlled pump concept was cheaper, easier to maintenance, more robust, lower noise and higher efficiency over the whole range. But the performance of speed-controlled pump system relies on the electric motor and the system response may be influenced by the tribology problems at low-speeds and higher rotational inertia (e-motor rotor).

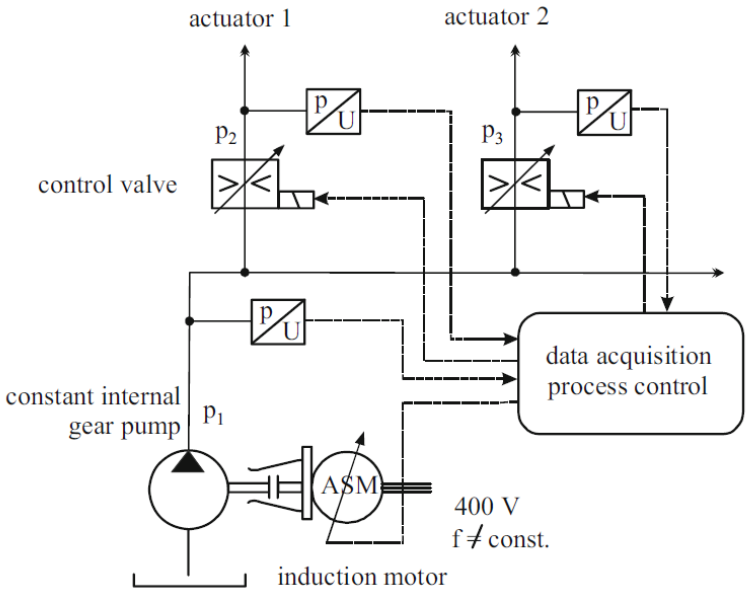

Figure 2.17 EH-LS system with speed control pump (Lovrec, et al., 2008)

Scherer discussed several advanced control strategies mentioned in previous paragraphs and pointed out that each of them leads to an energy efficient system. However, if the consumers reach cylinder end stops, the velocity inputs and the actual flow do not match. For this problem, an electronic control concept using load pressure feedback was proposed to prevent flow oversupply (Scherer, et al., 2013).

As a conclusion, electro-hydraulic load sensing concept can be implemented by two means: a variable displacement pump driven by a constant speed motor or a constant displacement pump in combination with a variable speed motor. The second way has shown a large range of advantages but it requires frequency converter and pressure feedback. An important point is that the dynamic response of the load sensing systems is not as good as fixed supply pressure systems, as both pump displacement control and (usually) electric motor speed control, is significantly slower than conventional fixed supply pressure valve control method.

2.3.3 Separate meter in and meter out systems

A number of other options for improving the energy-efficiency of hydraulic systems are possible. Researchers recognized that the coupling of meter in and meter out orifices in one proportional control valve is not ideal. The mechanical connection makes the system robust and easy to control (one signal to one control valve, one valve to one actuator). However, the system has unnecessary energy losses during most operating situations. Research about energy saving by decoupling the two metering orifices was presented by Jansson and Palmberg (Jansson & Palmberg, 1990).

Research about the control characteristics and energy saving for motion control and pressure control was presented for different load conditions (Liu, et al.,

2009). The simulated results showed that separate meter-in and meter-out (SMIMO) could reduce energy consumption and it could achieve satisfactory speed control accuracy with the optimization of system parameters (see Figure 2.18).

Most of time, SMIMO is studied and applied during actuator moving. The constant position demand of a cutting tool head was controlled by SMIMO successfully with the help of electronic control and an artificial imbalance (Rath & Zaev, 2013). Due to the separated-orifice control, more degrees of freedom are involved in SMIMO system compared with traditional valve-control system. Hence more sensors are required and the control to the system is more complex. Sensors cost and lack of robustness is the drawbacks of SMIMO.

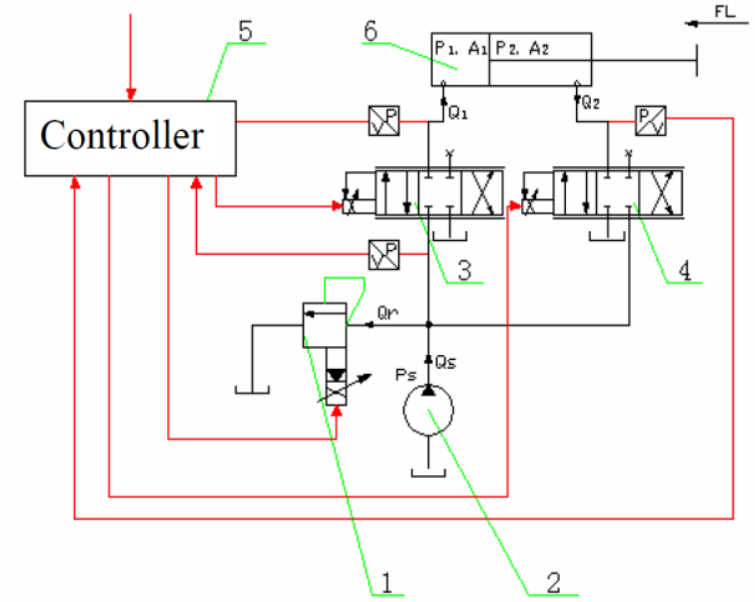

Figure 2.18 Schematic of separate meter in and meter out system (Liu, et al., 2009)

2.3.4 Varying effective area cylinders

For high energy-efficiency, an alternative approach is to redesign the actuator. In a multi-cylinder system, if the effective area of each cylinder can be adjusted to make all the actuators have the same load pressure, then the constant supply pressure matches this load pressure and the pump flow fits the requirements of all the actuators, the efficiency should be higher than a conventional throttling valve-controlled system. The most common cylinder with varying effective area is the multi-stage cylinder (or called telescopic cylinder) which is widely used in lifting equipment such as launchers, tippers and construction equipment (Miao & Wang, 2011). For forward motion the pistons extend from the big ones to the small ones, and for backward motion pistons retract from the small ones to big ones in orders. When each piston rod extends and retracts, the effective area of the cylinder is changing (see Figure 2.19). Therefore, the supply pressure doesn't need to be changed but the output force of the cylinder can be changed (Fan, et al., 2010).

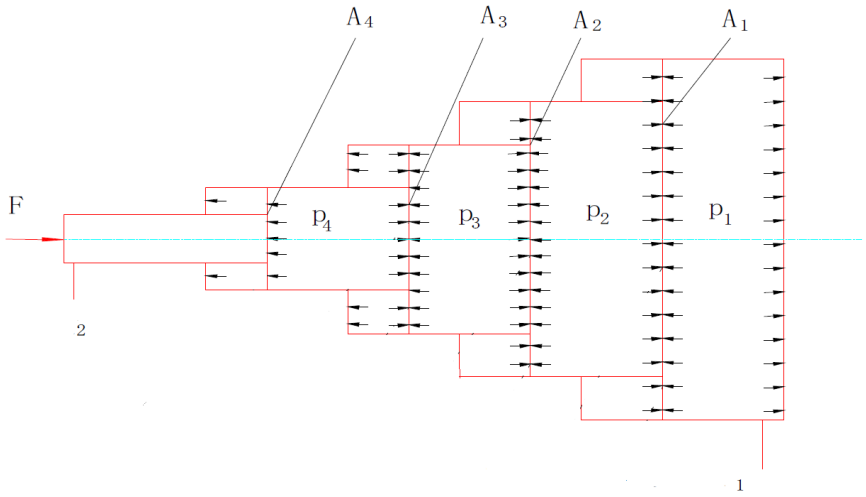

Figure 2.19 A typical multi-stage cylinder

The typical multi-stage cylinder has limitations: there are only several fixed stroke points where the effective area can be changed; it can't be adjusted flexibly in real time according to the changing load. A new design of varying effective area cylinder was proposed for a controllable area according to the load (Yang, et al., 2014). This design adopts four switching valves and one cylinder with multiple chambers (see Figure 2.20). The control of each switching valve determines whether the corresponding sub-chamber is connected to the two main chambers (A_l and A_R) or not. The design with four sub-chambers gives 16 different values of extending force and 16 different values of retracting force, which is accommodates a large range of load.

Varying effective area actuation requires a relatively sophisticated mechanical design according to specific application. It is not suitable to be realised on low-cost applications. Moreover, the area-switching can't give a smooth system response.

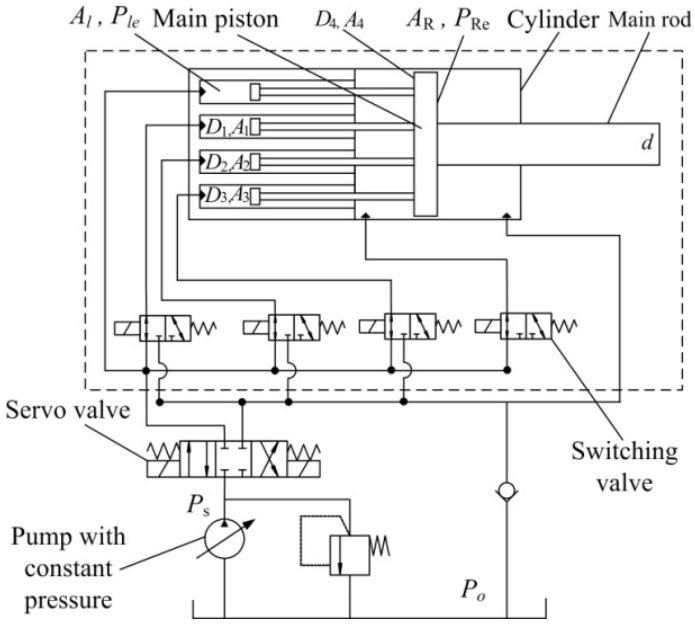

Figure 2.20 Hydraulic circuit using the cylinder with varying effective area (Yang, et al., 2014).

2.3.5 Switching valve control actuation

Conventional valve-controlled hydraulic actuation dissipates energy over the control valves. Switched mode (on-off) control began to be researched in order to minimise these pressure losses (Jeronymo, et al., 1996). An appropriate mathematical model of a switching control hydraulic system in Figure 2.21 has been derived (Manhartsgruber, et al., 2005). This switching control system consisted of two switching valves, a hydraulic cylinder to lift a dead load, pipelines where wave propagation occurred, and some hydraulic accumulators to attenuate pressure pulsations. The model included a set of ODEs describing the actuator dynamics, a transfer matrix transmission line model in the frequency domain, and time variant non-linear valve flow equations.

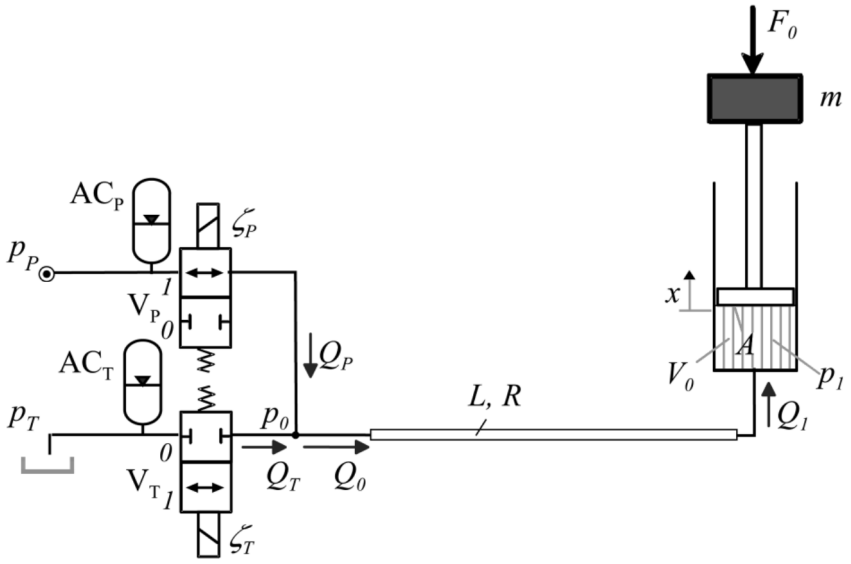

Figure 2.21 Hydraulic circuit of the switching control system (Manhartsgruber, et al., 2005)

Another switched inertance device (SID) was proposed and investigated (Johnston, 2009). This SID made use of the capacitive effect of the fluid volume whilst a small diameter line can have an inductive effect (commonly known as 'inertance'). It has two configurations: flow booster (see Figure 2.22) and pressure booster (see Figure 2.23). The HP supply port is connected to a pump and the LP supply port is connected to a reservoir. When the valve is switched to the HP supply port, a high velocity flow develops from the HP supply port to the delivery port. When the valve is switched to the LP supply port, flow is drawn from the LP supply port to the delivery port due to the fluid inertance. By adjusting the ratio of time between the HP supply port open and the LP supply port open, the delivery flow rate and pressure can be varied.

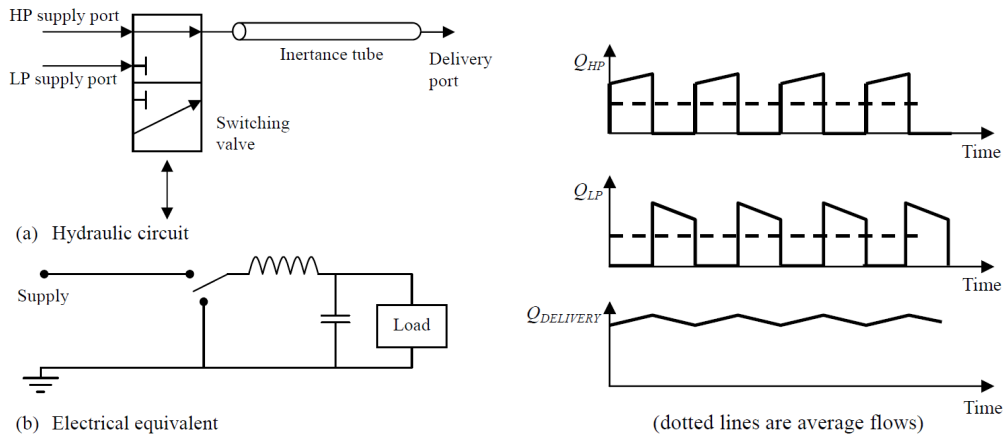

Figure 2.22 Flow booster: schematic diagram and ideal operation (Johnston, 2009)

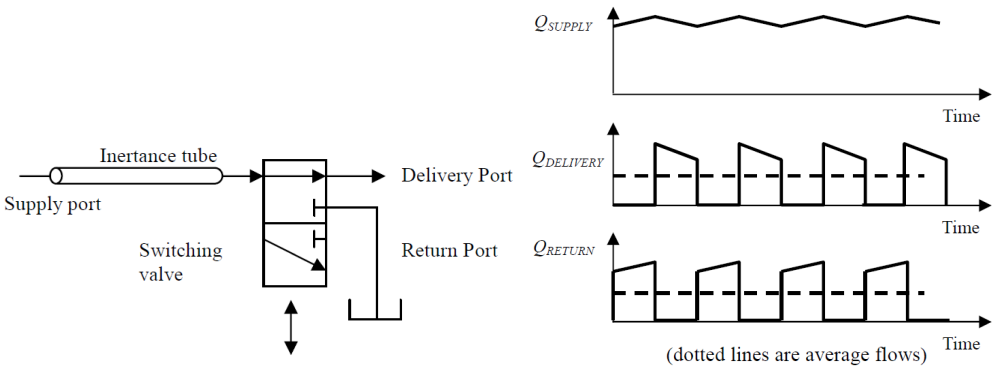

Figure 2.23 Pressure booster: schematic diagram and ideal operation (Johnston, 2009)

The simulation results from Johnston showed that the SID achieved an energy-efficiency up to 90% in the flow boost configuration and 80% in the pressure boost configuration. But the experimental energy-efficiencies were lower. In order to simulate the SID more accurately and to get better performance, an analytical method which can describe this switched inertance device in the time domain and frequency domain had been developed (Pan, et al., 2014). The experimental results showed that this analytical model could be used to predict the SID performance effectively. Moreover, parameter optimization like tube dimension, switching frequency and ratio could be investigated by using this analytical model.

The mechanical design and optimized control of the high speed switching valves is another challenge for switching valve control to get a good performance. Some improvements like short switching time, low leakage and high flow are required compared to the current commercial valves. A high-speed valve concept was proposed that used a phase shift between two tiers of continuously rotating valve spools to achieve a pulse-width modulation (Van de Ven & Katz, 2011). Another high speed switching valve was designed comprising of two seat-type valves and a high-speed pilot valve (Hu, et al., 2011). The dynamic performance from the simulated and experimental data showed that the valve on-off responses were rapid enough for the motion control of a single-piston hydraulic free-piston engine. A spool type linear-acting fast switching valve was described together with its simulation performance (Sylwester, et al., 2012). The idea of the multi-groove concept was used for spool design in this linear valve (see Figure 2.24).

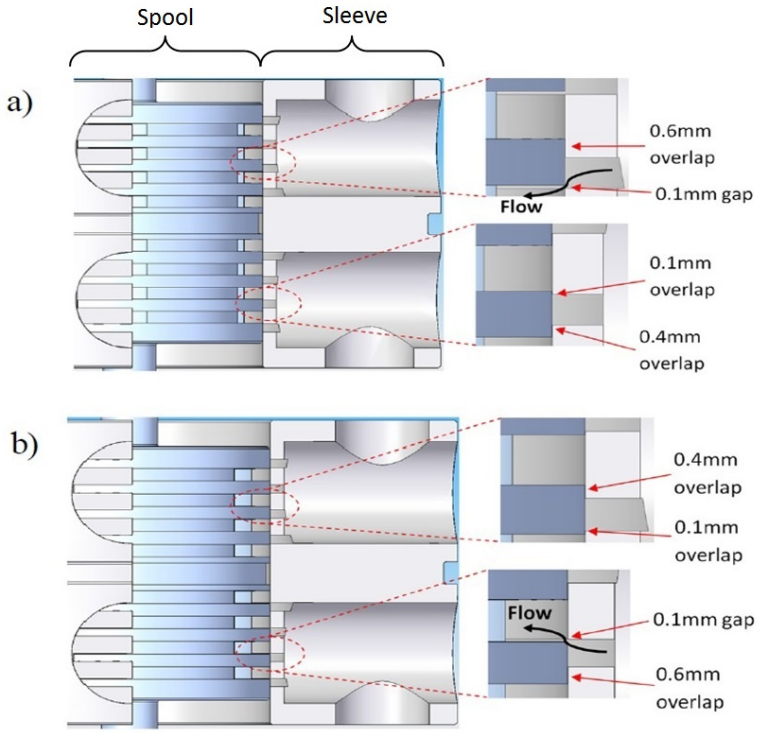

Figure 2.24 Cross-section view of the spool – sleeve,
a) extreme upper spool location, b) extreme lower spool location (Sylwester, et al., 2012)

The switching valve control may create serious noise because of the pulse nature of fluid motion. An active attenuator for pressure pulsation cancellation in a switched inertance hydraulic system was validated effective experimentally (Pan, et al., 2013). This noise attenuator decreased the pressure by superimposing an anti-phase control signal. The performance of this attenuator working on high pressure and flow conditions needs to be investigated in future research.

2.3.6 Electro-hydrostatic actuation (EHA)

An electro-hydrostatic actuator (EHA) does not require a conventional throttling valve, so it can minimize pressure losses and reduces heat generation. Generally, the EHA is a combination of an electric motor, a bidirectional pump, and a hydraulic actuator. An electric motor connected to the hydraulic pump controls the flow rate and pressure of the working fluid to the cylinder by regulating the velocity and torque of the motor. The pressure difference in the actuator chambers, in turn, results in force on the external load and the movement of this load (Lee, et al., 2013).

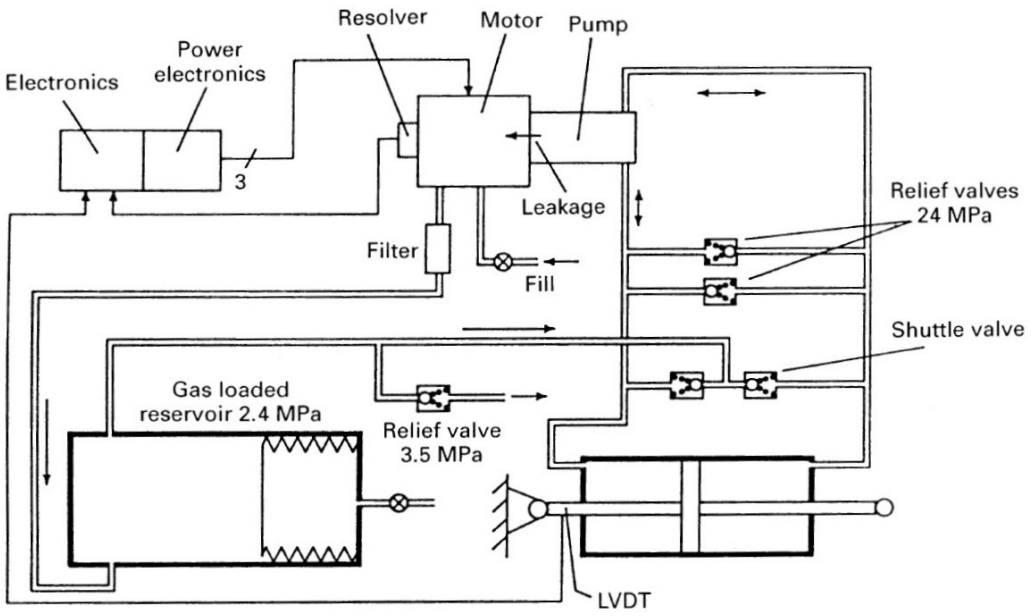

Figure 2.25 Block diagram of the prototype EHA for A320 Aileron (Crowder & Maxwell, 1997)

EHAs have been widely used on aircraft because the flight control system requires compact, reliable, light weight and energy-efficient devices compared with conventional bulk hydraulic systems. A comprehensive dynamic simulation model for the electro-hydrostatic flight actuator prototype developed at Lucas Aerospace was shown and validated experimentally (Crowder & Maxwell, 1997). Besides the civil aircraft, the EHA was verified by ground and flight tests on the F-18 system research aircraft (Navarro, 1997). The EHA showed a good performance compared to a standard aileron actuator and has more load capability. EHAs are becoming the common solution for the primary flight control back up actuators both in civil and military aircrafts.

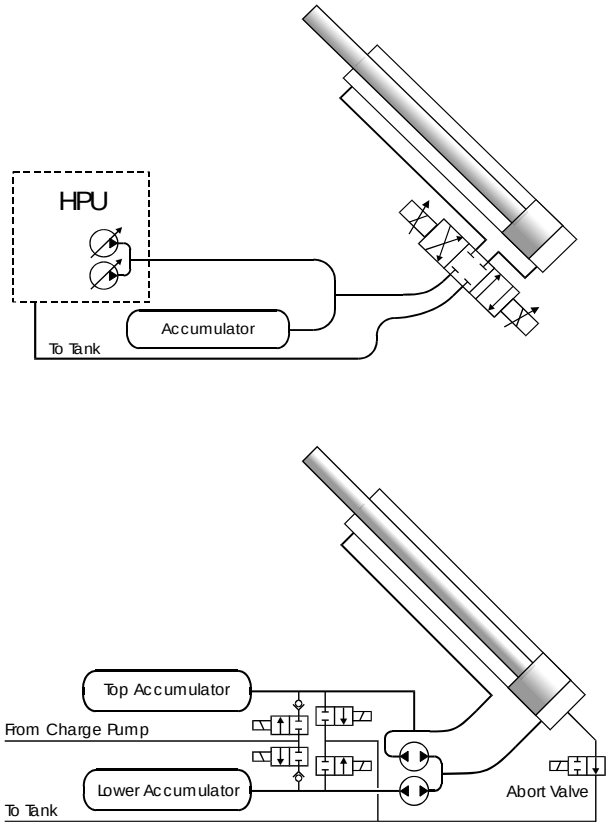

Figure 2.26 Conventional configuration (top) and new EHA configuration (bottom) to hydraulic jack of a flight simulator (Cleasby & Plummer, 2008)

In addition, EHAs have been applied on the six degree-of-freedom motion system in the modern flight simulator (see Figure 2.26). A high efficiency electro-hydrostatic actuation (EHA) design was proposed and experimentally validated on a Boeing 787 Dreamliner simulator (Cleasby & Plummer, 2008). The EHA exhibits 90% power saving compared with conventional fixed supply pressure valve-controlled actuation both in the theoretical prediction and measured results.

Robotics is another potential field of EHA application due to its energy saving compared with conventional valve-control hydraulic system. A commercial EHA system called the Mini Motion Package (MMP) was adopted in a 5 DOF power assistant robot (Khoa, et al., 2012).

Compared to conventional multi-axis hydraulic systems, EHA systems do not need long pipe lines; each axis is self-contained. EHA systems achieve fast response and high accuracy by using an electric servo motor as the control device. Nevertheless, the dynamic response is still inferior to many valve-controlled actuation systems. The performance of the EHA system can be very sensitive to variation within the system parameters such as variety of effective bulk modulus and the leakage coefficient which vary with the changing working environment (Kim & Murrenhoff, 2012). In addition, for multi-axis systems, the weight and size disadvantage of having an EHA for each axis can be significant.

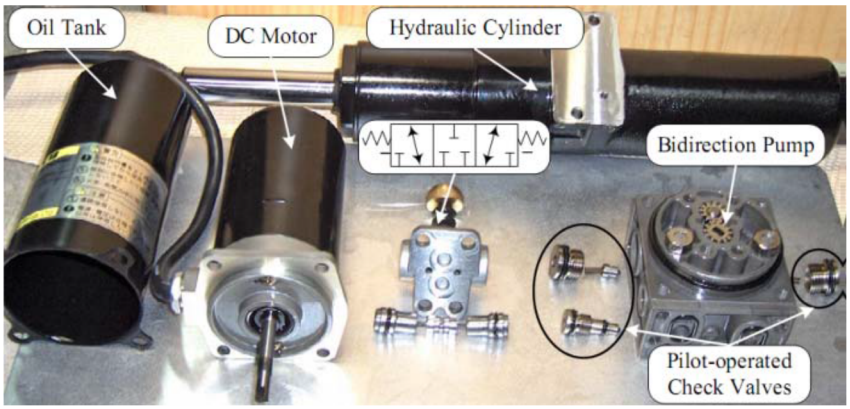

Figure 2.27 The layout of MMP (Khoa, et al., 2012)

2.3.7 Variable pressure valve-controlled hydraulic actuation

A control strategy of maximizing the valve opening of the highest load branch was presented for the purpose of energy saving (Scopesi, et al., 2011). Scopesi's control algorithm 'Variable pressure valve-controlled hydraulic actuation' (VPVHA) aimed to reduce the energy loss by setting a minimum supply pressure and maximizing the valve opening of the highest load branch. The research plant was considered to have a fixed displacement pump connected to a brushless DC motor, and some cylinders, each connected to a proportional 4/2 valve (see Figure 2.28).

The VPVHA controller had two parts: feed forward and feedback. The feed forward was an inverse model which could predict the required angular velocity of the servo pump and the spool position of the control valves. The feedback controller was used to correct the feed forward command. The actual positions of cylinders were used as feedback signals. Scopesi designed a simple P controller to alter motor speed and valve spool positions.

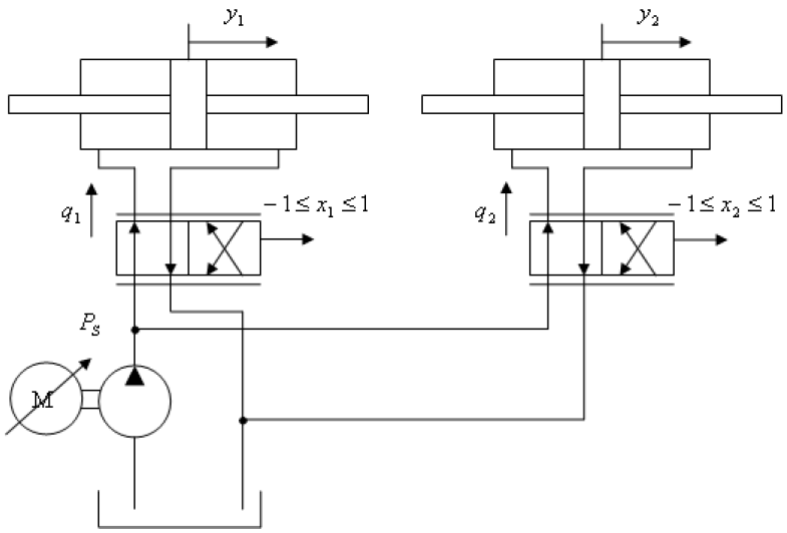

Figure 2.28 The hydraulic circuit of the plant for VPVHA research (Scopesi, et al., 2011)

No pressure compensator or pressure feedback was used in VPVHA control algorithm, which was a big difference between VPVHA and load sensing system. The pump flow was designed to be varied according to the demand of flow by a servo motor. Moreover, position feedback was involved to enhance the accuracy, which is a big difference with Mettälä's research (Mettälä, et al., 2007).

The simulation results showed the VPVHA could save energy up to 70% compared with the traditional fixed supply pressure system. The position tracking showed a satisfactory dynamic response as well. The experimental tests are required to validate this novel method. In Figure 2.28, the VPVHA was applied to equal area cylinders, which could bring one less unknown freedom than unequal area cylinders. A detailed mathematical modelling of unequal area cylinder motion control was developed and the performance of proposed backstepping control was shown in simulation (Schwarzgruber, et al., August 2014).

For further research, some motion demands other than sine waves should be tested, such as a square wave which is better to observe the dynamic performance of VPVHA. In addition, a simplistic load was presented as a combination of mass and damper in Scopesi's simulation. In real applications, the load prediction process may need to be much more complex. Accurate load prediction is essential to realise VPVHA experimentally.

2.4 Concluding remarks

Hydraulic power transmission is utilized in a wide range of applications. As a fast growing industry, hydraulically actuated robot is attracting increasing more and more attention. High energy-efficiency along with good control ability will be the main interests in future research. Computed-torque control is a classic and effective method to meet the typical requirements to motion control accuracy, but it is only normally investigated for electrical rather than hydraulic robots.

The conventional fixed supply pressure valve-controlled actuation is simple but inefficient. Lots of other hydraulic actuation methods have been investigated. Load sensing is a common idea to improve efficiency for mobile machines. Electro-hydraulic load sensing (EH-LS or ELS) shows advantages like smaller LS-margin, more user friendliness and fast response compared with hydro-mechanical load sensing (HM-LS). But it relies on the good and stable performance of the sensors to get the satisfactory feedback signals. Some extra processing work is often required to smooth and/or compensate the feedback signals (Cheng, et al., 2014).

Separate meter-in and meter-out (SMIMO) brings energy saving by decoupling the two orifices in one proportional control valve. But more sensors are required as there are more control signals available to controller (Eriksson & Palmberg, 2010). Variable effective cylinder area actuation matches the load pressure by changing the effective area in cylinder. However it requires specific and complex manufacturing. Switching valve control allows high energy efficiency but the noise problem exists and a high-speed switching valve is also essential. Electro-hydrostatic actuation (EHA) is not very suitable for multi-axis systems where a single power source would save space and weight.

Scopesi proposed a variable pressure valve-controlled hydraulic actuation method (VPVHA) in 2011 (Scopesi, et al., 2011). VPVHA showed good

performance in simulation for a simple two-axis system with single pump system. It had the following advantages:

- Energy efficient: the throttle loss over control valve is minimised, and the pump generates exactly the flow required.
- Cost efficient: a servo motor with a fixed displacement pump is usually cheaper than a variable displacement pump, and only are motor and pump is required.
- Compact: no pressure compensators, and the use of electronic controller, and a single servo-motor and fixed capacity pump, which makes VPVHA suitable for weight-sensitive applications such as robotics.
- Easy tuning: the VPVHA feedback controller adopts simple P(I) control which is easy to implement and tune for a good system response.

The cylinder used in the Scopesi's model was equal-area type. This project will modify it to suit the un-equal area type of cylinders which are used for a robotic arm. Moreover, the realistic complex loads will be considered rather than the simple load in Scopesi's simulation model. To differentiate it, a modified name is given to the hydraulic actuation design proposed in this project: load prediction-based variable supply pressure valve-control, and the abbreviation is VPVC. The VPVC method will be validated on the motion control of a two-axis robotic arm, and both the simulation tests and experimental tests are presented.

Chapter 3

3 Control Algorithm

This chapter will illustrate the development of the control algorithm of variable supply pressure valve-controlled (VPVC) system. The first section is a general description of the VPVC control algorithm. Then two separate sections illustrate the two parts of the VPVC controller: feed forward and feedback. For the purpose of performance comparison between VPVC and conventional fixed supply pressure valve-controlled (FPVC) systems, the control algorithm of FPVC is also described in this chapter.

3.1 Introduction to VPVC control algorithm

In this project, as an example system, the motion of a two-axis robotic arm will be controlled. The robotic arm has two rotational joints: shoulder and elbow (see Figure 3.1). Each joint is actuated by an unequal area actuator.

The proposed hydraulic circuit of this 2 degree-of-freedom (DOF) robotic arm hydraulic actuation system is shown in Figure 3.2. The power source of this system is an AC brushless servo motor and a fixed capacity axial-piston pump in order to achieve high performance with a light weight and low cost. Two direct drive valves control the flow rate into the individual actuators. From the above description, it is clear that the controller is required to send out the motor speed command and the valve opening (spool positions) commands. More generally, the control algorithm should be capable of handling any number of actuators, but two actuators will be used to illustrate the algorithm in this chapter.

Figure 3.1 The two-axis robotic arm

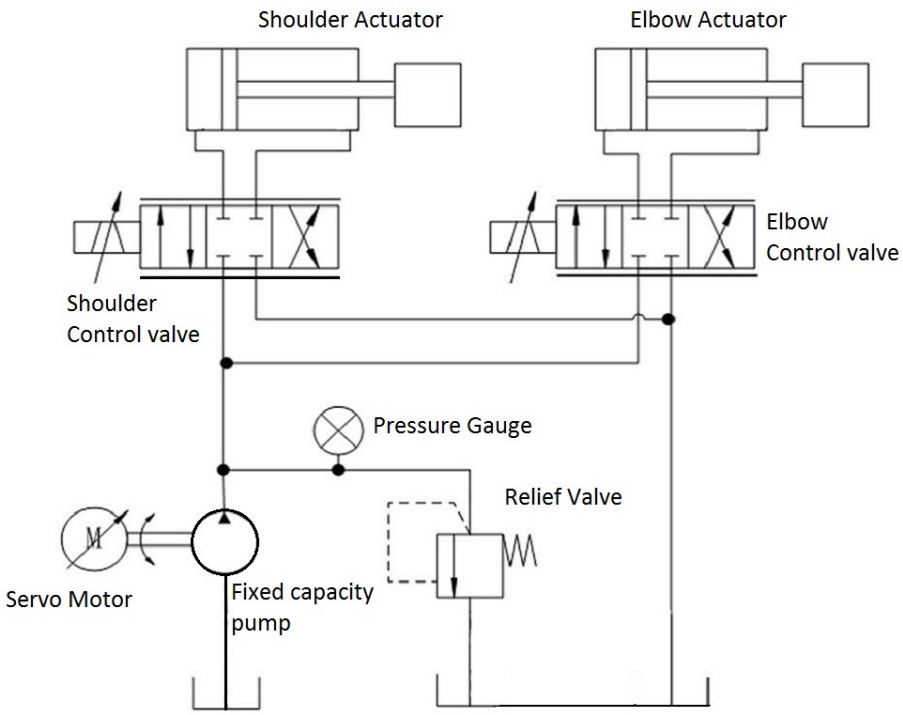

Figure 3.2 The hydraulic circuit diagram of the plant

The VPVC controller consists of two parts: a feed forward part and a feedback part. The feed forward part is an inverse model of the plant. The inverse model predicts the required motor speed along with the required corresponding spool positions of the two valves, and these command signals are intended to achieve the minimum required supply pressure. The feedback part uses the measured positions of the actuators to adjust the feed forward command signals (motor speed command and valve opening commands). A proportional controller is used for the motor speed feedback control and proportional-integral controllers for the valve opening feedback control. The final command signals to the plant are the sum of feed forward part and feedback part (see Figure 3.3).

In Figure 3.3, the circumflex ($\hat{}$) represents the output command signal of the feed forward controller. The tilde ($\tilde{}$) represents the final control signals, which act as the command signals to the local valves and the motor control loops embedded in the plant.

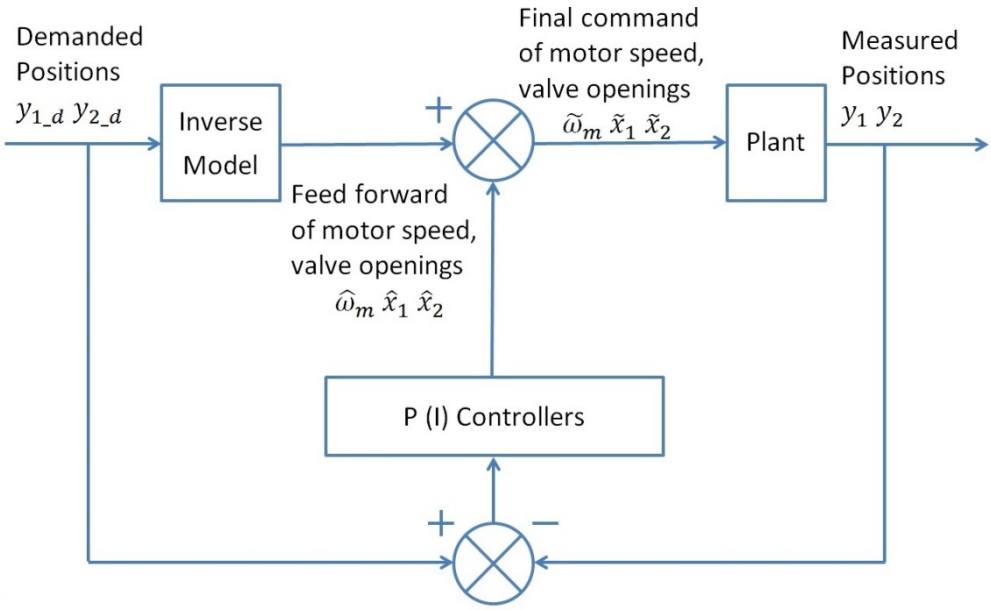

Figure 3.3 Simplified diagram of VPVC control algorithm

In the figure:

- ω_m represents the motor speed command; x_1 and x_2 represent the spool position command of the shoulder valve and the elbow valve respectively.
- y_{1_d} and y_{2_d} represent the demanded linear position of the shoulder actuator and the elbow actuator respectively.
- y_1 and y_2 represent the actual measured linear position of the shoulder actuator and the elbow actuator respectively.

From the above introduction, it is clear that the feed forward part is the core of the VPVC control algorithm. If the inverse model is good, the feed forward part dominates the final command signals. The control algorithm of the VPVC controller is intended to reduce energy waste by maximizing the valve opening and minimizing the supply pressure. Therefore, energy efficiency is increased by reducing throttling loss over the control valves and reducing the power generated by the power pack (the servo motor and the fixed capacity pump). The detailed illustration of the feed forward part will be in the next section.

3.2 Feed forward part of VPVC controller

3.2.1 Minimum supply pressure prediction

The process of VPVC feed forward control is illustrated by the flow chart in Figure 3.4. For each actuator with a given motion demand, the VPVC feed forward controller computes the required supply pressure with two different assumptions: the required supply pressure when the valve controlling this actuator is fully open; the required supply pressure when the pressure in the thrust chamber of this actuator reaches the critical value for no cavitation.

The required supply pressure estimated when the individual control valve is fully open is called P_{SO}, and the one to avoid cavitation in the thrust chamber is P_{SC}, and a specific valve command x_{SC} can be calculated with this condition. The final choice of P_S = max (P_{SO1}, P_{SO2}, P_{SC1}, P_{SC2}), where subscripts 1 and 2 refer to the shoulder actuator and the elbow actuator respectively. The actuator which has this P_S (the higher load requirement) is the master actuator (MA). The control valve command to this actuator is fully open or x_{SC}.

The spool position for the other valve (valve of non-MA) should be recomputed with this predicted P_S. The motor speed command is calculated by the flow rate requirements to the two actuators and compressibility flow for the predicted P_S change. The prediction of P_{SO} and P_{SC} for the individual actuator with given demanded motion is a crucial procedure, which will be introduced in detail as follows.

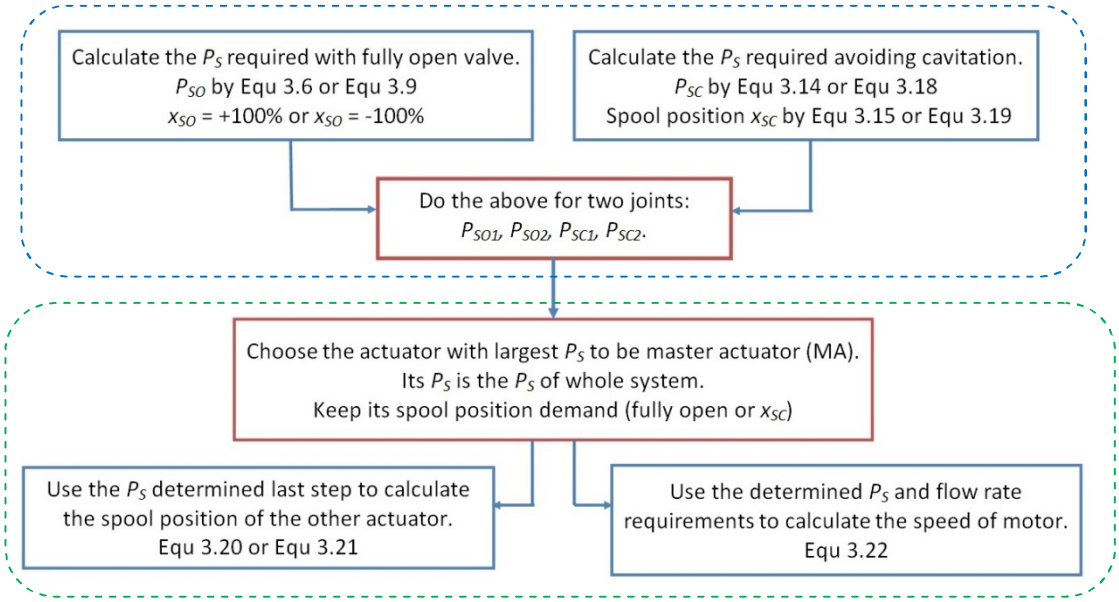

Figure 3.4 The flow chart of the VPVC feed forward controller

3.2.1.1 Supply pressure required with fully open valve setting (P_{SO})

During extension, the return line is connected to the rod side chamber which has pressure P_B and the supply line is connected to the piston side chamber which has pressure P_A (see Figure 3.5). The flow rate requirements can be obtained from the motion demand: $Q_a = A_p\, v$, $Q_b = A_r\, v$.

where:

- Q_a is the flow rate into the piston side chamber, and Q_b is the flow rate out of the rod side chamber.
- A_p is the area of the piston side, and A_r is the area of the rod side.
- P_S is the supply pressure, and P_r is the return pressure.
- v is the linear velocity of the motion demand, and F is the required actuation force generated by the hydraulic actuator.

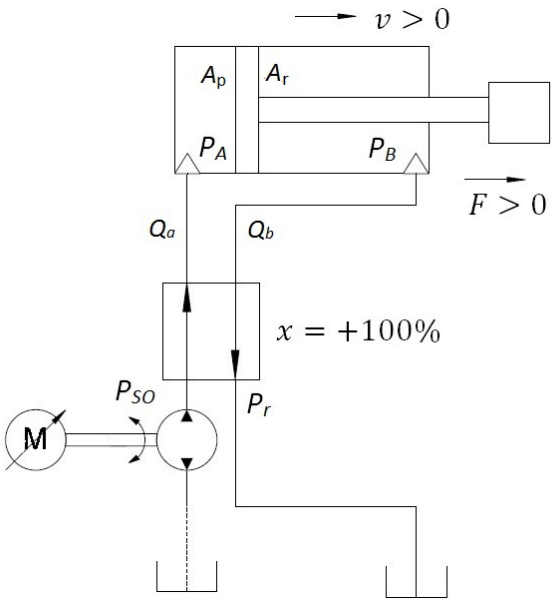

Figure 3.5 The simplified diagram to calculate P_{SO} when extending

The pressure drops across the valve can be represented as follows:

$$\Delta P_{valve\_a} = P_{SO} - P_A \tag{3.1}$$

$$\Delta P_{valve\_b} = P_B - P_r \tag{3.2}$$

Then the orifice equation gives:

$$Q_a = K_V x \sqrt{\Delta P_{valve\_a}} \tag{3.3}$$

$$Q_b = K_V x \sqrt{\Delta P_{valve\_b}} \tag{3.4}$$

where K_V is the valve constant which can be obtained from the rated information in the valve catalogue, and x is the valve opening (from +1 to -1).

If the valve is fully open i.e. x is +100%, and then from Equation (3.2) and Equation (3.4) P_B can be calculated with an assumption of P_r's value and the known K_V from the valve catalogue.

$$P_A A_p - P_B A_r = F \tag{3.5}$$

From Equation (3.5) P_A can be evaluated now.

Finally, back to Equation (3.1) and Equation (3.3) the required P_S i.e. P_{SO} can be estimated. For simplicity, the ratio of area for actuator A_p/A_r is represented as α.

$$P_{SO} = \frac{(\alpha^3 + 1)}{\alpha}\frac{A_r^2 v^2}{K_V^2} + \frac{F}{A_p} + \frac{P_r}{\alpha} \tag{3.6}$$

When retracting, the return line is connected to the piston side P_A and the supply line is connected to the rod side chamber P_B (see Figure 3.6).

Hence, the pressure drops across the valve can be represented as follows:

$$\Delta P_{valve\_a} = P_A - P_r \tag{3.7}$$

$$\Delta P_{valve\_b} = P_{SO} - P_B \tag{3.8}$$

Assume the valve is fully open i.e. x is -100%, then using a similar process as for P_{SO} when extending, the P_{SO} when retracting can be predicted:

$$P_{SO} = (\alpha^3 + 1)\frac{A_r^2 v^2}{K_V^2} - \frac{F}{A_r} + \alpha P_r \tag{3.9}$$

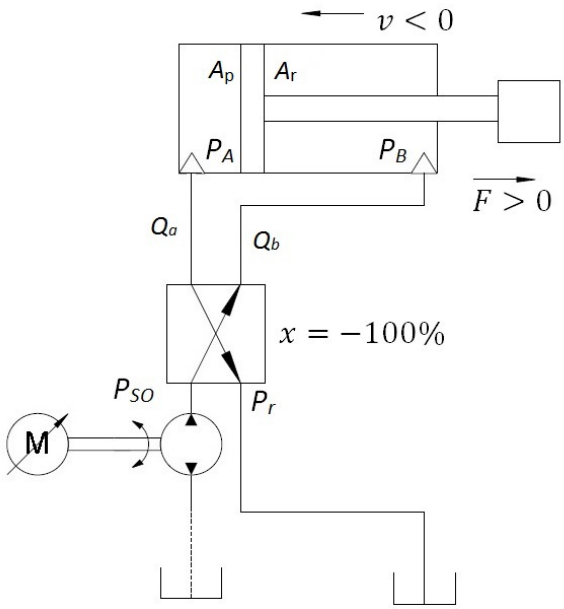

Figure 3.6 The simplified diagram to calculate P_{SO} when retracting

3.2.1.2 Supply pressure required to avoid cavitation (P_{SC})

The previous prediction P_{SO} is based on the assumption of a fully open control valve. However, the controller has to check whether the pressure in the thrust chamber (piston side chamber when extending and rod side chamber when retracting) is high enough to avoid cavitation. The solution to this problem is to impose a pressure equal to a critical threshold value P_{th} in the thrust chamber, thus to compute the required P_S along with the corresponding valve opening according to the motion demand. As introduced before, the predicted supply pressure with this condition is named as P_{SC}.

When extending, supply line is connected to the piston side chamber, which pressure is set to a critical pressure of P_{th} (in this research, P_{th} is set at 2 bar).

$$\Delta P_{valve\_a} = P_{SC} - P_{th} \tag{3.10}$$

$$\Delta P_{valve\_b} = P_B - P_r \tag{3.11}$$

$$\frac{\Delta P_{valve\_a}}{\Delta P_{valve\_b}} = \frac{Q_a^2}{Q_b^2} = \frac{A_p^2}{A_r^2} = \alpha^2 \tag{3.12}$$

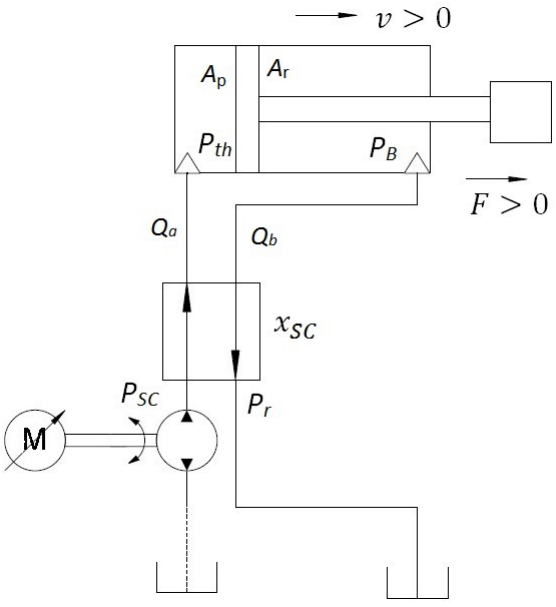

Figure 3.7 The simplified diagram to calculate P_{SC} when extending

With the force equation:

$$P_A A_p - P_B A_r = F \tag{3.13}$$

The value of P_{SC} can be calculated:

$$P_{SC} = (\alpha^3 + 1)P_{th} - \frac{\alpha^2}{A_r}F - \alpha^2 P_r \tag{3.14}$$

The corresponding spool position for the valve to control this actuator is computed:

$$x_{SC} = \frac{A_p v}{K_V \sqrt{P_{SC} - P_{th}}} \tag{3.15}$$

When retracting, P_S is connected to P_B, which is set to a minimum threshold pressure of P_{th} (see Figure 3.8).

$$\Delta P_{valve\_a} = P_A - P_r \tag{3.16}$$

$$\Delta P_{valve\_b} = P_{SC} - P_{th} \tag{3.17}$$

Following the same procedure as for P_{SC} when extending, P_S can be predicted:

$$P_{SC} = \left(\frac{1}{\alpha^3} + 1\right) P_{th} + \frac{1}{A_p \alpha^2} F - \frac{P_r}{\alpha^2} \tag{3.18}$$

The corresponding spool position for the valve to control this actuator is computed:

$$x_{SC} = \frac{A_r v}{K_V \sqrt{P_{SC} - P_{th}}} \tag{3.19}$$

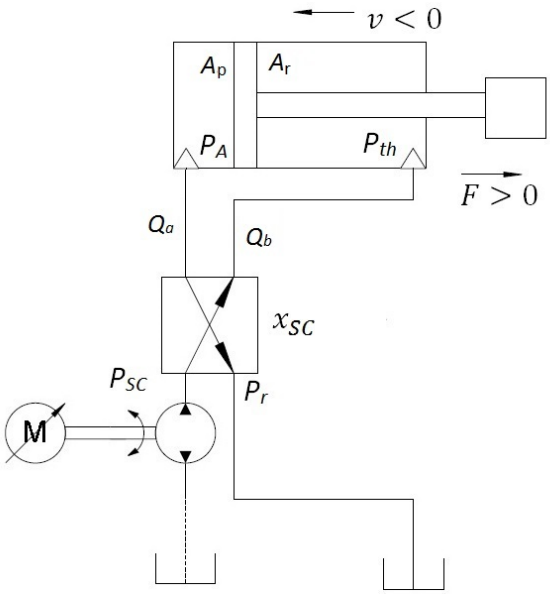

Figure 3.8 The simplified diagram to calculate P_{SC} when retracting

The final choice of P_S = max (P_{SO1}, P_{SO2}, P_{SC1}, P_{SC2}), where subscripts 1 and 2 refer to the shoulder actuator and the elbow actuator respectively. The actuator which has this selected P_S is the master actuator (MA). Hence the valve opening of the MA is fully open (+100% or -100%) or for cavitation avoidance is given by Equation (3.15) or Equation (3.19).

3.2.1.3 Valve opening of the Non-MA and motor speed calculation

After the determination of P_S for the whole system and the valve opening of the MA, the valve of the other actuator (non-MA) is designed to be controlled using the conventional throttling method. If the other actuator is required to extend, its valve opening is calculated by the following equation:

$$x_j = \frac{A_r v_j}{K_V \sqrt{\frac{P_S A_p - P_r A_r - F_j}{\alpha^2 A_p + A_r}}} \tag{3.20}$$

If the non-MA actuator is required to retract, its valve opening is:

$$x_j = \frac{A_p v_j}{K_V \sqrt{\frac{(P_S A_r - P_r A_p + F_j)\alpha^2}{\alpha^2 A_p + A_r}}} \tag{3.21}$$

where x_j is the valve opening command of the non-MA actuator; v_j and F_j are its velocity demand and required hydraulic actuation force respectively.

As the final P_S has been determined, and with the given desired flow rate of each actuator, the required motor speed ω_m can be computed from Equation (3.22):

$$\omega_m = \frac{\frac{d}{dt}\left(\frac{P_S}{K}\right) + \sum_{j=1}^{2} Q_j}{D_P} \tag{3.22}$$

where K is the effective stiffness of the oil inside the supply hoses, and D_P is the displacement of pump.

3.2.2 Load prediction

From the last subsection, it can be concluded that the required hydraulic actuation force F is required for the whole prediction algorithm. Depending on the application, the load force calculation will vary. However some ability to model the load will be required in order to apply the feed forward part of the controller. For the robotic arm used here, the forces are associated with the mass of the 'hand' load and the arm itself. Computed-torque method is used for predicting the motion required force: with the given motion demand to each actuator (linear position demand, linear velocity demand and linear acceleration demand), the required torque for each joint is computed by applying the Lagrange equation of the second kind, which incorporates inertia and weight related items.

$$\frac{d}{dt}\left(\frac{\partial L}{\partial \dot{\theta}_1}\right) - \frac{\partial L}{\partial \theta_1} = q_1 \tag{3.23}$$

$$\frac{d}{dt}\left(\frac{\partial L}{\partial \dot{\theta}_2}\right) - \frac{\partial L}{\partial \theta_2} = q_2 \tag{3.24}$$

where $L = T - V$, L is the Lagrangian of this two-joint robotic arm; T is the total kinetic energy and V is the total potential energy of the robotic arm. q_1 and q_2 are the generalized forces, hence in this case they are the torques required by the shoulder joint and the elbow joint respectively. The θ_1 and θ_2 are defined in Figure 3.9.

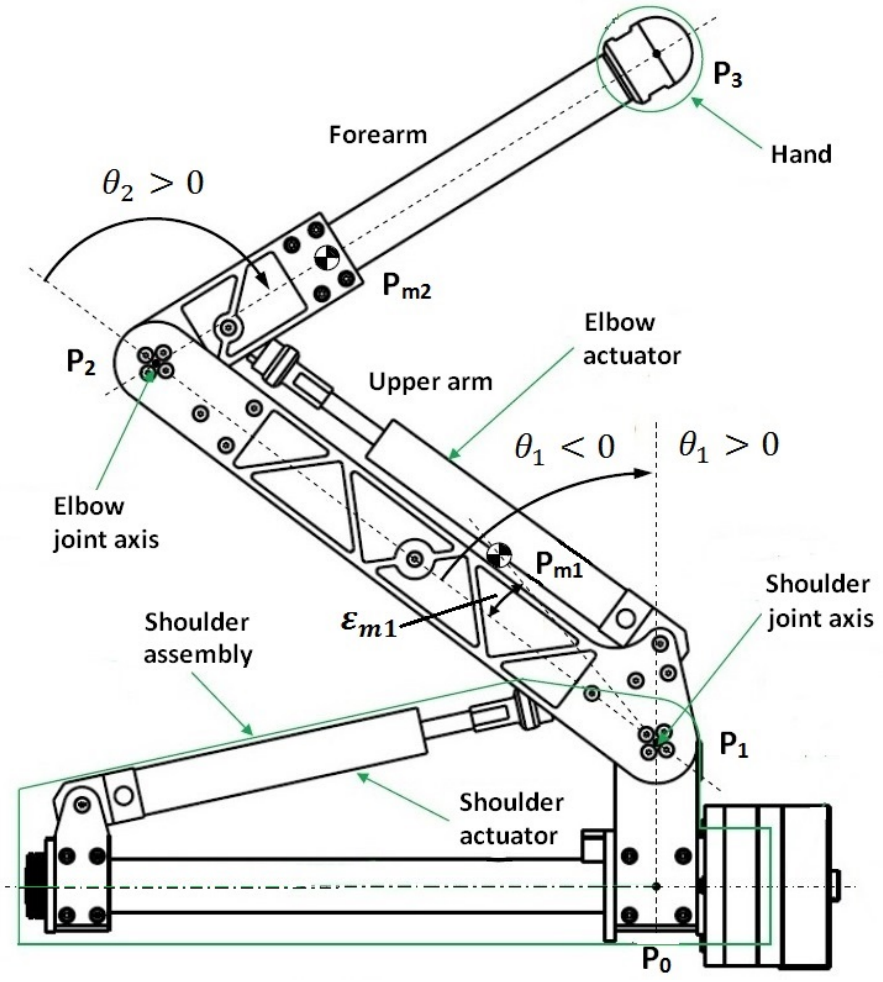

Figure 3.9 Geometry of the robotic arm

The results of Equation (3.23) and Equation (3.24) are as follows:

$$\begin{aligned} q_1 = {} & (I_1 + I_2 + I_3 + L_1^2 M_2 + L_1^2 M_3 + L_2^2 M_3 + C_1^2 M_1 + C_2^2 M_2)\ddot{\theta}_1 \\ & + (I_2 + I_3 + L_2^2 M_3 + C_2^2 M_2)\ddot{\theta}_2 - g L_1 (M_2 + M_3) \sin\theta_1 \\ & - g M_1 C_1 \sin(\varepsilon_{m1} + \theta_1) \\ & - g(L_2 M_3 + C_2 M_2) \sin(\theta_1 + \theta_2) \\ & + L_1 (L_2 M_3 + C_2 M_2)\left(2\ddot{\theta}_1 + \ddot{\theta}_2\right) \cos\theta_2 \\ & - L_1 (L_2 M_3 + C_2 M_2)\left(\dot{\theta}_2{}^2 + 2\dot{\theta}_1\dot{\theta}_2\right) \sin\theta_2 \end{aligned} \tag{3.25}$$

$$\begin{aligned} q_2 = {} & (I_2 + I_3 + L_2^2 M_3 + C_2^2 M_2)\ddot{\theta}_1 + (I_2 + I_3 + L_2^2 M_3 + C_2^2 M_2)\ddot{\theta}_2 \\ & - g(L_2 M_3 + C_2 M_2) \sin(\theta_1 + \theta_2) \\ & + L_1 (L_2 M_3 + C_2 M_2)\ddot{\theta}_1 \cos\theta_2 + L_1 (L_2 M_3 \\ & + C_2 M_2)\dot{\theta}_1{}^2 \sin\theta_2 \end{aligned} \tag{3.26}$$

where:

- M_1 is the mass of upper arm (including the elbow actuator), I_1 is its inertia with respect to upper arm gravity centre, through P_{m1};
- M_2 is the mass of forearm (without hand), I_2 is its inertia with respect to forearm gravity centre, through P_{m2};
- M_3 is the mass of the hand, I_3 is the inertia of the hand with respect to the hand gravity centre P_3;
- L_1 is the distance between P_1 and P_2; L_2 is the distance between P_2 and P_3; C_1 is the distance between P_1 and P_{m1}; C_2 is the distance between P_2 and P_{m2}.

The actuation force F_1 and F_2 required are the values of torques computed divided by the lever arms $l_1(\theta_1)$ and $l_2(\theta_2)$ which vary with angular positions θ_1 and θ_2. The lever arms are shown in Figure 3.10 and their method of calculation is in subsection 4.3.3.

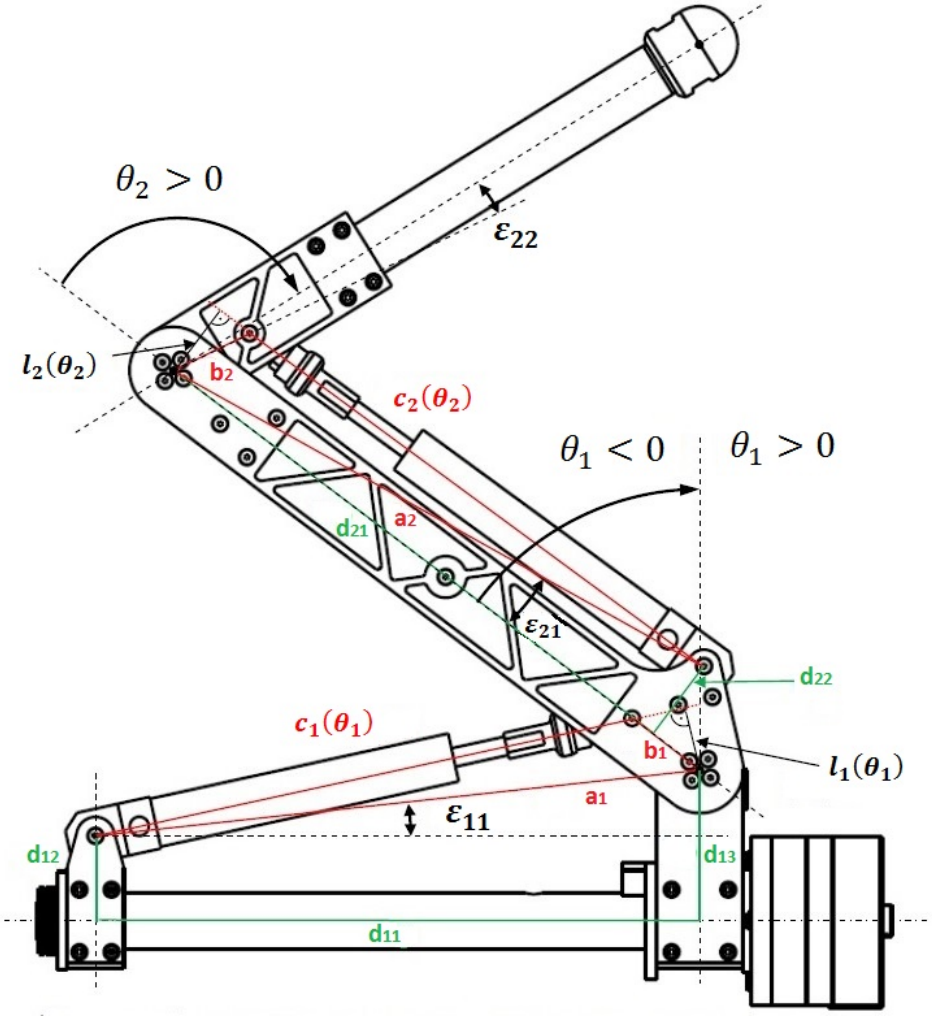

Figure 3.10 Dimension specification of the robotic arm

With the consideration of viscous damping force inside the actuator, the required hydraulic actuation force prediction equations are modified as follows:

$$F_1 = \frac{q_1}{l_1(\theta_1)} + K_f v_1 \tag{3.27}$$

$$F_2 = \frac{q_2}{l_2(\theta_2)} + K_f v_2 \tag{3.28}$$

where K_f the viscous damping coefficient. The friction in the real actuation is complex. But only the viscous damping force is considered in the VPVC controller and the coefficient is assumed to be constant. Subsection 5.2.4 will illustrate the viscous damping force in detail from the point of view of modelling.

As a summary of this section, the feed forward part of the VPVC controller comprises an inverse model of the plant. It needs to predict the required motor speed and the valve openings for the two control valves according to the motion requirements. Firstly, the controller computes the required actuation force, and then predicts the minimum required supply pressure together with the corresponding valve openings. Finally, the motor speed command is calculated by the flow rate requirements and the changing rate of the predicted P_S. The VPVC feed forward control algorithm aims to minimize the pressure loss over the control valve which is located on the highest load branch, which makes the system achieve a higher energy efficiency compared with the conventional fixed supply pressure valve-controlled hydraulic system.

3.3 Feedback part of VPVC controller

The feedback part of VPVC controller uses the actual measured positions of the actuators to close the loops. The function of feedback controller is to correct the predicted command signals from the feed forward part.

3.3.1 Feedback control to the motor speed

The angular speed of the servo motor is tuned by the position feedback of the master actuator (MA). As introduced in section 3.1, the circumflex (^) represents the output command signal of the feed forward controller. The tilde (~) represents the final command signal. y_{MA_d} represents the demanded linear position of the master actuator and y_{MA} represents the actual measured linear position of the master actuator. Figure 3.11 shows that a proportional-gain (P) controller is used to adjust the flow into the system by observing the position error of the MA. The P controller is a proportional gain K_{P_motor} multiplied by the sign of MA's valve opening, which takes into account the direction of the flow imposed by the valve.

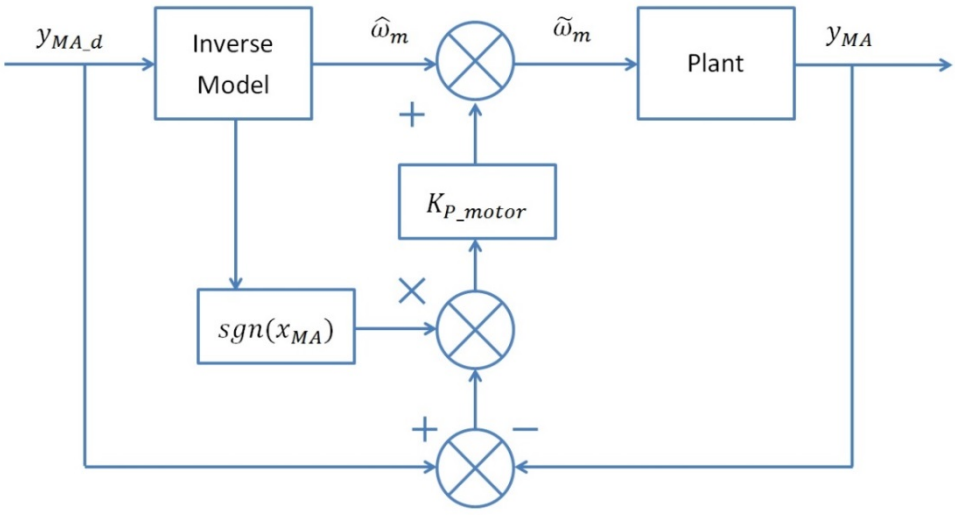

Figure 3.11 Feedback of motor speed command

Hence the final command signal of the motor speed is:

$$\tilde{\omega}_m = \hat{\omega}_m + K_{P\_motor}(y_{MA\_d} - y_{MA})sgn(x_{MA}) \tag{3.29}$$

3.3.2 Feedback control to the commands of control valves

The valve opening (spool position) command is modified by its own actuator position feedback. The error between the demanded actuator position and the measured position is processed via a proportional-integral (PI) controller (see Figure 3.12). Both actuators (MA and non-MA) adopt PI feedback control.

The final valve command signals are as follows:

$$\tilde{x}_j = \hat{x}_j + (K_{P\_valve} + \frac{K_{I\_valve}}{s})(y_{j\_d} - y_j) \tag{3.30}$$

where j = 1, 2 represents the shoulder actuator and the elbow actuator respectively.

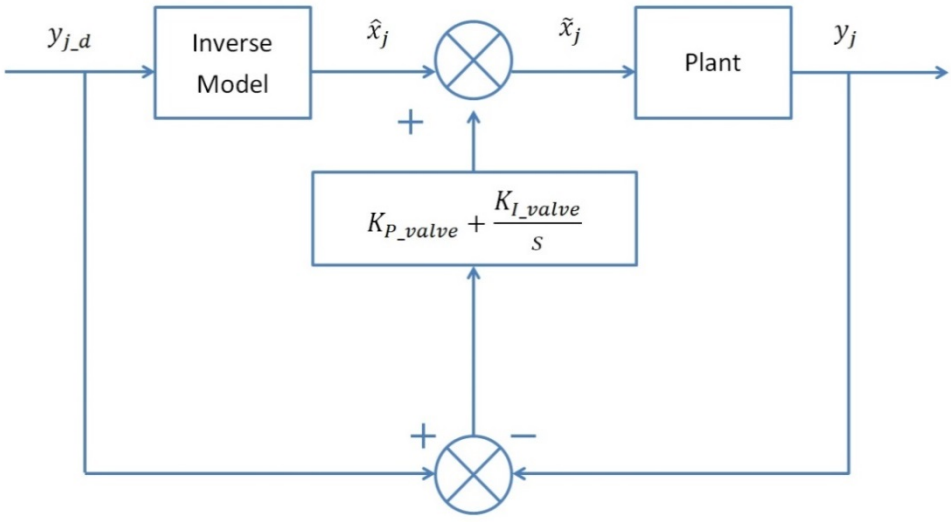

Figure 3.12 Feedback of valve opening command

As a summary of this section, the feedback part of the VPVC control algorithm is classical closed loops which aim to correct for the errors of the feed forward prediction and eliminate the unexpected disturbances during tests. The signals used in the closed loops are actual linear positions of the two actuators, derived from measured joint angles. For motor speed closed loop control, a P controller is used to process the position error of the MA; and for each valve command closed loop, a PI controller is used to reduce the corresponding position error of the actuator.

3.4 FPVC control algorithm

The control concept of the conventional fixed supply pressure valve-controlled (FPVC) hydraulic actuation system is much simpler than VPVC control algorithm. The motor speed is a constant which has to be set high enough to keep a fixed supply pressure, with the assistance of a relief valve. Hence no extra controller is designed for the motor speed.

For the valve commands, FPVC has no feed forward part. Only proportional-integral (PI) feedback controller is used for each control valve. The input signal of each PI controller is the linear position error of the actuator. And the output signal is the final command of this valve (see Figure 3.13).

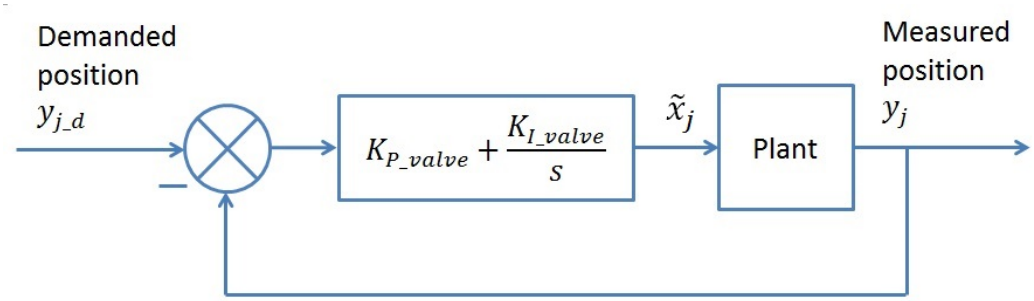

Figure 3.13 Control concept of FPVC controller

The command signal of the valve can be represented as:

$$\tilde{x}_j = (K_{P\_valve} + \frac{K_{I\_valve}}{s})(y_{j\_d} - y_j) \tag{3.31}$$

The value of the gains in the VPVC controller and FPVC controller will be tuned and determined separately in Chapter 6.

3.5 Concluding remarks

This chapter shows a comprehensive illustration of the VPVC control algorithm. The VPVC controller has two parts: a feed forward part and a feedback part. The feed forward part uses the computed-torque method to get the required hydraulic actuation force by a given motion demand. With the calculated required force, the VPVC feed forward part determines the minimum required supply pressure with these assumptions: maximize the valve opening of the control valve which controls the actuator with the higher load (master actuator i.e. MA) ensuring no cavitation occurs in any thrust chamber. Based on the determination of the minimum required P_S, the valve command signals and motor speed command are calculated as the results are of feed forward part. The feedback part adopts a P controller to adjust the motor speed with the position error of the MA and two individual PI controllers to adjust the valve opening commands with the corresponding position error of actuator.

The FPVC control algorithm uses an individual PI controller to each control valve. The PI controller receives the error between the demanded position and the measured position of the actuator and sends out the command signal to the corresponding control valve.

In short, FPVC performance relies on the PI feedback control of the two valves totally. In the VPVC control algorithm, the feed forward part (command signals prediction with the given demand) plays a significant role while the feedback part corrects for modelling errors and disturbances.

Chapter 4

4 Two-axis Robotic Arm System

This chapter gives a description of the two-axis robotic arm hydraulic actuation system which is developed for the validation of benefits of the VPVC over the FPVC. Firstly, an overview is provided to introduce the system schematic. Then a section describes the hydraulic components. The third section provides a comprehensive description of the robotic arm including the geometry and specifications. After that, the electric sensors are introduced. In the last section, the individual signal processing and the real-time test platform are described.

4.1 Overview of the robotic arm system

The two-axis robotic arm hydraulic actuation system can be divided into three different domains: controller domain, hydraulic domain and mechanical domain. The xPC Target environment is used as the real time controller in this research. The real time controller transmits the command signals of the motor speed ω_d and two control valve openings x_{d_1} and x_{d_2} to the hydraulic test rig. The hydraulic system drives two unequal area actuators, which are installed on the robotic arm. The robotic arm is fixed on the ground. The angular positions of the two joints (θ_1 and θ_2) are measured and received by the real-time controller for the feedback control (see Figure 4.1). In addition, there are monitoring system to measure the valve openings x_{a_1} and x_{a_2}, the actuation forces F_1 and F_2, the supply pressure P_{S_actual} and the motor speed ω_{actual} during the experiment for the performance asssement.

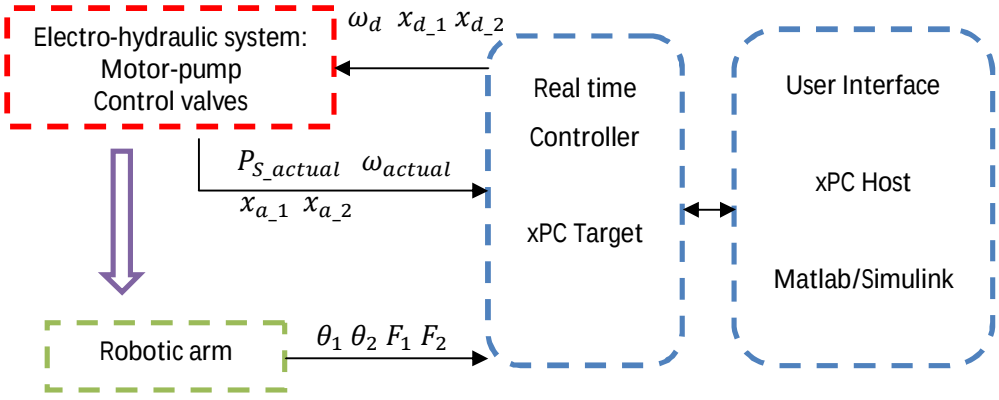

Figure 4.1 The schematic of the two-axis robotic arm system (blue zone is controller domain, red zone is hydraulic domain and green zone is mechanical domain)

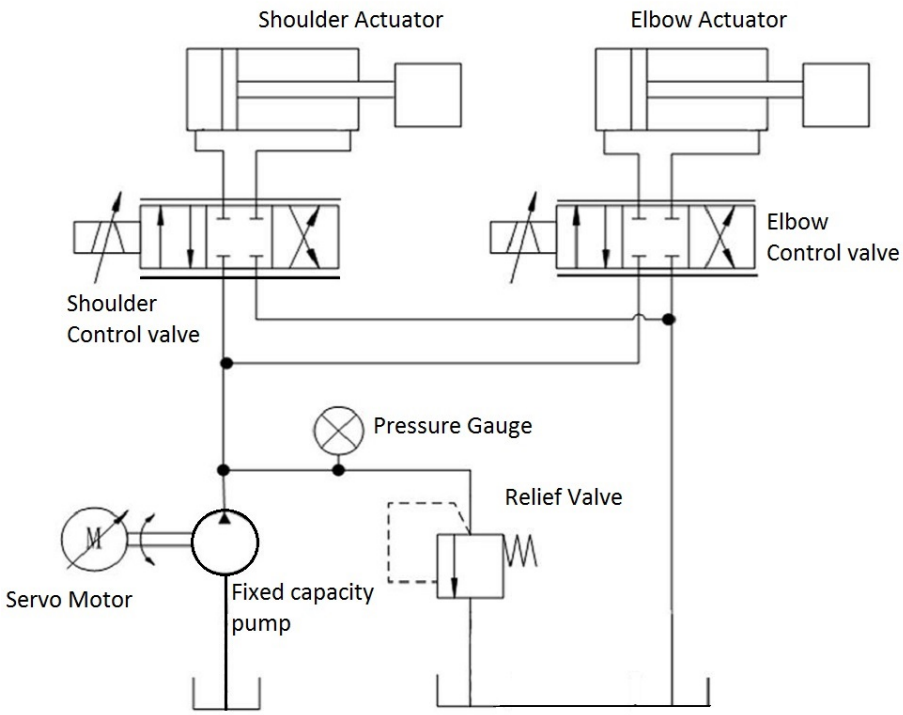

Figure 4.2 The hydraulic circuit of the two-axis robotic arm

The hydraulic circuit is shown in Figure 4.2. It has an AC brushless servo motor and a fixed capacity axial-piston pump as the power source; two direct drive valves and two unequal area actuators. The motor drive receives the analogue command signal from the controller; and the two valves control the flow into the actuators with the voltage commands from the controller. The two actuators rotate the revolute joints. Hence the control valves can control the rotational motion of the two joints in the flexion/extension plane (see Figure 4.3).

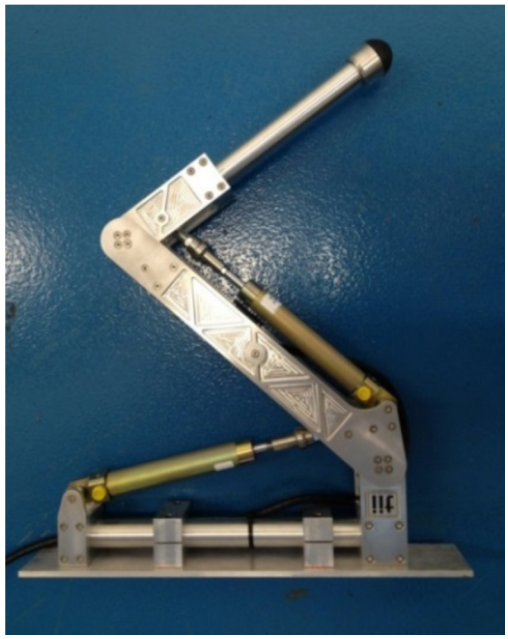

Figure 4.3 The two-axis robotic arm (with the original foot/hand from the manufacturer IIT)

The robotic arm used in this project is an inverted Robot Leg HyQ-LegV2.1 from Italian Institute of Technology (IIT). It is built in aluminium alloy. Both joints have a range of motion of 120^{o} and a relative encoder for the measurement of angular position.

The real-time control platform adopts the xPC Target environment which supports real-time code generated by MATLAB®/Simulink®. Two data acquisition boards from National Instruments are inserted in the target PC for input and output signal interfacing.

4.2 Hydraulic system

The hydraulic test rig is shown in Figure 4.4. A manifold block has been designed for integrating the power source and the valves. For the purpose of achieving a reasonable load pressure, a steel disc is used as the robot hand. A detailed description for the individual hydraulic components will be presented in this section.

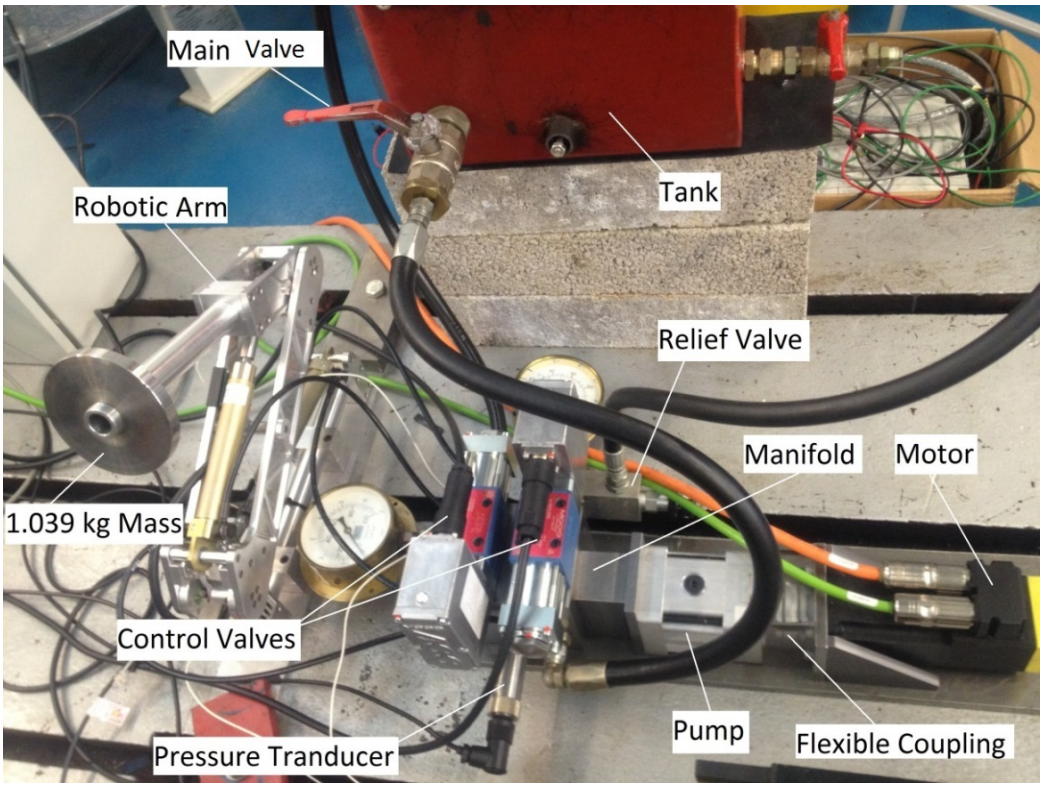

Figure 4.4 The test rig of the two-axis robotic arm

4.2.1 Pump and motor

4.2.1.1 Pump

From the documentation of HyQ-LegV2.1 (Semini, 2010), it is obtained that the effective stroke of each cylinder is 0.078 m. The maximum required flow rate is calculated as follows: completing the full stroke within 0.2 second is the maximum velocity demand. Hence the maximum linear velocity is obtained as v_{max} = 0.39 m/s. The maximum requirement of the flow rate for the whole system should be:

$$Q_{max} = 2A_p v_{max} = 9.4\ L/min \quad (4.1)$$

where A_p represents the piston area 2.01 cm^2. Assume the ideal operating condition, if the maximum angular speed of the pump is set at ω_{max} = 3000 rev/min, the capacity of the fixed displacement pump D_P is calculated as follows:

$$D_P = \frac{Q_{max}}{\omega_{max}} = 3.13\ cc/rev \quad (4.2)$$

For the target of high efficiency and lightweight in this research, a micro axial-piston pump from Takako Industries is selected. The axial-piston pump has a higher energy-convert efficiency compared with the gear pump in similar size (see Figure 4.5). This series of micro pumps adopt a spherical valve plate design which offers them high efficiency at both low and high speed conditions. They are compact size and low weight, which is ideal for the applications where weight and size are crucial (Takako Industries, 2010).

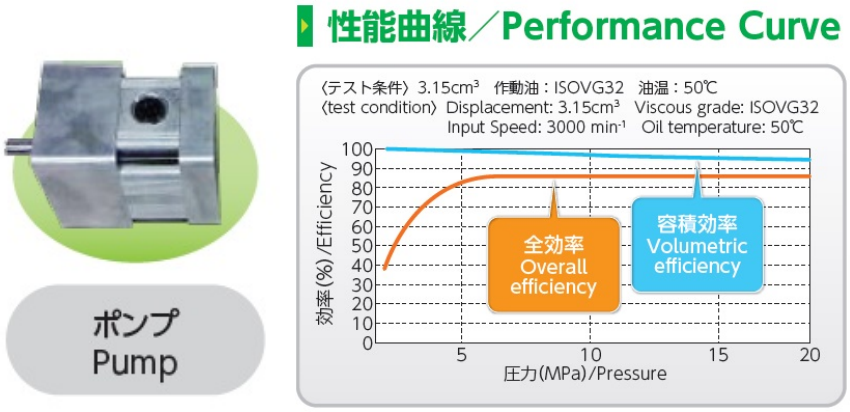

Figure 4.5 The axial-piston micro pump TF 315 from Takako Industries and its performance curve (Takako Industries, 2010)

The selected model is TF 315, which has a capacity of 3.14 cc/rev. Its maximum output pressure is 210 bar and the maximum angular speed is 3000 rev/min. The maximum linear velocity for extension is recomputed with the actual pump capacity and consideration of volumetric efficiency of $\eta_v = 0.95$:

$$v_{max} = \frac{D_P \omega_{max}}{2A_p} \eta_v = 0.37\ m/s \tag{4.3}$$

Hence the full range of extension motion could be completed within 0.21 second, which is considered acceptable.

The general specifications of this micro pump TF 315 are shown in Table 4.1.

Model	**TF 315 from Takako Industries**
Capacity	3.14 cc/rev
Max Operating Pressure	210 bar
Max Speed	3000 rev/min
Rotation Direction	Bi-direction
Weight	1.94 kg
Shaft Diameter	12 mm

Table 4.1 The basic specifications of the micro pump TF 315

4.2.1.2 Motor and its accessories

BSM-N series AC brushless servo motor from Baldor is chosen for driving the fixed capacity pump (see Figure 4.6). The BSM-N series can provide the industrial motion control with low inertia to attain the fast position tracking ability. The model chosen for this hydraulic system is BSM-63N-375AF.

The matched motor drive is MicroFlex Analog series from ABB Drives. It accepts an analogue speed. The model of FMH2A09TR-EN23W from this series is selected. It is a single phase input (110-230 VAC) with continuous current rating of 9 Amps. The incremental encoder feedback to give the actual motor speed is available. A 24 VDC supply is required to provide power to the controlling electronics in MicroFlex Analog. The electro-magnetic compatibility (EMC) filter can remove high frequency noise from the power supply to protect the MicroFlex Analog. The layout of the motor drive and its accessories is shown in Figure 4.7. The general parameters of the motor are listed in Table 4.2.

Figure 4.6 The BSM-N series servo motor from Baldor (Baldor, 2010)

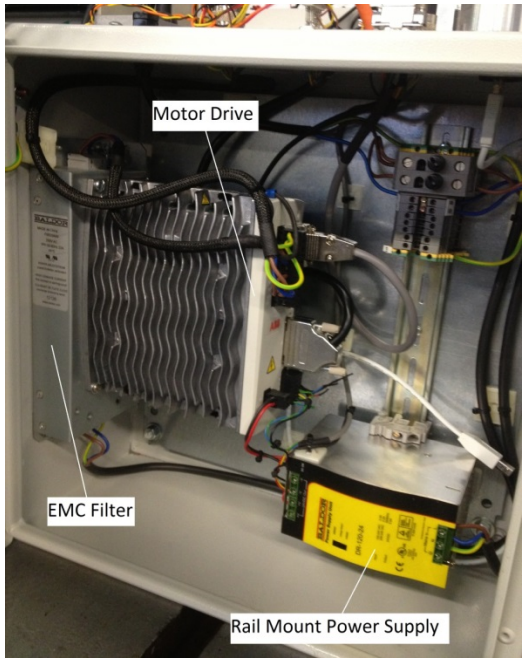

Figure 4.7 The motor drive MicroFlex Analog with its accessories (EMC filter and power supply)

Model	**BSM-63N-375AF from Baldor**
Cont. Stall Torque	2.09 Nm
Cont. Stall Current	2.82 A
Peak Torque	8.36 Nm
Peak Current	10.1 A
Torque Constant	0.82 Nm/A
Voltage Constant	70.3 V_{PK}/krpm
Resistance and inductance	5.92 Ω 13.65 mH
Inertia	0.5645 kg-cm^2
Speed at 300 Bus Volts	4000 rev/min
Max Speed	10000 rev/min
Encoder Feedback: Line count	2500ppr
Shaft Diameter	11 mm (with a key 4×4×12 mm)

Table 4.2 The specifications of the servo motor BSM-63N-375AF

4.2.1.3 Accessories of the power pack

A flexible coupling is required to connect the motor shaft and the pump shaft. Zero-Max SERVOCLASS® SC Series is chosen due to its zero backlash, low hysteresis and low inertia. The model used in this research is SC040R-A (see Figure 4.8). An extra key space is made to the specification of motor shaft.

Figure 4.8 Flexible coupling for servo motor and pump (Zero-Max, 2014)

Model No	**SC040R-A from Zero-Max**
Max Operating Torque	10 Nm
Max Speed	10000 rev/min
Inertia	29.5×10^{-6} kgm^2
Weight	122 g

Table 4.3 The general specifications of the flexible coupling SC040R-A from Zero-Max

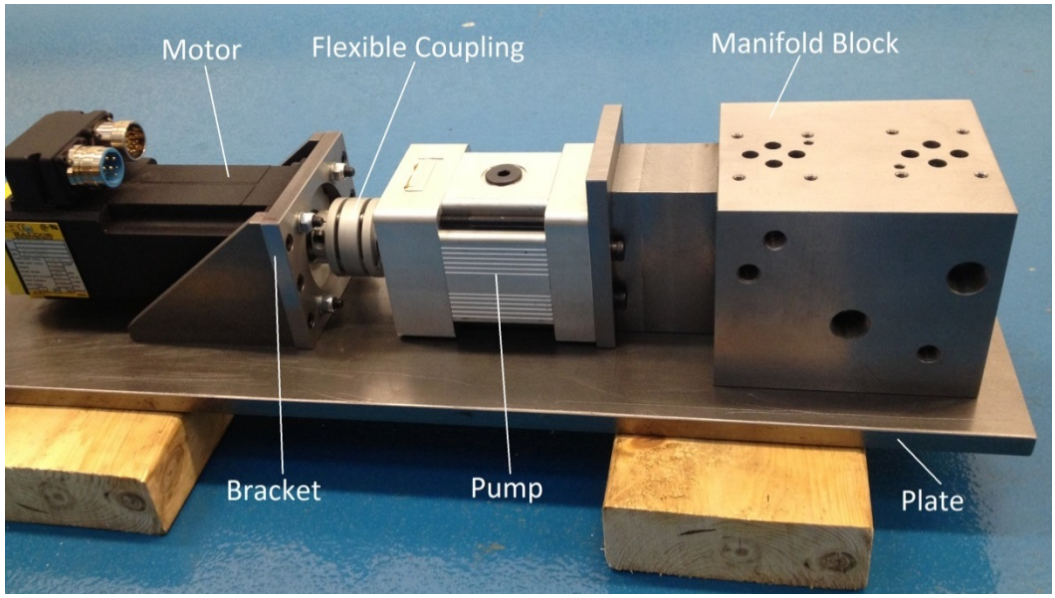

Figure 4.9 Assembled power pack and the manifold block

For fixing the motor-pump, a U shape bracket is designed and manufactured. The U shape bracket fixes the motor on a steel plate (see Figure 4.9). The manifold block which will be introduced is also fixed on that plate in subsection 4.2.4.

4.2.2 Valve

D633 Series valves from Moog are used as the control valves in this research (see Figure 4.10 left). They are direct drive valves with integrated electrical closed loop control for the spool position. The model used in this system is D633-R02K01M0NSM2. The rated flow of this model is 5 L/min at a pressure drop ΔP_{rated}= 35 bar per metering land. It is 4-way version (see Figure 4.10 right).

The spool position is centred when there is no electric supply. The maximum operating pressure is 350 bar for P, A and B port, 50 bar for T port. It requires 24 VDC power supply (pin A and pin B of the connector in Figure 4.11). The spool position command is proportional to (U_D – U_E): ±100% spool stroke is ±10 VDC. The actual spool position value can be measured at pin F. In this research, two identical valves will be used for the control of the two joints.

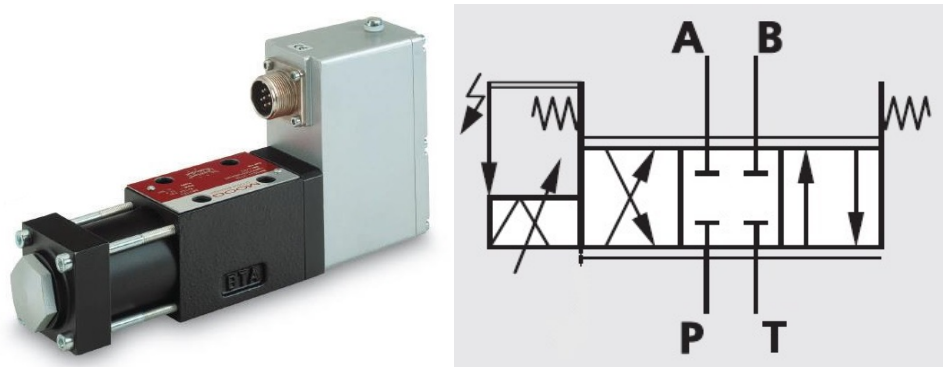

Figure 4.10 D633 Series direct drive valve from Moog Company and its 4-way version diagram (Moog, 2005)

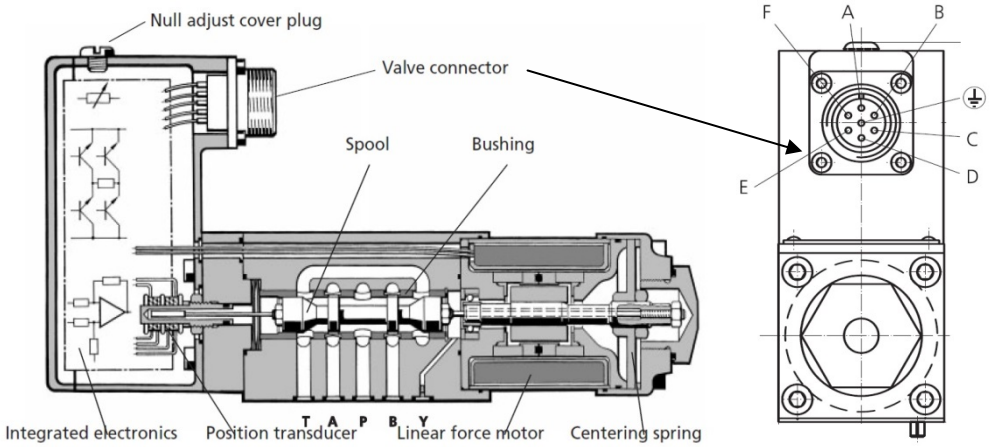

Figure 4.11 The 6+PE connector of D633 series

The mounting drawing and the performance curves of the D633 are shown in Appendix 1.1. The general information of this valve is shown in Table 4.4.

Model	**D633-R02K01M0NSM2 from Moog**
Rated flow rate	5 L/min at $\Delta \boldsymbol{P}_{\boldsymbol{rated}}$ = 35 bar
Command signal	0 to ± 10 VDC
Output (actual value spool position)	4 to 20 mA 12 mA: spool is in centred position.

Table 4.4 The basic information of direct drive valve D633 from Moog Company

4.2.3 Actuator

The hydraulic actuators equipped on the robotic arm are from Hoerbiger Micro Fluid Company. The model No is LB6-1610-0080-4M (see Figure 4.12). It is an unequal area cylinder. The stroke is 80 mm (mechanical joint limits are reached at 1mm and 79mm rod extension). The piston diameter is 16 mm and the rod diameter is 10 mm.

Figure 4.12 The hydraulic cylinder LB6-1610-0080-4M from Hoerbiger

Model	**LB6-1610-0080-4M from Hoerbiger**
Stroke	80 mm
Piston/rod diameter	16 mm/ 10 mm
Piston area	2.01 cm^2
Annular area	1.23 cm^2
Max operating pressure	160 bar
Max piston speed	4 m/s
Connection ports	M10×1 (metric thread)

Table 4.5 The general information of the hydraulic cylinder LB6-1610-0080-4M

4.2.4 Manifold and hoses

For the purpose of compact hydraulic drive system, a manifold block is designed for connecting the pump, valves, hoses and the pressure transducer (see Figure 4.13). The top surface is for mounting the two control valves. The bottom surface is for fixing this manifold block to the plate via 4 threaded holes. The pump surface is for connecting the pump. The description of the ports is in Table 4.6.

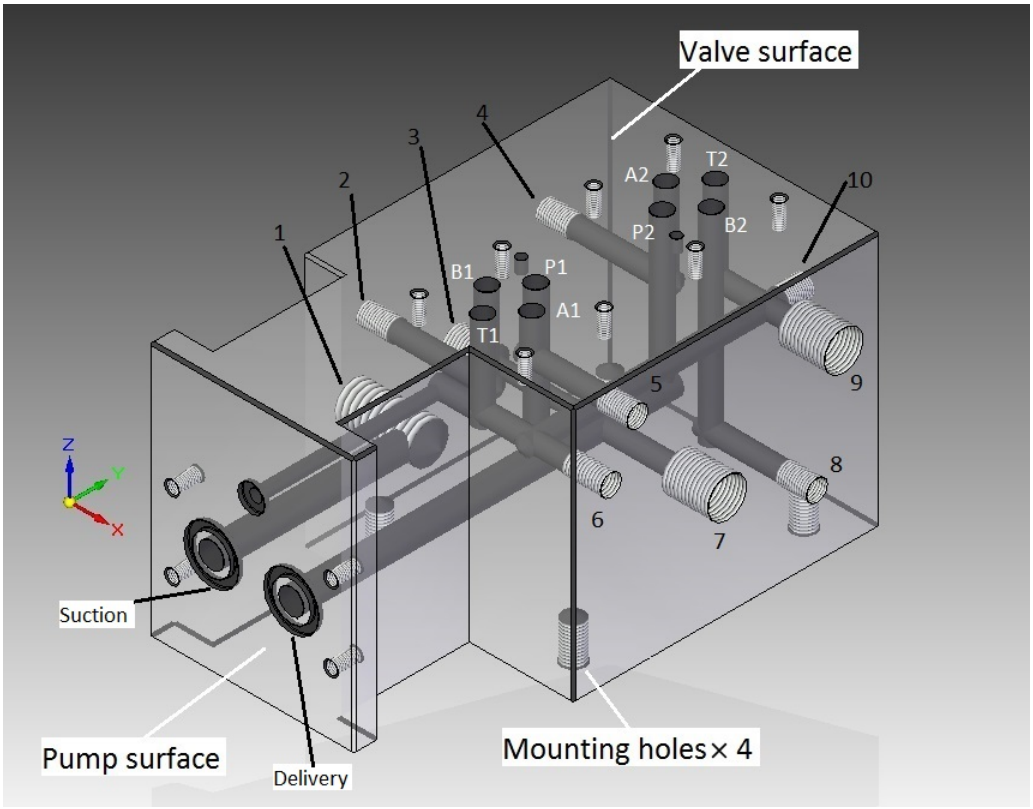

Figure 4.13 The 3D model of manifold block

Port No	Description
1	Suction port connecting to the tank
2	B port for the shoulder actuator
3	Pressure transducer port
4	A port for the elbow actuator
5	A port for the shoulder actuator
6	Blanking plug for tank
7	Relief valve (pressure port)
8	B port for the elbow actuator
9	Return line connecting to the tank
10	Blanking plug for tank

Table 4.6 Ports specifications of the manifold block

The hoses connecting the valve ports (A and B) on the manifold block and the ports of the actuators are micro pipes from Hoerbiger. Each pipe is 0.5 m length and the inner diameter is 3 mm. These micro pipes connect the actuator ports with banjo fittings and O-rings (see Figure 4.14).

Figure 4.14 The micro pipes with the banjo fittings from Hoerbiger

The volumes of the supply galleries, as well as the total volume of manifold, micro pipes and internal cylinder chamber when piston is in mid-stroke are required in the modelling of the hydraulics. The estimations for these effective volumes are shown in Figure 4.15 and Table 4.7.

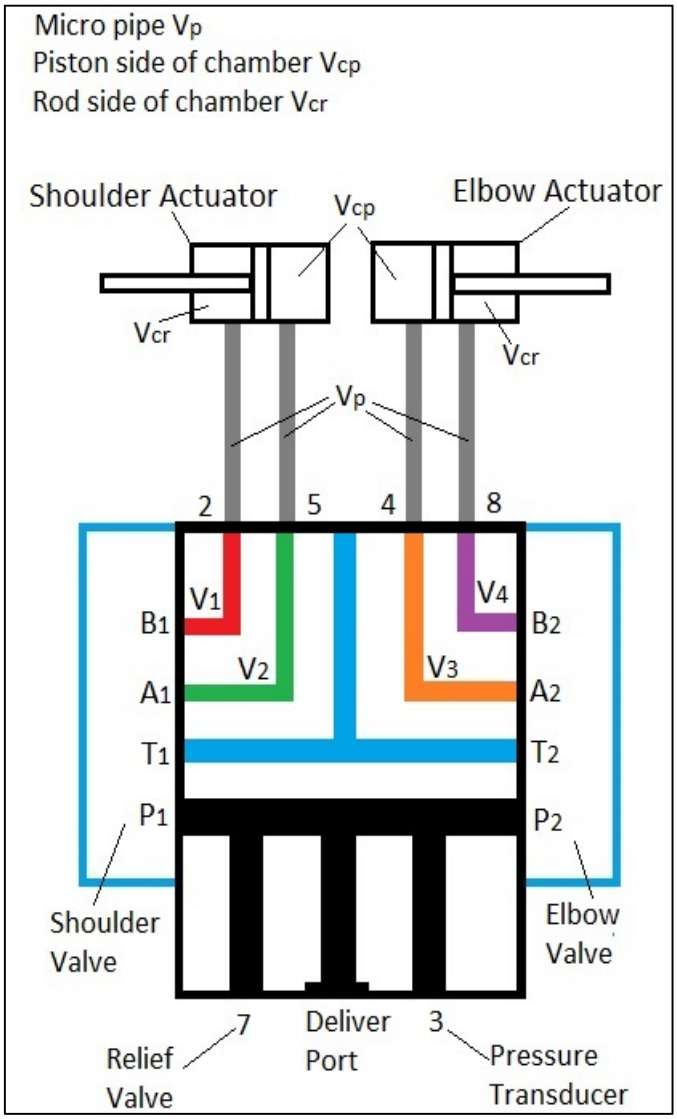

Figure 4.15 The simplified diagram for the volume estimation of the effective hoses

Descriptions	Corresponding paths in Figure 4.16	Value in cm^3
The volume of supply galleries	Black paths	20
Shoulder: piston-side volume when mid-stroke	V_2 (green path) + V_P + V_{cp}	13
Shoulder: rod-side volume when mid-stroke	V_1 (red path) + V_P + V_{cr}	10
Elbow: piston-side volume when mid-stroke	V_3 (orange path) + V_P + V_{cp}	12
Elbow: rod-side volume when mid-stroke	V_4 (purple path) + V_P + V_{cr}	14

Table 4.7 The descriptions and estimations of the volumes of the effective hoses

4.2.5 Other hydraulic components

The reservoir size is 12 Litre which is enough for this system requirement of a maximum flow rate of 9.4 L/min mentioned in subsection 4.2.1. There is a main on/off valve on the suction line (see Figure 4.4). The relief valve is a Pilot Operated Relief Valve Cartridge, 2 Port, Balanced Piston, RPEC-LAN from Sun Hydraulics.

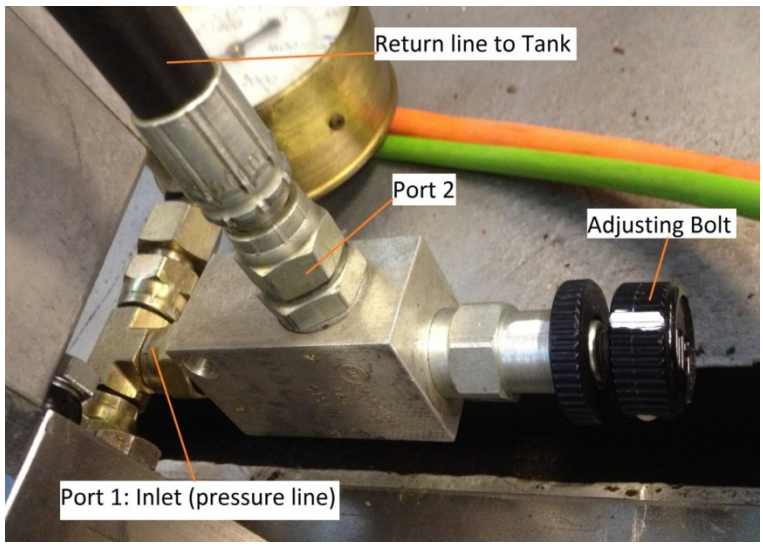

Figure 4.16 The assembled relief valve from Sun Hydraulics

4.3 Robotic arm

4.3.1 General description

The Hydraulically Actuated Quadruped (HyQ) is a robot developed by the Institution Italian of Technology (IIT). The HyQ is 80 kg, and built in aerospace-grade aluminium alloy and stainless steel (see Figure 4.17). Each of its four legs has 3 rotational joints that are actuated by the hydraulic cylinders introduced in subsection 4.2.3. HyQ has been extensively tested in the laboratory and outside terrains. It has completed various walking gaits and highly dynamic motion like running and jumping (Semini, et al., 2011).

In this research, a leg from HyQ robot, the HyQ-LegV2.1 is inverted and used as a two-joint robotic arm. It is mounted on a steel plate by two clamps and then the plate is fixed on the test base (see Figure 4.18). The motion of the robotic arm in this research is in the sagittal plane only.

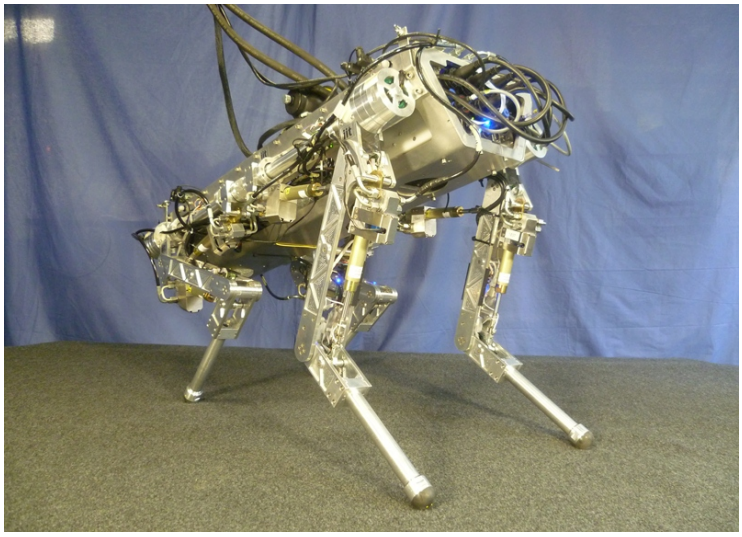

Figure 4.17 The HyQ robot in kneeling position (Semini, et al., 2011)

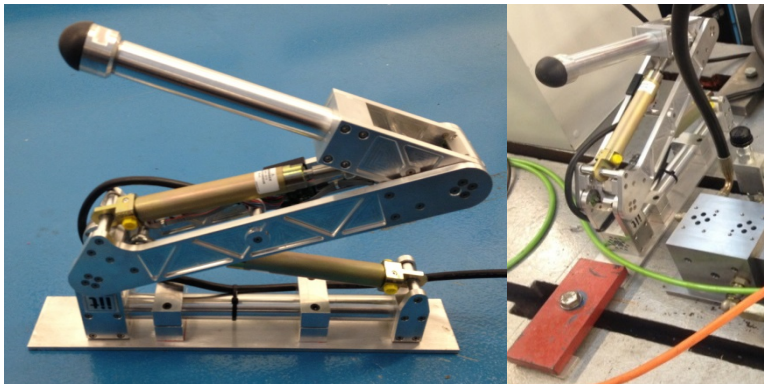

Figure 4.18 The fixture of the robotic arm (inverted HyQ-LegV2.1)

The robotic arm comprises of a mechanical frame: shoulder assembly (torso), upper arm, forearm and hand. One rotational joint – the shoulder joint is between the torso and upper arm, and the other joint – the elbow joint is between the upper arm and forearm. Two hydraulic cylinders actuate the rotational motion of the two joints separately (see Figure 4.19).

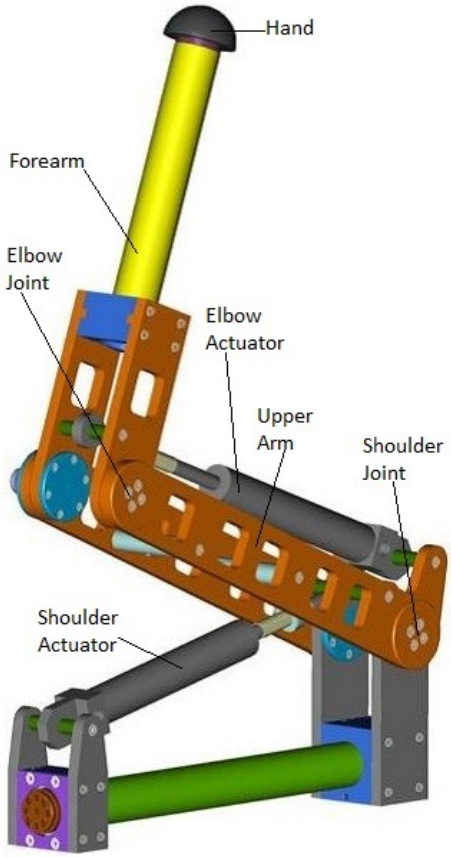

Figure 4.19 3D model of the robotic arm

4.3.2 Specifications and geometry

The specifications and geometry of the robotic arm are shown in Figure 4.20 and Figure 4.21. The corresponding data are in Table 4.8. The variables' definitions are the same as introduced in subsection 3.2.2.

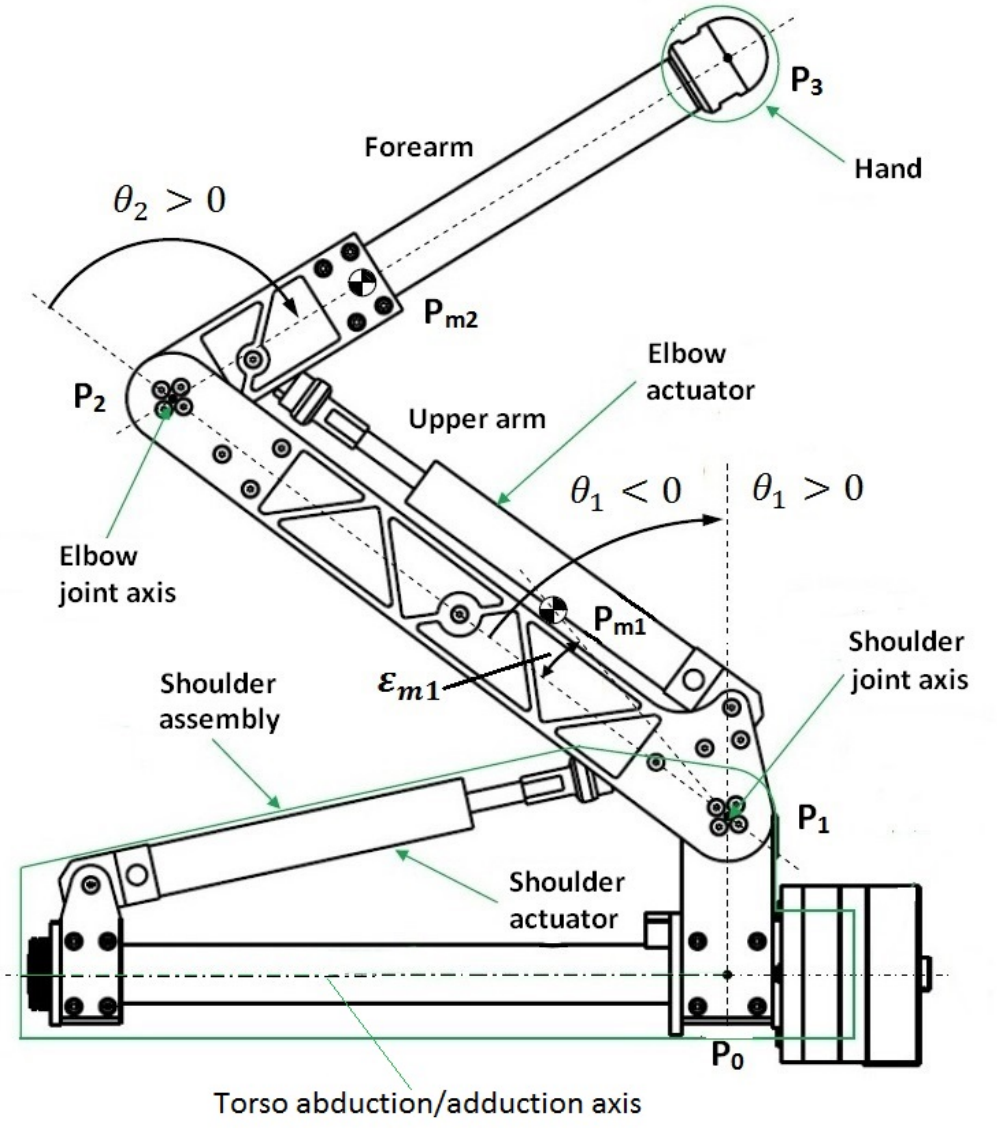

Figure 4.20 The components and axes of the robotic arm

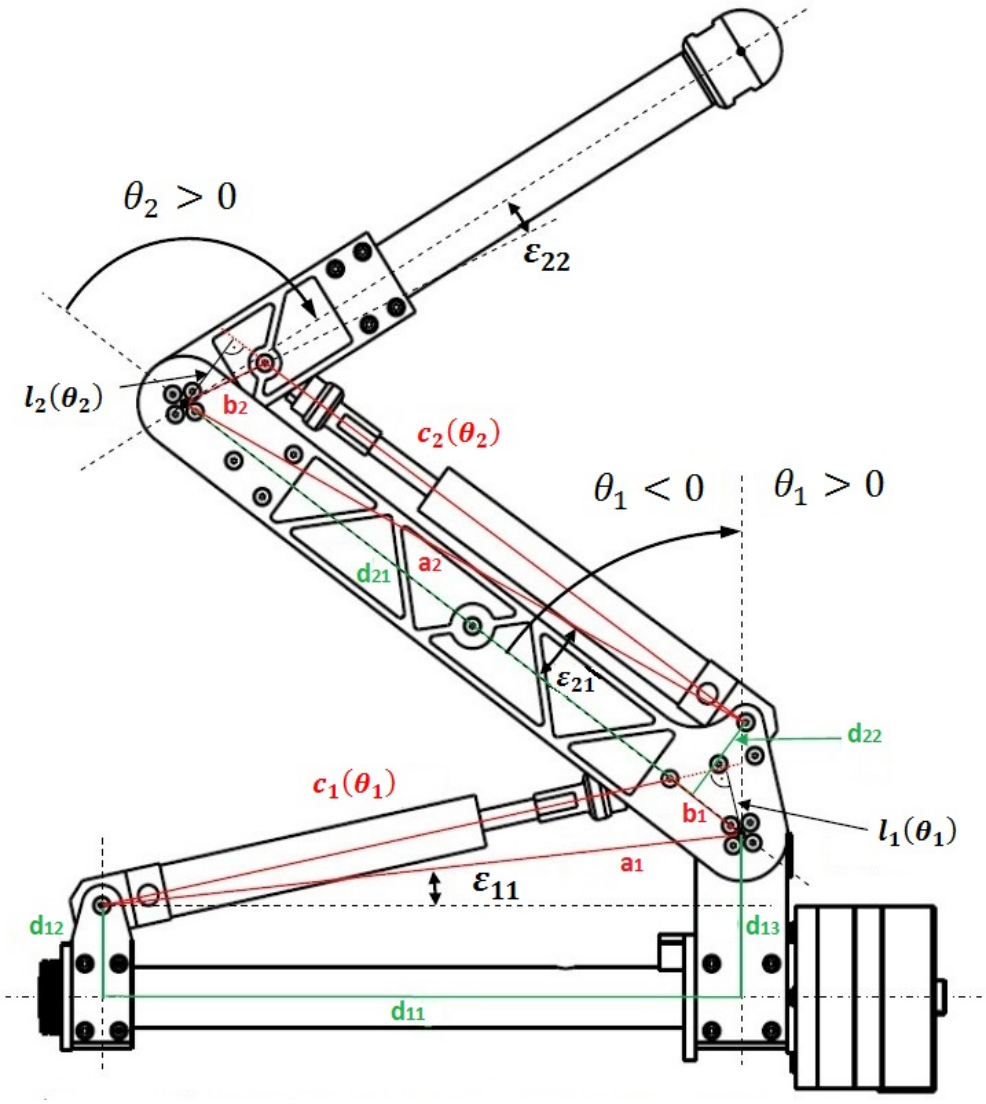

Figure 4.21 The dimensions of the robotic arm

Shoulder Assembly	
P_0P_1 (d_{13})	0.08 m
Mass M_0	2.482 kg (including the shoulder actuator)
Inertia I_0	0.00745 kgm^2 (with respect to torso abduction/adduction axis, through P_0)
d_{11}	0.32 m
d_{12}	0.045 m
a_1	0.3219 m
b_1	0.045 m
ε_{11}	6.24 degree
Upper Arm	
P_1P_2	0.35 m
P_1P_{m1}	0.164 m
Mass M_1	1.772 kg (including the elbow actuator)
Inertia I_1	0.0239 kgm^2 (with respect to upper arm gravity centre, through P_{m1})
d_{21}	0.3186 m
d_{22}	0.045 m
a_2	0.3218 m
b_2	0.045 m
ε_{m1}	7.9 degree
ε_{21}	8.04 degree
Forearm	
P_2P_3	0.33 m
P_2P_{m2}	0.103 m
Mass M_2	0.739 kg
Inertia I_2	0.0035 kgm^2 (with respect to forearm gravity centre, through P_{m2})
ε_{22}	6.0 degree

Table 4.8 The dimensions and specifications of the robotic arm (no hand)

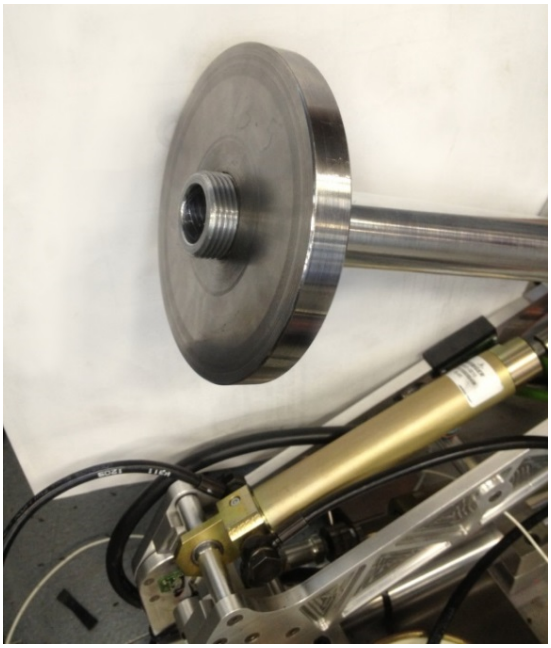

Figure 4.22 The hand mass in the two-axis robotic arm system

In this research, a steel disc of 1.039 kg is used in all the tests in place of the robot hand (see Figure 4.22). Its thickness is 1.35 cm, the outer diameter is 11.6 cm and inner diameter is 3 cm. The centre of gravity of the new hand is located at P_{m3} along the axis of P_2P_3.

Hence the specifications of the new hand are shown in Table 4.9.

Hand	
P_2P_{m3}	0.30325 m
Mass M_3	1.039 kg
Inertia I_3	0.00304 kgm^2 (with respect to hand gravity centre, through P_{m3})

Table 4.9 The specifications of the new hand

4.3.3 Motion Range

The linear hydraulic actuators drive the rotational motion of the two. It is important to determine the relation between the actuator length and joint angle. The equations to calculate the actuators' length $c_1(\theta_1)$ and $c_2(\theta_2)$ in Figure 4.21 are Equation 4.4 and Equation 4.5.

$$c_1(\theta_1) = \sqrt{a_1^2 + b_1^2 - 2a_1 b_1 \cos\left(\frac{\pi}{2} + \theta_1 + \varepsilon_{11}\right)} \tag{4.4}$$

$$c_2(\theta_2) = \sqrt{a_2^2 + b_2^2 - 2a_2 b_2 \cos(\pi - \theta_2 - \varepsilon_{21} - \varepsilon_{22})} \tag{4.5}$$

The shoulder angle θ_1 is from -70^0 to 50^o and the elbow angle θ_2 is 20^0 to 140^o. Equation 4.4 and 4.5 calculate the length range of the two actuators in Table 4.10. From the results, it is clear that the actuator adopted should have a stroke of at least 78 mm. From the subsection 4.2.3, the chosen is able to fully actuate the joint to achieving the designed motion range of 120^o.

As mentioned in subsection 3.2.2, the required actuation force prediction equations need the values of the lever arms. The equations to calculate the lever arms $l_1(\theta_1)$ and $l_2(\theta_2)$ are shown as follows:

$$l_1(\theta_1) = a_1 \sin\left(\cos^{-1}\left(\frac{a_1^2 + c_1(\theta_1)^2 - b_1^2}{2a_1 c_1(\theta_1)}\right)\right) \tag{4.6}$$

$$l_2(\theta_2) = a_2 \sin\left(\cos^{-1}\left(\frac{a_2^2 + c_2(\theta_2)^2 - b_2^2}{2a_2 c_2(\theta_2)}\right)\right) \tag{4.7}$$

θ_1	$c_1(\theta_1)$	θ_2	$c_2(\theta_2)$
-70^0	0.2822 m	20^0	0.3600 m
50^o	0.3602 m	140^o	0.2820 m
Shoulder Stroke	0.078 m	Elbow Stroke	0.078 m

Table 4.10 The strokes of the actuators on robotic arm

4.4 Sensors

4.4.1 Relative encoder

From Chapter 3, it is obvious that the actual positions of the two joints as the only feedback signals are very important to the system. The AEDA-3300-BE1 relative encoders from AVAGO Technologies Company are used for the measurement of the actual angular positions of the two joints. AEDA-3300 series is a three-channel (quadrature A & B output with index Z) optical incremental encoder. It is ultra-miniature (diameter 17 mm) which is easy to be mounted in the joints. The specifications of the AEDA-3300-BE1 are in Table 4.11.

Figure 4.23 The AEDA-3300 relative encoders from AVAGO Technologies Company (Avago Technologies, 2006)

Model	AEDA-3300-BE1 from AVAGO Technologies
Counts per revolution	20000 (80000 counts with 4X decoding)
Principle of operation	Optical disc
Output signal	Three digital channels A, B and index Z
Power supply	5 V
Max rotational speed	12000 RPM

Table 4.11 The specifications of AEDA-3300-BE1 relative encoder

In this research, two relative encoders are used for the angular position measurement of the two joints separately. The outputs are integrated in an electronic hub-board, which has a cable with a 32-pin connector. To connect the relative encoders, the pins introduced in Table 4.12 are used.

Pin	Signal	Description
1	Vcc	Power supply to the hub-board: 5Vc.c. IN
2	GND	Ground Pin
3	Enr1: A+	Output signal A for the shoulder joint
5	Enr1: B+	Output signal B for the shoulder joint
7	Enr1: Z+	Index Z for shoulder joint
9	Enr2: A+	Output signal A for the elbow joint
11	Enr2: B+	Output signal B for the elbow joint
13	Enr2: Z+	Index Z for elbow joint

Table 4.12 The description of encoder-pins on the hub-board connector

4.4.2 Load cell

In the FPVC and VPVC control, force signals are not used for the feedback control. But the observation of the actuation force signals is necessary for the comparison between the prediction/simulation and the actual values. The load cell used in this research is model 8417-6005 from Burster Company. The output signal of the load cell is positive voltage, which represents tension force applied on the load cell and negative represents compression force. It has nominal proportional gain of 500 N/V. A mechanical testing machine from Instron calibrated the actual relations for the two load cells separately.

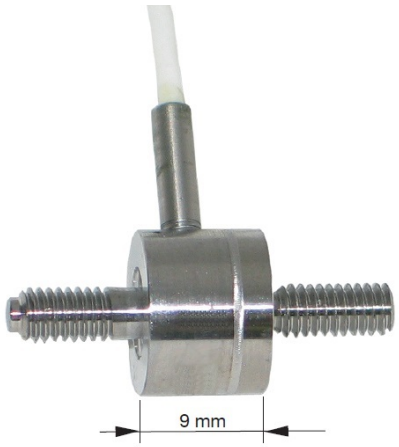

Figure 4.24 The Burster load cell 8417-6005 (Burster, 2012)

Model	**8417-6005 from Burster**
Measurement range	Tension force 0 to +5 kN Compression force 0 to -5 kN
Principle of operation	Strain gauges
Output signal	Analogue (Voltage)
Calibrated equations (U is the output voltage)	Shoulder load cell: Force (N) = 530 U (V) – 40 Elbow load cell: Force (N) = 540 U (V) - 21

Table 4.13 The specifications of load cell 8417-6005 from Burster Company

4.4.3 Pressure transducer

A HAD 3300 series pressure transmitter from HYDAC Company is used for the measurement of the actual supply pressure. The chosen model is HAD 3744-B-250-000. The specifications are listed in Table 4.14.

Figure 4.25 HDA 3700 series pressure transmitter from HYDAC Company (HYDAC, 2006)

Model	**HAD 3744-B-250-000 from HYDAC**
Measurement range	0 to 250 bar
Output signal	0 to 10 V (i.e. Gain is 25 bar/V)
Supply voltage	12 to 30 V
Accuracy	0.5%
Mechanical connection	G ¼ A male thread
Electrical connection	4-pole Binder plug (without connector)

Table 4.14 The specifications of the HAD 3744-B-250-000 pressure transducer from HYDAC

4.5 Signal processing and real-time control platform

This robotic arm system uses the xPC Target environment to implement the real-time tests. A host PC is used to build the model and download code to the target PC. The target PC sends out and receives the signals by two data acquisition boards NI PCI-6221 from National Instruments (see Figure 4.26). This section will introduce the interfacing and the real-time control platform will be described.

xPC Target is a solution for prototyping, testing and deploying real-time system using standard PC hardware. It is a platform that uses a target PC, separate from a host PC, for running real-time applications based on Simulink models. A summary of the signals to which the target PC needs to be interfaced is given in Table 4.15. The way these signals are converted to or from physical units is given in Appendix 3.

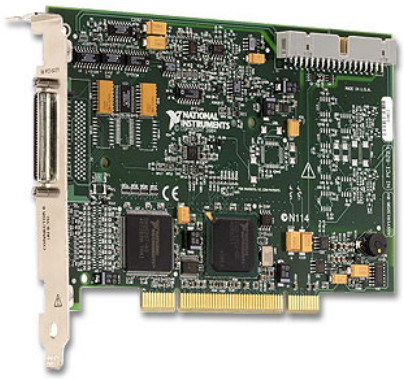

Figure 4.26 Data acquisition board NI PCI 6221 from National Instruments Company (National Instruments, 2008)

Signal	Component/sensor	Form	Pin Type
The motor speed command ω_d	Motor drive	Voltage	Analogue output
Command of the shoulder valve x_{d_1}	Shoulder valve	Voltage	Analogue output
Command of the elbow valve x_{d_2}	Elbow valve	Voltage	Analogue output
The motor speed feedback ω_actual	Motor drive	Voltage	Analogue input
Actual opening of shoulder valve x_{a_1}	Shoulder valve	Voltage	Analogue input
Actual opening of elbow valve x_{a_2}	Elbow valve	Voltage	Analogue input
Actual angular position of shoulder joint counts_shoulder	Shoulder encoder	Counts	Counter input
Actual angular position of elbow joint counts_elbow	Elbow encoder	Counts	Counter input
Actual supply pressure P_{S_actual}	Pressure transducer	Voltage	Analogue input
Actual actuation force of shoulder actuator *F_1*	Shoulder load cell	Voltage	Analogue input
Actual actuation force of elbow actuator *F_2*	Elbow load cell	Voltage	Analogue input

Table 4.15 The specifications of signals in the test rig

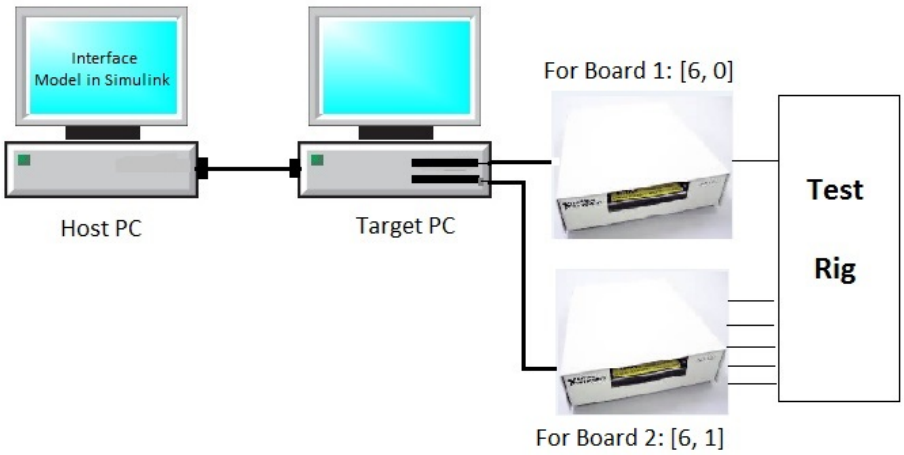

Figure 4.27 The simplified layout of xPC Target platform

The NI PCI-6221 board from National Instrument is a data acquisition board (DAQ). Each NI PCI-6221 has 2 analogue outputs (±10 V range), 16 analogue inputs (range option: ±10 V, ±5 V, ±1 V and ±0.2 V) and 24 digital I/O inputs. Due to the three analogue outputs required in this research, two NI PCI-6221 boards are used. They are inserted into the target PC. Each board has its individual connector block for signal wiring (see Figure 4.27 and Table 4.16).

Board	**Slot Location** **[Bus Number, Slot Number]**	**Description**
1	[6, 0]	For motor command only
2	[6, 1]	For motor speed feedback For command of two valves For measurement of two valves For two relative encoders For two load cells For pressure transducer

Table 4.16 The descriptions of the two NI PCI 6221 data acquisition boards

The interface in Simulink is shown in Figure 4.28. It is clear that the controller sends out 3 analogue outputs: motor speed command to Board 1, and valve opening commands to Board 2. The controller receives two actual positions of the two joints for feedback control from Board 2. And there are signals monitored from Board 2: actual supply pressure, actual openings of the two valves, actual motor speed and actual actuation force of the two actuators.

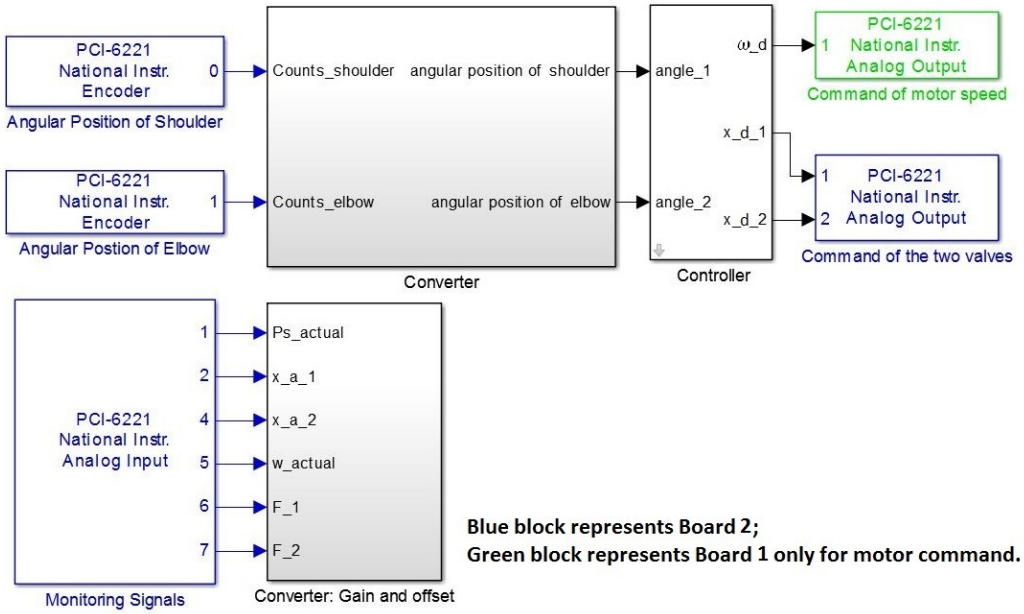

Figure 4.28 The interface of data acquisition boards in Simulink model

Chapter 5

5 System Modelling

This chapter will describe the modelling of the two-axis robotic arm. The modelling contains three domains: controller, hydraulics and mechanical. The VPVC and FPVC are modelled separately in MATLAB®/Simulink®, but they control the same robotic arm plant model in Simulink®/SimMechanics®. For the VPVC system, the hydraulic modelling consists of the motor-pump, the control valves, the manifold and the massless actuators. But in the FPVC system, no model of the motor-pump is required as the supply pressure is set at a fixed value.

5.1 Overview of the system model

The two-axis robotic arm system is modelled to enable simulation of controller performance. In the system controlled by the VPVC algorithm, the controller sends out command signals (the motor speed command and two control valves commands) to the hydraulic system, which generates the actuation force for the joints of the robotic arm. The hydraulic system in the VPVC model has the motor-pump, two control valves, the manifold and two actuators (see Figure 5.1).

In the FPVC control algorithm, the motor speed is set at a constant value which is high enough to drive flow through the relief valve and thus keep a fixed supply pressure. Hence in the hydraulic system modelling of the FPVC system, the supply pressure will be simply expressed in the form of a constant block; there is no model of the motor-pump (see Figure 5.2).

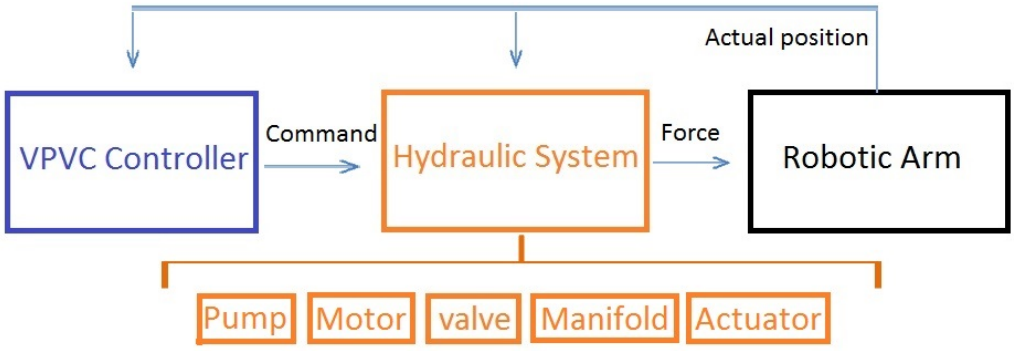

Figure 5.1 The schematic of modelling the VPVC system

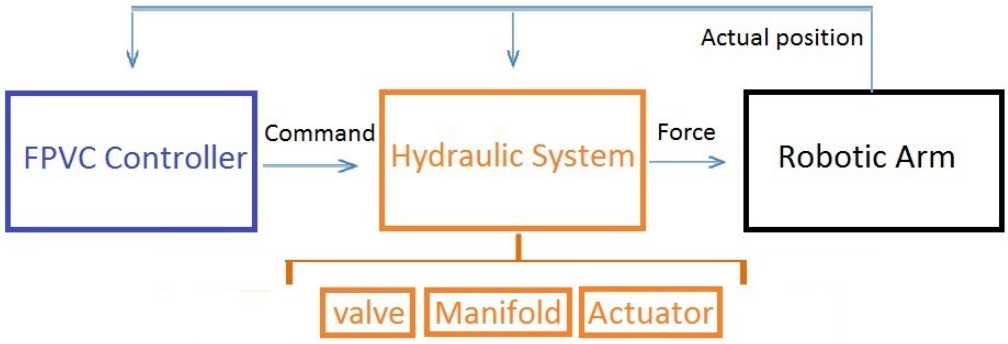

Figure 5.2 The schematic of modelling the FPVC system

The controller and the hydraulic system are modelled in MATLAB®/Simulink®. The mechanical domain (i.e. the robotic arm) is modelled in SimMechanics® which is a subset of Simulink®. Simulink® is a graphical programming tool for modelling, simulating and analysing dynamic systems. It has a graphical editor as the user interface, where the model is built by the blocks from the libraries. Simulink® is integrated with MATLAB®, which enables the user to incorporate the MATLAB® algorithms (Mathworks, 2014). SimMechanics® is a special modelling and simulation environment for a multi-body mechanical system. It uses the blocks representing bodies, joints, constraints and forces. It simulates the corresponding motion for the parameterized model which is suitable for this application: motion control of a robotic arm. An automatically generated 3D animation enables the visualization of the system dynamics.

5.2 Modelling of the hydraulics

5.2.1 Modelling of the motor-pump

The electric motor generates an angular velocity ω and a torque T as follows:

$$T = Js\omega + C\omega + D_P(P_S - P_r) \tag{5.1}$$

where J is the sum of motor shaft inertia, pump shaft inertia and flexible coupling inertia, P_S is the pressure in the supply hoses (i.e. outlet pressure of the pump), P_r is the pressure in the return line (i.e. inlet pressure of the pump), C is the viscous friction factor and D_P is the displacement of the pump.

From the Figure 5.3, the compressibility of the oil in the supply hoses can be expressed as follows:

$$sP_S = \frac{B}{V_{ps}}(Q_{pump} - Q_{out}) \tag{5.2}$$

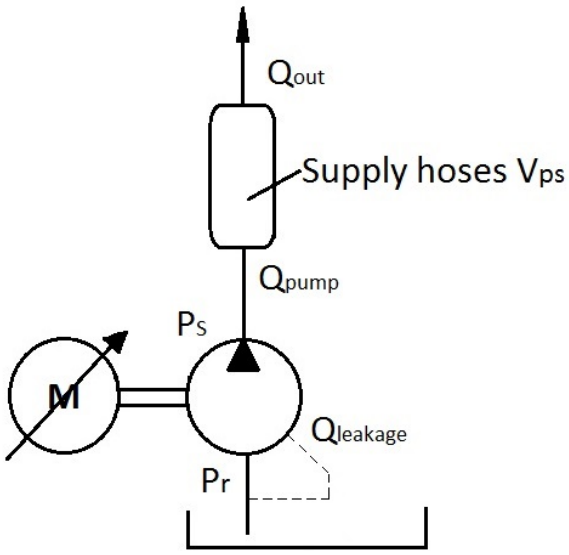

Figure 5.3 The diagram of motor-pump and supply hoses

where the Q_{pump} is the output flow from the pump (flow into the supply hoses), Q_{out} is the consumed flow rate by the actuators. B is the bulk modulus of the oil, and V_{ps} is the volume of the supply hoses.

Also,

$$Q_{pump} = \omega D_P - Q_{leakage} \tag{5.3}$$

$$Q_{leakage} = L_P(P_S - P_r) \tag{5.4}$$

where $Q_{leakage}$ is the internal leakage flow of the pump and L_P is the factor of the internal leakage of the pump.

Thus the pump and the supply hoses are modelled based on Equations 5.1 to 5.4. The block diagram in Simulink is shown in Figure A.5 of Appendix 2.1.

The motor drive produces the torque by the current I_a in the control loop (see Equation 5.5). The voltage equilibrium is shown in Equation 5.6.

$$T = K_t I_a \tag{5.5}$$

$$V = K_t\omega + I_a(sL + R) \tag{5.6}$$

where K_t is the torque constant of the motor drive, L and R are the inductance and resistance of the electric circuit in the motor drive respectively.

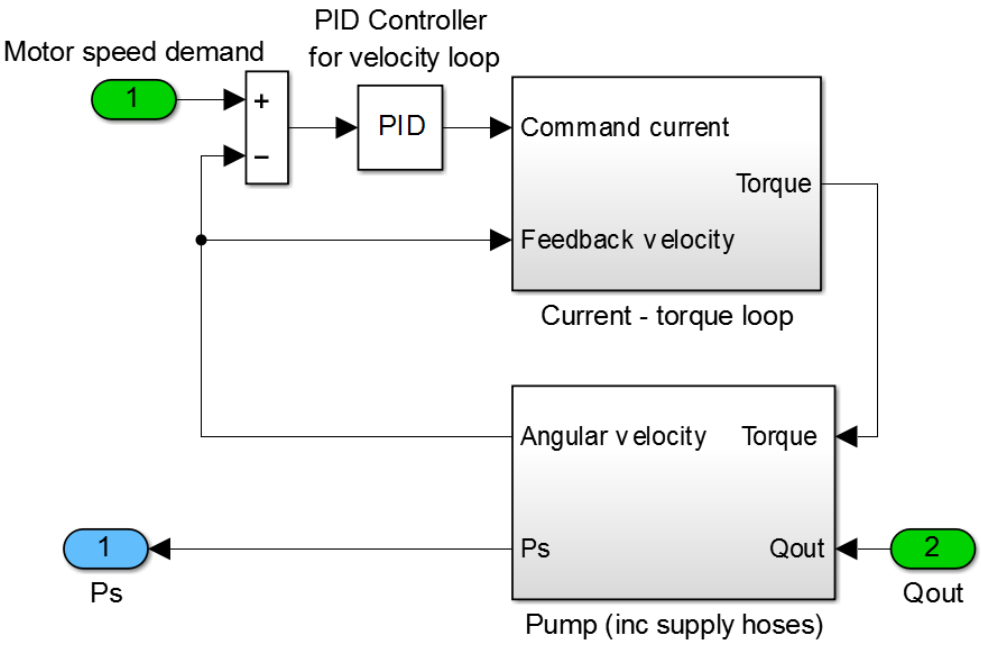

Figure 5.4 The model of motor-pump in Simulink

With a PID controller for the current loop, the block diagram in Simulink is presented in Figure A.6 in Appendix 2.1. Another PID controller is used for the speed adjustment. The parameters for these two PID controllers are obtained from the motor manufacturers Mint Workbench software (Baldor, 2010), which can output the setting information after auto-tuning of the motor. The values of these parameters are listed in Table 5.2. The overall model of motor-pump is shown in Figure 5.4.

5.2.2 Modelling of the control valve

The idealised model of the valve dynamics is a second order lag.

$$x = \frac{1}{\frac{s^2}{\omega_V^2} + \frac{2\zeta_V s}{\omega_V} + 1} u \tag{5.7}$$

where x is the valve opening and u is the control signal (normalised from -100% to +100%). In addition, a slew rate limit is imposed to constrain the maximum velocity of the valve spool. The step response of this spool model is shown in Figure 5.5. It matches the step response plot from the catalogue of D633 (see Appendix 1.1: Figure A.2).

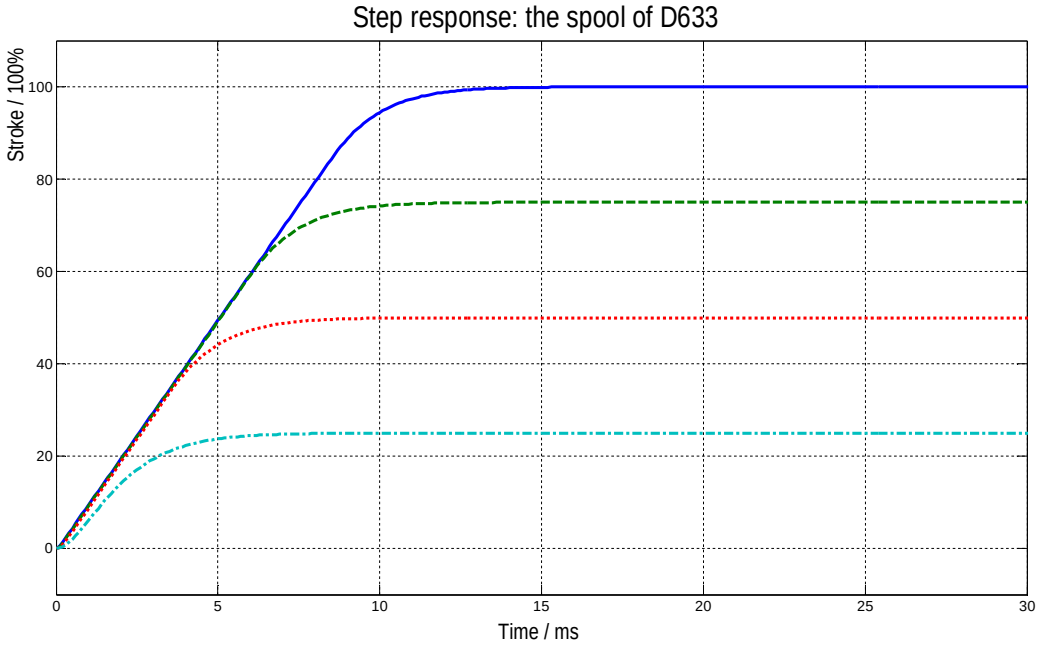

Figure 5.5 Step response of the spool model

From Figure 5.6, the orifices in the valve are modelled mathematically as follows:

$$Q_a = K_V x \phi(P_S - P_A) \text{ for } x \geq 0 \quad (5.8)$$

$$Q_a = K_V x \phi(P_A - P_r) \text{ for } x < 0 \quad (5.9)$$

$$Q_b = K_V x \phi(P_B - P_r) \text{ for } x \geq 0 \quad (5.10)$$

$$Q_b = K_V x \phi(P_S - P_B) \text{ for } x < 0 \quad (5.11)$$

where the function $\phi(\bullet)$ is a square root with modified sign:

$$\phi(\Delta P) = sgn(\Delta P) \left|\sqrt{|\Delta P|}\right| \quad (5.12)$$

Q_a and Q_b, P_A and P_B are the output flow rates, pressure from A port and B port of the spool respectively. K_V is the valve constant which can be obtained from the rated data provided by the valve catalogue. The block diagram of control valve model is shown in Figure A.7 of Appendix 2.1.

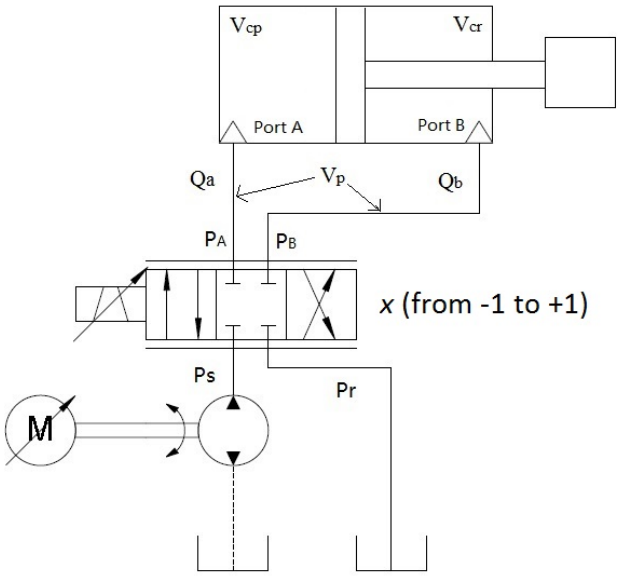

Figure 5.6 Hydraulic circuit for control valve modelling

5.2.3 Modelling of the manifold

The manifold consists of the flow paths in the steel manifold block and the micro pipes connecting manifold block with the actuator ports. In the modelling flow-pressure characteristic of the manifold, all the four manifold paths are simply assumed identical. From the comparison tests between simulation and experiments, the rated flow rate of manifold Q_{r_m} at single path pressure drop of 35 bar ΔP_{r_m} is set at 50 L/min.

$$Q = Q_{r\_m}\sqrt{\frac{\Delta P_m}{\Delta P_{r\_m}}} \tag{5.13}$$

where Q is the calculated flow through the manifold path, and ΔP_m is the pressure drop over this manifold path (from port on the valve to the port on the actuator). The block diagram of the manifold model is shown in Figure A.8 of Appendix 2.1.

5.2.4 Modelling of the actuator

According to the Equation of Continuity,

$$Q_a = A_p v + L_c(P_A - P_B) + \frac{V_m + V_p + V_{cp} + A_p v}{B}\dot{P}_A \tag{5.14}$$

$$Q_b = A_r v + L_c(P_A - P_B) - \frac{V_m + V_p + V_{cr} - A_r v}{B}\dot{P}_B \tag{5.15}$$

where L_c is the cross piston leakage factor, and v is the linear velocity of the actuator. V_m is the volume of the corresponding path in the manifold (V_1, V_2, V_3 or V_4 shown in Figure 4.15). V_p was introduced as the volume of one micro pipe; V_{cp} and V_{cr} are the volume of piston side chamber and rod side chamber when the piston is in the mid-stroke position respectively.

The effective actuation force F can be expressed as follows:

$$P_A A_p - P_B A_r - F_c - F_f = F \tag{5.16}$$

where F_c is the stopping force from the cushions on the chamber ends. F_f is the viscous friction force inside the cylinder. F_c is assumed to include the soft stop force F_{cs} and the hard stop force F_{ch}. The soft stop force F_{cs} is modelled to be proportional to the product of velocity and position squared. The soft stop force is triggered when the piston is distance y_s away from the mid-stroke position. The hard stop force F_{ch} is modelled to be proportional to the position. The hard stop force is triggered when the piston y_h away from the mid-stroke position.

$$F_c = F_{cs} + F_{ch} = K_{cs}(y - y_s)^2 v + K_{ch}(y - y_h) \tag{5.17}$$

where K_{cs} and K_{ch} are the factors of soft stop force and hard stop force respectively. y is the distance from the mid-stroke.

In practice, the friction inside the cylinder is complicated. In this research, the friction force is simply considered as proportional to the linear velocity (i.e. assumed to be viscous friction force only). So it is given by:

$$F_f = K_f v \tag{5.18}$$

K_f is the factor of the viscous friction force. The value of K_f is determined by validation tests experimentally. It varies with different actuators, different moving directions and different motion types (see Table 5.1).

Motion Type	**K_f for Shoulder in N / (m/s)**		**K_f for Elbow in N / (m/s)**	
	Extension	**Retraction**	**Extension**	**Retraction**
Square Wave	2500	2500	4000	4000
Sine Wave	2800	2400	2200	2200

Table 5.1 The estimated values of the viscous friction factor K_f

The block diagram of the actuator model is shown in Figure A.9 of Appendix 2.1. Note that the piston mass is lumped in with the robotic arm mechanical model, so piston inertia forces are not included here.

5.2.5 Overview of the final model of hydraulic system

The final model of the hydraulic system in Simulink is shown in Figure 5.7. The green inputs represent the command signals (motor speed command and spool position commands) from the controller domain. The light blue input is the linear position and velocity of the two actuators sensed from the mechanical domain. The pink outputs are the actuation forces generated by this hydraulic system, which drive the prismatic joints on the robotic arm. The parameters for the hydraulic system model are listed in Table 5.2.

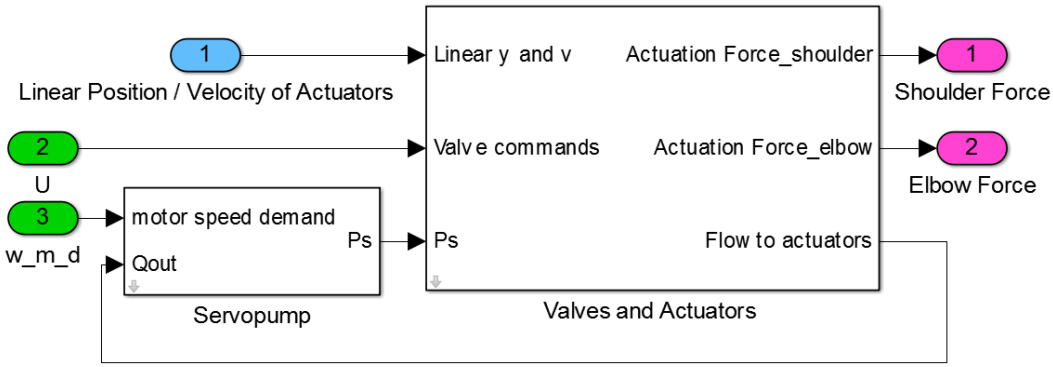

Figure 5.7 The model of the hydraulic system in Simulink

Motor	
Inertia, J	0.0000564 kgm^2
Torque Constant, K_t	0.82 Nm/Amp
Voltage limitation	320 V
Current limitation	10.1 Amp
Resistance, R	5.92 Ohm
Inductance, L	0.001365 H
PID controller for the torque loop	Proportional gain K_P = 2.80
	Integral gain K_I = 5978
	Derivative gain K_D = 0
PID controller for the velocity loop	Proportional gain K_P = 1.11
	Integral gain K_I = 110
	Derivative gain K_D = 0
Pump	
Displacement, D_P	3.14 cc/rev
Viscous damping, C	0.0002 Nm / (rad/s)
Valve	
Rated flow at single path pressure drop of 35 bar	5 L/min
Bandwidth (90^o lag) frequency, ω_V	50Hz
Damping ratio, ζ_V	0.707
Slew rate (time for fully open at max speed)	12 ms
Manifold	
Rated flow at ΔP = 35 bar (single path), Q_{r_m}	50 L/min
Internal volume of each micro pipe, V_p	1.5 cm^3
Volume of flow paths in manifold block for port B on shoulder actuator, V_1	4 cm^3
Volume of flow paths in manifold block for port A on shoulder actuator, V_2	5 cm^3

Volume of flow paths in manifold block for port A on elbow actuator, V_3	4 cm^3
Volume of flow paths in manifold block for port B on elbow actuator, V_4	8 cm^3
Actuator	
Piston Area/Annulus area, A_p / A_r	2.01/1.23 cm^2
Leakage factor across the piston at ΔP = 70 bar, L_c	0.15 L/min
Volume of piston side chamber, V_{cp}	6.5 cm^3
Volume of rod side chamber, V_{cr}	4.5 cm^3
System Characteristics	
Return line pressure , P_r	1e5 Pa
Effective bulk modulus, B	0.15 G N/m^2
Volume of supply hoses, V_{ps}	20 cm^3

Table 5.2 The parameters of the hydraulic system

5.3 Modelling of the robotic arm

The robotic arm (including the mechanical parts and the hydraulic actuators) is modelled by SimMechanics blocks. The SimMechanics blocks are classified as body blocks, joint blocks, sensor/actuation blocks and other function blocks. The body defines a rigid body with customized properties like mass, inertia and coordinate systems. The joints constrain the mechanical degrees of freedom between two connecting rigid bodies. The sensors and actuation blocks are provided for the motion sensing and motion control in the simulation.

5.3.1 The definition of coordinate system and ground

The world coordinate system used in this research follows the right-hand-rule convention. The final 3D model of the two-axis robotic arm with its coordinate system definition is presented in Figure 5.8. Please note all the lengths mentioned in this section are in metres. The shoulder joint and elbow joint are rotating within the x-z plane (sagittal plane) around y-axis, and clockwise rotation/torque is positive. Gravity acts in negative z direction with a vector of 9.81 m/s^2. The SimMechanics analysis mode is forward dynamics.

The base of the model is a simple ground plane which represents the ground body. The ground plane defines the reference position of the world coordinate system, and all the subsequent body positions are based on this reference. In the SimMechanics modelling environment, each body has its own local coordinate system to define a user-definable number of ports besides the centre of gravity (CG), indicated by a prefix 'CS' (coordinate system).

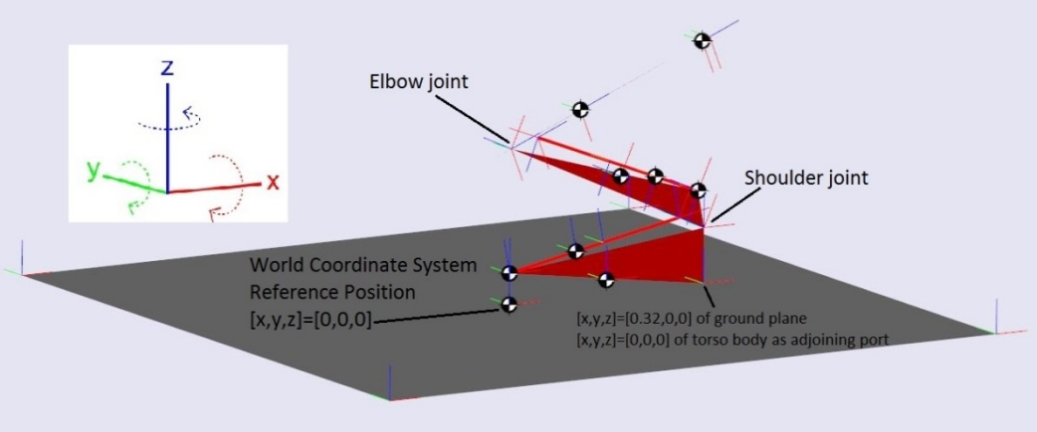

Figure 5.8 The definition of world coordinate system in SimMechanics model

In Figure 5.8, the CG of the ground plane is located at [x, y, z] = [0, 0, 0], which is relative to the previous body it is attached to: the ground body. This kind of port is named as 'adjoining' port, which is the connection port with previous base body. The adjoining port of a body block is defined as the zero reference of this body coordinate system. The CS1 of ground plane is located at [x, y, z] = [0.32, 0, 0], relative to the CG port of the ground plane, which is used to attach the port CS2 of the torso body (see Figure 5.9). In the torso body block, CS2 is the connection port with the ground plane by the weld joint. Hence CS2 is the adjoining port of the torso body, and its location in the torso parameters block is defined as [x, y, z] = [0, 0, 0]. Then all the other ports in the torso body (including its CG) are positioned with the reference of CS2. Note: the robotic arm is modelled as if the two joints were in 0^{o} position as defined in Figure 4.21.

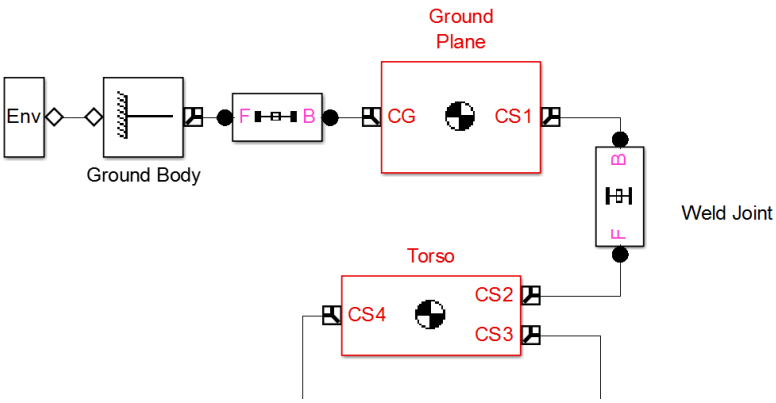

Figure 5.9 The model of the environment, ground body, ground plane and torso in SimMechanics

5.3.2 Torso

As shown in Figure 5.9, the torso attaches the ground body at port CS2 (corresponding to P_0 in Figure 4.20) which is its adjoining port [x, y, z] = [0, 0, 0]. It has two coupling ports: CS3 (corresponding to P_1 in Figure 4.20) to the upper arm (shoulder joint) and CS4 to the shoulder actuator body (see Figure 5.10).

Because the torso is fixed on the ground during the test, its CG position is irrelevant and has been assumed as a centre point [x, y, z] = [-0.16, 0.02, 0] relative to the adjoining port CS2.

The mass of the torso/shoulder assembly (including the shoulder actuator) M_0 is 2.482 kg and the inertia I_0 is 0.00745 kgm^2 as listed in Table 4.8. This inertia from the HyQLeg-V2.1 catalogue is only specified along the x-axis. Again, however, as the torso is fixed on the ground, its inertia is somewhat redundant. The inertia matrix is set as below.

$$\begin{bmatrix} I_0 & 0 & 0 \\ 0 & I_0 & 0 \\ 0 & 0 & I_0 \end{bmatrix} = \begin{bmatrix} 0.00745 & 0 & 0 \\ 0 & 0.00745 & 0 \\ 0 & 0 & 0.00745 \end{bmatrix} \quad (5.19)$$

CS3 is located at [x, y, z] = [0, 0, 0.08] relative to CS2. CS4 is located at [x, y, z] = [-0.32, 0, 0.045] (corresponding to [-d_{11}, 0, d_{12}] in Figure 4.21) relative to CS2 (see Figure 5.9). The model of the torso in Simulink has been shown together with the environment and ground blocks in Figure 5.9.

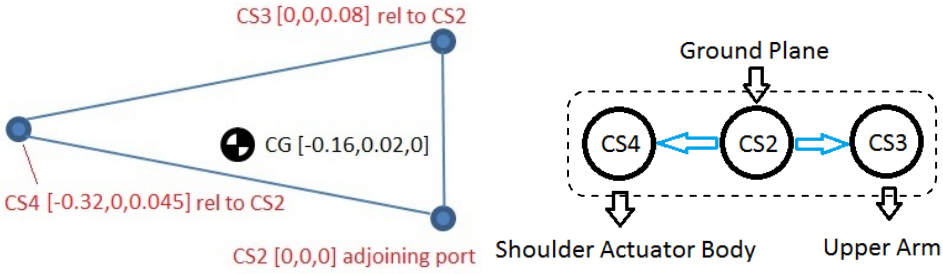

Figure 5.10 The simplified diagram of the torso model (note: the port pointed to by a blue arrow means it is positioned with the reference to the port from which the arrow originates)

5.3.3 Upper arm and shoulder joint

As shown in Figure 5.11, the upper arm body is connected to the torso by its adjoining port CS1 (P_1 in Figure 4.20). It provides CS1 port for the coupling with the piston of the shoulder actuator, CS2 port (P_2 in Figure 4.20) for the coupling with the forearm (elbow joint) and CS4 port for the coupling with the body of the elbow actuator.

The CG of the upper arm (including the elbow actuator) is located at [x, y, z] = [0.0225, 0, 0.162] relative to its adjoining port CS1. The mass M_1 of the upper arm including the elbow actuator is 1.772 kg and the inertia I_1 is 0.0239 kgm^2 about the y-axis through its gravity centre P_{m1} as listed in Table 4.8. So the inertia matrix input for the upper arm is shown below.

$$\begin{bmatrix} I_1 & 0 & 0 \\ 0 & I_1 & 0 \\ 0 & 0 & 0 \end{bmatrix} = \begin{bmatrix} 0.0239 & 0 & 0 \\ 0 & 0.0239 & 0 \\ 0 & 0 & 0 \end{bmatrix} \tag{5.20}$$

The CS2 is located at [x, y, z] = [0, 0, 0.35] (corresponding to [0, 0, P_1P_2] in Figure 4.20) relative to CS1. CS3 is located at [x, y, z] = [0, 0, 0.045] (corresponding to [0, 0, b_2] in Figure 4.21) relative to CS1. The CS4 is located at [x, y, z] = [0.045, 0, 0.0251] relative to CS1.

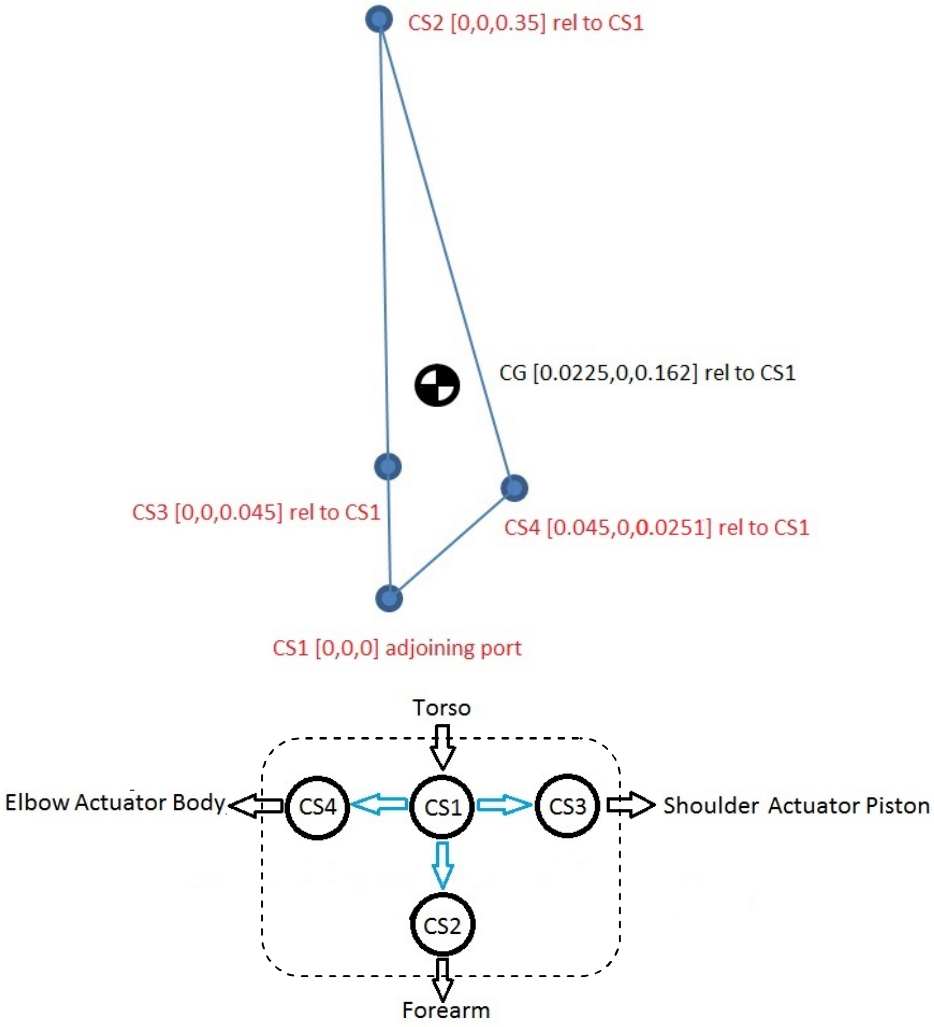

Figure 5.11 The simplified diagram of upper arm model

The adjoining port of the upper arm CS1 in Figure 5.11 and the CS3 port of the torso in Figure 5.10 are coupled together by a revolute joint – the shoulder joint (the blue block in Figure 5.12). The B port in the joint block is connected with the base body and the F port is connected the following body. In the parameters dialog of the joint block, the rotation axis can be edited together with the reference coordinate system setting. In this research, two rotational joints (shoulder and elbow) are rotating around the y-axis. The reference coordinate system is the world coordinate system. The blue block with a label 'IC' is to set the initial angular position of the joint. The green block in Figure 5.12 is an angular position sensor which outputs the measured angle in degree.

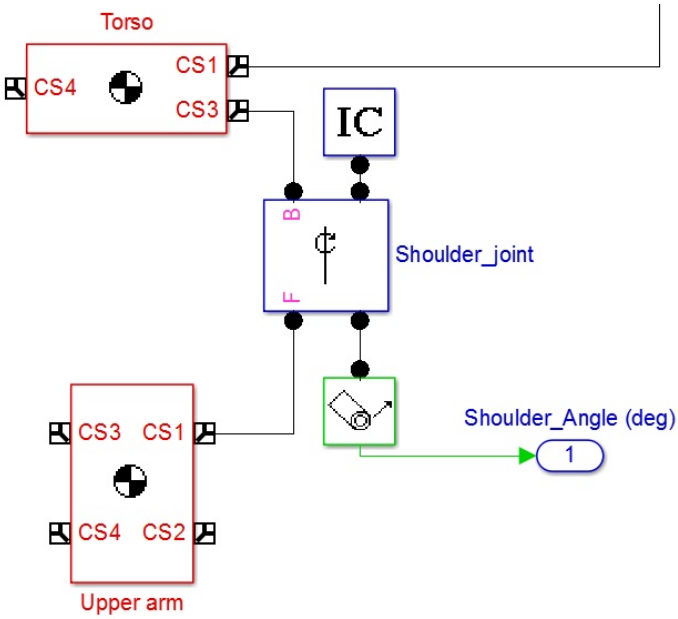

Figure 5.12 The model of torso, upper arm, attached via revolute shoulder joint in SimMechanics

5.3.4 Forearm and elbow joint

As shown in Figure 5.13, the forearm body is connected to the upper arm by its adjoining port CS1 (P_2 in Figure 4.20). It provides CS2 port (P_3 in Figure 4.20) for the connection with hand and CS4 port for the connection with the piston of the elbow actuator.

The CG of the forearm is located at [x, y, z] = [0, 0, 0.122] (P_2P_{m2} in Figure 4.20). The mass M_2 is 0.739 kg and the inertia I_2 is 0.0035 kgm^2 with respect to forearm gravity centre, through P_{m2} in the y-axis as listed in Table 4.8. So the inertia matrix input for forearm's parameter block is shown below.

$$\begin{bmatrix} I_2 & 0 & 0 \\ 0 & I_2 & 0 \\ 0 & 0 & 0 \end{bmatrix} = \begin{bmatrix} 0.0035 & 0 & 0 \\ 0 & 0.0035 & 0 \\ 0 & 0 & 0 \end{bmatrix} \quad (5.21)$$

CS2 is located at [x, y, z] = [0, 0, 0.33] (corresponding to [0, 0, P_2P_3] in Figure 4.20) relative to CS1. The CS4 is located at [x, y, z] = [0.0047, 0, 0.0448] (corresponding to [$b_2\sin(\varepsilon_{22})$, 0, $b_2\cos(\varepsilon_{22})$] in Figure 4.21) relative to CS1.

The adjoining port of the forearm (CS1 in Figure 5.13) and the CS2 port of the upper arm in Figure 5.11 are coupled together by a revolute joint – the elbow joint (the blue block in Figure 5.14). Like the shoulder joint introduced in last subsection, there is an IC block to set the initial position of the elbow joint and a sensor block to measure the angle.

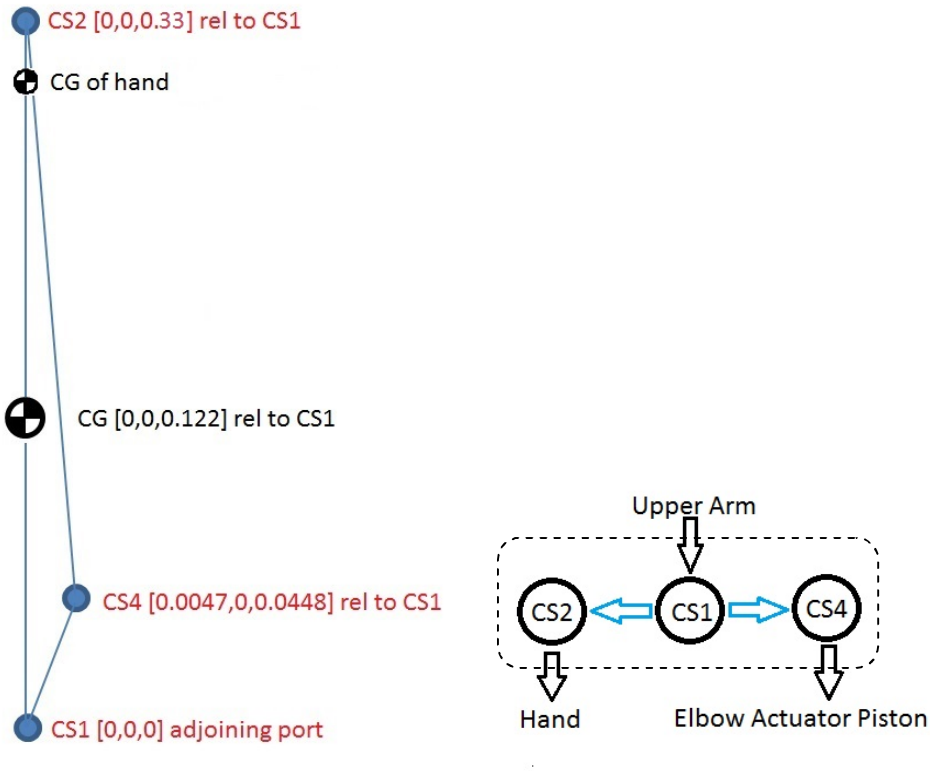

Figure 5.13 The simplified diagram of forearm model

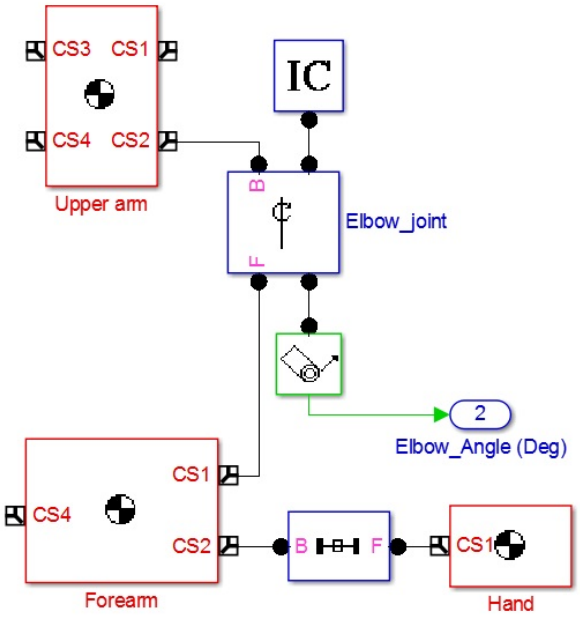

Figure 5.14 The model of the upper arm, forearm, attached via revolute elbow joint in SimMechanics

5.3.5 Hand

The hand body is modelled simply as locating its CG only. Its adjoining port is port CS1 (P_3 in Figure 4.20). And the CG is located at [x, y, z] = [0, 0, -0.02675] relative to CS1 as mentioned in subsection 4.3.2. The hand body is connected with forearm via a weld joint (see Figure 5.15).

The mass M_3 is 1.039 kg and the inertia I_3 is 0.00304 kgm^2 with respect to its CG P_{m3} in y-axis.

$$\begin{bmatrix} I_3 & 0 & 0 \\ 0 & I_3 & 0 \\ 0 & 0 & 0 \end{bmatrix} = \begin{bmatrix} 0.00304 & 0 & 0 \\ 0 & 0.00304 & 0 \\ 0 & 0 & 0 \end{bmatrix} \quad (5.22)$$

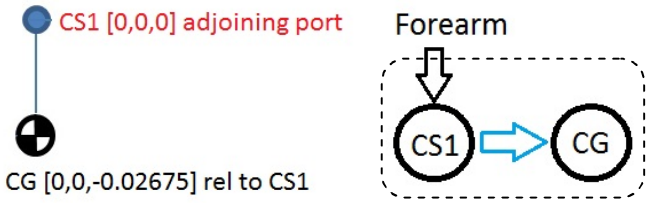

Figure 5.15 The simplified diagram of hand model

5.3.6 Hydraulic actuator

The model of the hydraulic actuator in SimMechanics is designed to receive the actuation force from the hydraulic domain. The structure of the shoulder actuator is presented in Figure 5.16.

5.3.6.1 The actuator body

The port CS1 of the actuator body is collocated via a revolute joint at torso port CS4. The length of the actuator is 157 mm from the actuator datasheet hence the other end of the actuator body (i.e. port CS2) should be located at a distance of 157 mm away from CS1. The robotic arm is modelled as if the two joints were in 0^o position. Therefore the inclination of this actuator can be calculated with the dimensions in Figure 4.21.

$$\nu = \tan^{-1}\frac{(d_{13}-d_{12}+b_1)}{d_{11}} = 14.04^o \quad (5.23)$$

The position of the actuator body port CS2 relative to CS1 can be calculated with the inclination and the actuator body length by the following equations.

$$x = 0.157\cos\nu = 0.1523 \quad (5.24)$$

$$z = 0.157\sin\nu = 0.0381 \quad (5.25)$$

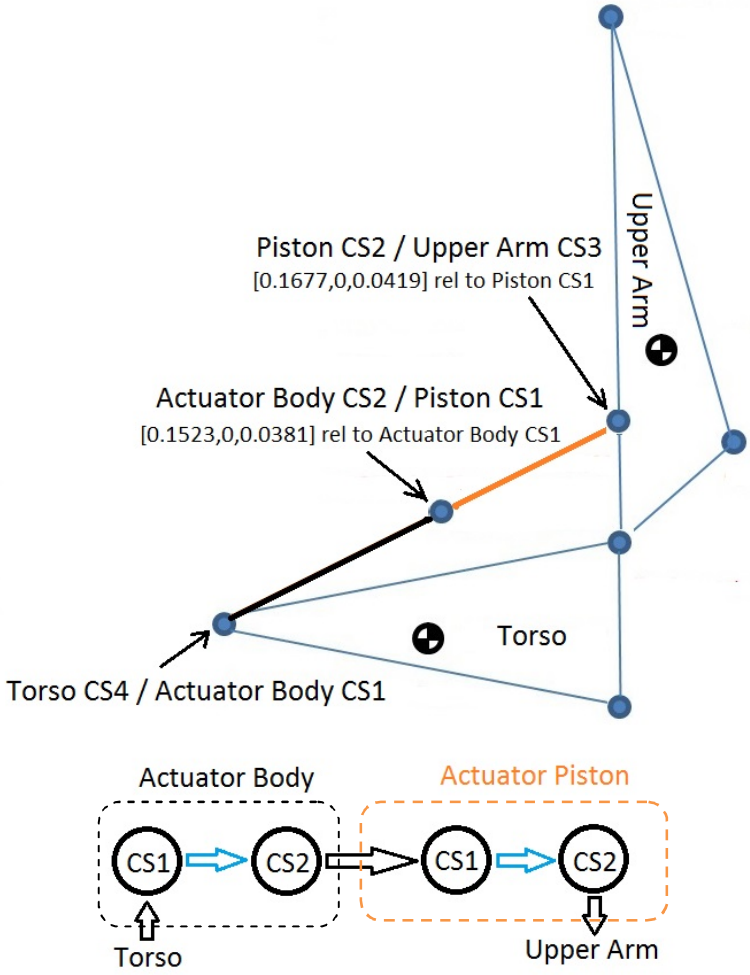

Figure 5.16 The simplified diagram of the shoulder actuator (black means the body of the shoulder actuator and orange means the piston)

5.3.6.2 The actuator piston

The port CS1 of the piston is coupled with the actuator body port CS2 via a prismatic joint. Hence the CS1 of the piston is set as the adjoining port of the piston block. The relative position of the other port CS2 is required to be calculated.

$$x = d_{11} - 0.1523 = 0.1677 \tag{5.26}$$

$$z = d_{13} - 0.0381 = 0.0419 \tag{5.27}$$

5.3.6.3 Orientation of the actuator

The positions of both body and piston of the shoulder actuator are figured out (see the coordinates in Figure 5.16). The prismatic joint connecting them allows the linear motion in the x-axis of the actuator. However, this x-axis has a slip angle of 14.04^{o} with the x-axis in the world coordinate system. To realise this, the coordinate system of CS1 in the actuator body is rotated by [0, -14.04^{o}, 0] (rotation from the x-axis in world coordinate system, clockwise is positive). The rotation is applied in the parameters block of the actuator body. Therefore all the subsequent ports of the actuator body and piston inherit this coordinate system rotation, which makes the correct linear motion of the shoulder actuator.

The model of the shoulder actuator in SimMechanics is shown in Figure 5.17. The actuator force (yellow block) from the hydraulic domain actuates the prismatic joint to mobilise the linear motion between the actuator body and piston. The sensor (green block) outputs the linear position (relative extension of the actuator) and linear velocity of the piston.

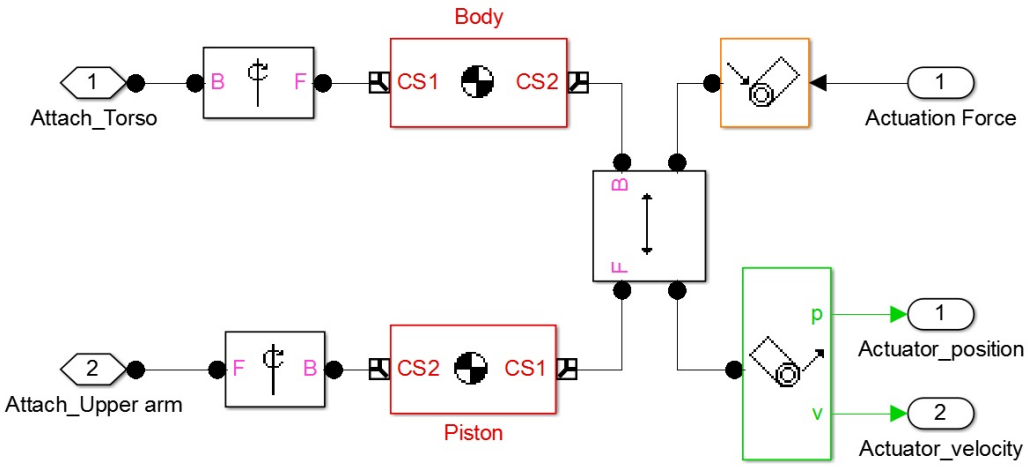

Figure 5.17 The model of the shoulder actuator (body and piston) in SimMechanics

The implementation of the elbow actuator is identical, so it is not repeated here. The simplified diagram and the port positions are shown in Figure 5.18. The inclination of the elbow actuator is -96.328^{o}.

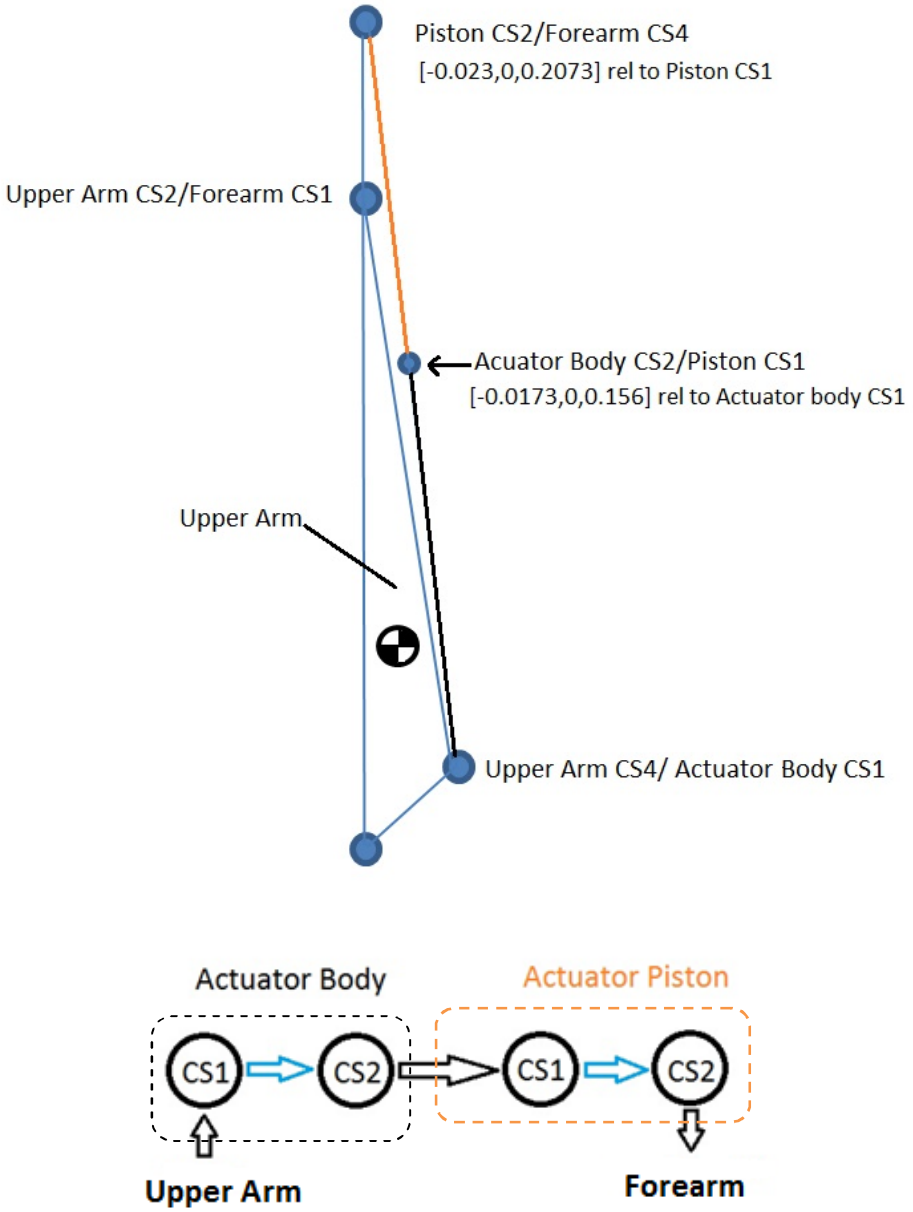

Figure 5.18 The simplified diagram of the elbow actuator (black means the body of the elbow actuator and orange means the piston rod)

5.3.7 The robotic arm model overview

The robotic arm modelled by SimMechanics blocks is shown in Figure 5.19. The pink ports represent the connections with the hydraulic domain and the controller domain. The light blue outputs represent the angular position sensed from the mechanical domain. All the parameters can be found in the M-file in Appendix 2.2.

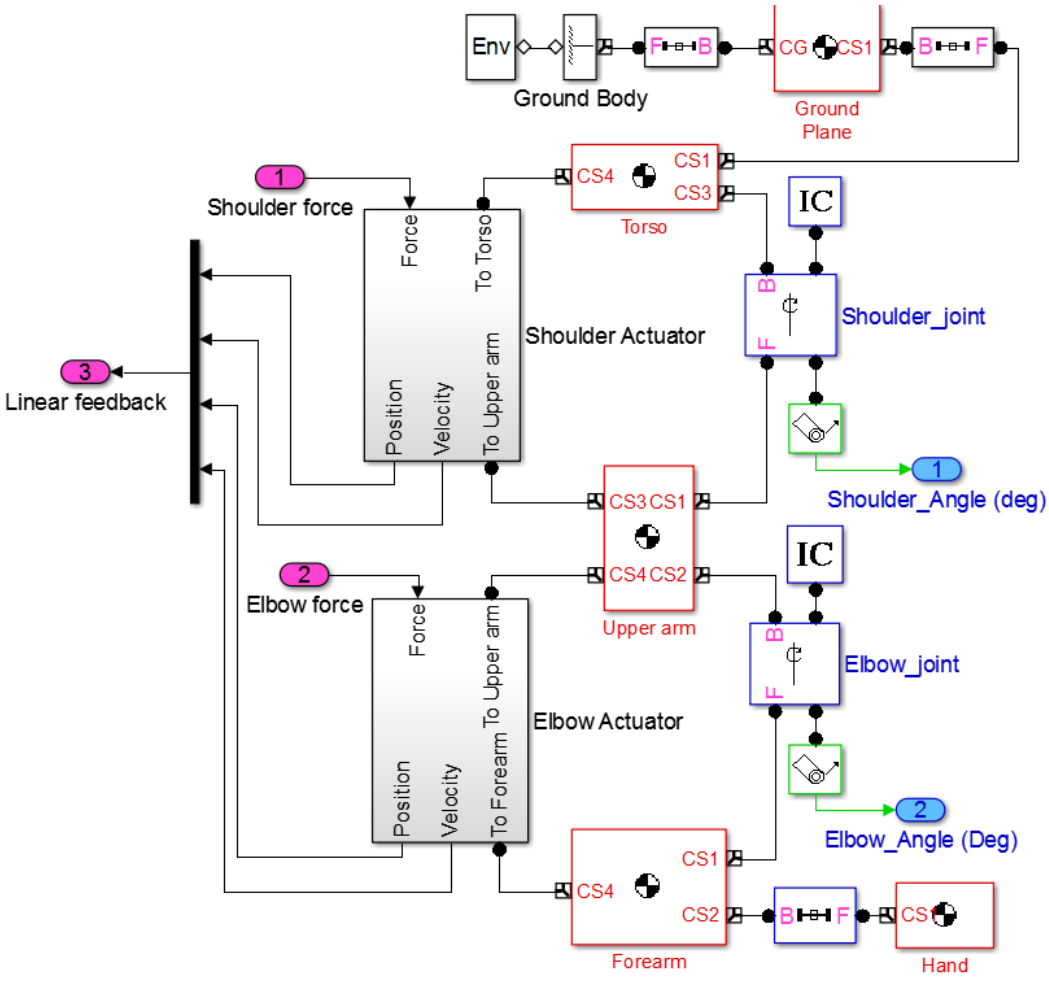

Figure 5.19 The overview of the robotic arm model in SimMechanics

5.4 Modelling of the controllers

5.4.1 Modelling of the FPVC controller

As introduced in Chapter 3, FPVC uses simple Proportional Integral (PI) controllers for the electro-hydraulic position control. In Figure 5.20, the P and I represent proportional gain and integral gain respectively.

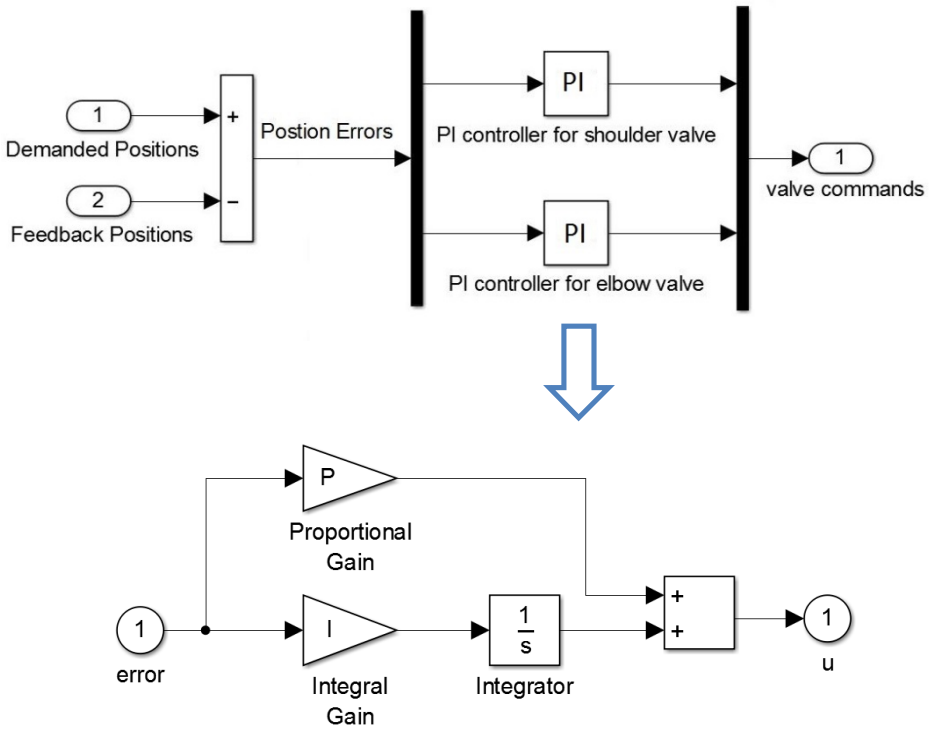

Figure 5.20 The diagram of FPVC controller and the inside view of the PI block

5.4.2 Modelling of the VPVC controller

The modelling of the VPVC controller is carried out according to the algorithm description in Chapter 3. The feed forward part predicts the system commands (the motor speed and spool positions for the two control valves). The model built in Simulink is presented in Figure 5.21. The blue block in Figure 5.21 is calculating the required P_S for each actuator with a given motion demand. This block corresponds to the blue dashed zone in Figure 3.4. The green block in Figure 5.21 is the checks for the MA and calculation of the feed forward commands, which corresponds to the green dashed zone in Figure 3.4.

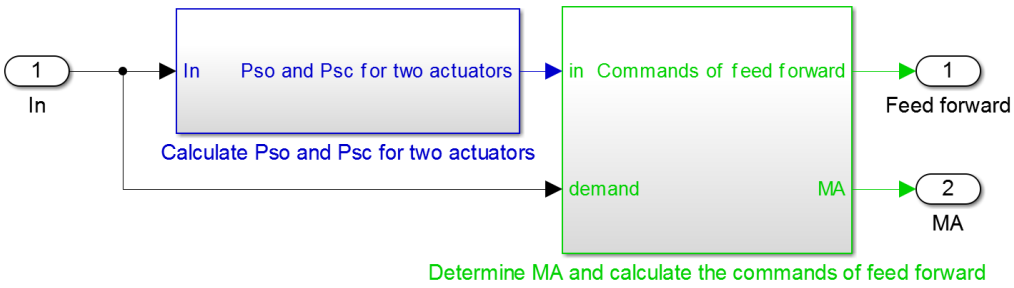

Figure 5.21 The feed forward part of the VPVC controller in Simulink

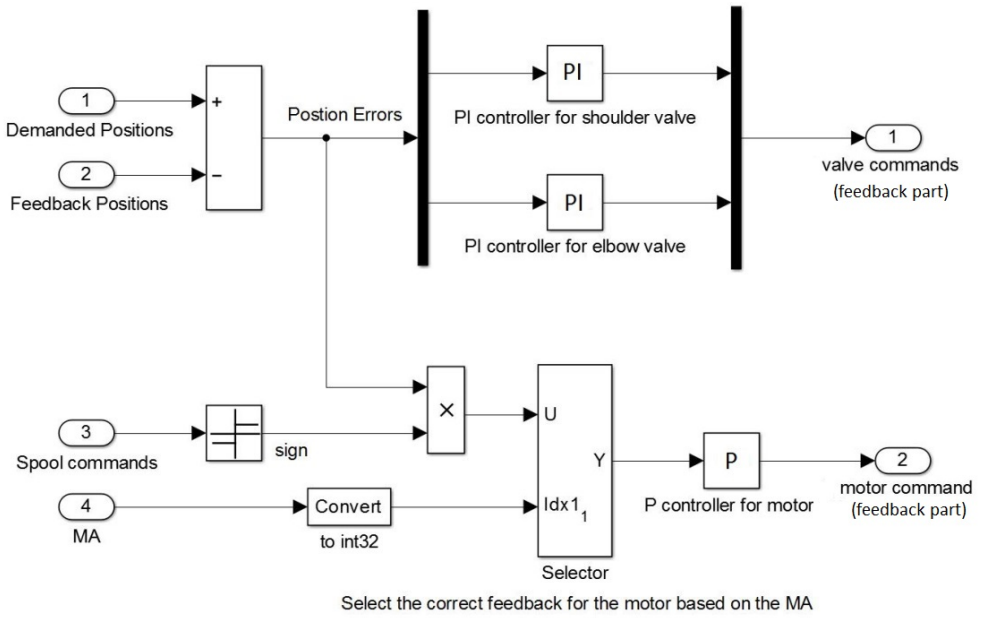

Figure 5.22 The feedback part of the VPVC controller in Simulink

The model of the feedback part in Simulink is shown in Figure 5.22. The corresponding diagrams are in Figure 3.11 and Figure 3.12. The linear position errors are the input signals to these P(I) controllers. For the motor feedback, the model has to select the MA's error first.

The final model of the VPVC controller is shown in Figure 5.23.

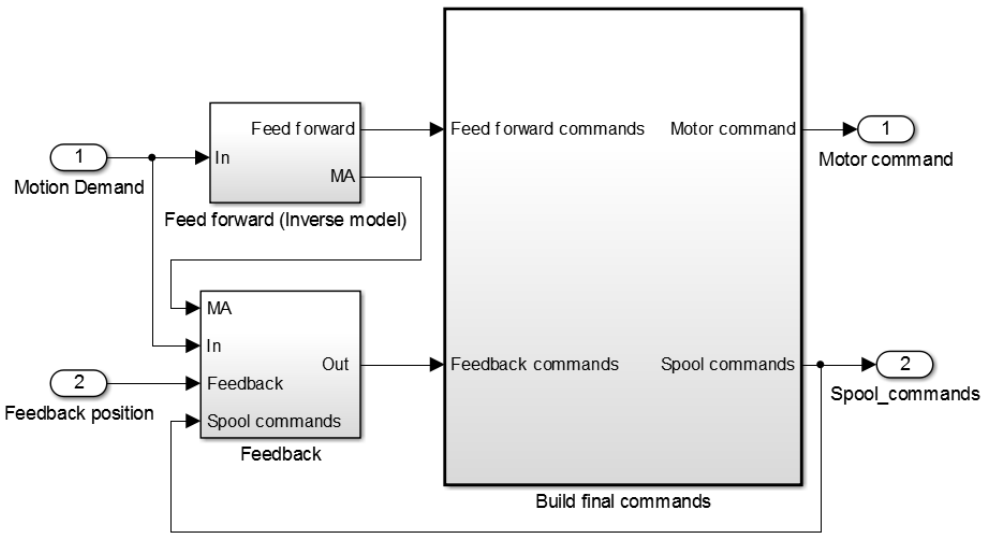

Figure 5.23 The VPVC controller model in Simulink

5.5 The final model

The final model of system for the simulation research is presented in Figure 5.24. The block 'Controller' can be different controllers (FPVC and VPVC) with different motion demands (sine wave or square wave). The parameters are in Appendix 2.2.

The numerical solver information is shown in Table 5.3. The controller model is also used to generate real time code to implement the controller for experimental testing, and the solver is included in the table.

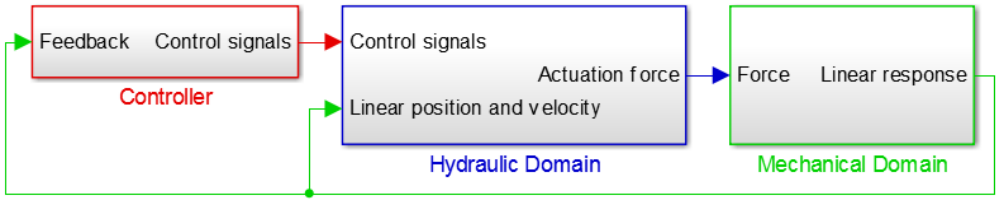

Figure 5.24 The final simulation model of the two-axis robotic arm in Simulink

Solver Type	Fixed-step Ode3 Bogacki-Shampine	
Sampling Time (simulation)	FPVC 0.001 s	VPVC 0.0004 s
Sampling Time (real time implementation)	FPVC 0.001 s	VPVC 0.001 s

Table 5.3 The numerical solver information

Chapter 6

6 Simulation Results

In this chapter, the simulated results of FPVC and VPVC will be presented and discussed. The dynamic performance will be analysed and the hydraulic power consumption will be compared between FPVC and VPVC. For FPVC, the square wave demand motion with varied PI controller settings and the sine wave demand motion with varied amplitude and frequencies will be shown and discussed. For VPVC, similar results are presented; except that the square wave demand is low-pass filtered so that it can be differentiated.

For the FPVC, the fixed supply pressure is set at 38 bar which is the highest continuous pressure of the system. The maximum continuous torque of the servo motor is 2.09 Nm, which for a loss-free pump equates to a maximum continuous supply pressure of 41.8 bar. This is reduced to 38 bar due to the mechanical efficiency of the pump.

This chapter has 4 sections. The structure is as follows:

- FPVC square wave motion simulation results
- FPVC sine wave motion simulation results
- VPVC filtered square wave motion simulation results
- VPVC sine wave motion simulation results

6.1 FPVC square wave simulation results

The simulation inputs a square wave motion demand to each joint. The square wave is 10 degrees amplitude with a frequency of 0.1Hz. The aim of this section is to observe and analyse the dynamic response when a joint has a step motion demand and to find out the steady state error, hence a low frequency together with a long enough time are used to guarantee that the steady state is reached. The shoulder demand is delayed by 1 second compared to the elbow joint, to allow the cross-coupling between joints to be observed.

The procedure for determining the gains in the two valve PI controllers is: fixing the value of the gains in the shoulder valve PI controller, vary the value of the gains in the elbow valve PI controller to get different response plots. Adopt a best value of the gains in the elbow valve PI controller from the last step, and vary the value of gains in the shoulder valve PI controller. Choose the best value of gains for the shoulder valve PI controller.

Firstly, setting the gains of the shoulder PI controller to $K_p = 60$ and $K_I = 10$, the elbow PI controller is varied from $K_p = 70$ to 100 with $K_I = 10$. The performance is less sensitive to the value of integral gain K_I, hence its value is fixed at $K_I = 10$ for the series tests and only the influence of various proportional gain K_P values is shown and discussed. Table 6.1 show the settings used in this series of tests.

Test No	***Shoulder PI Controller***		***Elbow PI Controller***	
	K_P	**K_I**	**K_P**	**K_I**
1	60	10	70	10
2	60	10	80	10
3	60	10	90	10
4	60	10	100	10

Table 6.1 Tests for FPVC square wave response simulation – various elbow PI controller settings

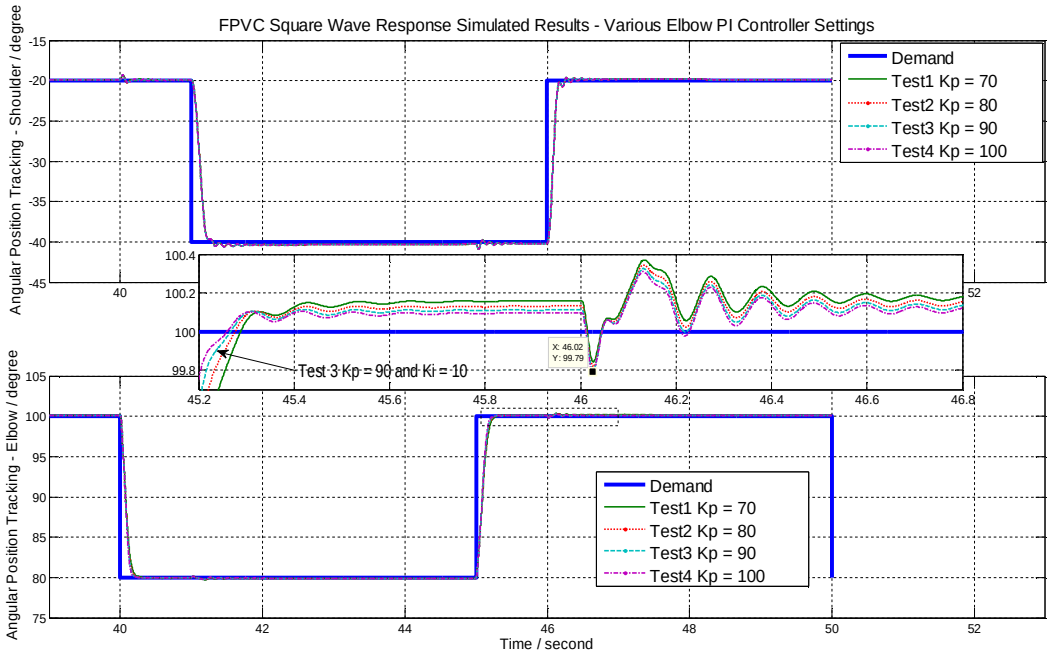

Figure 6.1 FPVC square wave simulated response– various elbow PI controller settings

The simulated angular positions are shown in Figure 6.1. From the figure, it can be found that both the two joints achieve very small steady state error, and the shoulder joint response changes little with various elbow PI controller settings (top subplot). The shoulder oscillates slightly at time 40 second and 45 second because of the mutual force that the elbow motion applies on the shoulder at those moments. The same situation happens on the elbow joint as well: at time 41 second and 46 second, the elbow response is disturbed due to the shoulder's transient step motion.

Different elbow responses are provided with different values of K_P in elbow PI controller. From the bottom subplot in Figure 6.1, the response is getting faster with the increasing value of elbow proportional gain K_P. But high proportional gain also gives less damping, i.e. A much serious error at 46.02 second with Test 4 K_P = 100. Generally, Test 3 with K_P = 90 and K_I = 10 has a relatively fast response with acceptable damping. So these are chosen as the best elbow PI controller settings. Next the shoulder valve PI controller will be tuned. Table 2 shows the settings used in these tests.

Test No	*Shoulder PI Controller*		*Elbow PI Controller*	
	K_P	K_I	K_P	K_I
5	50	10	90	10
6	60	10	90	10
7	70	10	90	10
8	80	10	90	10

Table 6.2 Tests for FPVC square wave response simulation – various shoulder PI controller settings

The simulated angular responses are in Figure 6.2. Varying the PI controller settings of the shoulder, the elbow response changes little (bottom subplot). A slight disturbance on the elbow response can be seen when shoulder moves rapidly (i.e. time 41 second and 46 second). Similar disturbances occur on the shoulder response at time 40 second and 45 second (top subplot). Test 6, Test 7 and Test 8 with high proportional gain have a short rise time compared with Test 5. Test 8 exhibits more oscillations so it requires longer time to steady state (zoom A and zoom B). Hence from Test 7, K_P = 70 and K_I = 10 are selected to be the gains of the shoulder PI controller.

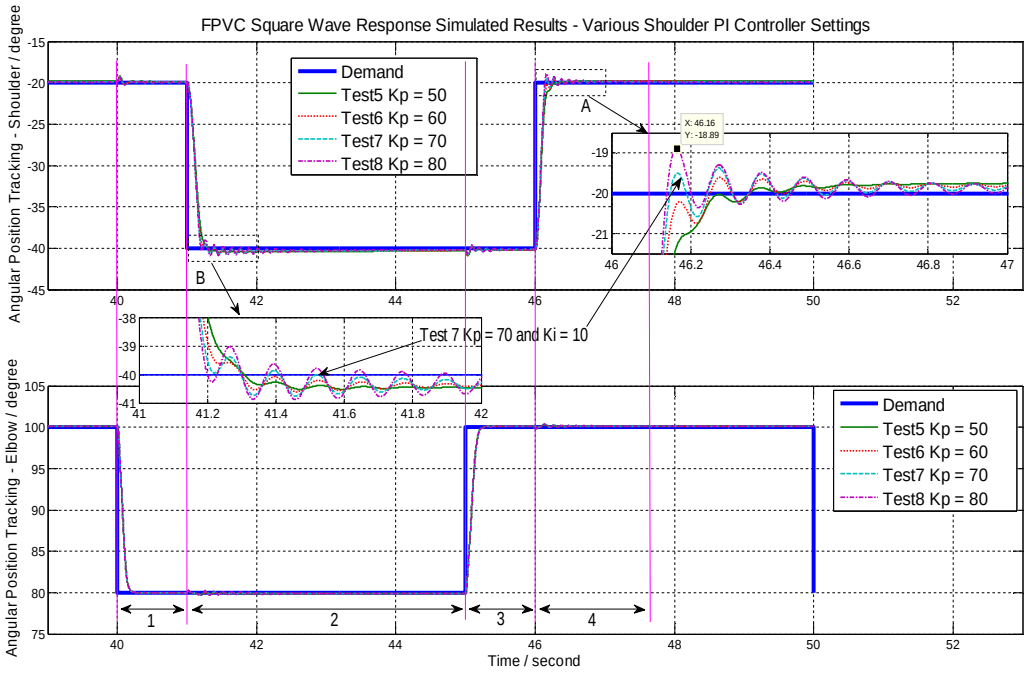

Figure 6.2 FPVC square wave simulated response – various shoulder PI controller settings

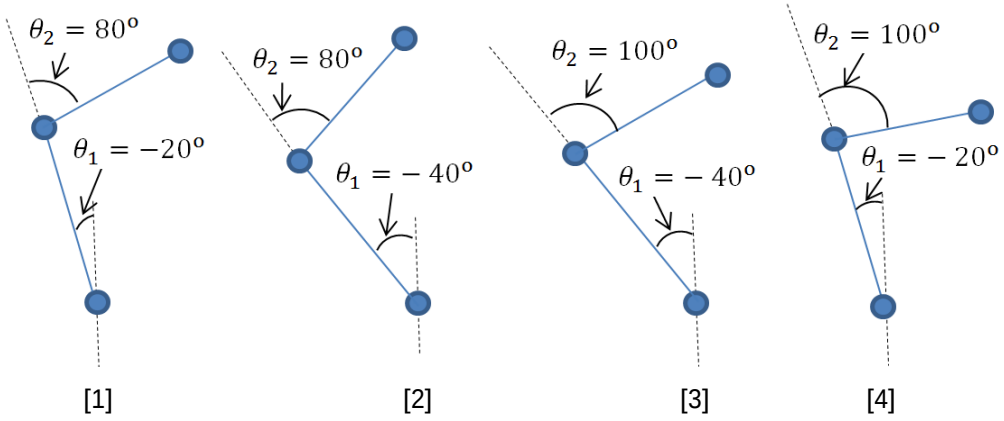

Figure 6.3 Various positions of the robotic arm with square wave motion

From Figure 6.1 and Figure 6.2, it can be found that there is always a minor offset about 0.5^o after each step motion until the steady state, regardless of the different PI controller settings. It is believed that this offset is caused by the gravity effect and motion inertia due to the various position changings. The various positions of the robotic arm can be divided in 4 stages (see the pink boundary lines in Figure 6.2). And the corresponding gestures are shown in Figure 6.3. When the robotic arm moves from [1] to [2], the angular position of shoulder joint is from -20^o to -40^o. The motion inertia generates a minor deflection. In addition, the gravity force of the robotic arm acts on the left side of the vertical central axis. In other words, the robotic arm has a trend to rotate towards anti-clockwise at position [2]. Similar reason, when the position switches from [3] to [4], the angular position of shoulder joint has a minor offset towards the clockwise.

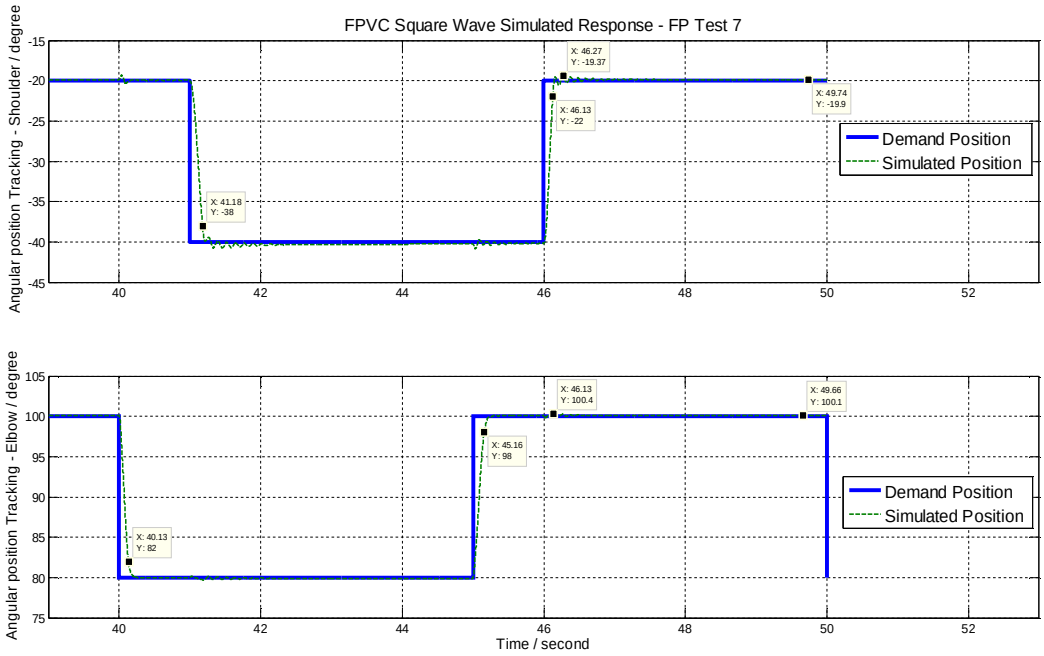

Figure 6.4 FPVC square wave simulated response – FP Test 7

The simulated result of Test 7 (Shoulder: K_P = 70 and K_I = 10 Elbow: K_P = 90 and K_I = 10) is plotted in Figure 6.4 for detailed discussion and for comparison with experimental results in Chapter 7.

From Figure 6.4, the shoulder performance has more oscillations than elbow joint. The shoulder reaches 90% of the step size after 0.13 second for extension and 0.18 second for retraction. The steady state error of shoulder is 0.1^o. The elbow reaches 90% of the step size after 0.13 second for extension and 0.16 second for retraction. The steady state error of elbow is 0.1^o.

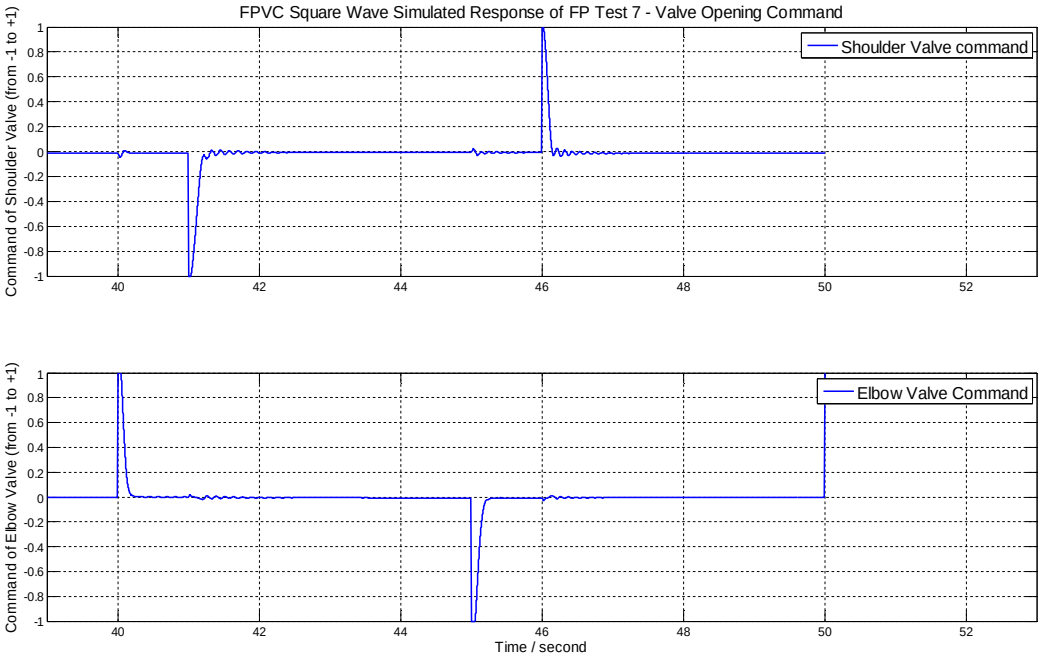

Figure 6.5 FPVC square wave simulated results of FP Test 7 – valve opening command

The valve command signals are plotted in Figure 6.5. It can be observed the shoulder valve command has more oscillations than elbow. Both the valves saturate for a short time saturation when a step demand occurs. The corresponding experimental results will be shown and analysed in Section 7.1.

The PI controller tuning method for FPVC is illustrated above: fix PI controller setting of shoulder first, then alter the value of elbow PI controller to get a best performance; then fix the elbow PI controller and tune the shoulder's controller. This procedure is also used for the experimental system.

6.2 FPVC sine wave simulation results

A key aim of this thesis is to validate that a better energy-efficiency can be achieved with VPVC than FPVC. Sine waves will be the motion demand in this series of hydraulic power consumption comparison tests. The names of this series tests begin with Com (the abbreviation of comparison). The test of FPVC is named ComX-FP, while the corresponding test of VPVC is ComX-VP. The hydraulic power consumed and dynamic responses will be compared between FPVC and VPVC. In each comparison test, the frequencies of the demands to the two joints are different and the amplitudes are the same (see Table 6.3)

This section will introduce the simulated sine wave response for FPVC. The supply pressure is still set at 38 bar. In all the comparison tests of FPVC, the two valve PI controllers adopt the gains from the last section: shoulder valve PI controller $K_P = 70$ with $K_I = 10$ and elbow valve PI controller $K_P = 90$ with $K_I = 10$.

Test Name	***Shoulder Demand***		***Elbow Demand***	
	Motion Range	**Frequency**	**Motion Range**	**Frequency**
Com1	-60^o to 0^o	0.3Hz	70^o to 130^o	0.4Hz
Com2	-60^o to 0^o	0.4Hz	70^o to 130^o	0.5Hz
Com3	-60^o to 0^o	0.5Hz	70^o to 130^o	0.6Hz
Com4	-60^o to 20^o	0.3Hz	50^o to 130^o	0.4Hz
Com5	-60^o to 20^o	0.4Hz	50^o to 130^o	0.5Hz
Com6	-60^o to 20^o	0.5Hz	50^o to 130^o	0.6Hz

Table 6.3 Comparison tests information

The mean power consumed by the system is calculated for each simulated test. The power consumed is calculated from the supply pressure P_s and the sum of flow rates supplied to the two cylinders (Equation 6.1).

$$P_S \times \sum_{i=1}^{2} Q_i \tag{6.1}$$

This power will be called hydraulic power consumed. In Chapter 5, it was stated that the pump with the electric motor is not modelled. The power consumed by the relief valve won't be considered and calculated. Detailed results For Test Com3-FP and Test Com4-FP will be shown and discussed next.

From Figure 6.6, it can be seen that angular position tracking of the two joints is generally satisfactory in Com3-FP. The amplitude ratio of shoulder motion is 1.003 and of elbow motion is 1. But due to the lag of 0.05s for shoulder and 0.04s for elbow, the dynamic errors can be up to 5.8^o and 5.2^o respectively (Figure 6.7); which are 9.7% and 8.7% of the total range of demand motion (60 degrees).

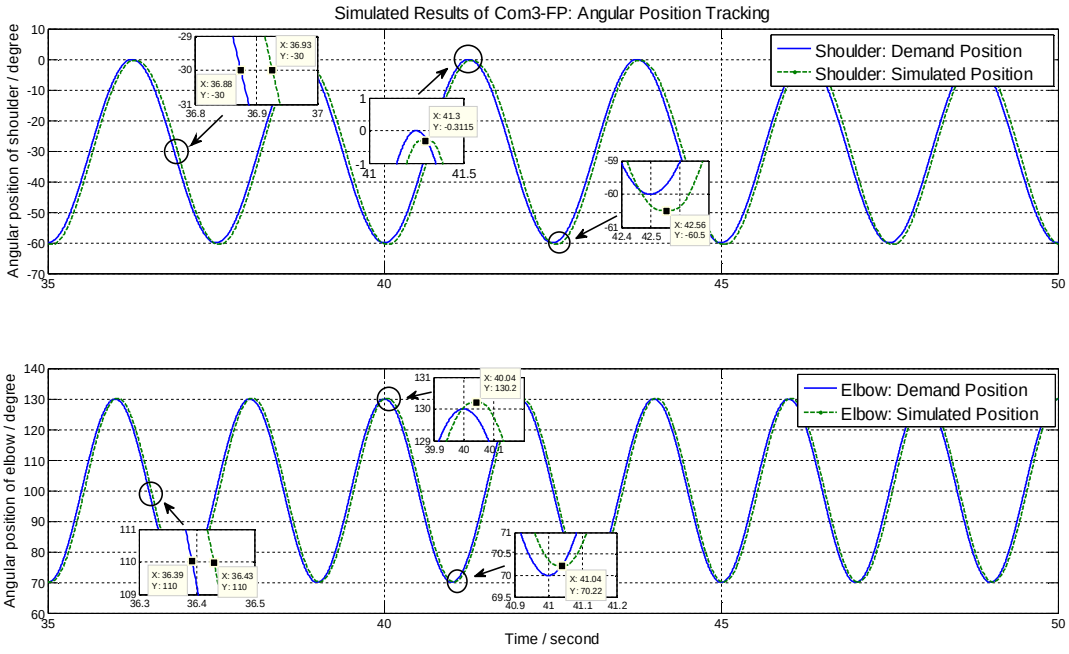

Figure 6.6 Angular position tracking of simulated Test Com3-FP

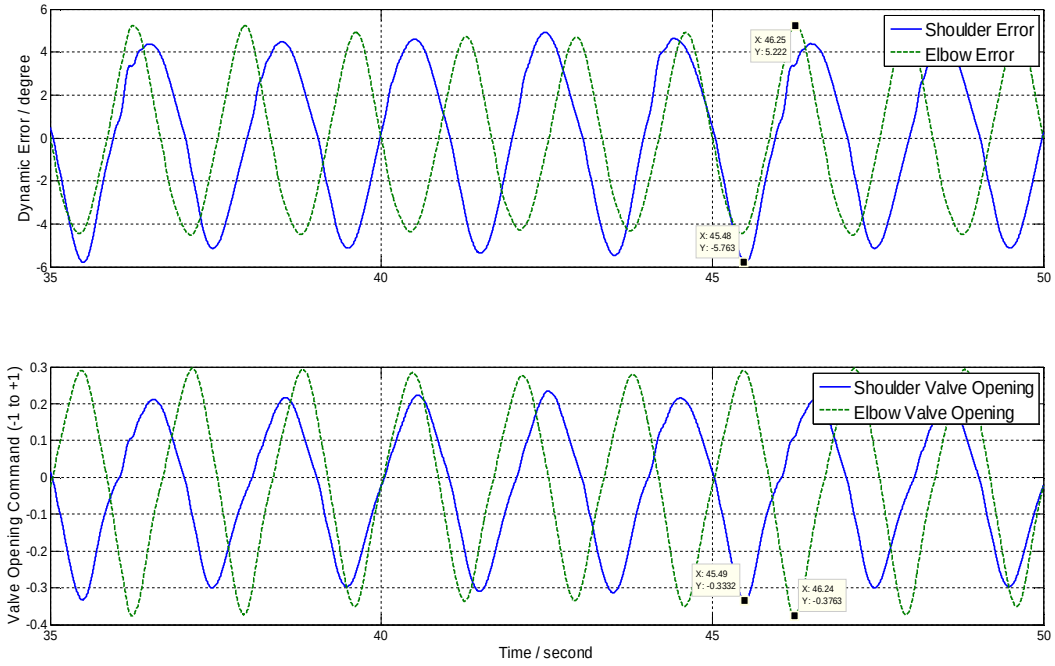

Figure 6.7 Dynamic error and valve opening command of simulated Test Com3-FP

The bottom plot of Figure 6.7 shows the valve opening command signals to the two joints. The valve opening command represents the drive capability of FPVC with a P_S of 38 bar. In Test Com3-FP, the maximum valve opening command signals are 33% for shoulder valve and 38% for elbow valve. The mean hydraulic power consumed for Com3-FP simulation is 59.81W.

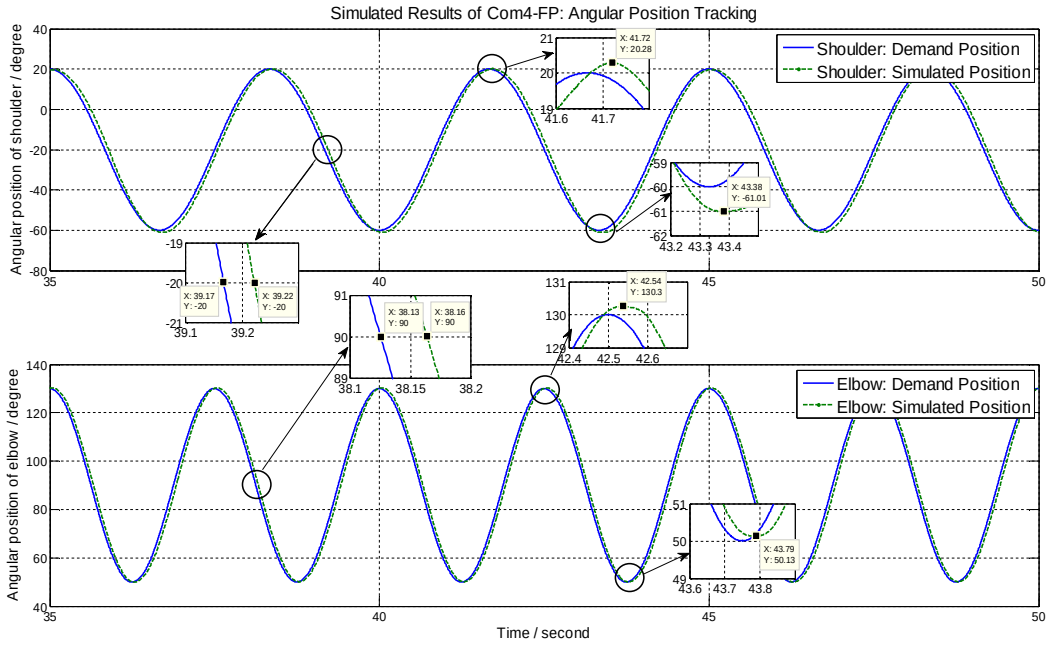

Figure 6.8 Angular position tracking of simulated Test Com4-FP

Com4-FP has a larger motion range of 80^{o} (Figure 6.8). Similar to Com3-FP, visible phase delay can be found in the position tracking of the two joints: the simulated position of the shoulder joint has a delay of 0.05s and the elbow is 0.03s. The amplitude ratios are 1.016 for shoulder motion and 1.002 for elbow motion.

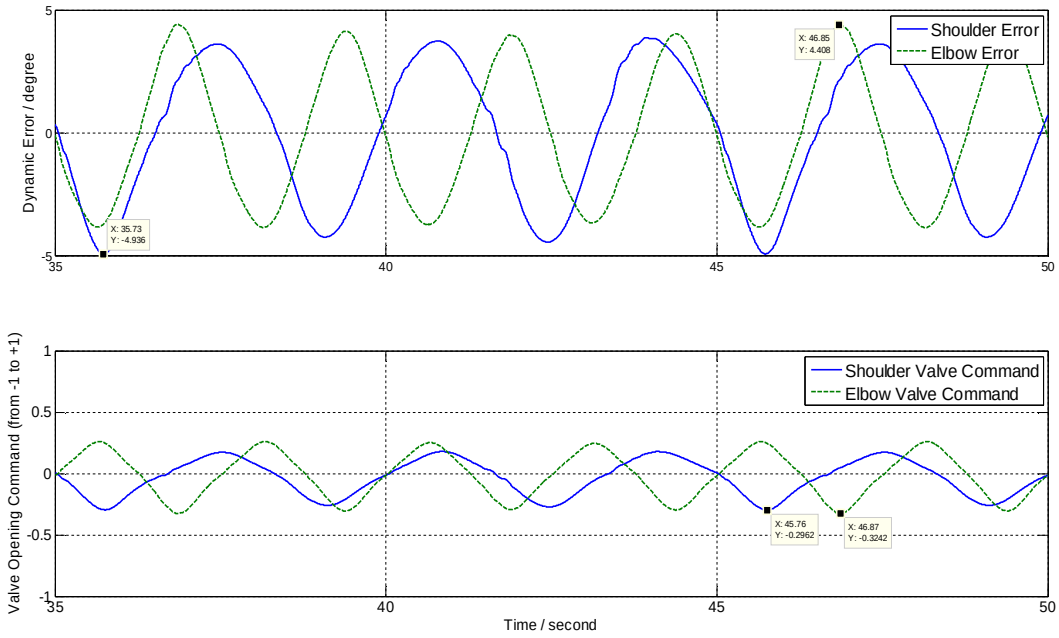

Figure 6.9 Dynamic error and valve opening command of simulated Test Com4-FP

From Figure 6.9, it can be found that the maximum dynamic errors are 5.0^{o} for the shoulder and 4.4^{o} for the elbow, which are equivalent to 6.3% and 5.5% of the total motion range. The maximum valve opening command signals are up to 30% for the shoulder and 32% for the elbow in the Com4-FP simulation. The mean hydraulic power consumed for Com4-FP is 50.93W.

Test	*Max valve opening (absolute)*		*Max Dynamic Error (absolute in degree)*		*Phase Delay (degree)*		*Amplitude Ratio (Feedback/Demand)*		*Mean Simulated Hydraulic Power (W)*
	S	*E*	*S*	*E*	*S*	*E*	*S*	*E*	
Com1-FP	18%	21%	3.1	2.8	-5.4	-4.32	$60.5^o/60^o$	$60.0^o/60^o$	38.50
Com2-FP	29%	26%	4.4	4.0	-7.2	-7.2	$60.3^o/60^o$	$60.0^o/60^o$	49.19
Com3-FP	33%	38%	5.8	5.2	-9	-8.64	$60.2^o/60^o$	$60.0^o/60^o$	59.81
Com4-FP	30%	32%	5.0	4.4	-5.4	-4.32	$81.3^o/80^o$	$80.2^o/80^o$	50.93
Com5-FP	43%	43%	7.1	6.0	-7.2	-7.2	$81.0^o/80^o$	$80.1^o/80^o$	65.09
Com6-FP	70%	63%	11.6	7.7	-12.6	-8.64	$81.0^o/80^o$	$80.0^o/80^o$	79.20

Table 6.4 Summary of simulated results of comparison tests – FPVC

The summary of simulated comparison tests for FPVC is presented in Table 6.4 (where *S* presents shoulder joint and *E* presents elbow joint). From the data, it can be seen that the amplitude ratios of all the tests are close to 1. The phase delay is the major contributing factor to the dynamic error. FPVC controller is simply composed of two valve PI controllers. Each PI controller sends out valve opening command and receives the simulated position of cylinder as feedback. Its control algorithm relies on cylinder position feedback only without any feed forward, which causes an inevitable lag. The dynamic errors are increasing with increasing demand frequencies and/or demand amplitude. The dynamic errors of the first five FPVC tests are within 10% of total motion range and only Test Com6-FP has an error up to 14.5%, which proves the gain tuning results of the square wave motion is effective.

6.3 VPVC filtered square wave simulation results

From Section 3.2, it is clear that the force prediction is indispensable to VPVC feed forward control. The force prediction requires the first derivative and the second derivative calculation of the motion demand for getting velocity and acceleration; these are used in the force prediction equations to implement VPVC feed forward. Hence a standard square wave can't be used as the demand motion to VPVC due to the infinite derivatives at transient steps. To solve this problem, a filtered square wave is used in VPVC tests. A 2^{nd}-order low-pass filter with a cut-off frequency of 2Hz and damping ratio of 0.707 is connected after the standard square wave generator in Matlab/Simulink. The input demand generation is shown in Figure 6.10.

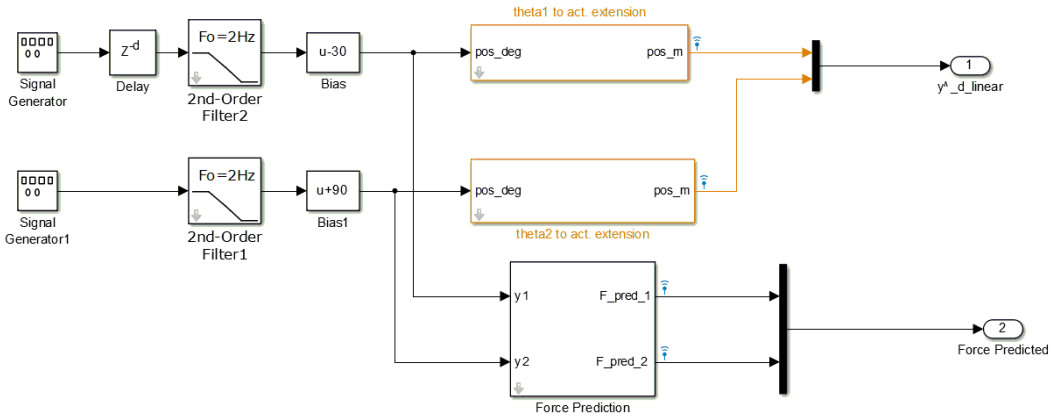

Figure 6.10 Input generation to VPVC filtered square wave motion

VPVC filtered square wave simulation follows a similar procedure to the FPVC square wave simulation: vary the setting of elbow valve PI controller with a fixed setting of shoulder valve PI controller; then vary the setting of shoulder valve PI controller with the best setting of elbow valve PI controller from the last step. An extra step is required for the motor P controller tuning. Estimation of an effective value of K_P in the motor P controller is shown as below.

From Section 3.3, it is stated that the feedback part of the motor speed command can be expressed as follows:

$$\Delta\omega = K_P e_{MA} sgn(x_{MA}) \tag{6.2}$$

where $\Delta\omega$ is the feedback part of the motor speed command, which helps correct the linear position error of the master actuator (e_{MA}), and x_{MA} is the valve opening command of the master actuator.

Assume the master actuator valve is fully open so its position is determined by the motor speed.

$$\Delta Q = D_P \Delta\omega \tag{6.3}$$

where ΔQ is the extra flow to the master actuator, and D_P is the capacity of the axial piston pump.

A rough estimation of K_P will be now carried out. The rate of change of position error is related to the flow.

$$\frac{de_{MA}}{dt} = \frac{\Delta Q}{A} sgn(x_{MA}) \tag{6.4}$$

where *A* is the action area of the piston (piston side A_p when extension, rod side A_r when retraction). Combined with Equation 6.2 and Equation 6.3, the error dynamics are given by:

$$\frac{de_{MA}}{dt} = \frac{D_P K_P e_{MA}}{A} \tag{6.5}$$

Thus to obtain an error elimination time constant of Δt:

$$K_P = \frac{A}{\Delta t D_P} \tag{6.6}$$

This gives a value of K_P = 4000 with the piston side area A_p and an error-elimination time constant Δt of 0.1 second. If the error-elimination time is doubled, a value of K_P = 2000 is found. Considering the response time in FPVC square wave test 7, a trial value of K_P = 3000 is used during the two valve PI controllers adjustment. After the tuning of the two valve PI controllers, the tuning of motor P controller will be followed.

Firstly, setting the gains of the shoulder PI controller to K_p = 70 and K_I = 10, which are the same as the gains chosen for the FPVC simulation; the elbow PI controller is varied from K_p = 60 to 180 with K_I = 10. The performance is less sensitive to the value of integral gain K_I, hence its value is fixed at K_I = 10 for the tests and only the influence of various proportional gain K_P values will be shown and discussed. Table 6.5 shows the settings used in this series of tests.

Test No	***Motor P Controller***	***Shoulder PI Controller***		***Elbow PI Controller***	
	K_P	**K_P**	**K_I**	**K_P**	**K_I**
1	3000	70	10	60	10
2	3000	70	10	120	10
3	3000	70	10	180	10

Table 6.5 Tests of VPVC filtered square wave response simulation– various elbow PI controller settings

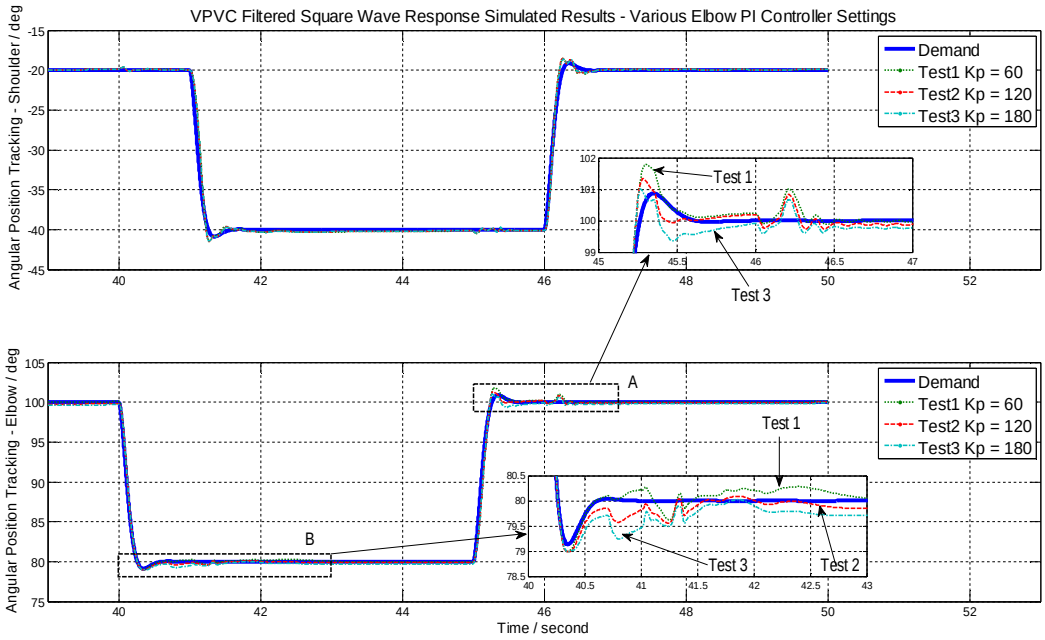

Figure 6.11 VPVC filtered square wave response simulated results – various elbow PI controller settings

The simulated response of VPVC filtered square wave motion demand is shown in Figure 6.11. The shoulder's performance changes little with different settings of elbow valve PI controller (top subplot). The shoulder joint oscillates slightly at time 40.2 second and 45.2 second because of the mutual force that the elbow motion applies on the shoulder at those moments. A similar but more significant phenomenon is seen on the elbow joint at time 41.2 second and 46.2 second, especially at 46.2 second (zoom A in Figure 6.11).

From the bottom subplot of Figure 6.11, it can be seen that in Test 3 high gain can bring a fast response to get close to the demand during the rising (zoom A). But the high gain also leads larger errors after rising (i.e. 45.5 second in zoom A). In zoom B, Test 3 has a more significant oscillation. Test 2 reaches a smaller steady state error compared with the other two tests. Combining these considerations, a moderate setting of Test 2, $K_P = 120$ with $K_I = 10$, is chosen for the elbow valve PI controller. After fixing the setting of the elbow valve PI controller, the setting of the shoulder valve PI controller is altered (Table 6.6).

Test No	Motor P Controller	Shoulder PI Controller		Elbow PI Controller	
	K_P	K_P	K_I	K_P	K_I
4	3000	60	10	120	10
5	3000	100	10	120	10
6	3000	140	10	120	10

Table 6.6 Tests of VPVC filtered square wave response simulation– various shoulder PI controller settings

From Figure 6.12, it can be seen that Test 6 gives larger errors during 41.4 second to 41.8 second on shoulder performance. From zoom A, it is observed that Test 6 brings a faster response. In zoom B, Test 4 shows a slightly larger error compared with Test 5 and Test 6. In conclusion, Test 5, K_P = 100 and K_I = 10, is the best setting for shoulder valve PI controller.

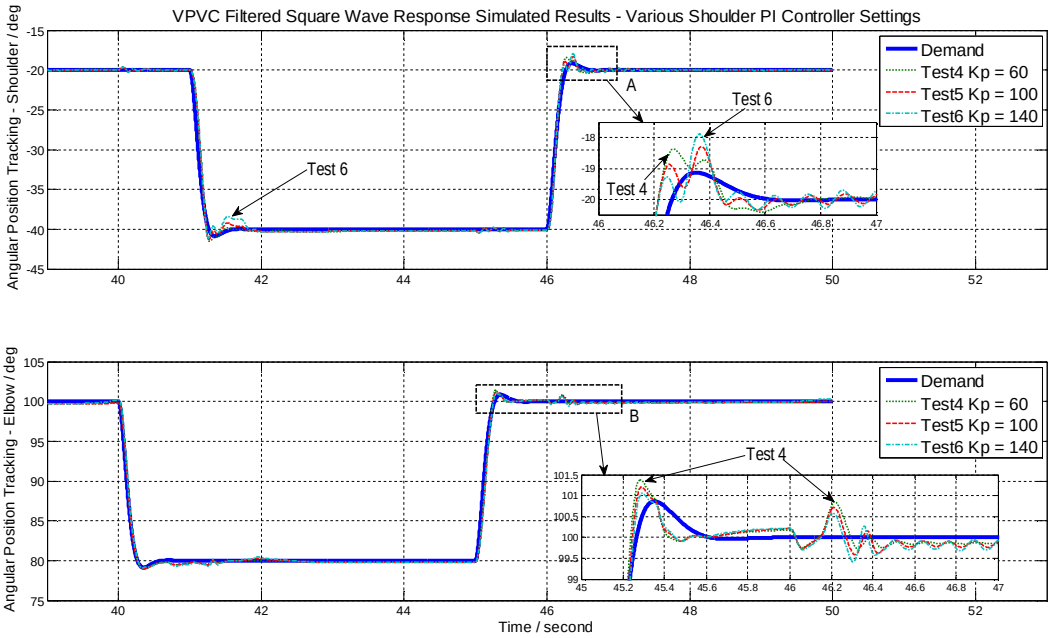

Figure 6.12 VPVC filtered square wave response simulated results – various shoulder PI controller settings

Test No	*Motor P Controller*	*Shoulder PI Controller*		*Elbow PI Controller*	
	K_P	**K_P**	**K_I**	**K_P**	**K_I**
7	2000	100	10	120	10
8	3000	100	10	120	10
9	4000	100	10	120	10

Table 6.7 Tests of VPVC filtered square wave response simulation– various motor P controller settings

Next, with the determined settings of two valve PI controllers, the tuning of the motor P controller is from K_p = 2000 to K_p = 4000 (Table 6.7).

From Figure 6.13, it can be observed that obviously different responses are shown with varied motor P controller settings. In zoom A and zoom B from top subplot, Test 9 (K_P = 4000) brings much larger amplitude of oscillation. In zoom C and zoom D from bottom subplot: Test 7 has larger errors compared with the other two tests. In overall consideration, Test 8 (K_P = 3000) is the most appropriate gain for the motor P controller. Hence the final settings of three controllers in VPVC are determined and listed in Table 6.8. All the following tests of VPVC will adopt these settings, including experiment and simulation.

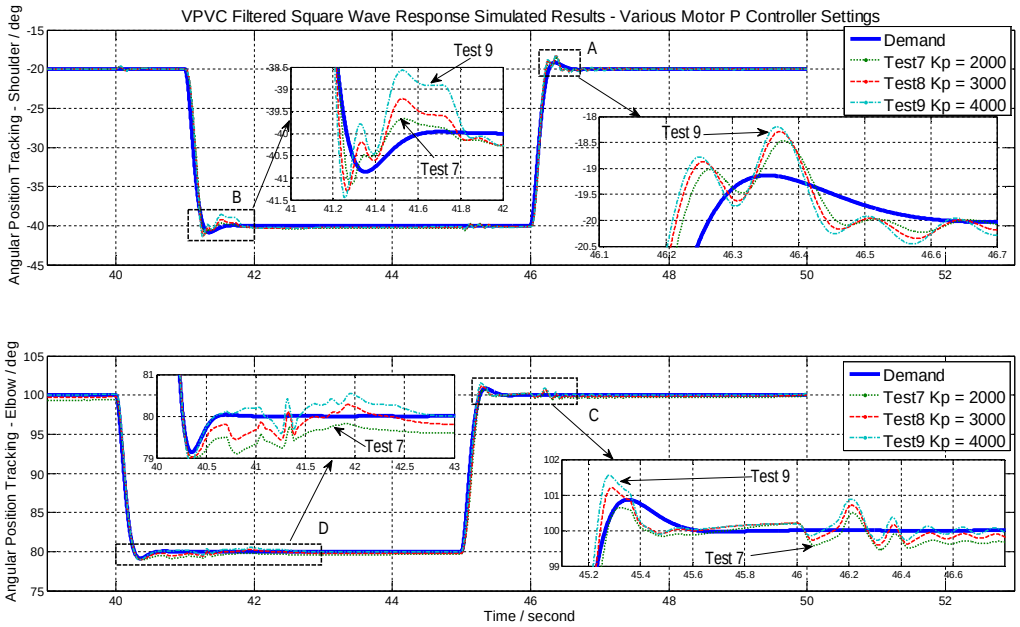

Figure 6.13 VPVC filtered square wave response simulated results – various motor P controller settings

	K_P	K_I
Motor Speed Controller	3000	---
Shoulder: Valve Controller	100	10
Elbow: Valve Controller	120	10

Table 6.8 The gains of P(I) controllers in VPVC

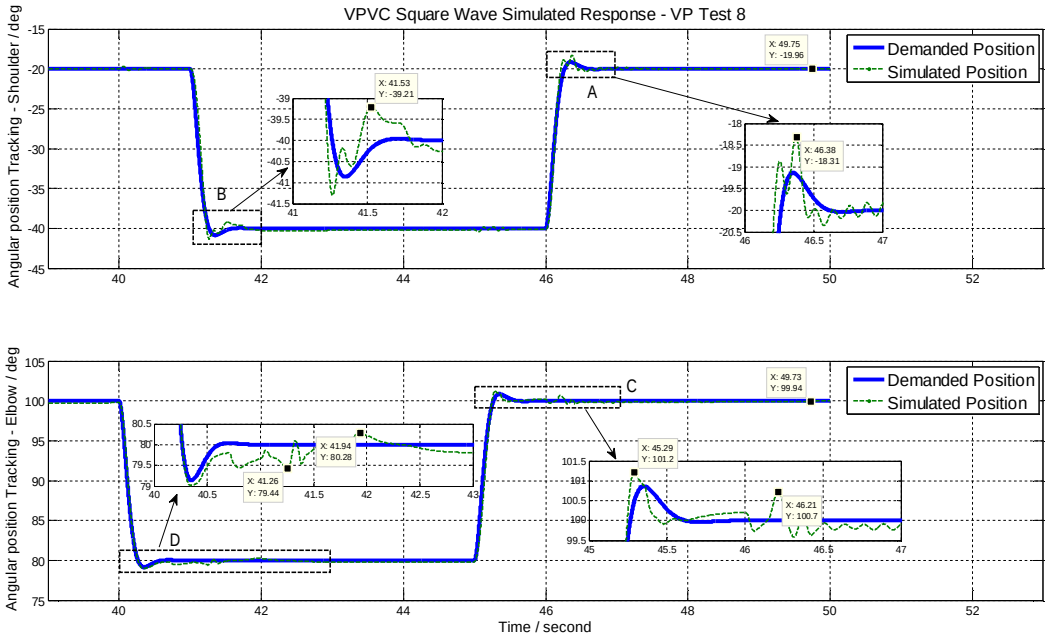

Figure 6.14 VPVC filtered square wave simulated response – VP Test 8

The simulated response of VPVC with the determined controllers' setting (Test 8 setting) is shown in Figure 6.14, it can be concluded that VPVC filtered square wave response is generally satisfactory. Both joints achieve very small steady state error.

In zoom B of Figure 6.14, a serious oscillation is found on shoulder position tracking during 41.3 second to 41.8 second. During that period, the master actuator (MA) is 1 which means the shoulder actuator is the master actuator (bottom subplot in Figure 6.15). The shoulder valve opening command is nearly fully open because P_{SO} (see Section 3.2) is used in the VPVC control algorithm (41.3 second to 41.8 second top subplot in Figure 6.15), so the shoulder actuator has a relatively large flow input to generate this error.

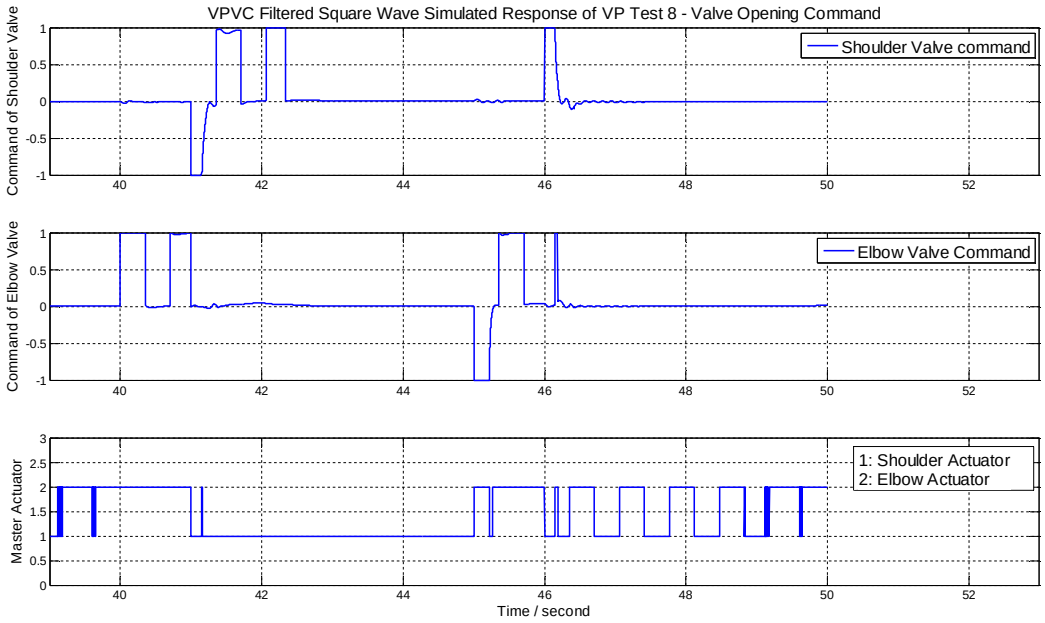

Figure 6.15 VPVC filtered square wave simulated response of Test 8 – valve opening command

In zoom C of Figure 6.14, a mutual force is applied on the elbow joint when the shoulder is in motion. The elbow presents an obvious oscillation up to 0.7^{o} at that moment.

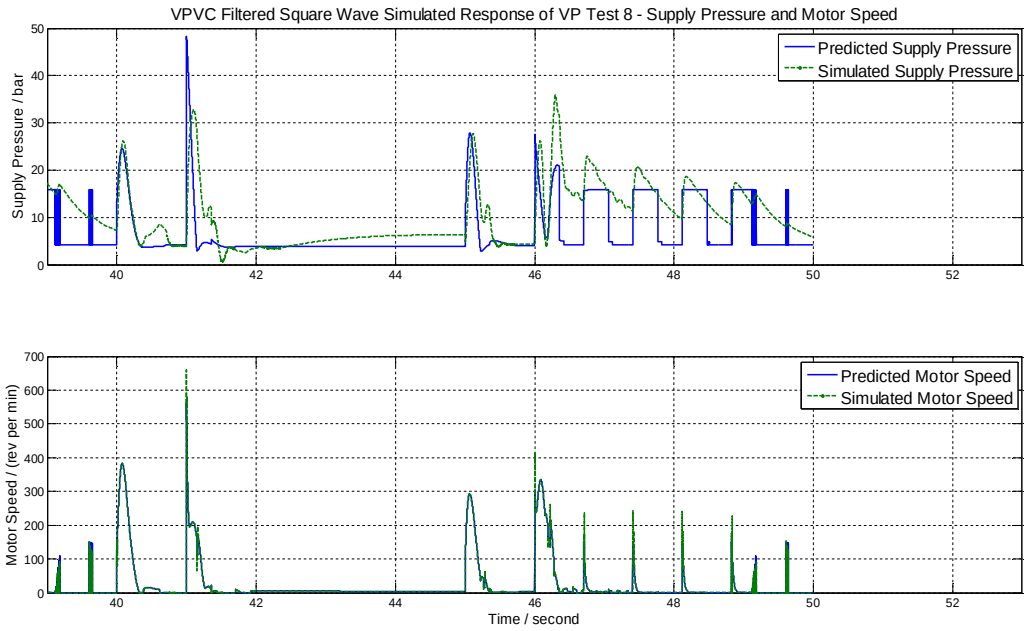

Figure 6.16 VPVC filtered square wave simulated response of Test 8 – supply pressure and motor speed

The supply pressure and motor speed of Test 8 are presented in Figure 6.16. The predicted supply pressure is the ideal result from the feed forward controller only. Besides that, the simulated model considers the leakage across the piston inside the actuator. Hence the simulated supply pressure can't keep constant as predicted; the simulated supply pressure is decreased due to the leakage flow (see the constant predicted supply pressure at some points between 47s and 49s in Figure 6.16). From the bottom subplot, the motor response is fast in simulation. The simulated supply pressure and motor speed will be compared with experimental data in the next chapter.

6.4 VPVC sine wave simulation results

This section will present VPVC simulated response of sine wave motion demand (i.e. VPVC comparison tests).

In all comparison tests, VPVC controllers adopt the gains from VPVC filtered square wave section (Table 6.8): Motor P controller K_P = 3000, shoulder valve PI controller K_P = 100 with K_I = 10 and elbow valve PI controller K_P = 120 with K_I = 10. The coefficients of predicted viscous friction in VPVC controller adopt the setting of sine wave motion friction (stated in Section 5.2). Similar to FPVC sine wave simulation section, Com3-VP and Com4-VP will be presented and discussed in detail. After that, a summary of hydraulic power consumed and dynamic errors of all the VPVC comparison tests will be shown and compared with the FPVC simulated results.

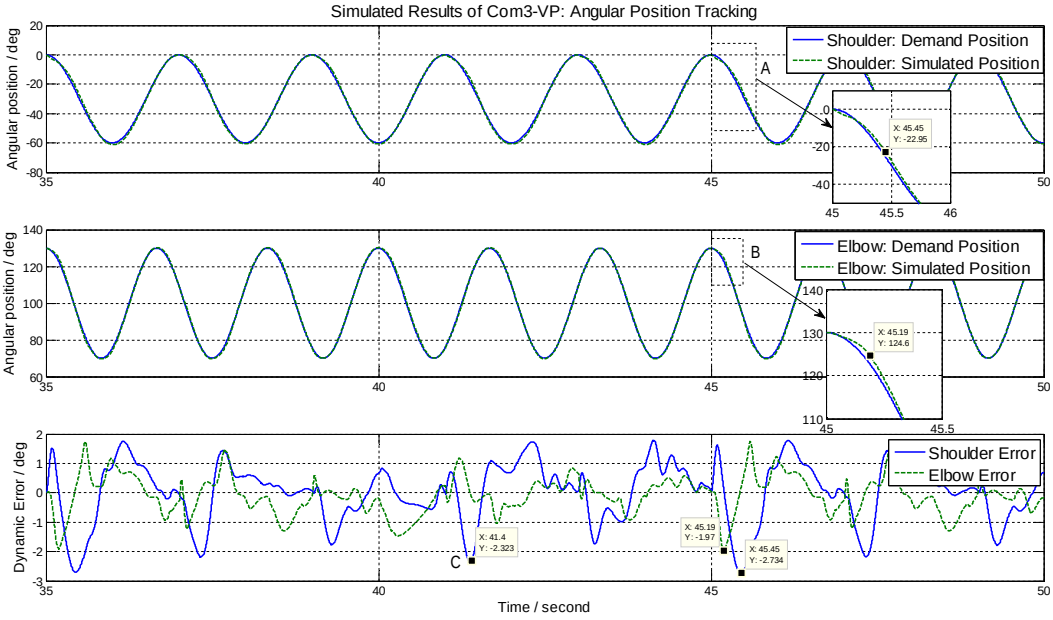

Figure 6.17 Angular position tracking of simulated Test Com3-VP

From Figure 6.17, it is clear that the simulated position tracking of Com3-VP is satisfactory. The phase delay phenomenon is very slight for the two joints. It is believed that feed forward dominates in the VPVC controller, hence the simulated response doesn't show a lag as serious as the FPVC simulated results. The dynamic errors are plotted on the bottom subplot of Figure 6.17. The maximum dynamic error for the shoulder is 2.7^{o} at 45.45 second and the elbow is 2.0^{o} at 45.19 second, which are equivalent to 4.5% and 3.3% of the total range of demand motion (60 degrees).

The predicted P_S and the simulated P_S are plotted on the top subplot in Figure 6.18. The general trend of the simulated P_S matches the predicted P_S. The simulated P_S peaks at 40 bar around but it is from 10 bar to 20 bar for most of the duty cycle. The motor speed response is fast and the sharp transients can be tracked successfully. The maximum motor speed is up to 610 rpm.

The maximum dynamic error for the shoulder happens at 45.45 second and the elbow's maximum error happens at 45.19 second. From 44.7 second to 45.5 second, the master actuator is the shoulder actuator (F in Figure 6.19). The MA changes its direction of movement at 45 second, which brings a sudden step in predicted supply pressure (zoom D in Figure 6.18) because the P_S prediction equations switch depending on extension or retracion (Section 3.2). The feed forward of motor speed command involves the derivative of pressure (Equation 3.22). Hence the feed forward part of the motor speed command has a negative infinite value due to predicted P_S's step, and then the motor speed command has a short zero speed period because the command is limited to be positive.

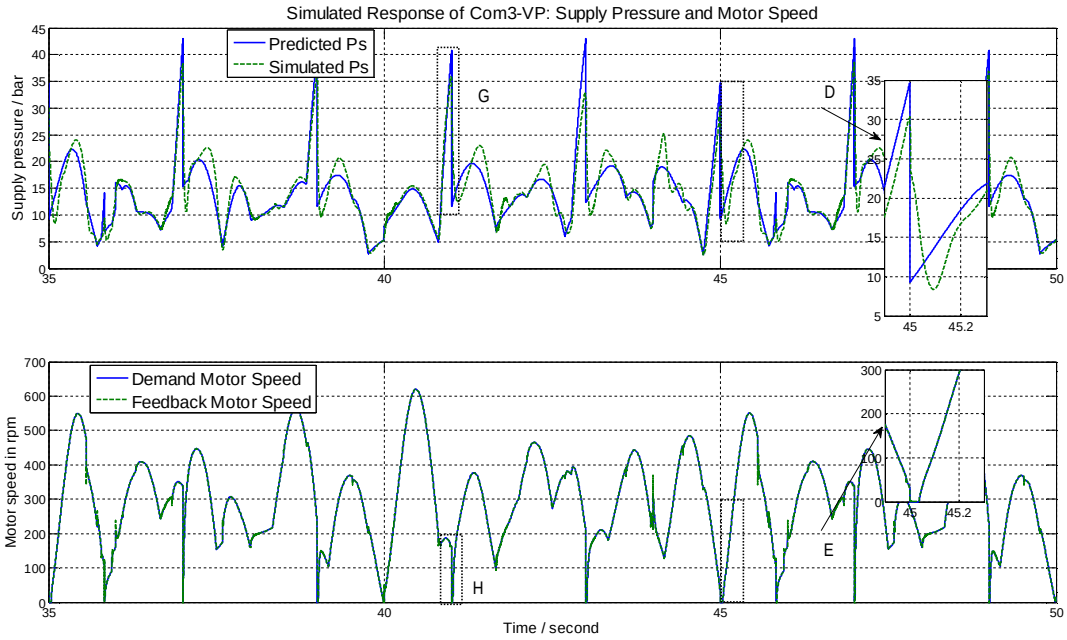

Figure 6.18 Supply pressure and motor speed of simulated Test Com3-VP

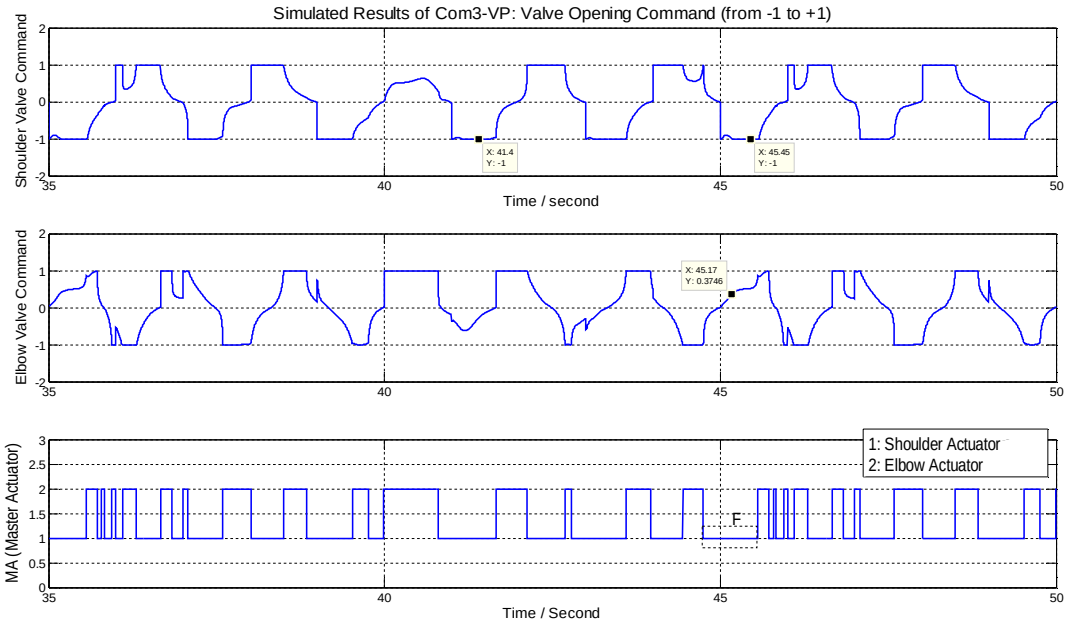

Figure 6.19 Valve opening command of simulated Test Com3-VP

It can be seen that the simulated motor speed command has a short period of zero demand after 45 second (zoom E in Figure 6.18). The predicted supply pressure drops instantaneously, which would command a large negative motor speed if motor speed were not limited to zero. As a result, the simulated pressure does not reduce as rapidly as required (zoom D in Figure 6.18). The VPVC controller requires about 0.5s to recover from this difference between simulated value and ideally predicted value. The master actuator is the shoulder actuator and its valve opening command is nearly -1 hence its simulated response of the shoulder shows a large dynamic error at 45.45 second (top subplot in Figure 6.19 and bottom subplot in Figure 6.17).

Similar phenomena can be found and explained at other steps of predicted P_S. For example, the shoulder joint has a large dynamic error of 2.3^o at 41.4 second (Figure 6.17). At 41 second, the predicted P_S falls rapidly (G in Figure 6.18) due to the shoulder actuator changing direction. A short zero saturation happens on motor speed command (H in Figure 6.19). A large error of shoulder position is generated 0.4 second later.

As a conclusion, the simulated response of Com3-VP is very satisfactory. The angular position tracking results present a minor phase lag and the dynamic errors are within 5%. The mean hydraulic power of Com3-VP is 23.71W, which is much less than 59.81W of Com3-FP.

Com4-VP has a larger amplitude of 80 degrees and lower frequencies (0.3Hz for shoulder and 0.4Hz for elbow) demand than Com3-VP. The angular position tracking of the simulated Test Com4-VP is presented in Figure 6.20. The elbow's performance is better than shoulder's performance. The shoulder has visible position errors after each changing of direction. The phase lag for both the joints is small. The maximum dynamic error is 4.2^{o} for shoulder and 3.0^{o} for elbow. They happen at 45.13 second and 45.23 second (A and B in Figure 6.20). They are located within the period after a predicted P_S step (C in Figure 6.21). The corresponding motor speed command is briefly zero (D in Figure 6.21).

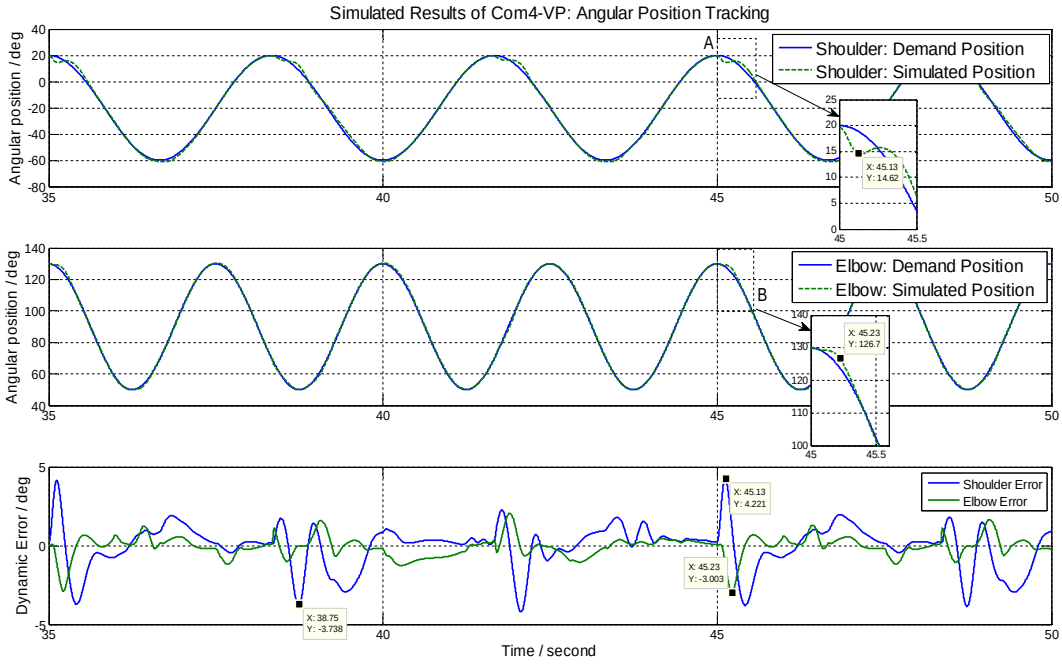

Figure 6.20 Angular position tracking of simulated Test Com4-VP

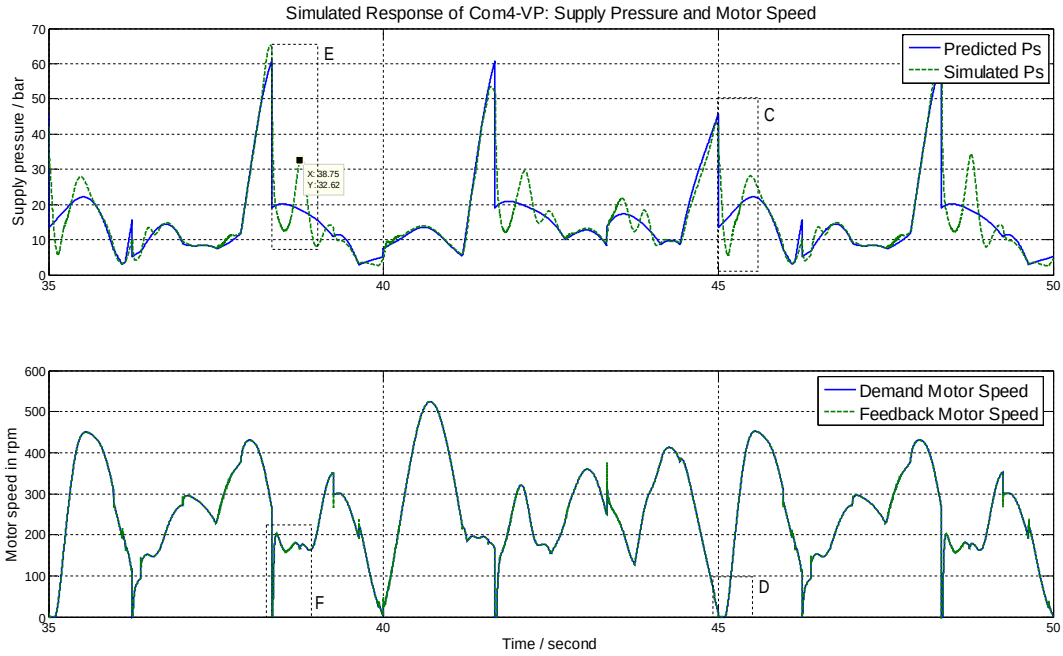

Figure 6.21 Supply pressure and motor speed of simulated Test Com4-VP

As explanation on Test Com3-VP, because of the zero motor speed command brought about by the step in predicted P_S, the pressure in supply hoses experiences a period of inevitable decreasing. The improper P_S is being integrated hence the system requires some time to recover back to proper working condition. There is another example: shoulder's error is 3.7^o at 38.75 second (bottom subplot in Figure 6.20 and E and F in Figure 6.21).

The maximum dynamic errors of Com4-VP are equvialent to 5.25% for shoulder and 3.75% for elbow of the total range of demand motion (80 degrees). The mean hydraulic power of simulated Test Com4-VP is 21.61W.

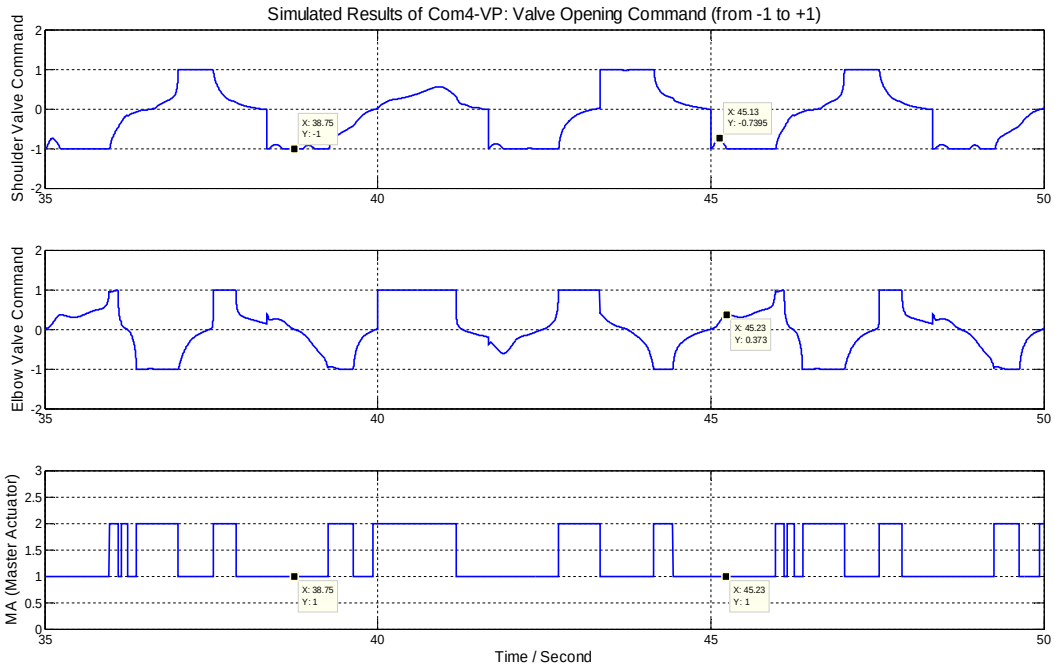

Figure 6.22 Valve opening command of simulated Test Com4-VP

All the dynamic errors and the mean consumed hydraulic power of VPVC simulated tests are summarized in Table 6.9 (where S represents the shoulder joint and E represents the elbow joint).

Test	***FPVC***			***VPVC***			***Saving %***
	Max Dynamic Error (degree)		***Mean Simulated Hydraulic Power (W)***	***Max Dynamic Error (degree)***		***Mean Simulated Hydraulic Power (W)***	
	S	***E***		***S***	***E***		
Com1	3.1	2.8	38.50	3.2	2.7	10.88	71.74%
Com2	4.4	4.0	49.19	2.6	1.5	16.47	66.52%
Com3	5.8	5.2	59.81	2.7	2.0	23.71	60.36%
Com4	5.0	4.4	50.93	4.2	3.0	21.61	57.57%
Com5	7.1	6.0	65.09	4.2	2.2	32.57	49.96%
Com6	11.6	7.7	79.20	4.3	3.1	48.44	38.84%

Table 6.9 Summary of simulated results of comparison tests FPVC and VPVC

The saving of consumed hydraulic power by VPVC for each comparison test is calculated by Equation 6.7.

$$\frac{FPVC\ hydraulic\ power - VPVC\ hydraulic\ power}{FPVC\ hydraulic\ power} \quad (6.7)$$

In general, the VPVC simulated results show lower maximum dynamic errors compared with FPVC simulated results (Table 6.9). Only Test Com1-VP has similar values to Com1-FP. The maximum dynamic errors of FPVC simulated tests increase with a more aggressive demand signal (ascending amplitude and/or ascending frequencies).

VPVC simulated results show less change when the frequency of demand is increasing. The maximum dynamic errors for the first three VPVC tests (total motion range of 60 degrees) vary from 2.6^o to 3.2^o for shoulder and from 1.5^o to 2.7^o for elbow; and last three VPVC tests (total motion range of 80 degrees) vary from 4.2^o to 4.3^o for shoulder and from 2.2^o to 3.1^o for elbow. All the VPVC tests' maximum dynamic errors are within 5.4% for shoulder and 4.5% for elbow of the total motion range. Thus VPVC simulated results show a good tracking response.

It is clearly that VPVC can save a great amount of hydraulic power compared with FPVC for a range of load conditions. The saving increases when the load decreases because FPVC has a high waste with low load. The energy saving by VPVC can be improved greatly if the loss via relief valve in FPVC is included.

As a conclusion of this chapter, simulation results indicate that VPVC is an efficient control method for this two-joint robotic arm system simulated tests compared to a traditional fixed supply pressure system. The dynamic performance of VPVC is satisfactory as well.

Chapter 7

7 Experimental Results

The experimental results of FPVC and VPVC will be shown and discussed in this chapter. The simulated tests in the last chapter will be validated experimentally. The differences between the simulated and experimental results will be analysed. For the sine wave tests, the dynamic performance and the hydraulic power consumed will be compared between FPVC and VPVC experimentally. For FPVC experiment, all the tests use a fixed supply pressure of 38 bar which is set by the relief valve. For VPVC experiments, the relief valve is set to a cracking pressure of 100 bar.

This chapter has 4 sections. The structure is as follows:

- FPVC square wave motion experimental results
- FPVC sine wave motion experimental results
- VPVC filtered square wave motion experimental results
- VPVC sine wave motion experimental results

7.1 FPVC square wave motion experimental results

7.1.1 Experimental results of FPVC controller tuning

The experimental tests begin with various settings of the elbow PI controller. The test information is the same as for the simulated tests (Table 6.1), so is not repeated.

From Figure 7.1, a similar response can be seen to the simulated results of Figure 6.1. The shoulder joint and the elbow joint have very small steady state errors. The experimental response of shoulder changes little with different elbow valve PI controller settings. It has short oscillations at time 40 second and 45 second due to the mutual force of the elbow step motion, and the same situation is seen in the elbow's response (at time 41 second and 46 second).

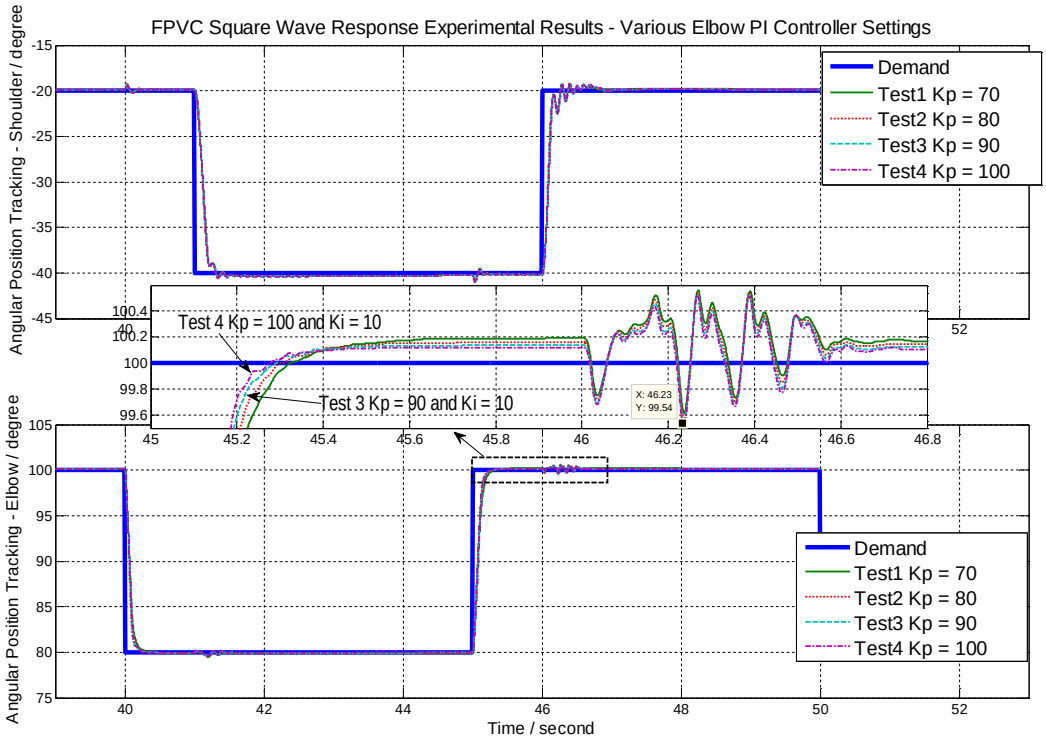

Figure 7.1 FPVC square wave response experimental response - various elbow PI controller settings

Different responses with various elbow PI controller settings can be observed on the elbow position tracking. High proportional gain K_P brings a fast response and a smaller steady state error, but some oscillation appears (Test 4). Test 3 (K_P = 90 and K_I = 10) gives a fairly well damped response with a satisfactory steady state error. Hence in this experimental validation section, the same setting as for the simulated results is found to be the appropriate setting for the elbow valve PI controller.

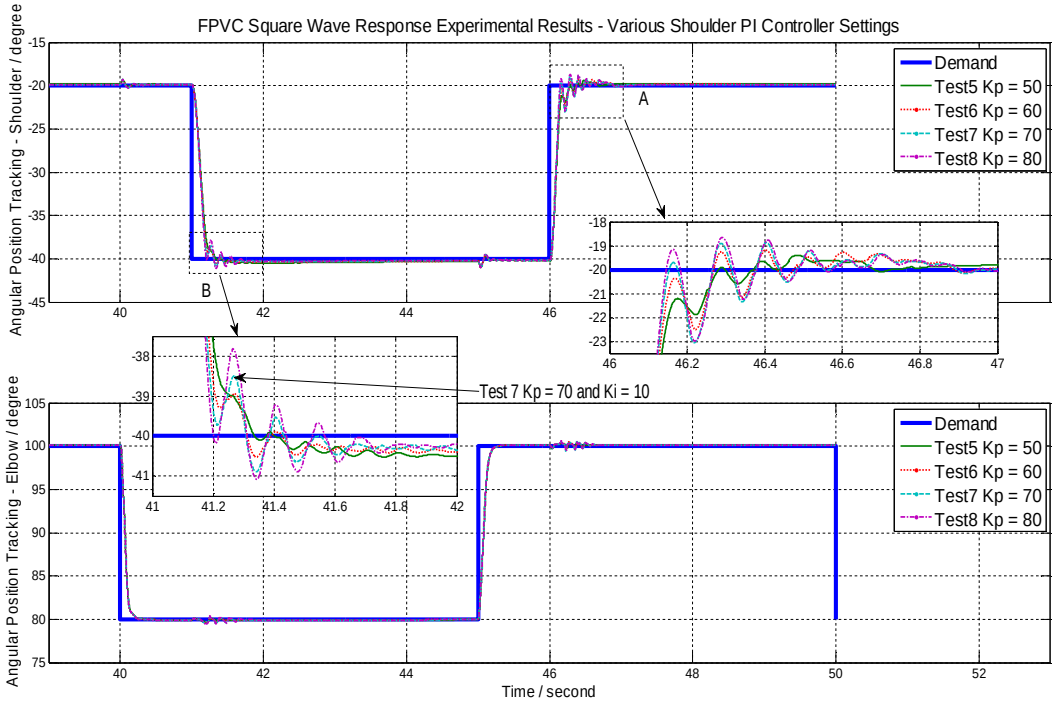

Figure 7.2 FPVC square wave response experimental response - various shoulder PI controller settings

The information for the tests of various shoulder valve PI controller settings is the same as Table 6.2. The experimental responses are plotted in Figure 7.2.

From Figure 7.2, the responses of the elbow change little with the different shoulder PI controller settings. But the shoulder responses show obvious differences. Test 5 and Test 6 have slightly slower response than Test 7 and Test 8 during rising. Test 8 shows a more serious vibration compared with the other 3 tests. Test 5 presents larger steady state errors. Considering the response time and steady state error Test 7 is a reasonable choice, which is the same conclusion as for the simulated results.

7.1.2 Comparison between simulation and experimental results of FP Test 7

The simulated results and experimental results of FP Test 7 are plotted in Figure 7.3 and Figure 7.4. From Figure 7.3, it can be concluded that the simulated response matches the experimental response generally. The experimental response has very closed rise time and steady state error values to the simulated response (All the points highlighted in Figure 7.3 are data from the experimental response). The shoulder experimental response reaches 90% of the step size after 0.13 second for extension and 0.18 second for retraction. The steady state error for the shoulder is 0.11^{o}. The elbow reaches 90% of the step size after 0.12 second for extension and 0.14 second for retraction. The steady state error for the elbow is 0.1^{o}.

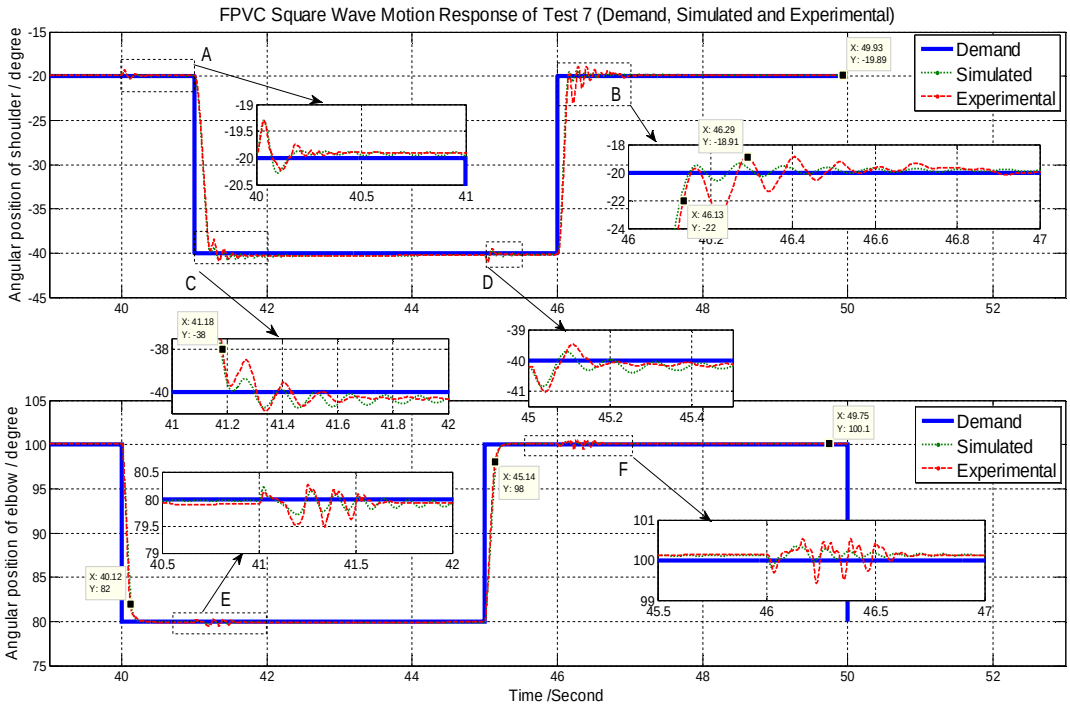

Figure 7.3 FPVC square wave response of Test 7 - simulation Vs experiment

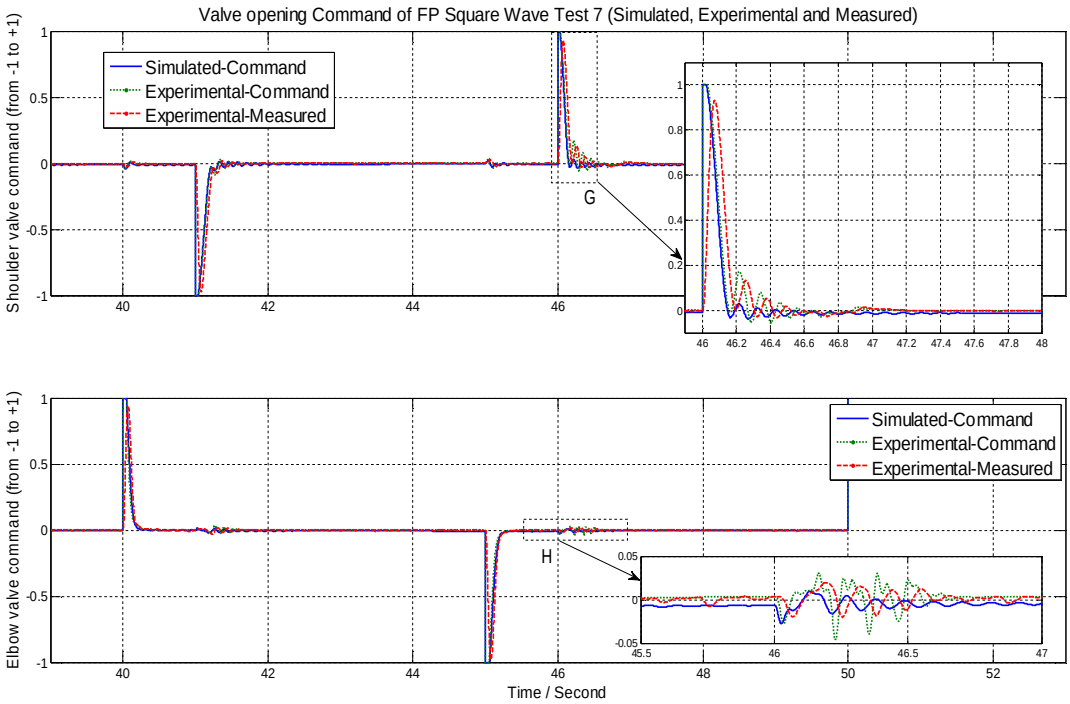

Figure 7.4 Valve command and spool position for FPVC square wave response Test 7 - simulation Vs experiment

From Figure 7.4, it can be seen that valve command saturates briefly after a step motion demand. The experimental commands match the simulated commands reasonably well. The measured valve spool positions are also plotted.

7.1.3 Discussion about the differences between simulation and experimental results of FPVC with square wave motion

Six zoomed plots in Figure 7.3 are presented to show the oscillations in detail. Most of the comparisons show that the experimental response has larger amplitude of oscillation and shorter setting time than the simulated response. In modelling of the hydraulic domain (Section 5.2), a simplified friction is built inside the actuator. The friction force is simply assumed to be proportional to the velocity of the piston, i.e. viscous friction. The viscous friction coefficient for the square wave motion of FPVC and the filtered square wave motion for VPVC

is a constant value determined from trial tests to make the simulated response match the experimental response during the rising period after a step motion demand. However in the real experimental system, besides viscous friction, more complex friction behaviour is presented: coulomb friction, pressure loss in the hoses and manifold and the static friction when close to stationary etc. The simple viscous friction with one constant proportional gain in the simulation model can't represent all the experimental friction elements during all the stages. For example, the real pseudo-static friction (i.e. close to zero velocity) should adopt a much larger gain compared the one used in the model. So the simulated model generates smaller damping to dissipate the power hence a longer setting time is shown in simulated result close to steady state.

More generally, there are a number of sources of modelling error. The bulk modulus is a constant estimated by trial tests, but in reality it will vary with pressure and amount of entrained air. When modelling hydraulic actuators, estimated volumes of the chambers are adopted in the pressure build-up blocks (Section 4.2 and Section 5.2). The mechanical domain in the simulated model assumes that the two cylinder bodies and pistons are massless. Simplified integrated centres of gravity and inertias are used (Section 5.3).

It is believed that the differences between simulated and experimental data are due to all the above limitations and assumptions. The differences are not able to be predicted exactly but they are acceptable. Some of the above possible reasons for differences between simulated and experimental data will be analysed in detail in the appropriate sections.

7.2 FPVC sine wave experimental results

In this section, the experimental results of FPVC sine wave motion (comparison tests of FPVC) will be shown and discussed. The dynamic performance and the hydraulic power consumed will be analysed experimentally and the differences between the simulated and the experimental results will be discussed. Com3-FP will be the example to be discussed in detail. At the end, a summary of the experimental results of FPVC sine wave motion will be presented.

7.2.1 Comparison between simulation and experimental results of Com3-FP

Both the simulated tracking and the experimental tracking of Com3-FP are shown in Figure 7.5. Generally, the experimental motion matches the simulated results very well. Only some minor differences happen at the direction-switching points. The shoulder shows a phase delay of 0.06 second and 0.04 second for the elbow, which are close to the simulated results of Com3-FP. The amplitude ratios are 0.997 for shoulder and 0.995 for elbow respectively, which are slightly different from the simulated results which are 1.003 and 1 respectively. (Note: all the datatips in Figure 7.5 are from experimental response.)

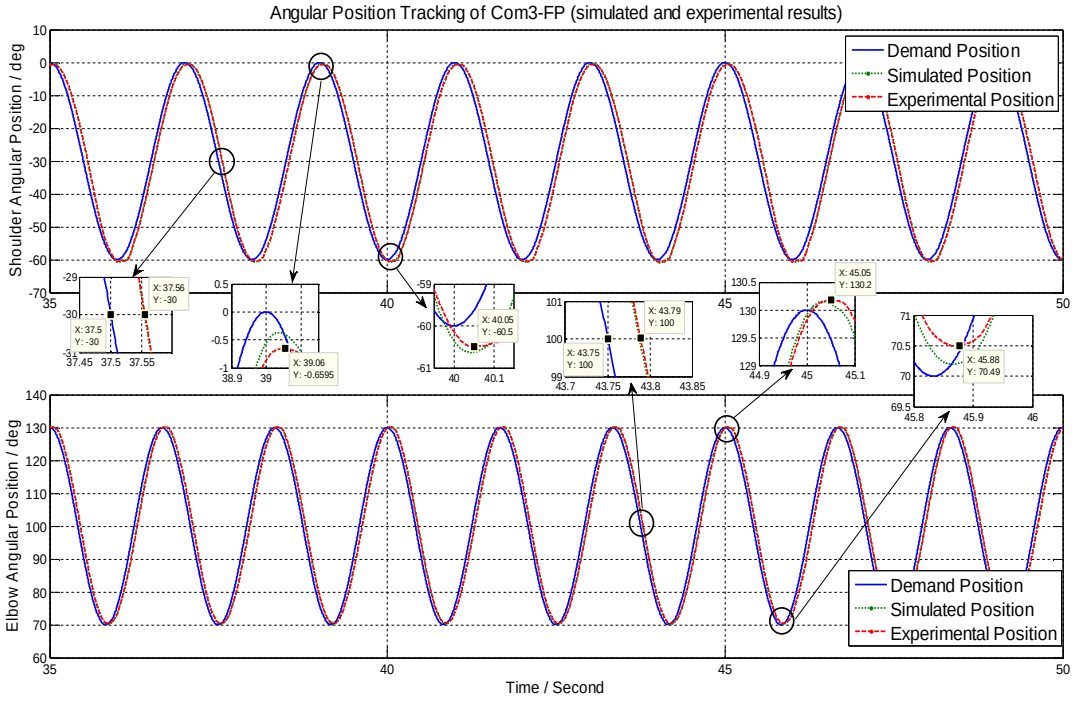

Figure 7.5 Comparison between simulated and experimental position tracking of Com3-FP

The measured supply pressure and the measured motor speed are shown in Figure 7.6. This verifies that the system is driven by the correct required supply pressure and motor speed in the experimental test.

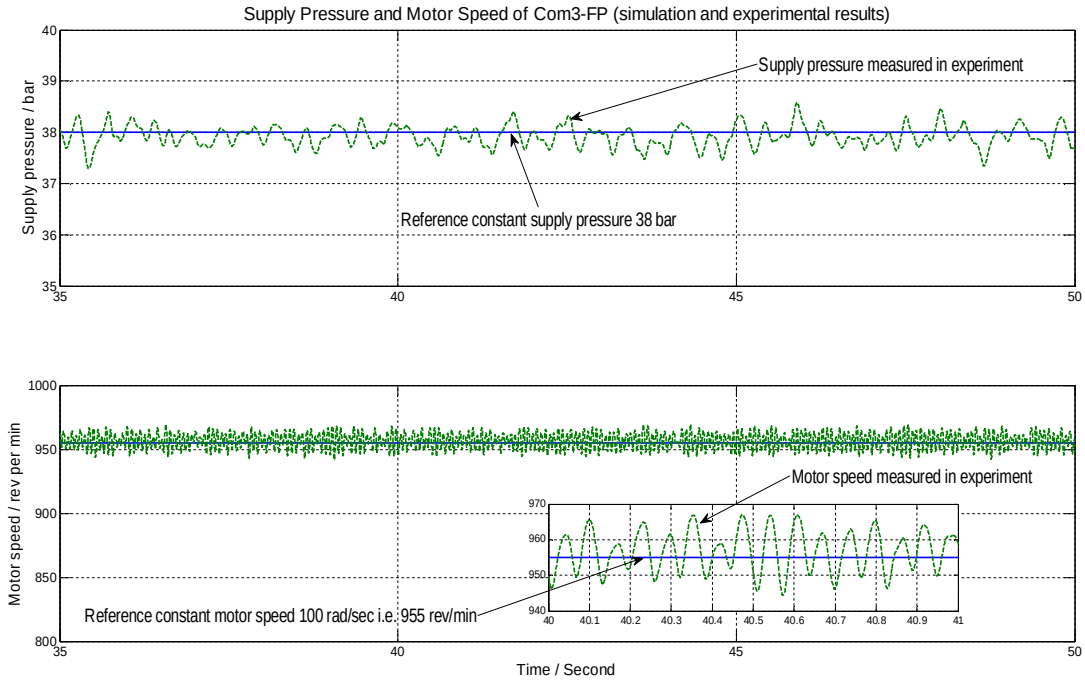

Figure 7.6 Measured supply pressure and measured motor speed in experiment of Com3-FP

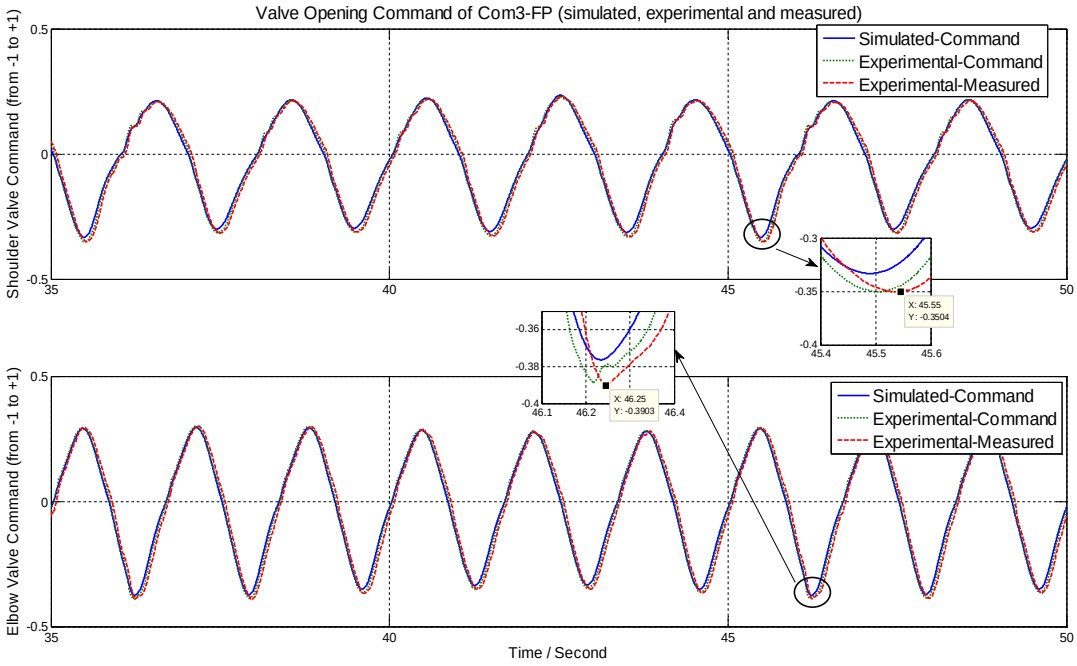

Figure 7.7 Valve opening command and measured spool position of Com3-FP

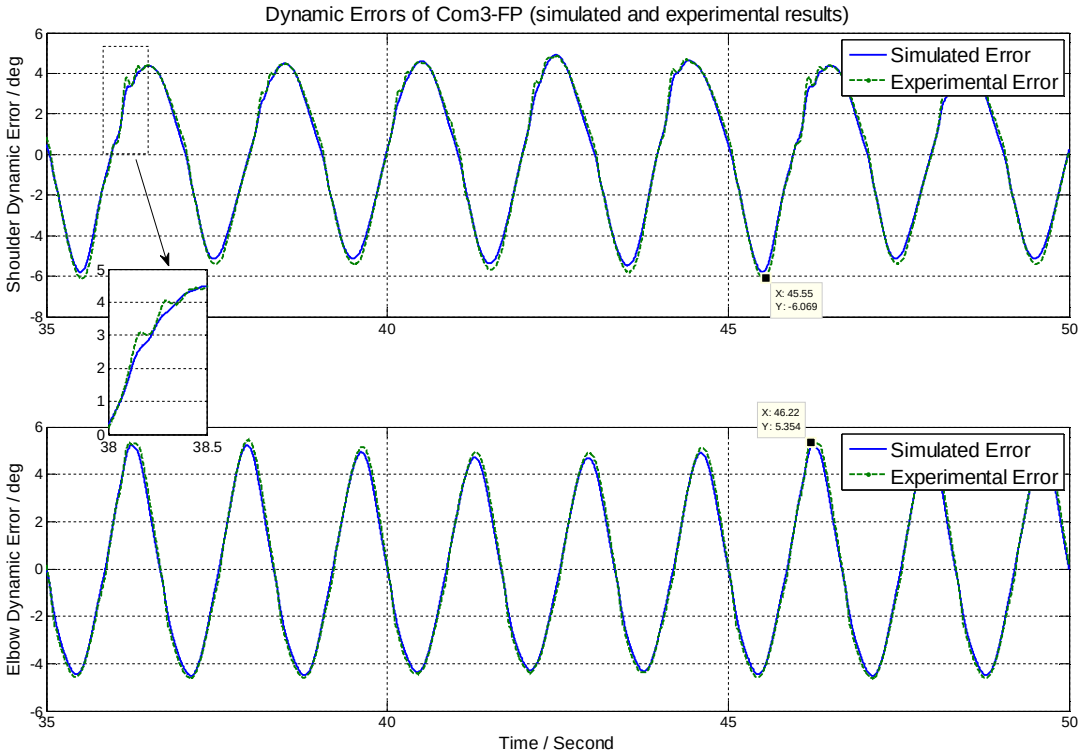

Figure 7.8 Comparison of the simulated and the experimental dynamic errors of Com3-FP

The valve opening command signals are presented in Figure 7.7. For the experiment, the measured spool positions are plotted as well.

The experimental dynamic errors are plotted together with the simulated dynamic errors in Figure 7.8. The general trends of the experimental waves match the simulated waves well. Acceptable differences happen at the time of maximum valve opening command and the time of valve command oscillations.

The simulated actuation force and the experimental force measured by the load cells mounted on the piston rods are compared in Figure 7.9. Generally, the measured forces match the simulated forces with acceptably small differences.

The experimental hydraulic power consumed in Com3-FP is 57.20W, which is close to simulated hydraulic power of Com3-FP of 59.81W. The operating is noisy due to the valves throttling behaviour and the high speed rotation of motor.

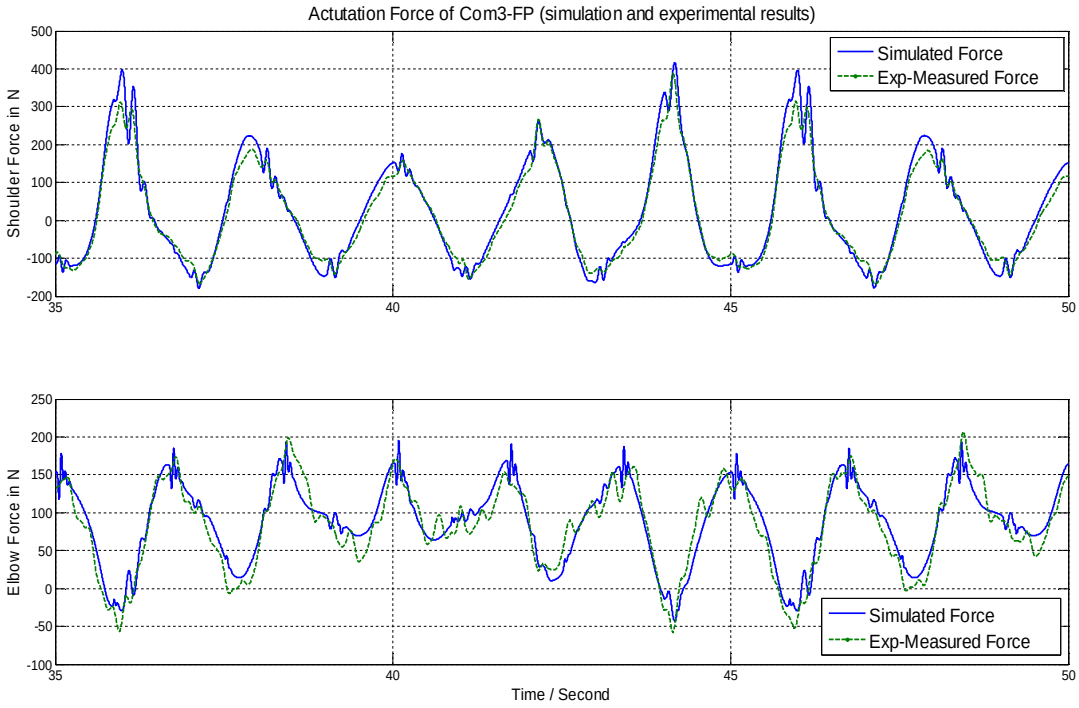

Figure 7.9 Comparison of simulated and experimental actuation force of Com3-FP

7.2.2 Discussion about the differences between simulated and experimental results of FPVC with sine wave motion

From Figure 7.7, it is found that the experimental valve command signals fit the simulated valve command signals well. And the experimental measured spool positions track the command satisfactorily with a small lag. Small differences between the simulated command and the experimental command are visible at maximum valve opening points (two zoomed plots).

In the simulated model, an estimated value of the cross piston leakage coefficient is used for the simulation (Section 5.2), which is a possible reason to the differences in Figure 7.7. And the viscous friction coefficient for the sine wave motion tests is a general setting determined from a number of experiments of 6 sine wave motion tests (Section 5.2). The simplified and unchanged friction model can't simulate the real experimental friction force perfectly for every sine wave motion test.

Besides the friction, there are some other possible sources of modelling error which have been mentioned in subsection 7.1.3.

Test	*Exp Max-valve opening (absolute)*		*Exp Max-Dynamic Error (absolute in degree)*		*Exp Phase Delay (degree)*		*Exp Amplitude Ratio (Feedback/Demand)*		*Exp Mean-hydraulic Power (W)*
	S	*E*	*S*	*E*	*S*	*E*	*S*	*E*	
Com1-FP	19%	22%	3.1	3.3	-6.48	-4.32	$60.5^o/60^o$	$59.8^o/60^o$	38.14
Com2-FP	30%	26%	4.5	4.3	-8.64	-7.2	$60.3^o/60^o$	$59.8^o/60^o$	48.03
Com3-FP	35%	39%	6.1	5.4	-10.8	-8.64	$59.8^o/60^o$	$59.7^o/60^o$	57.20
Com4-FP	28%	33%	4.8	4.7	-6.48	-4.32	$81.0^o/80^o$	$80.0^o/80^o$	49.04
Com5-FP	45%	46%	7.4	6.4	-10.08	-7.2	$80.6^o/80^o$	$79.8^o/80^o$	64.01
Com6-FP	68%	65%	11.4	8.7	-16.2	-10.8	$80.6^o/80^o$	$79.8^o/80^o$	79.07

Table 7.1 Summary of experimental results of comparison tests – FPVC (S and E represent shoulder and elbow respectively)

A summary of the experimental results for the FPVC comparison tests is shown in Table 7.1. Compared with the summary of the simulated results (Table 6.4), the experimental results show similar features: the amplitude ratios of all the tests are close to 1, and the phase delay is the main reason to the dynamic error. The dynamic errors increase with the increasing load. The experimental hydraulic power consumed is close to the simulated result in each test. The FPVC experimental results will be compared with the VPVC experimental results in Section 7.4.

7.3 VPVC filtered square wave experimental results

7.3.1 Experimental results of VPVC controller tuning

Firstly, three tests are carried out to determine the best setting of the elbow valve PI controller. The test information is the same as for the simulated tests (Table 6.5), so is not repeated. The experimental response plots with different elbow PI controller settings are shown in Figure 7.10. In zoom A, it is clear that Test 3 has more serious oscillation in the elbow's response. Then in zoom B, Test 1 shows a slower response compared with the other two tests. With the above considerations, Test 2 (K_P = 120 and K_I = 10) is the most reasonable setting for the elbow valve PI controller, the same choice as for the simulated results.

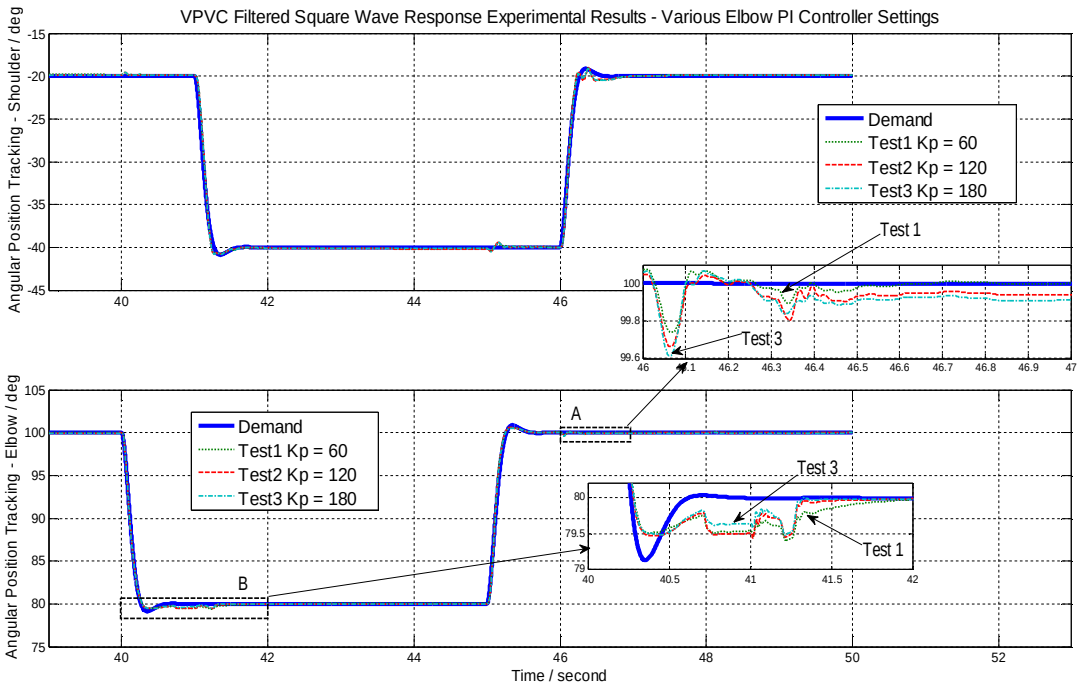

Figure 7.10 VPVC filtered square wave experimental response - various elbow PI controller settings

The test information for the various shoulder valve PI controller settings is the same as Table 6.6. The experimental results are plotted in Figure 7.11.

From Figure 7.11, it is clear that different settings of the shoulder valve PI controller cause obvious differences in shoulder's response. In zoom A, high proportional gain K_P, Test 6, causes larger amplitude of oscillation; Test 4 and Test 5 show a slower response compared with Test 6. In zoom B, the same conclusion as zoom A: Test 6 shows a faster response but larger oscillation and Test 4 presents a slightly slower response to steady state. In conclusion, Test 5 (K_P = 100 and K_I = 10) is the most appropriate setting for the shoulder valve PI controller.

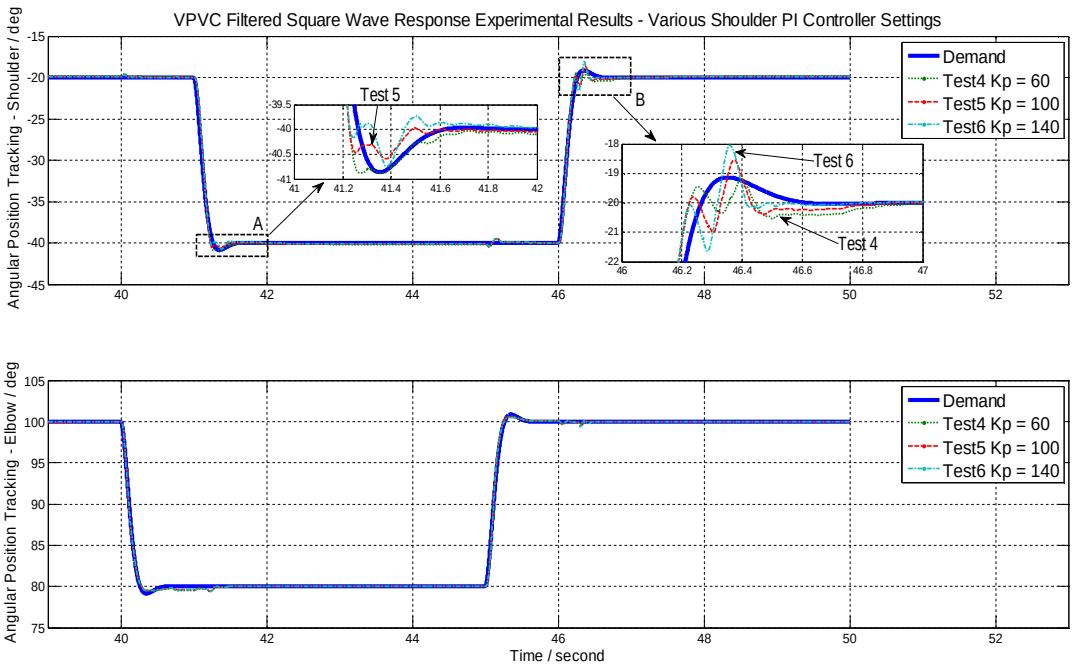

Figure 7.11 VPVC filtered square wave experimental response - various shoulder PI controller settings

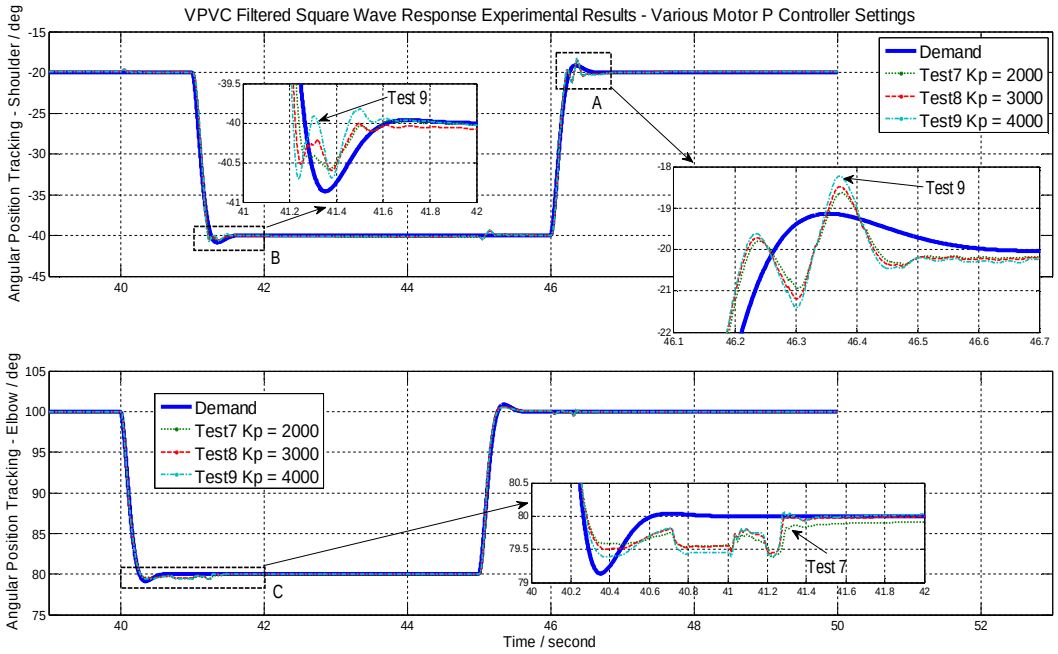

Figure 7.12 VPVC filtered square wave experimental response - various motor P controller settings

Next, the tuning of the setting for the motor P controller is followed with the determined settings for the two valve PI controllers. The test information for the motor P controller tuning are the same as Table 6.7.

In Figure 7.12, it can be seen that obviously different responses of the two joints are caused by the varied motor P controller settings. In zoom A and B, Test 9, which has a high gain of K_P = 4000, presents a more serious oscillation compared with the other two Tests. Then in Zoom C, it is observed that Test 7 has a much larger position error. By taking an overall consideration, Test 8 (K_P = 3000) is the most appropriate gain for the motor P controller. Hence the final settings of three controllers in VPVC are determined, the same as for the simulated results in Table 6.8. In the next subsection, the simulated results and experimental results of Test 8 will be plotted for comparison and discussion.

7.3.2 Comparison between simulation and experimental results of VP Test 8

Figure 7.13 shows the comparison between simulated results and experimental results for VP Test 8. The steady state errors of the experimental results are very small (all the highlighted points in Figure 7.13 are experimental data). The interference due to mutual force is obvious on both actuators.

Similar to subsection 7.1.3, it is concluded that for most of the cases in Figure 7.13: the simulated response shows less damping compared with the experimental response when the joints are moving around demanded steady state position (i.e. zoom A, C, E and F in Figure 7.13). It is believed that the real pseudo-static friction (i.e. close to zero velocity) should adopt a much larger gain compared the one used in the simulated model. So the simulated model generates a smaller damping hence more serious oscillation is shown in the simulated results when joints are close to steady state.

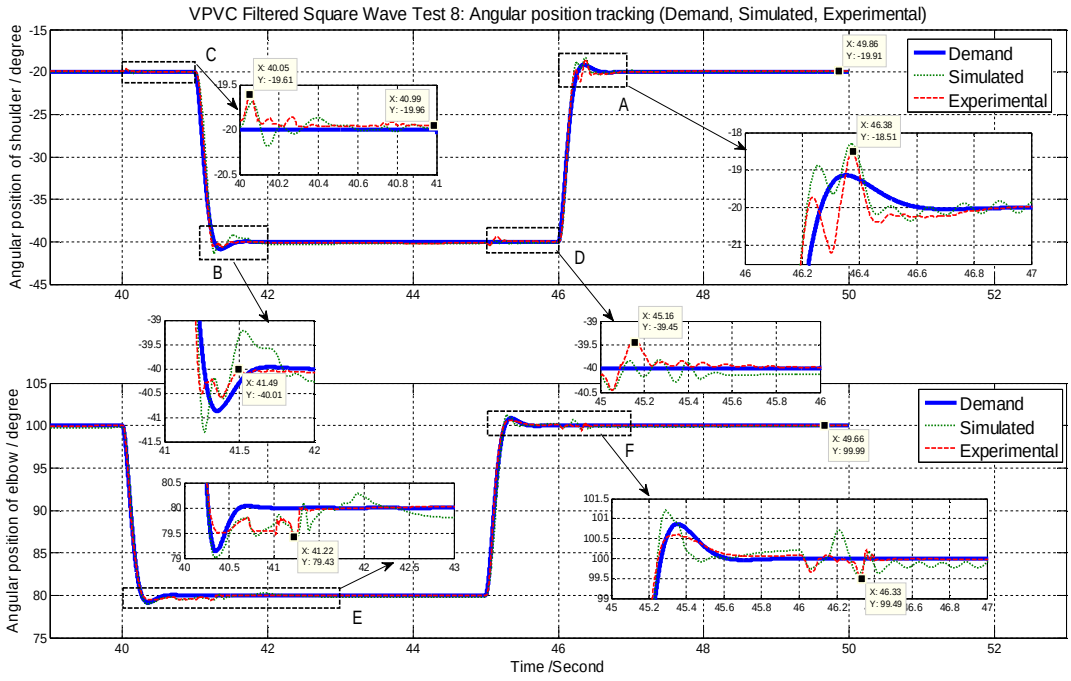

Figure 7.13 VPVC filtered square wave response of VP Test 8 - simulation Vs experiment

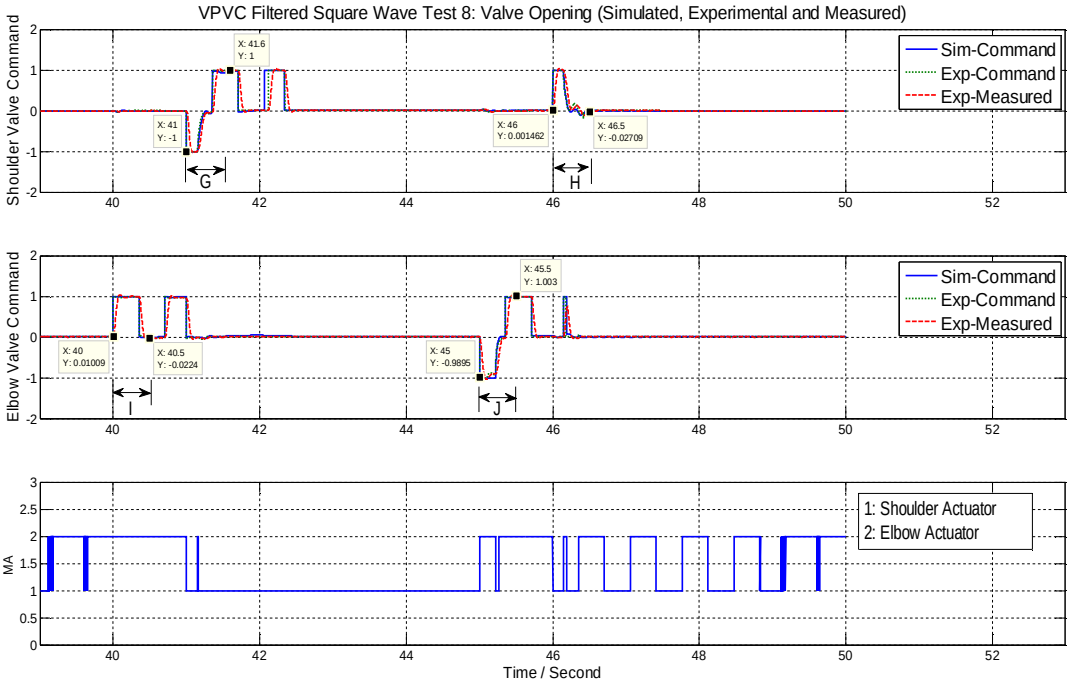

Figure 7.14 Valve command and spool positions of VPVC filtered square wave VP Test 8 - simulation Vs experiment

From Figure 7.14, the valve command signals are plotted. The experimental-measured valve opening signals show the valves track the command satisfactorily. The valves open for about 0.5 second to 0.6 second for the rising motion demand (G, H, I and J in Figure 7.14).

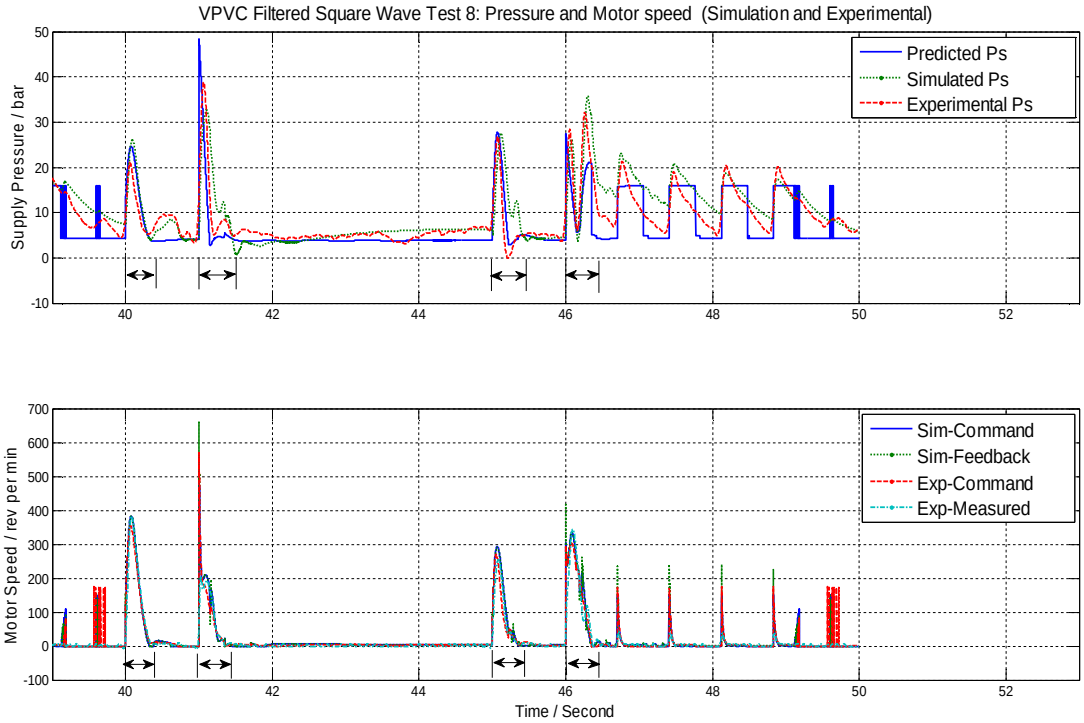

Figure 7.15 Supply pressure and motor speed of VPVC filtered square wave VP Test 8 - simulation Vs experiment

From Figure 7.15, it is clear that the motor generates flow when the transient step motions are demanded. The corresponding changes happen on the supply pressure. Generally speaking, the experimental-measured supply pressure matches the simulated supply pressure well. Due to the leakage across the piston, the experimental supply pressure decreases in the same way as simulation results (see the constant predicted supply pressure at some points between 47 second and 49 second).

7.3.3 Discussion about the tracking response of VPVC with filtered square wave motion

In experiment, the VPVC controller predicts the hydraulic force required by the given motion demand, which should be the sum of the required actuation force and the friction force (Equation 5.16). For the actuation force, simplified integrated centres of gravity and inertias are used in the prediction equations derived by the Lagrange equation of the second kind (Equation 3.25 and Equation 3.26). For the friction prediction, the same simplification as for modelling the friction in the hydraulic domain is adopted in the controller. The same constant viscous damping coefficient is used to predict the friction in the VPVC controller (Chapter 5). The inevitable errors in predicting the required actuation force and predicting the friction force cause the inaccuracy in the hydraulic force prediction. And then the inaccurate required hydraulic force in the VPVC controller causes the inaccurate predicted required supply pressure, which is the most essential parameter of VPVC feed forward controller.

Besides the force prediction, the bulk modulus and the volume of supply hoses are required to calculate the feed forward part of motor speed command in VPVC controller (Equation 3.22). Estimated values are used for these two parameters, so the errors between estimated and real values contribute part of imperfect performance in experiment.

As a conclusion, all the above modelling errors can't be avoided when predicting the load and estimating some system characteristics in VPVC controller. The errors between the demand and experimental results shown in this section are acceptable.

7.4 VPVC sine wave experimental results

In this section, the experimental results of VPVC with sine wave motion demand will be presented. Similar to the Section 7.2, Test Com3-VP will be the example to be discussed in detail. The differences between simulated Com3-VP and experimental Com3-VP will be analysed in subsection 7.4.1. Next a detailed illustration to the operating of VPVC controller is interpreted in subsection 7.4.2. The third subsection is an investigation to compare the different tracking response between VPVC and VPVHA control theory in terms of the feedback control to the MA. Then Com3-FP and Com3-VP will be compared experimentally to show the differences between FPVC and VPVC directly in subsection 7.4.4. At the end of this section, a summary of experimental hydraulic power consumed and dynamic errors of all the VPVC comparison tests will be shown and compared with the FPVC experimental results.

7.4.1 Comparison between simulation and experimental results of Com3-VP

Both the simulated and the experimental position tracking of Com3-VP are plotted in Figure 7.16. Generally speaking, the experimental waves fit the simulated data well. The experimental phase delay phenomenon is very slight.

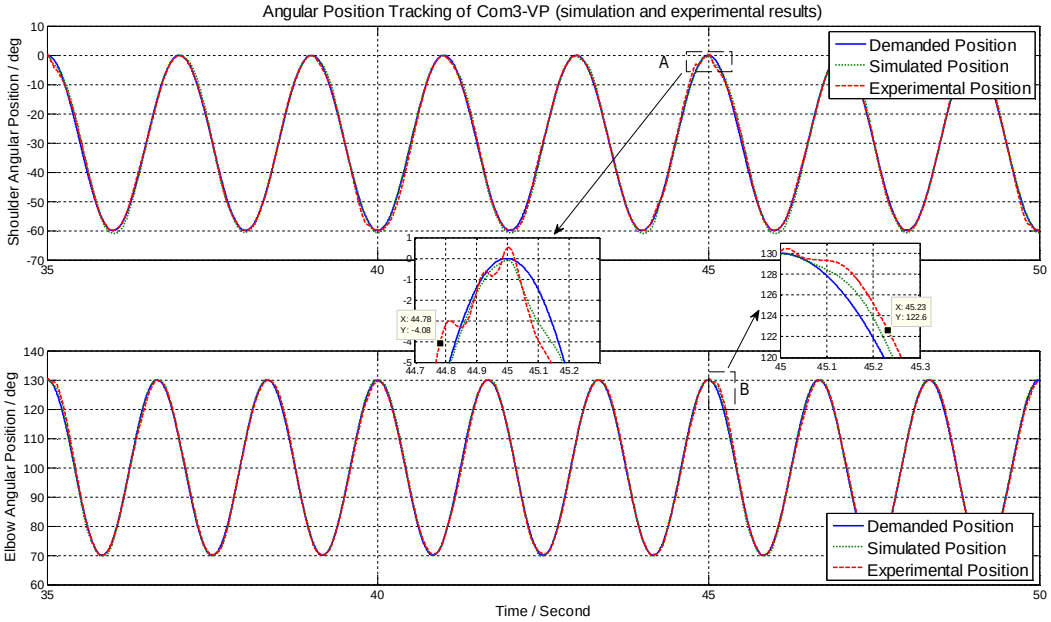

Figure 7.16 Comparison of simulated and experimental position tracking of Com3-VP

From Figure 7.17, it is seen that the experimental dynamic errors are larger than the simulated but the general trends of experimental dynamic errors are similar to the simulated, and the maximum experimental dynamic errors (2.6^{o} for shoulder and 3.4^{o} for elbow) are still within a satisfactory range.

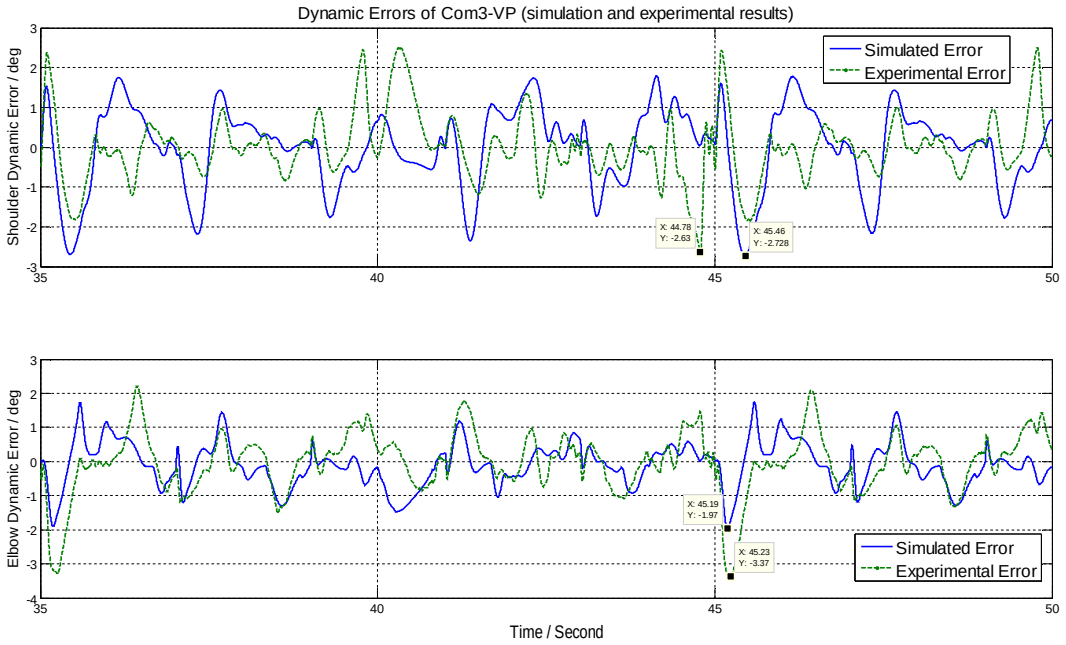

Figure 7.17 Dynamic errors of Com3-VP - simulation Vs experiment

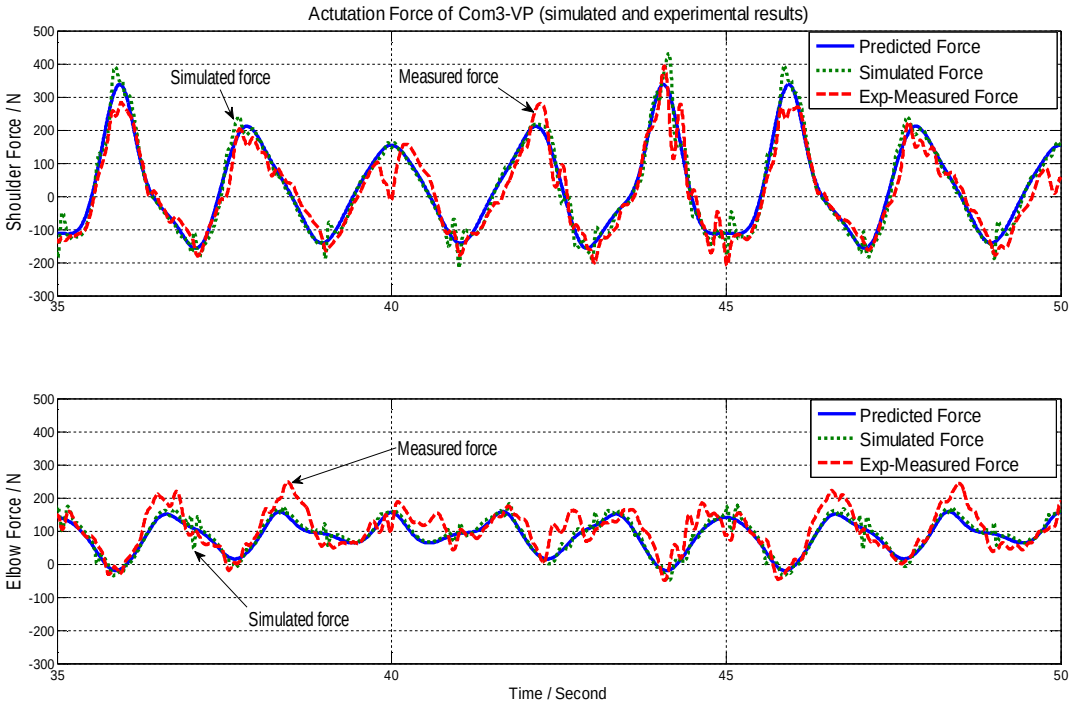

Figure 7.18 Actuation force of Com3-VP - simulation and experiment

The simulated actuation force and experimentally measured force are presented in Figure 7.18. The simulated actuation forces for the two joints fit the predicted actuation forces well with some additional small vibration. The measured forces have similar trends to the simulated forces with some acceptable differences.

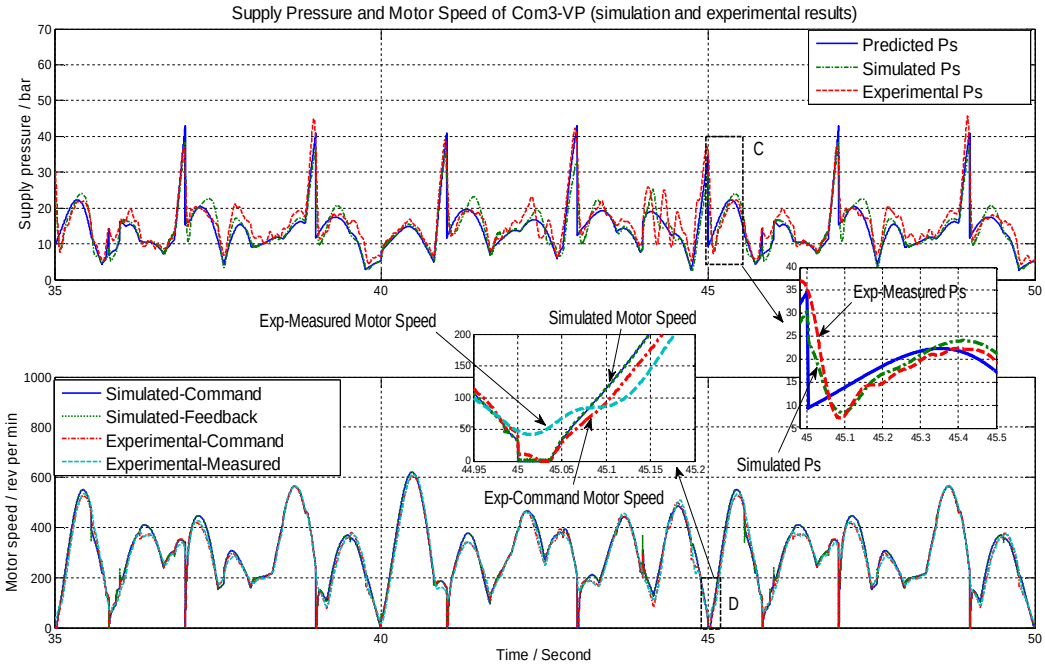

Figure 7.19 Supply pressure and motor speed of Com3-VP - simulation Vs experiment

From Figure 7.19, it is found that zero speed command (red line) happens at 45 second in experiment (zoom D). But in the real experiment, the motor speed does not track the zero command successfully: during 45 second to 45.1 second, the experimental measured speed (blue line) is about 50 to 100 rpm instead of zero in simulation. More flow is generated into the supply hoses in the experiment; hence the P_S in experiment is higher than the simulated P_S for a while (zoom C). The dynamic errors here in the experiment are larger than in simulation (see points highlighted in Figure 7.17). Generally speaking, the experimental supply pressure fits the simulated supply pressure. The supply pressure is from 10 bar to 20 bar for most of the duty cycle. The hydraulic power consumed in experiment Com3-VP is 24.98W which is closed to simulated result of 23.71W.

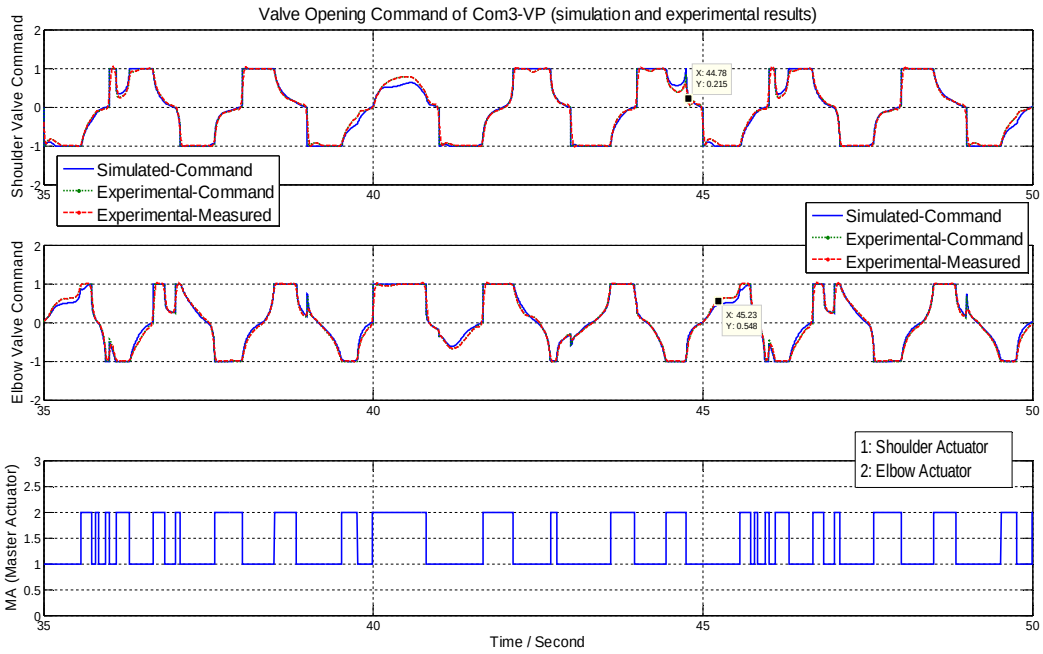

Figure 7.20 Valve command and spool positions of Com3-VP - simulation and experiment

The valve opening command signals of simulation and experiment are plotted in Figure 7.20. The simulated command signals generally fit the experimental command well with some differences when valve is being throttled. This is due to some differences in the position feedback between the simulation and experiment. A significant issue to mention is that VPVC showed a very low noise level in the experimental tests. No relief valve was working to throttle the pump flow, and the motor speed is varied according to the motion demand. Compared with the FPVC, a new advantage of VPVC was discovered.

7.4.2 Detailed illustration of VPVC control algorithm in experiment

A detailed operating process for the VPVC control algorithm is described in this subsection. Figure 7.21 shows the output signals from VPVC controller. As the flowchart illustrated in Figure 3.4, firstly, the VPVC feed forward controller computes the required minimum supply pressure for each cylinder according the predicted actuation force from applying Lagrange equations of the second kind. For each cylinder, the feed forward part of VPVC controller has to compute two minimum supply pressure values with two assumptions: P_{SO} is the supply pressure when its control valve is fully open; P_{SC} is the supply pressure when the pressure in the thrust chamber achieves the critical value of no cavitations.

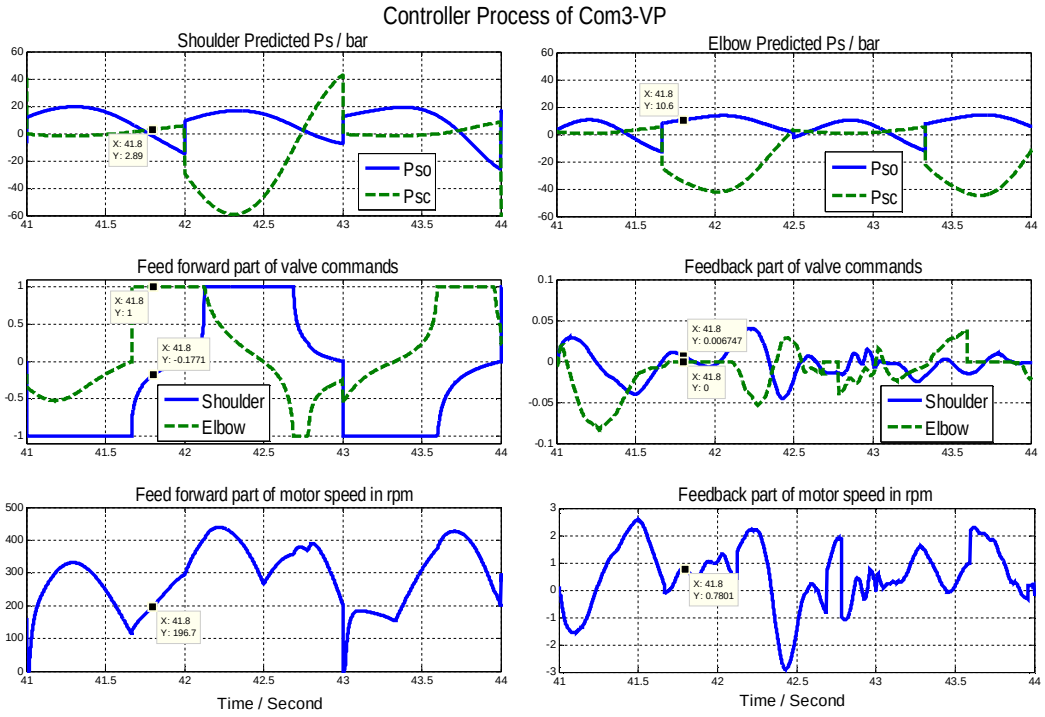

Figure 7.21 The detailed process of VPVC controller for Com3-VP

The circumstance at 41.8 second will be chosen to be an example. In Figure 7.21, at 41.8 second, the predicted pressure P_{SO} of the elbow joint (10.6 bar) is the highest pressure so is selected to be the target supply pressure for the whole system (see the top row subplots in Figure 7.21). Thus the MA (master actuator) is the elbow actuator and its valve opening (feed forward part) is +1 (i.e. fully open). The shoulder actuator which is non-MA is throttled conventionally with the determined supply pressure of 10.8 bar. Thus the computed opening of the shoulder valve is -0.177 by Equation 3.21 (see the middle left subplot in Figure 7.21). The corresponding motor speed to achieve the flow rate requirements including compressibility flow for the required pressure change is computed as the feed forward part of motor speed command by Equation 3.22 (see the bottom left subplot in Figure 7.21).

The actual measured position values of the two joints are used as input signals to the feedback controller of VPVC (see the top row subplots in Figure 7.22). Through the individual PI controller to the valves, the feedback part of the valve command is calculated separately and shown in the middle right subplot in Figure 7.21: at 41.8 second, the feedback part of the shoulder valve command is about 0.007 and the elbow zero. Hence the final valve commands to the two valves are: shoulder valve command -0.170 and elbow valve +1.

From the middle row subplots in Figure 7.22, the actual measured valve opening of 41.8 second is shown: the actual opening of shoulder valve is -0.176 and elbow 0.9985. The actual measured valve opening values are close to the theoretical valve commands with the allowance of measurement uncertainties (minor offset and/or internal filter influence).

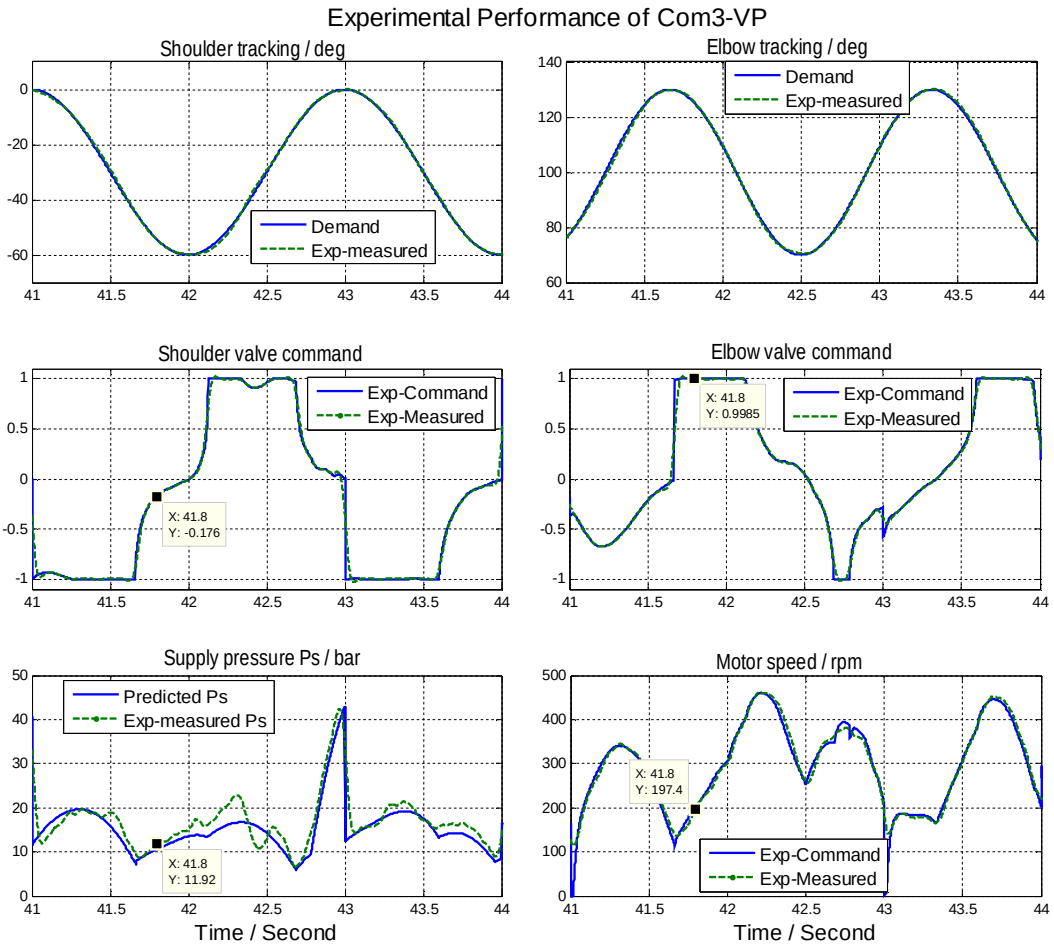

Figure 7.22 The experimental performance of Com3-VP

The feedback controller for the motor speed command is a P controller which uses the actual position of the MA as the input signal. The feedback part of motor speed command is shown in the bottom right subplot in Figure 7.21. At 41.8 second, the feedback part of motor speed command is 0.78 rev/min. Together with the motor speed command feed forward of 196.7 rev/min in the bottom left subplot in Figure 7.21, the final motor speed command is 197.5 rev/min. From the bottom right subplot in Figure 7.22, the actual measured speed of the motor in experiment is 197.4 rev/min at 41.8 second, which is nearly the same as the command.

The actual measured supply pressure in experiment is 11.9 bar at 41.8 second which is a bit higher than the predicted value of 10.6 bar. Simplifications and uncertainties in the VPVC inverse model (e.g. related to leakage and bulk modulus) cause the actual supply pressure to have a slight but acceptable difference from the predicted supply pressure. Generally, every part in the VPVC controller works properly and the VPVC controlled system has a satisfactory performance in the experiment.

7.4.3 Different tracking performance between VPVC and VPVHA

The VPVHA control algorithm from Scopesi's research didn't always apply position feedback to control the valve of the master actuator (Scopesi, et al., 2011). The position feedback control of the master actuator (MA), as shown in Figure 7.23, will be triggered only if there is zero (or almost zero) spool position command from the feed forward control, and aims to eliminate the actuator position error in that situation. Scopesi pointed out in his VPVHA: if the desired position is a step, there is mostly a zero flow requirement into the feed forward controller and then zero spool position demand. However, due to inevitable position error, it is necessary to augment the feed forward command and to open the valve, to move the actuator so as to cancel the position error. It can be concluded: in VPVHA, for most of time, the control valve of the MA has no feedback control. The accuracy of the MA relies on the prediction results from the feed forward part, and the feedback adjustment of motor speed.

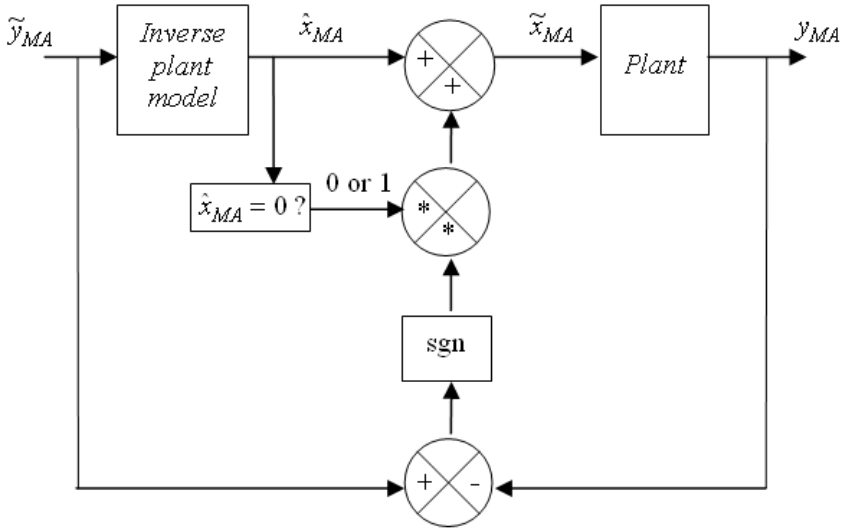

Figure 7.23 Feedback control for the master actuator (valve command) (Scopesi, et al., 2011)

In this project, experimental tests are involved. The feed forward part of VPVC can't predict the real behaviour perfectly. Thus closed loop control of the MA control valve is necessary all the way in VPVC. In Section 3.3, it was stated that: in VPVC feedback control, the control valves of both two actuators (MA and non-MA) had feedback control all the time. Next, a detailed experimental comparison between the VPVC and the VPVHA algorithm will be given in Figure 7.24 and Figure 7.25. The test Com3-VP is the example to show the difference.

In Figure 7.24, the two top subplots are the position tracking performance of VPVC and VPVHA. The two bottom subplots are the corresponding valve command signals. From Figure 7.25, the top left subplot shows: during period A, the master actuator (MA) is the shoulder actuator. Back to Figure 7.24 bottom left subplot, the value of the shoulder valve command is x_{sc} rather than ±1, indicating that P_{SC} is working as the required supply pressure, i.e. the shoulder actuator tries to avoid cavitation in the thrust chamber during this deceleration period (see Section 3.2.1).

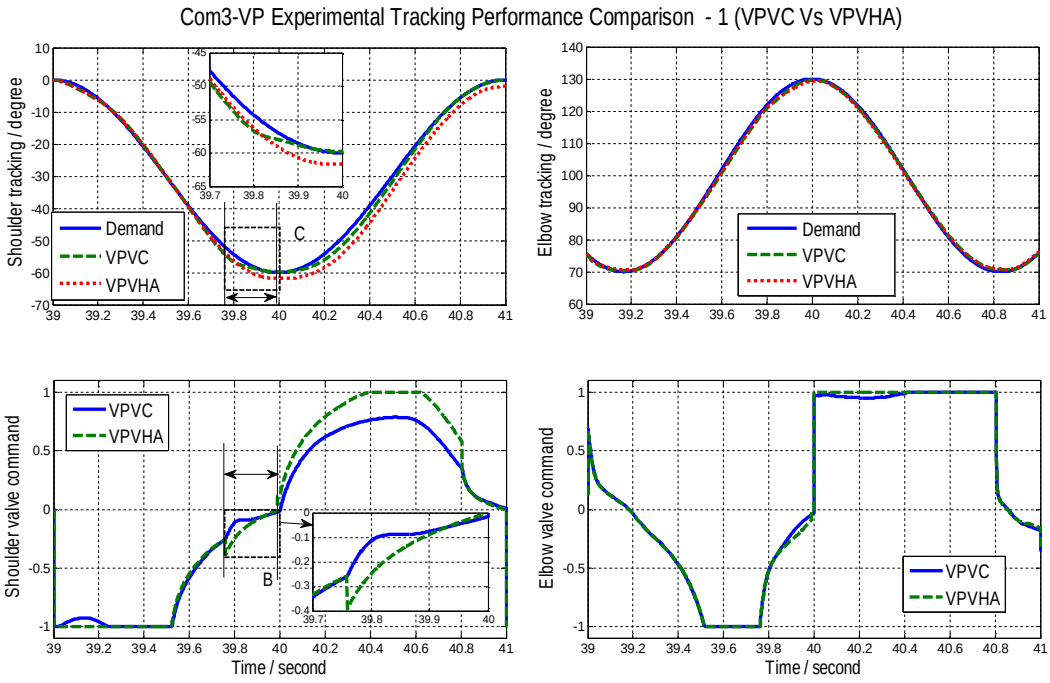

Figure 7.24 Com3-VP experimental tracking performance comparison – 1

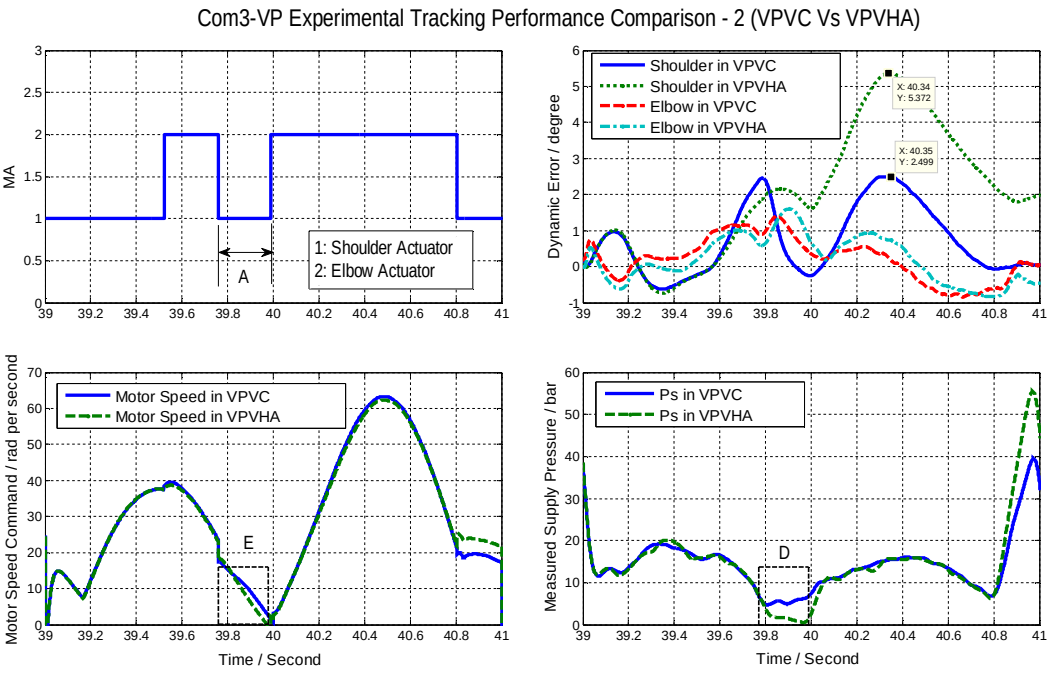

Figure 7.25 Com3-VP experimental tracking performance comparison – 2

Zoom B in the bottom left subplot of Figure 7.24 shows the shoulder valve command difference between VPVC and VPVHA. In VPVHA, the MA (shoulder actuator) is excessively faster than the demand due to the inaccuracies from the feed forward (valve opening is too large), which means the MA fails to maintain the threshold pressure. The pressure in the supply hoses decreases to an unwanted value consequently (see D in the bottom right subplot of Figure 7.25).

From zoom B and C in Figure 7.24, it is found that in VPVC the valve command of the MA resists the load effectively: the speed of the actuator slows down quickly as the demand dictates. This means, in VPVC, the feedback control of the MA valve improves the performance. Hence the supply pressure is kept at a reasonable value (see D in Figure 7.25).

The top right subplot of Figure 7.25 shows the dynamic errors: in VPVHA, the position error of the shoulder actuator is accumulated up to 5.37^{o} at 40.34 second because there is no feedback adjustment to the shoulder valve during period A. After period A, when the MA switches to the elbow actuator, the shoulder actuator valve (now it is the non-MA) starts to enable its own feedback control to recover to the demanded position and it takes about 1 second to reduce the dynamic error to 2^{o}. While in VPVC, the maximum dynamic error of the shoulder response is only 2.5^{o}.

The motor speed command is different between VPVC and VPVHA as well (see E in Figure 7.25), because in the two control algorithms, different MA position feedback signals were received by the P controller of the motor speed command.

Test	*VPVC* *Dynamic Error (degree)*				*VPVHA* *Dynamic Error(degree)*			
	Shoulder		*Elbow*		*Shoulder*		*Elbow*	
	Max	*Average*	*Max*	*Average*	*Max*	*Average*	*Max*	*Average*
Com1	3.1	0.90	2.0	0.75	5.1	4.11	8.2	2.62
Com2	3.3	0.72	2.5	0.63	4.2	0.97	2.6	0.70
Com3	2.6	0.68	***3.4***	0.65	5.4	1.16	3.2	0.71
Com4	3.2	0.75	2.1	0.53	6.0	1.11	5.0	0.73
Com5	2.7	0.77	2.9	0.63	4.8	1.02	3.0	0.75
Com6	4.4	0.93	***4.1***	0.77	5.4	1.15	3.5	0.80

Table 7.2 The dynamic errors of sine wave motion experimental tests (VPVC Vs VPVHA)

A summary of experimental dynamic errors for VPVC and VPVHA is given in Table 7.2. Both maximum and average values are listed. From the data, it is obvious that VPVC provides smaller dynamic errors for most cases. It is believed that, compared with the VPVHA, the VPVC algorithm which always uses feedback control to the MA valve can reduce the errors from the imperfect prediction in the feed forward controller, to get a better tracking performance in experiments.

7.4.4 Discussion about the tracking response of VPVC with sine wave motion

As explained in subsection 7.3.3, simplified integrated centres of gravity, inertias and simplified friction assumptions are used to predict the required hydraulic force (Equation 3.25 and Equation 3.26). Thus there are errors in the prediction of the minimum supply pressure, spool positions and the motor speed command.

As a conclusion, the experimental results of Com3-VP fit the simulated results well with some acceptable differences. The experimental dynamic errors are 2.6^{o} for shoulder and 3.4^{o} for elbow, which are equivalent to 4.3% and 5.7% of the total motion range (60 degrees). The prediction of actuation force with an estimated friction for the demanded motion is effective.

7.4.5 Experimental comparison between Com3-FP and Com3-VP

The experimental results of Com3-FP and Com3-VP will be compared and discussed in detail, showing the differences between these two control methods directly.

In Figure 7.26, it is clear that FPVC has obvious phase delay while VPVC phase lag is nearly invisible.

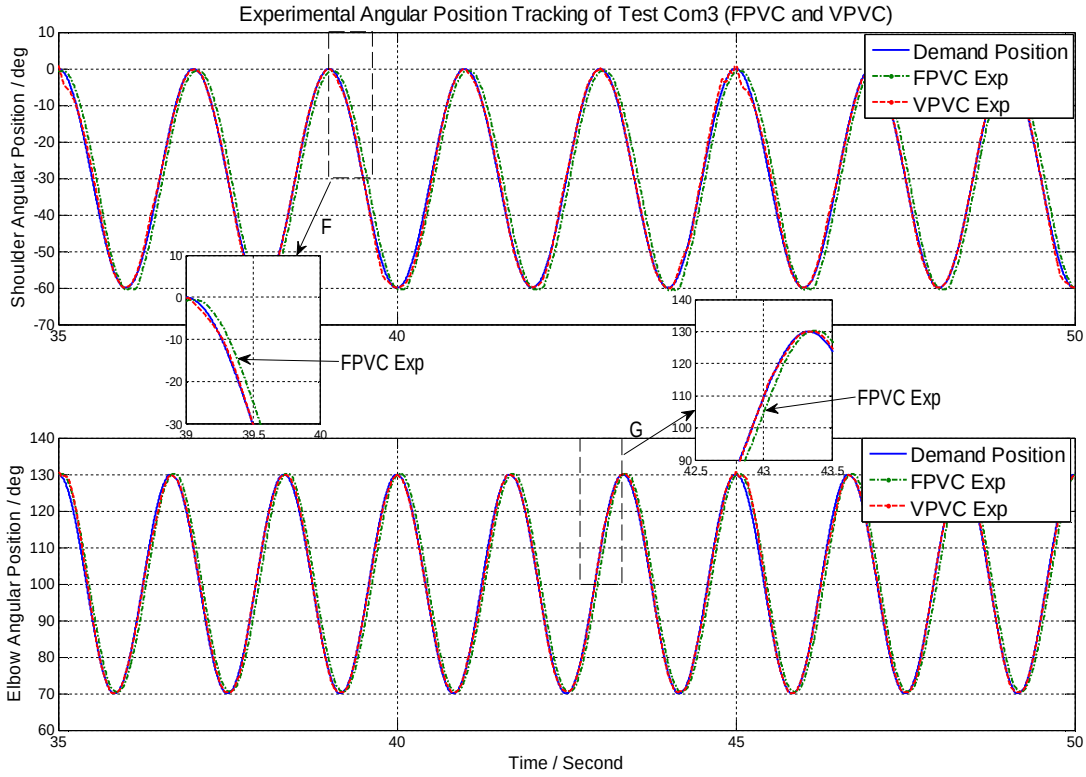

Figure 7.26 Experimental comparison of position tracking between Com3-FP and Com3-VP

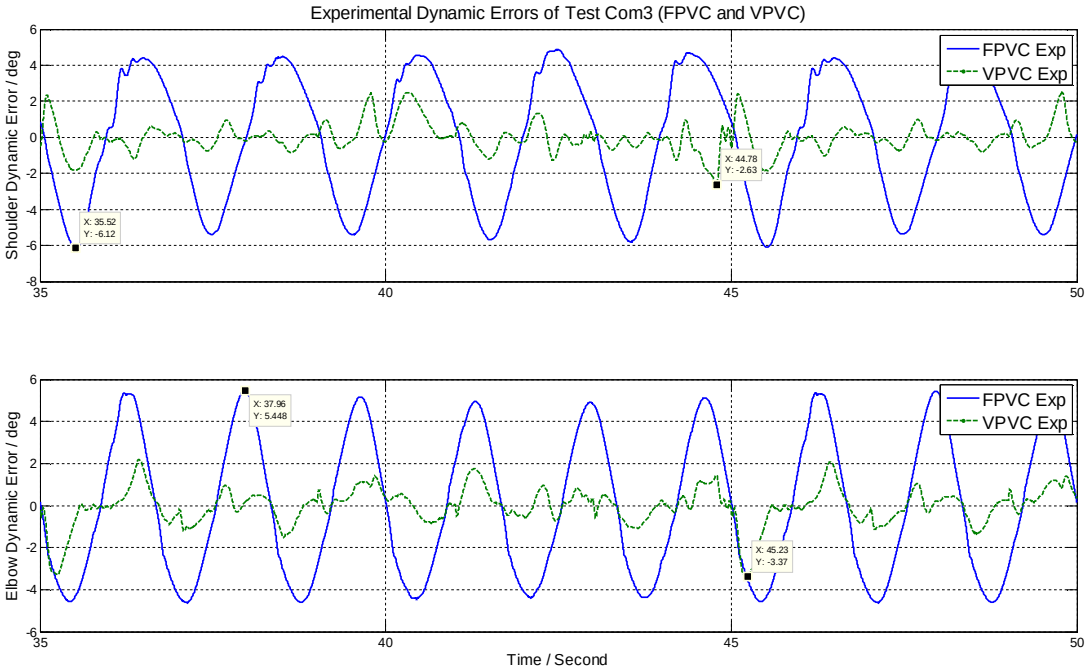

Figure 7.27 Experimental comparisons of dynamic errors between Com3-FP and Com3-VP

From Figure 7.27, it is found that the dynamic errors of FPVC have similar sine waves to the valve command waves of FPVC in Figure 7.28. The controller of FPVC consists of two valve PI controllers, which receive the dynamic errors and then output the valve opening commands. Hence they have similar wave shapes and the maximum dynamic errors coincide with the maximum valve opening commands.

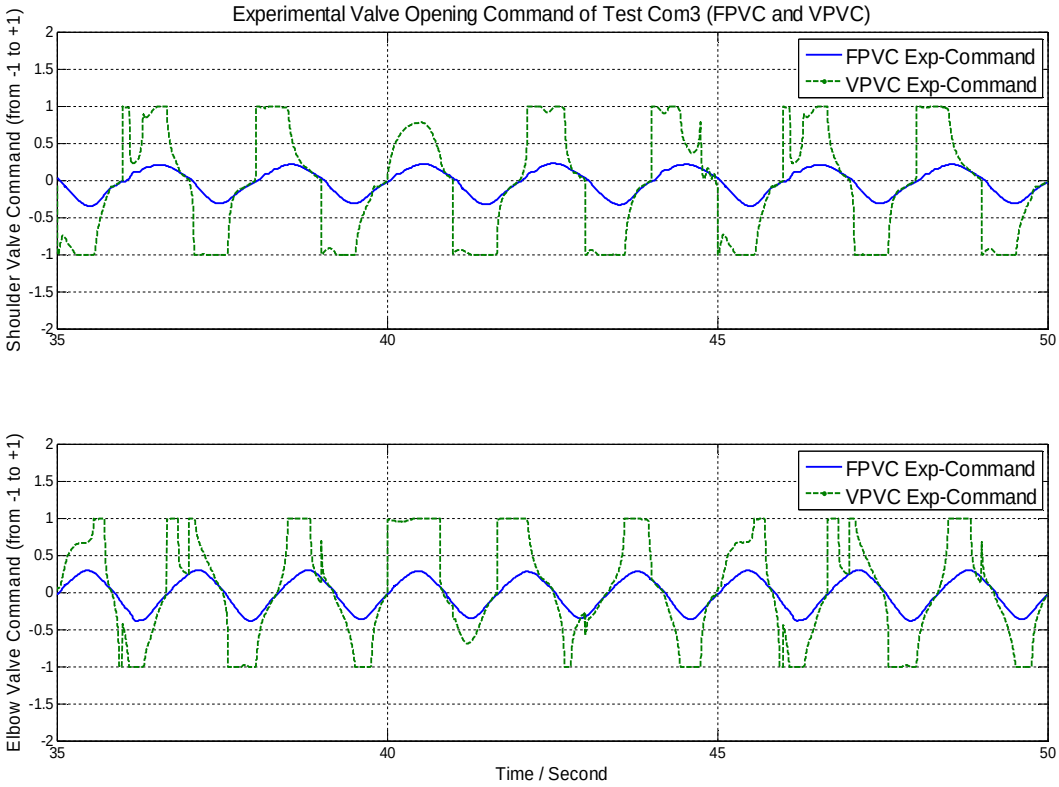

Figure 7.28 Experimental comparison of valve command between Com3-FP and Com3-VP

From Figure 7.28, it is seen that the valve commands of VPVC are more complex compared with sine wave shape of FPVC. For most of the duty cycle, the valve of one actuator is nearly fully open (MA) and the other one is throttled conventionally. VPVC minimises pressure loss across the valve of the MA, while FPVC is wasting energy by throttling the flow by both valves.

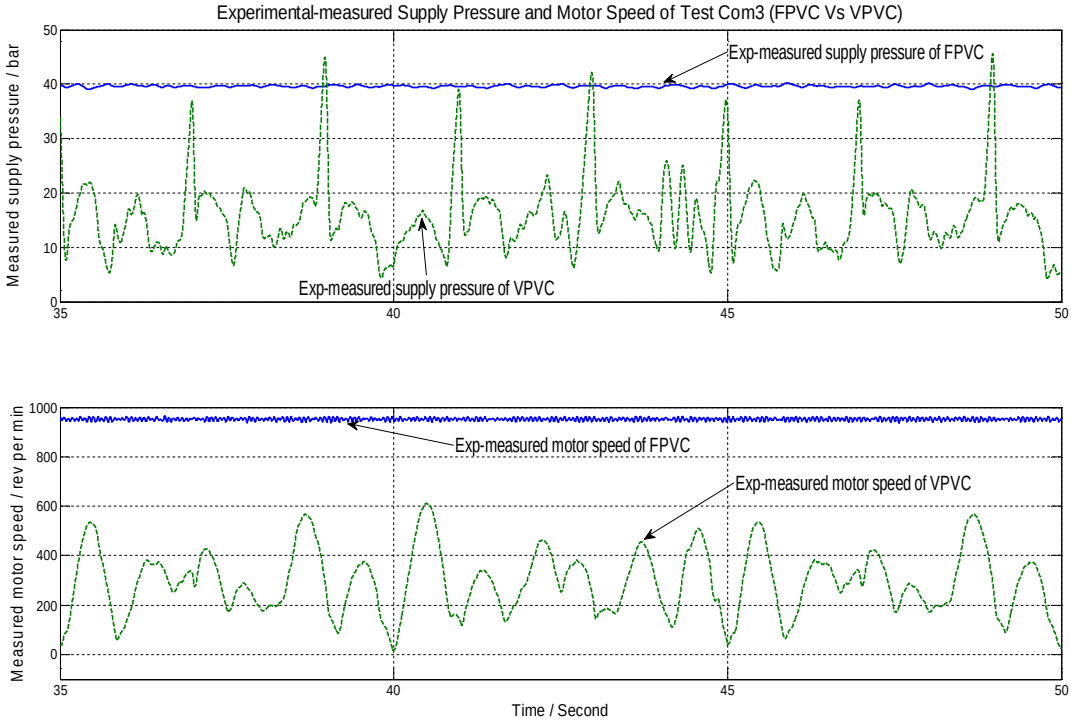

Figure 7.29 Experimental comparison of supply pressure and motor speed between Com3-FP and Com3-VP

Figure 7.29 shows the measured motor speed and supply pressure in the Com3-FP experiment and the Com3-VP experiment. The VPVC commands the appropriate motor speed to generate the required flow rate into the supply hoses, so a variable supply pressure is achieved (bottom subplot in Figure 7.29). The supply pressure varies from 5 bar to 45 bar, and most of the duty cycle it is within 10 bar to 20 bar. Compared with the constant supply pressure of 38 bar for FPVC, VPVC saves hydraulic power by reducing supply pressure. From the differences in the motor speed between FPVC and VPVC, it is clear that FPVC dissipates a great deal of input power by flow through the relief valve, but this loss is not included in the efficiency analysis which follows.

Test	FPVC			VPVC			Saving %
	Max Dynamic Error (degree)		Experimental Hydraulic Power (W)	Max Dynamic Error (degree)		Experimental Hydraulic Power (W)	
	S	E		S	E		
Com1	3.1	3.3	38.14	3.1	2.0	11.38	70.16%
Com2	4.5	4.3	48.03	3.3	2.5	16.93	64.75%
Com3	6.1	5.4	57.20	2.6	3.4	24.98	56.33%
Com4	4.8	4.7	49.04	3.2	2.1	22.06	55.02%
Com5	7.4	6.4	64.01	2.7	2.9	34.43	46.21%
Com6	11.4	8.7	79.07	4.4	4.1	50.25	36.45%

Table 7.3 Summary of experimental results of comparison tests FPVC and VPVC

Table 7.3 shows the experimental comparison of all the six sine wave tests between FPVC and VPVC. In all the comparison tests, VPVC shows smaller dynamic errors than FPVC. The maximum dynamic errors of FPVC tests are increase with ascending load (ascending amplitude and/or ascending frequencies). The VPVC dynamic errors don't change so much as FPVC among the various motion demands. All the dynamic errors of VPVC are within 6% of the total motion range, which means VPVC has a better tracking ability with one fixed setting of P(I) controllers.

For the hydraulic power consumed in experiments, VPVC gives a saving between 36.45% and 70.16%. The saving increases when the load decreases because FPVC has higher waste with low load. As mentioned in Section 6.4, the energy

saving by VPVC can be increased greatly if the power loss via the relief valve in FPVC is taken into account.

As a conclusion of this section, the experimental results show that VPVC is much more efficient compared with the conventional FPVC system. At the same time, VPVC brings a better dynamic response: much smaller phase delay and much smaller dynamic error. VPVC also brings out a very low noise level, which is very useful for the current hydraulic applications such as the evacuators and the military robots.

Chapter 8

8 Conclusions and Future Work

An efficient fluid power control method was developed in this research - variable supply pressure valve-controlled (i.e. 'VPVC' in this thesis), which was successfully validated on the motion control of a two-axis robotic arm. The VPVC controller was designed to calculate the minimum required supply pressure with the corresponding spool positions for the two individual control valves. This system was able to achieve a high energy-efficiency compared with the conventional fixed supply pressure valve-controlled (FPVC) actuation system. From the experimental results of the two-axis robotic arm system, the VPVC achieved an energy-saving up to 70% compared with the FPVC. The dynamic errors and noise level of the VPVC were also much smaller than the FPVC.

8.1 Conclusions

The conventional fixed supply pressure valve-controlled (FPVC) hydraulic actuation system dissipates energy due to control valves which reduce the fixed supply pressure to the individual cylinder pressures according to their load requirements. Conversely VPVC was designed to generate a variable and minimum required supply pressure together with the corresponding spool positions for the control valves according to the load-prediction.

The study began with the derivation of the control algorithm, then the system modelling and simulation tests. The two controllers (FPVC controller and VPVC controller) and the hydraulic system have been modelled in MATLAB®/Simulink®. The robotic arm has been modelled in Simulink®/SimMechanics®.

For the simulation study, firstly, the settings for the PI controller in the FPVC and VPVC were determined by tuning tests (square wave motion for the FPVC and filtered square wave motion for the VPVC). Next, a series of tests of FPVC and VPVC with the same sine wave motion demand were run, which aimed to compare the hydraulic power consumption and the accuracy of position tracking. From the comparison, it was found that the VPVC had higher energy-efficiency compared with the FPVC from the simulated results. The maximum saving was up to 71.74%. Moreover, the dynamic errors were greatly reduced by applying the VPVC due to its reduced phase lag.

The experimental tests were undertaken on the xPC Target real-time control platform. First of all, the PI controller settings have been validated experimentally. The small differences between the simulated and the experimental responses were explained.

Then the experimental tests of sine wave motion have been implemented. The detailed process of the VPVC control algorithm operation was illustrated experimentally, which was compared with the performance of the VPVHA proposed in 2011 (Scopesi, et al., 2011). The comparison showed that VPVC introduced in this thesis had a higher accuracy of position tracking compared with the proposed VPVHA algorithm. The comparison between FPVC and VPVC with sine wave motion verified the advantages of the VPVC in the simulated results, in terms of the energy-efficiency and the dynamic errors. For hydraulic power consumption, the VPVC experimental results presented a maximum energy-saving of 70.16% compared with the FPVC experimental results. If the energy loss via the relief valve in FPVC is included, the saving will be improved greatly.

In all the comparison tests, VPVC showed smaller dynamic errors than FPVC. All the dynamic errors of VPVC tests were within 6% of the total motion range, compared to 14% for FPVC, and the average dynamic errors of VPVC tests were within 1.5% of the total motion range. The maximum dynamic errors of FPVC tests increased with ascending load (ascending amplitude and/or ascending frequencies). The VPVC dynamic errors didn't change so much as FPVC among the various motion demands, which means VPVC has a better tracking ability with one fixed setting of the PI controllers.

The VPVC operation was much quieter than FPVC because it didn't need to drive flow through a relief valve to maintain the supply pressure. Very low noise level is a significant competitive advantage of VPVC, especially when it is applied on the construction machines and military robots.

It is clear that load-prediction based variable supply pressure valve-controlled hydraulic actuation is an energy-efficient hydraulic actuation method for a multi-axis system compared with a traditional fixed supply pressure valve-controlled hydraulic actuation system. The energy saving by VPVC is very dependent on

duty cycle i.e. motion demand, and also the load. Most saving will be achieved when the average of the maximum of both actuator forces is much lower than the peak value. The position tracking data indicated the VPVC gave higher position accuracy due to the dominant role of its feed forward control.

8.2 Recommendations for future work

The work presented in this thesis gives a number of areas in which further research could be undertaken.

- More cylinders should be involved in the future research of VPVC. The VPVC is proposed to be suitable for multi-axis systems. The robotic arm in this thesis has only two cylinders. A system with more hydraulic cylinders should be investigated to determine the energy saving potential of VPVC.
- The accuracy of the load-prediction in VPVC could be improved by getting more precise information about the load. Like the viscous friction estimation, and the CG positions of the individual parts, more detailed and exact information of the model will bring higher accuracy of the load-prediction; hence the VPVC performance will be improved.
- In the control algorithm of the VPVC, the stationary motion demand of the system requires zero or almost zero flow rate generated by the servomotor. From the current experimental results, it was found that the servomotor was not able to perform an exact zero speed when commanded by the VPVC controller. Hence the tracking performance was influenced.
- The minimum required supply pressure prediction equations were different according to the direction of motion. Hence the predicted supply pressure generated a sudden step when the cylinder was changing direction. In the real experiment, the system could not perform

as well because of the limitation in the speed of response of the motor-pump, linked to the hydraulic capacitance. Almost all of the maximum dynamic errors happened at the moment of direction changing. Although this is a fundamental problem, there is scope for further analysis.

- In this thesis, the closed loop position control was used for the two control valves in VPVC to eliminate the prediction errors from the feed forward controller. The proportional-integral (PI) control was adopted due to its simple implementation and good performance. Some alternative control methods could be investigated.
- The performance of VPVC control algorithm could be investigated with different loads, and varying/uncertain loads in further research.

References

Albers, P., 2010. *Motion Control in Offshore and Dredging.* Springer Science + Business Media.

Atherton, D. P. & Irwin, G. I., 1996. *Advanced Robotics and Intelligent Machines.* London: The Institution of Electrical Engineers.

Avago Technologies, 2006. *Data sheet for AEDA 3300-BE1.* [Online]
Available at:
http://www.avagotech.com/pages/en/motion_control_encoder_products/incremental_encoders/transmissive_encoders/aeda-3300-be1
[Accessed 21 July 2014].

Axin, M., Eriksson, B., Palmberg, J. & Krus, P., 2011. *Dynamic Analysis of Single Pump Flow Controlled Mobile Systems.* Tampere, 12th Scandinavian International Conference on Fluid Power.

Baileigh industrial, 2014. *Latest Bailiegh Catalogue - VOL 33.* [Online]
Available at: http://www.baileighindustrial.co.uk/media/uploads/documents/Catalogue-v332012.pdf
[Accessed 7 July 2014].

Baldor, 2010. *Baldor Products: AC brushless servo motor BSM-N Series.* [Online]
Available at: http://www.baldor.com/products/servomotors/n_series/bsm_nseries.asp
[Accessed 17 July 2014].

Bhatti, J. & Plummer, A. R., 2011. *HYDRAULIC RUNNING ROBOTS:THE PROSPECTS FOR FLUID POWER IN AGILE LOCOMOTION.* Tampere, The Twelfth Scandinavian International Conference on Fluid Power.

Boddy, C. L., Hopper, D. F. & Taylor, J. D., 1996. Advanced control systems for robotic arms. In: Atherton, D. P. & Irwin, G. I., ed. *Advanced Robotics and Intelligent Machines.* London: The Institution of Electrical Engineers, p. 41.

Boston Dynamics, 2008. *BigDog Overview Slides.* [Online]
Available at: http://www.bostondynamics.com/img/BigDog_Overview.pdf
[Accessed 12 July 214].

Boston Dynamics, 2014. *BigDog - The Most Advanced Rough-Terrain Robot on Earth.* [Online]
Available at: http://www.bostondynamics.com/robot_bigdog.html
[Accessed 13 May 2014].

Brokk, 2014. *Brokk 100 catalogue.* [Online]
Available at: http://www.brokk.com/img/informupl/B100_EN.pdf
[Accessed 12 July 2014].

Burster, 2012. *Full data sheet model 8417 (EN).* [Online]
Available at: http://www.burster.com/en/products/sensors/p/subminiature-tension-and-compression-load-cell-model-8417/v/
[Accessed 21 July 2014].

Chapple, P., 2003. *Principles of Hydraulic System Design.* First ed. Oxford: Coxmoor Publishing Company.

Cheah, C. C., Liu, C. & Slotine, J. J. E., 2006. Adaptive Tracking Control for Robots with Unknown Kinematic and Dynamic Properties. *The International Journal of Robotics Research,* March, 25(3), pp. 283-296.

Cheng, M., Xu, B. & Yang, H., 2014. *Efficiency Improvement for Electrohydraulic Flow Sharing Systems.* Aachen, 9th International Fluid Power Conference.

Chen, Y., Ma, G., Lin, S. & Gao, J., 2012. Adaptive Fuzzy Computed-Torque Control for Robot Manipulator with Uncertain Dynamics. *International Journal of Advanced Robotic System,* Oct, Volume 9.

Cleasby, K. G. & Plummer, A. R., 2008. *A novel high efficiency electro-hydrostatic flight simulator motion system.* Bath., Fluid Power and Motion Control (FPMC 2008), pp. 437-449.

Crowder, R. & Maxwell, C., 1997. Simulation of a prototype electrically powered integrated actuator for civil aircraft. *Proc Instn Mech Engrs,* 211(Part G), pp. 381 - 394.

DeBoer, C. & Yao, B., 2001. *Energy-efficient Motion Control of a Digital Hydraulic Joint Actuator.* New York, IMECE'01 ASME International Mechanical Engineering Congress and Exposition.

Djurovic, M. & Helduser, S., 2004. *New Control Strategies for Electrohydraulic Load-sensing.* Bath, Power Transmiss and Motion Control 2004, pp. 201-210.

Eriksson, B. & Palmberg, J. O., 2010. Individual Metering Fluid Power Systems: Challenges and Opportunities. *Systems and Control Engineering,* 4 July, 225(Part I), pp. 196-211.

Fan, C., Dong, M., Sun, Z. & Sun, W., 2010. *Reserch on Multilevel Sections Synchronous Expanding and Contracting Hydraulics Cylinder.* Changsha, 2010 International Conference on Digital Manufacturing & Automation, pp. 319-321.

Fanuc robotics, 2009. *Fanuc robotics product.* [Online]
Available at: http://www.fanucrobotics.co.uk/en/products/a_industrial-robots
[Accessed 12 June 2014].

Finzel, R. & Helduser, S., 2008. *Energy-Efficient Electro-Hydraulic Control Systems for Mobile Machinery/Flow Matching.* Dresden, The 6th International Fluid Power Conference.

Finzel, R., Helduser, S. & Jang, D., 2009. *Electro-hydraulic Control Systems for Mobile Machinery with Low Energy Consumption.* Hangzhou, 7th International Conference on Fluid Power Transmission and Control, pp. 214-218.

FMC technologies, 2014. *Schilling Robotics TITAN 4 Manipulator Datasheet.* [Online]
Available at: www.fmctechnologies.com/SchillingRobotics
[Accessed 12 July 2014].

GE, 2012. *Where jules verne meets star wars: GE's walking truck of the 1960s.*

Gen, E. & Shigeo, H., 2012. Study on Roller-Walker — Improvement of Locomotive Efficiency of Quadruped Robots by Passive Wheels. *Advanced Robotics,* 24 June, Volume 26:8-9, pp. 969-988.

Gotz, W., 1984. *Hydraulics Theory and Applications. From Bosch.* Stuttgart: Robert Bosch GmbH.

Guglielmino, E. et al., 2010. *Power Hydraulics - Switched Mode Control of Hydraulic Actuation.* Taipei, The 2010 IEEE/RSJ International Conference on Intelligent Robots and Systems, pp. 3031-3036.

Guizzo, E. & Deyle, T., 2012. Robotics Trends for 2012. *IEEE Robotics & Automation Magazine,* March, 19(1), pp. 119-123.

Habibi, S. & Goldenberg, A., 2000. Design of a New High-Performance ElectroHydraulic Actuator. *IEEE/ASME TRANSACTIONS ON MECHATRONICS,* 5(2), pp. 158-164.

Habibi, S. R. & Goldenberg, A. A., 1994. *Analysis and control of industrial hydraulic robots.* Lake Buena Vista, Proceedings of the 33rd Conference on Decision and Control, pp. 345-350.

Hansen, R. H., Anderson, T. O. & Pedersen, H. C., 2010. *Development and Implementation of an Advanced Power Management Algorithm for Electronic Load Sensing on a Telehandler.* Bath, Fluid Power and Motion Control.

Harms, H., 1994. *Development Trends in Mobile Hydraulic.* Aachen, 11th Fluid Power Conference.

Helbig, A., 2002. *Injection Molding Machine with Electronic-hydrostatic Drives.* Aachen, 3th International Fluid Power Colloquium, pp. 67-81.

Helduser, S., 2003. *Improved Energy Efficiency in Plastic Injection Molding Machines.* Tampere, 8th Scandinavian International Conference on Fluid Power SICFP 03.

Hu, J., Wu, W., Yuan, S. & Jing, C., 2011. Opening and closing of a novel high-speed switching valve. *Proceedings of the Institution of Mechanical Engineers, Part I: Journal of Systems and Control Engineering,* Volume 226, pp. 466-475.

Hunt, T. & Vaughan, N., 1996. *The hydraulic handbook.* 9th ed. Oxford: Elsevier Advance Technology.

HYDAC, 2006. *Catalogue of HDA 3700.* [Online]
Available at:
http://www.hydac.bg/language/bg/uploads/files/products__1/2d5893bf32edd262142daa0bce5deda2.pdf
[Accessed 22 July 2014].

IIT Advanced Robotics, 2014. *HyQ Robot.* [Online]
Available at: http://www.iit.it/en/advr-dls-hyq-robot.html
[Accessed 20 July 2014].

IIT, 2014. *Hydraulically Actuated Quadruped - HyQ from IIT.* [Online]
Available at: http://www.iit.it/en/advr-labs/dynamic-legged-systems/hydraulically-actuated-quadruped-hyq.html
[Accessed 13 May 2014].

Jansson, A. & Palmberg, J., 1990. Separate Controls of Meter-in and Meter-out Orifices in Mobile Hydraulic Systems. *SAE Transactions.*

JCB, 2014. *JCB Hydraulic Excavators.* [Online]
Available at: http://www.jcb.co.uk/Products/Machines/Hydraulic-Excavators.aspx
[Accessed 11 July 2014].

Jeronymo, C. E., Yamada, H. & Muto, T., 1996. Application of unified predictive control to on/off control of hydraulic system driven by fast switching solenoid valves. *JSME International Journal Series C: Dynamics Control Robotics Design and Manufacturing,* Volume 39, pp. 515-521.

Jing, J., 2010. Principle and Aplications of Load-sensing System. *Fluid Power Transmission and Control,* November, pp. 21-24.

Johnston, N. D., 2009. *A SWITCHED INERTANCE DEVICE FOR EFFICIENT CONTROL OF PRESSURE AND FLOW.* Hollywood, Proceedings of the ASME 2009 Dynamic Systems and Control Conference.

Khoa, L., KIM, C. & AHN, K. K., 2012. *Application of Grey predictor in controlling 5 DOF power assistant robot.* Jeju Island, 2012 12th International Conference on Control, Automation and Systems, pp. 354-359.

Kim, S. & Murrenhoff, H., 2012. Measurement of Effective Bulk Modulus for Hydraulic Oil at Low Pressure. *Transactions Of The Asme: Journal Of Fluids Engineering,* 134(2).

Koivo, A. J., 1989. *Fundamentals for Control of Robotic Manipulators.* Toronto: John Wiley & Sons, Inc.

Konaka, M., 1991. *National project on advanced robot technology in Japan.* Pisa, Italy, Proceedings of ICAR'91 – Fifth International Conference on Advanced Robotics, pp. 24-30.

KUKA, 2014. *KUKA KR 16 robots weld vehicle components at AL-KO.* [Online]
Available at: http://www.kuka-robotics.com/res/robotics/solutions/PDF/EN/2014_EN_AL-KO.pdf
[Accessed 11 July 2014].

Lantto, B., 1994. *On Fluid Power Control with Special Reference to Load-Sensing Systems and Sliding Mode Control,* Linkoping: Linkoping Studies in Science and Technology.

Lee, J. M., Park, S. H. & Kim, J. S., 2013. Design and Experimental Evaluation of a Robust Position Controller for an Electrohydrostatic Actuator Using Adaptive Antiwindup Sliding Mode Scheme. *The ScientificWorld Journal,* Volume 2013.

Liu, Y., Yang, H., Xu, B. & Zeng, D., 2009. *Simulation of Separate Meter-in and Meter-out Control of Electro-hydraulic Load Sensing System.* Hangzhou, The 7th International Conference on Fluid Power Transmission and Control, pp. 257-261.

Lovrec, D., Kastrevc, M. & Ulaga, S., 2008. Electro-hydraulic Load Sensing with a Speed-controlled Hydraulic Supply System on Forming-machines. *The International Journal of Advanced Manufacturing Technology.*

Malcolm, D. R., 1988. *Robotics: An introduction.* 2nd ed. Canada: Delmar Publishers Inc.

Manhartsgruber, B., Mikota, G. & Scheidl, R., 2005. Modelling of a Switching Control Hydraulic System. *Mathematical and Computer Modelling of Dynamical Systems: Methods, Tools and Applications in Engineering and Related Sciences,* 11(3), pp. 329-344.

Mathworks, 2014. *Product and Service: Simulink.* [Online]
Available at: http://www.mathworks.co.uk/products/simulink/
[Accessed 14 May 2014].

Mathworks, 2014. *Simulink: Real-time introduction.* [Online]
Available at: http://www.mathworks.co.uk/products/simulink-real-time/
[Accessed 14 May 2014].

Mathworks, 2014. *The features of Simulink.* [Online]
Available at: http://www.mathworks.co.uk/products/simulink/features.html
[Accessed 26 July 2014].

Mettälä, K., Djurovic, M., Keuper, G. & Stachni, P., 2007. *INTELLIGENT OIL FLOW MANAGEMENT WITH EFM: THE POTENTIALS OF ELECTROHYDRAULIC FLOW MATCHING IN TRACTOR HYDRAULICS.* Tampere, The 10th Scandinavian International Conference on Fluid Power, SICFP'07,.

Miao, Y. & Wang, S., 2011. *Failure Diagnosis of Hydraulic Lifting System Based on Multistage Telescopic Cylinder.* Beijing, Proceedings of 2011 International Conference on Fluid Power and Mechatronics, pp. 828-834.

Moir, I. & Seabridge, A., 2008. *Aircraft Systems: Mechanical, electrical, and avionics subsystems intergration.* 3rd ed. Chichester: John Wiley & Sons, Ltd.

Moog, 2005. *D633 and D634 Series Direct Drive.* [Online]
Available at: www.moog.com/d633series
[Accessed 17 July 2014].

Murrenhoff, H., Sgro, S. & Vukovic, M., 2014. *An Overview of Energy Saving Architectures for Mobile Applications.* Aachen, 9th International Fluid Power Conference (9th IFK), pp. 119-124.

National Instruments, 2008. *Products: NI PCI-6221.* [Online]
Available at: http://sine.ni.com/ds/app/doc/p/id/ds-15/lang/en
[Accessed 22 July 2014].

Navarro, R., 1997. *PERFORMANCE OF AN ELECTRO-HYDROSTATIC ACTUATOR ON THE F-18 SYSTEMS RESEARCH AIRCRAFT.* Irvine, California, 16th Digital Avionics Systems Conference.

Niku, S. B., 2011. *Introduction to Robotics: Analysis, Control, Applications.* 2 ed. John Wiley & Sons, Inc.

Ohri, J., Dewan, L. & Soni, M. K., 2008. Fuzzy adaptive dynamic friction compensator for robot. *International Journal of Systems Applications, Engineering and Development,* 2(4), pp. 157-161.

Ortega, R. & Spong, M. W., 1989. ADAPTIVE MOTION CONTROL OF RIGID ROBOTS - A TUTORIAL. *Automatica,* 25(6), pp. 877-888.

ORTS, 2014. *ORTS Maschinenfabrik - Ship and Dredger Grabs.* [Online]
Available at: http://www.ship-technology.com/contractors/handling/orts/orts1.html
[Accessed 11 July 2014].

Oxfordhoists, 2014. *Oxford Midi 180 Manual Hoist.* [Online]
Available at: http://www.oxfordhoistsandparts.co.uk/products/Oxford-Midi-180-Manual-Hoist.html
[Accessed 11 July 2014].

Pan, M., Johnston, N. & Hillis, A., 2013. Active control of pressure pulsation in a switched inertance hydraulic system. *Proceedings of the Institution of Mechanical Engineers, Part I: Journal of Systems and Control Engineering* , August, 227(7), pp. 610-620.

Pan, M. et al., 2014. Theoretical and experimental studies of a switched inertance hydraulic system. *Proc IMechE Part I: Journal of Systems and Control Engineering,* 228(1), pp. 12-25.

Plummer, A. P., 2007. Control Techniques for Structural Testing: A Review. *Journal of Systems and Control Engineering,* Volume 221, pp. 139-169.

Raibert, M., Blankespoor, K., Nelson, G. & Playter, R., 2008. *BigDog, the Rough-Terrain Quadruped Robot.* Seoul, Proceedings of the 17th World Congress: The International Federation of Automation Control, pp. 6-9.

Ranch, R., 2014. *JSC Learning Techniques Home.* [Online]
Available at: http://prime.jsc.nasa.gov/ROV/types.html
[Accessed 13 May 2014].

Rath, G. & Zaev, E., 2013. *Cylinder Pressures in a Position Controlled System with Separate Meter-in and Meter-out.* Linkoping, The 13th Scandinavian International Conference on Fluid Power.

ROBOT WELDING, 2014. *ROBOT WELDING The essential guide.* [Online]
Available at: http://robotwelding.co.uk/index.html
[Accessed 15 June 2014].

Sanz-Merodio, D., Garcia, E. & Gonzalez-de-Santos, P., 2012. Analyzing energy-efficient configurations in hexapod robots for demining applications. *Industrial Robot: An International Journal,* 39(4), pp. 357 - 364.

Scherer, M., Geimer, M. & Weiss, B., 2013. *Contribution on Control Strategies of FLow-on-demand Hydraulic Circuits.* Linkoping, 13th Scandinavian International Conference on Fluid Power .

Schwarzgruber, T., Passenbrunner , T. E. & Delre, L., 2014. *Control design for a multi input single output hydraulic cylinder system.* Cape Town, South Africa, 19th World Congress of the International Federation of Automatic Control.

Sciavicco, L. & Siciliano , B., 2000. *Modelling and control of robot manipulators.* 2nd ed. London: Springer-Verlag.

Scopesi, M., Plummer, A. R. & Du, C., 2011. *Energy Efficient Variable Pressure Valve Controlled Hydraulic Actuation.* Arlington, Dynamic Systems and Control Conference (DSCC) / Fluid Power and Motion Control (FPMC).

Semini, C., 2010. *Information Package on HyQ-LegV2.1,* Genoa: Italian Institute of Technology (IIT).

Semini, C. et al., 2011. Design of HyQ – a hydraulically and electrically actuated quadruped robot. *Proceedings of the Institution of Mechanical Engineers, Part I: Journal of Systems and Control Engineering,* 1 August, 225(I6), pp. 831-849.

Shi, H., Gong, G., Yang, H. & Mei, X., 2013. Compliance of hydraulic system and its applications in thrust. *SCIENCE CHINA Technological Sciences,* September, Volume 56, p. 2124–2131.

Siciliano, B., 2008. *Springer Handbook of Robotics (Chapter 2 Dynamics).*

Silva, M. F. & Tenreiro Machado, J. A., 2007. A Historical Perspective of Legged Robots. *Journal of Vibration and Control,* Volume 13, p. 1447–1486.

Sirouspour, M. R. & Salcudean, S. E., 2001. Nonlinear Control of Hydraulic Robots. *IEEE TRANSACTIONS ON: ROBOTICS AND AUTOMATION,* April, 17(2), pp. 173-182.

Sylwester, K. et al., 2012. *A HIGH FLOW FAST SWITCHING VALVE FOR DIGITAL HYDRAULIC SYSTEMS.* Tampere, The Fifth Workshop on Digital Fluid Power.

Takako Industries, 2010. *Small Axial Piston Pump Catalog.* [Online]
Available at: http://www.takako-inc.com/english/products/pdf/pump.pdf
[Accessed 17 July 2014].

Van de Ven, J. D. & Katz, A., 2011. Phase-Shift High-Speed Valve for Switch-mode Control. *Transactions of the ASME: Journal of Dynamic Systems, Measurement and Control,* January.Volume 133.

Wikimedia Commons , 2011. *Left landing gear of 747-8.* [Online]
Available at: http://commons.wikimedia.org/wiki/File:Left_landing_gear_of_747-8.jpg
[Accessed 15 June 2014].

Yang, J., Plummer, A., Johnston, N. & Xue, Y., 2014. Design, efficiency and control of a new kind of cylinder with varying effective area for mobile robots. *Journal of Systems and Control Engineering (submitted).*

Yang, Z., Fukushima, Y. & Qin, P., 2012. Decentralized Adaptive Robust Control of Robot Manipulators Using Disturbance Observers. *IEEE TRANSACTIONS ON CONTROL SYSTEMS TECHNOLOGY,* September, 20(5), pp. 1957-1365.

Yang, Z. et al., 2008. Mechatronic Model Based Computed Torque Control of a Parallel Manipulator. *International Journal of Advanced Robotic Systems,* 5(1), pp. 123-128.

Zero-Max, 2014. *Zero-Max ServoClass Couplings.* [Online]
Available at: http://www.zero-max.com/documents/Zero-Max_ServoClass.pdf
[Accessed 17 July 2014].

Appendixes

Appendix 1 Components information

Appendix 1.1 Control valve

Appendix 1.1.1 Mounting information

Mounting pattern
ISO 4401-03-03-0-94, without X port

mm

	P	A	B	T	X[1)]	Y	F_1	F_2	F_3	F_4	G
	Ø7,5	Ø7,5	Ø7,5	Ø7,5		Ø3,3	M5	M5	M5	M5	4
x	21,5	12,7	30,2	21,5		40,5	0	40,5	40,5	0	33
y	25,9	15,5	15,5	5,1		9	0	-0,75	31,75	31	31,75

inch

	P	A	B	T	X[1)]	Y	F_1	F_2	F_3	F_4	G
	Ø0.30	Ø0.30	Ø0.30	Ø0.30		Ø0.13	M5	M5	M5	M5	0.16
x	0.85	0.50	1.19	0.85		1.60	0	1.60	1.60	0	1.30
y	1.02	0.61	0.61	0.20		0.35	0	-0.03	1.25	1.22	1.25

[1)] Port X must not be drilled, not sealed at valve base.

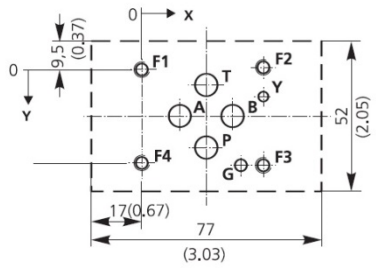

Figure A.1 Mounting drawing of D633 series valve (Moog, 2005)

Appendix 1.1.2 Performance curves

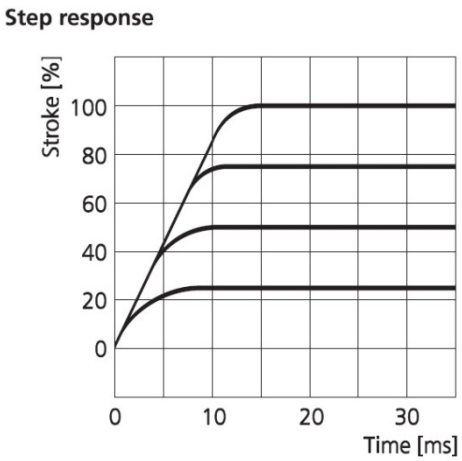

Figure A.2 Step response of D633 series valve (Moog, 2005)

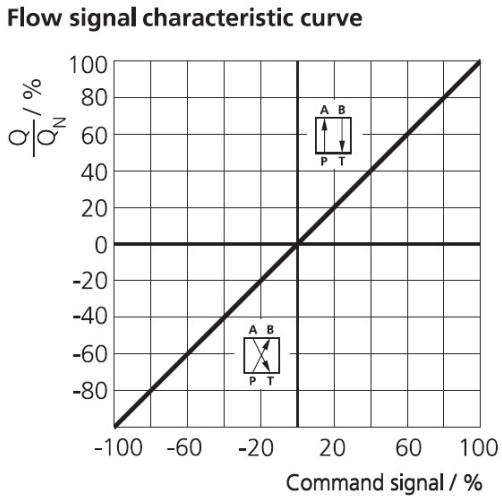

Figure A.3 Flow signal characteristic of D633 series valve (Moog, 2005)

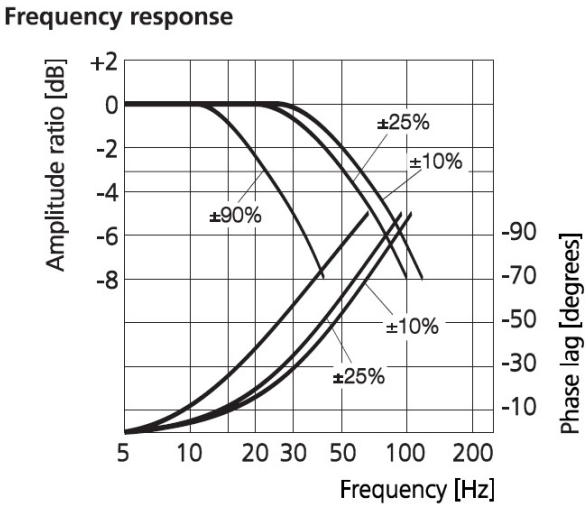

Figure A.4 Frequency response of D633 series valve (Moog, 2005)

Appendix 2 Model in Simulink and M-File for parameters

Appendix 2.1 Model in Simulink

Appendix 2.1.1 Motor-pump

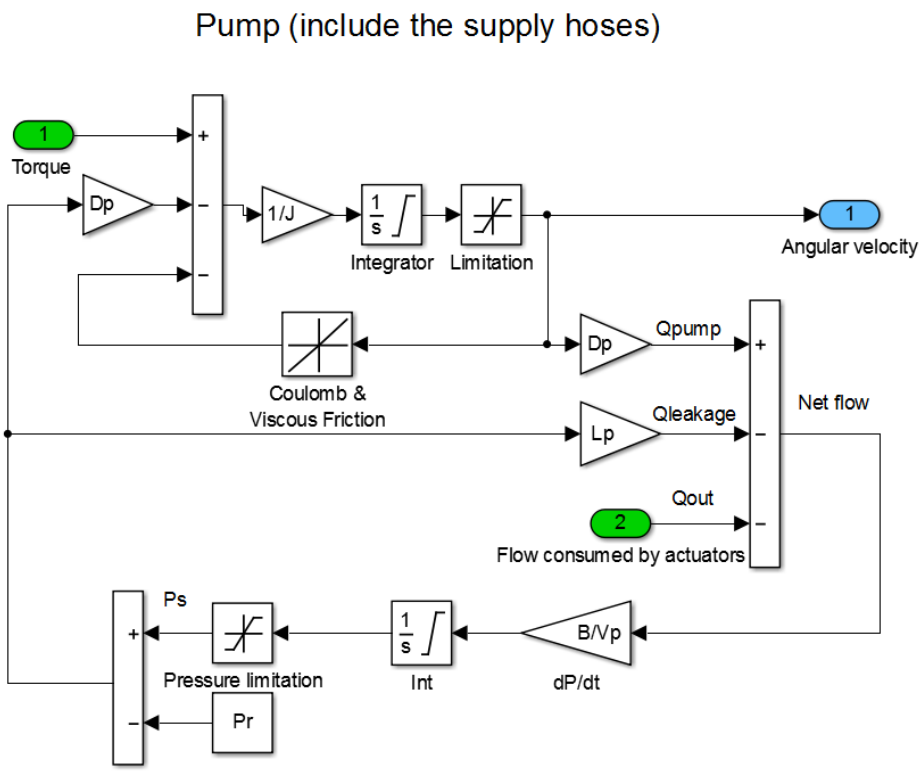

Figure A.5 The diagram of pump (include the supply hoses) in Simulink

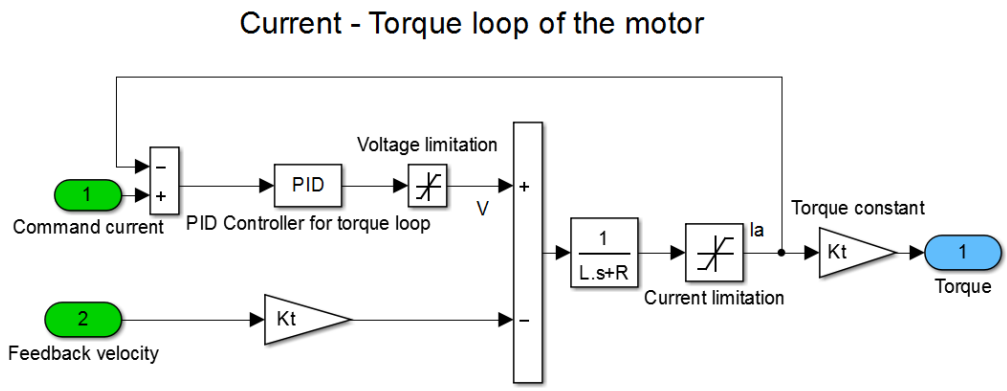

Figure A.6 The diagram of motor drive (current-torque loop) in Simulink

Appendix 2.1.2 Control valve

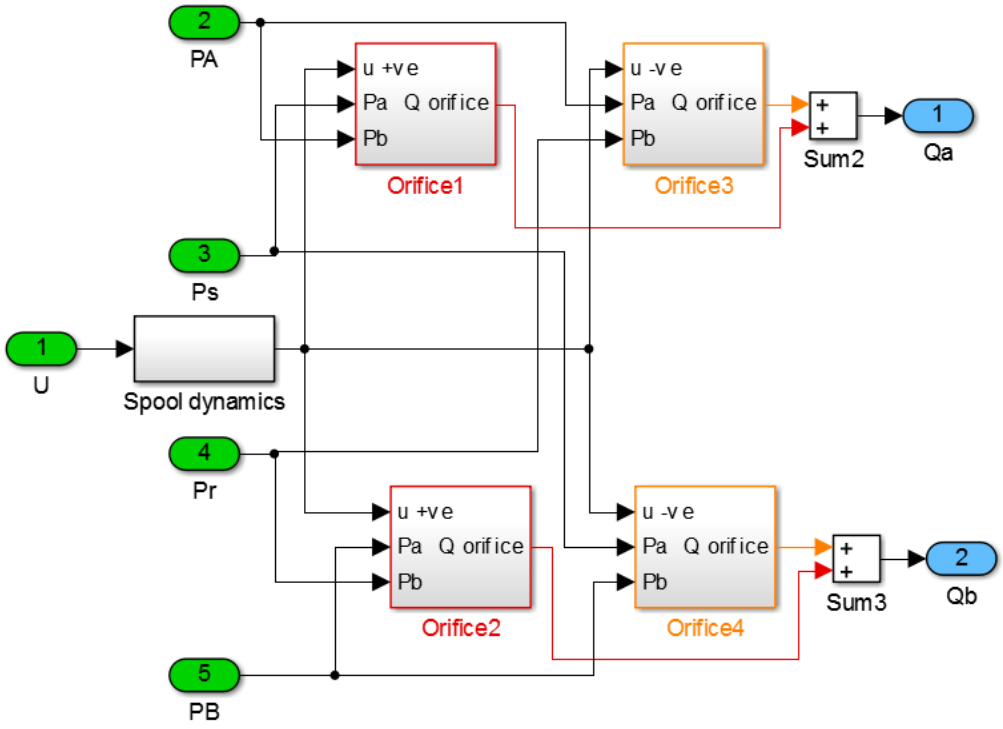

Figure A.7 The diagram of spool of the control valve in Simulink

Appendix 2.1.3 Manifold path

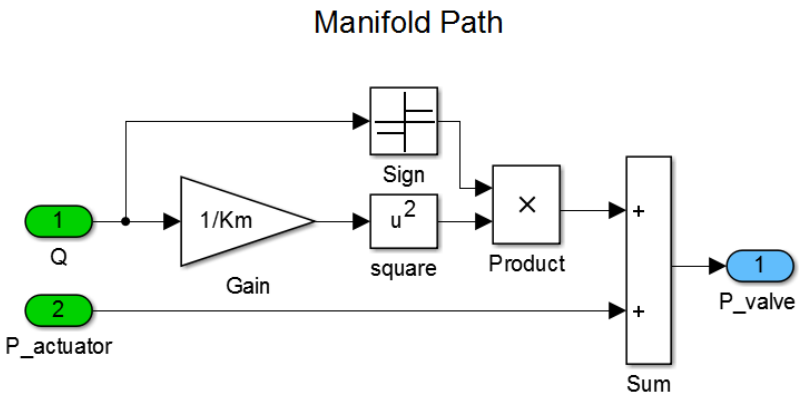

Figure A.8 The diagram of manifold path in Simulink

Appendix 2.1.4 Actuator

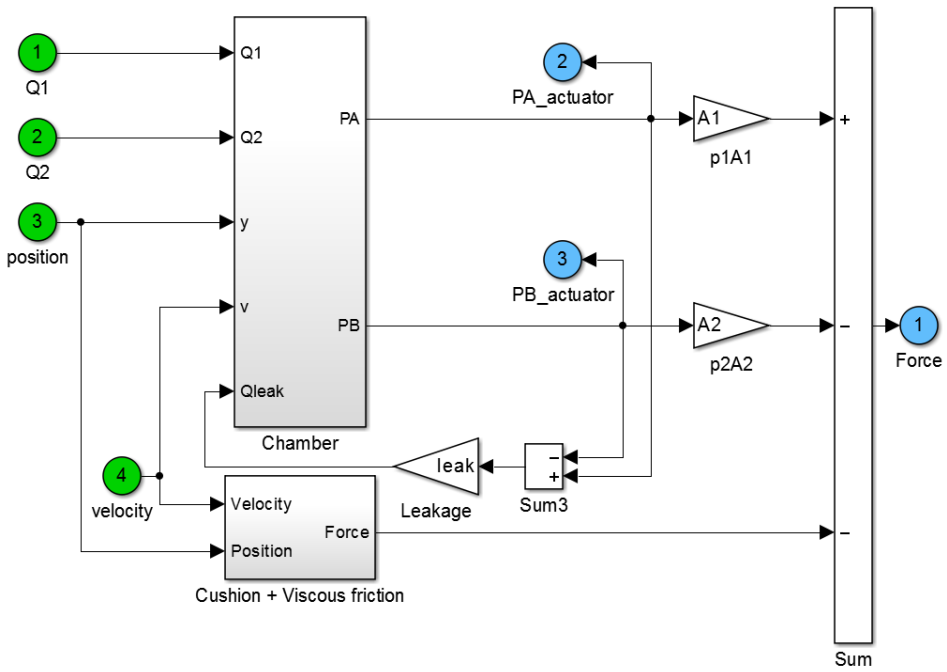

Figure A.9 The diagram of actuator in Simulink

Appendix 2.2 M-File for parameters

Appendix 2.2.1 Input generation

```
%% INPUT SIGNALS %%
input.sim_time = 50;   % Duration of the simulation
input.samples = 50/0.001; % Number of samples in the time signal
input.time = linspace(0,input.sim_time,input.samples)'; % Time
vector

freq1=0.5*2*pi;  %frequency of shoulder motion
freq2=0.6*2*pi;  %frequency of elbow motion

%Demanded acceleration for the two joints
input.input_A = 30*freq1*freq1*sin(freq1*input.time+pi/2);
input.input_B = 30*freq2*freq2*sin(freq2*input.time-pi/2);

% starting angle for the demanded motion%
demand.starting.angle_1 = -60;
demand.starting.angle_2 = 130;
```

Appendix 2.2.2 Controller

```
%% FPVC CONTROLLER %%

% Feedback parameter %;
ctrlsim.shoulder.kp = 70;  %PI controller for shoulder valve;
ctrlsim.shoulder.ki = 10;
ctrlsim.elbow.kp = 90;  %PI controller for elbow valve;
ctrlsim.elbow.ki = 10;

%% VPVC CONTROLLER %%

% Feed forward parameter %

ctrl.ff.A1_mdl = 2.01e-4; % actuator piston area m^2
ctrl.ff.A2_mdl = 1.23e-4; % actuator annulus area m^2
ctrl.ff.ratio = ctrl.ff.A1_mdl/ctrl.ff.A2_mdl; %Area ratio
ctrl.ff.V_hoses = 2e-5; % m^3, supply hoses volume
ctrl.ff.Pcav = 2e5; %Pa, cavitation pressure in Pa
ctrlexp.servop.Pr = 1e5; %Return pressure in tank in Pa;
ctrlexp.servop.B = 0.15; % Bulk modulus GPa;
mdl.servop.Dp = 3.14; % cm^3/rev, pump displacement
mdl.valve.Q_rated = 5; % l/min

% For predicting the viscous friction force in the cylinder %
ctrlexp.act.fric_factor_S_1 = 2800; % N/(m/s) Extension factor of
friction force in Shoulder cylinder
ctrlexp.act.fric_factor_S_2 = 2400; % N/(m/s) Retraction factor
of friction force in Shoulder cylinder
ctrlexp.act.fric_factor_E_1 = 2200; % N/(m/s) Extension factor of
friction force in Elbow cylinder
ctrlexp.act.fric_factor_E_2 = 2200; % N/(m/s) Retraction factor
of friction force in Elbow cylinder
```

```
% Feedback parameters
ctrlexp.fb.kp_mot = 3000; %P controller for motor speed;
ctrlexp.fb.kp_spool_1 = 100; %PI controller for shoulder valve;
ctrlexp.fb.ki_spool_1 = 10;
ctrlexp.fb.kp_spool_2 = 120; %PI controller for elbow valve;
ctrlexp.fb.ki_spool_2 = 10;
```

Appendix 2.2.3 Hydraulic system

```
%% HYDRAULIC PROPERTIES FOR SIMULATE THE TEST RIG %%
hydraulic.pressure.supply = 38; % Supply pressure in BAR
hydraulic.pressure.return = 1; % Return pressure in BAR
%hydraulic.motor = 100; % motor speed in rad/sec ONLY FOR FPVC
ctrlsim.actuator.fluid_bulk_mod = 0.15;   % Bulk modulus(GN/m^2)

% VALVE PROPERTIES %
hydraulic.valve.rated_flow = 5; % Valve rated flow rate in l/min
hydraulic.valve.lag_freq = 150;  % (Hz) The 90 deg frequency and
amplitude ratio specify the basic second order response of the
valve
hydraulic.valve.amp_ratio = -6; % (dB)
hydraulic.valve.slew_rate = 12; % (ms) Slew rate.This is the
maximum velocity of the spool, specified in terms of how long it
would take the valve to fully open at this velocity.
hydraulic.valve.body_sat_flow = 125;  % (l/min) Body saturation
flowrate.  This is the flow through the valve with 70bar pressure
drop with the spool removed i.e. a measure of the restriction
caused by the valve body.

% ACTUATOR PROPERTIES %
hydraulic.actuator.piston_area = 2.01;     % (cm^2)
hydraulic.actuator.annulus_area = 1.23;    % (cm^2)
ctrlsim.actuator.cross_piston_leakage = 0.15; % (l/min @ 70 bar)
hydraulic.actuator.starting_pressure = 20;  % Starting pressure
inside the actuator (bar)
hydraulic.actuator.friction_lim = 5000; % (N)Friction Limitation

% For simulate the friction in the actuator, e.g. sine wave %
ctrlsim.actuator.fric_factor_S_1 = 2800; % N/(m/s) Extension
factor of friction force in Shoulder cylinder
ctrlsim.actuator.fric_factor_S_2 = 2400; % N/(m/s) Retraction
factor of friction force in Shoulder cylinder
ctrlsim.actuator.fric_factor_E_1 = 2200; % N/(m/s) The Extension
factor of friction force in Elbow cylinder
ctrlsim.actuator.fric_factor_E_2 = 2200; % N/(m/s) The Retraction
factor of friction force in Elbow cylinder
```

Appendix 2.2.4 Robotic arm (SimMechanics)

```
%% MECHANICAL DOMAIN %%
% Upper arm %
arm.up.d11 = 0.32;
arm.up.d12 = 0.045;
```

```
arm.up.d13 = 0.08;
arm.up.b1 = 0.045;
arm.up.P1P2 = 0.35;
arm.up.cgx = 0.162;
arm.up.cgy = 0.0225;
arm.up.P1Pm1 = sqrt(arm.up.cgx^2 + arm.up.cgy^2);
arm.up.etam1 = atan(arm.up.cgy/arm.up.cgx);
arm.up.m1 = 1.772; %kg, include the mass of knee cylinder
arm.up.I1_body = [0.0239 0 0;0 0.0239 0;0 0 0]; %with respect to
CG of upper arm, for input of body block.
arm.up.a1 = sqrt(arm.up.d11^2+(arm.up.d13-arm.up.d12)^2);
arm.up.eta11 = atan((arm.up.d13-arm.up.d12)/arm.up.d11);

% Fore arm %
arm.fore.d21 = 0.3186;
arm.fore.d22 = 0.045;
arm.fore.b2 = 0.045;
arm.fore.P2P3 = 0.33;
arm.fore.P2Pm2 = 0.122;
arm.fore.m2 = 0.739;
arm.fore.I2_body = [0.0035 0 0;0 0.0035 0;0 0 0]; %with respect
to CG of upper arm, for input of body block.
arm.fore.a2 = sqrt(arm.fore.d21^2 + arm.fore.d22^2);
arm.fore.eta21 = atan(arm.fore.d22/arm.fore.d21);
arm.fore.eta22 = 6 * pi/180; % 6 degrees,

% Hand %
arm.hand.m3 = 1.039; %3.2;% the mass of hand
arm.hand.thickness = 1.35e-2; %4.2e-2; % the thickness of mass
cylinder in metre.
arm.hand.I3_body = [0.00304 0 0;0 0.00304 0;0 0 0]; %inertia of
hand, for input of body block.

% Shoulder %
arm.sh.m0 = 2.482;
arm.sh.I0 = 0.00745;
arm.sh.I0_body = [arm.sh.I0 0 0;0 arm.sh.I0 0;0 0 arm.sh.I0];

% GROUND PROPERTIES %
ground.position = [0 0 0]; %Position of ground
ground.spring = 1e5;
ground.damping = 3e2;
ground.friction = -550;
g = 9.81; %gravity acceleration.

% SIMULATION INITAL CONDITIONS: joint initial positions (degrees)%
arm.shoulder.initial.angle = -70;
arm.elbow.initial.angle = 140;
```

Appendix 3 Signal processing

Appendix 3.1 Individual signal processing

Appendix 3.1.1 Command signal of the motor speed

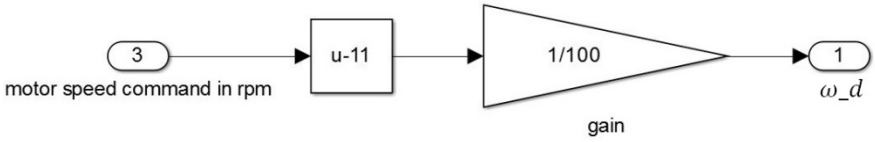

Figure A.10 The speed-to-voltage converter for motor command in the Simulink model

Appendix 3.1.2 Feedback signal of the motor speed

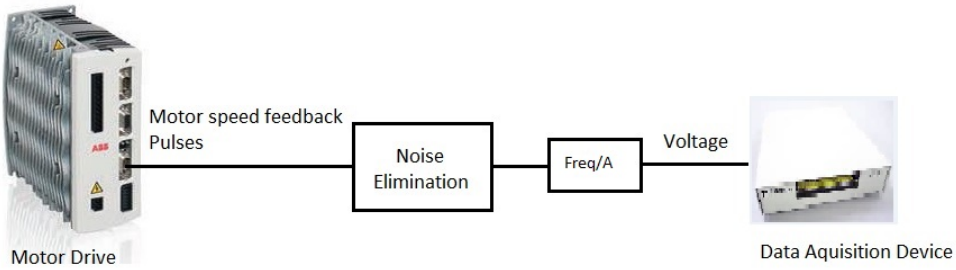

Figure A.11 The diagram of signal processing for motor speed feedback

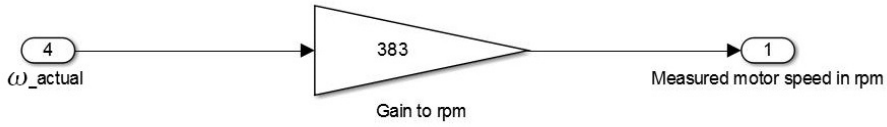

Figure A.12 The voltage-to-speed converter for motor feedback in the Simulink model

Appendix 3.1.3 Command signal of the control valve

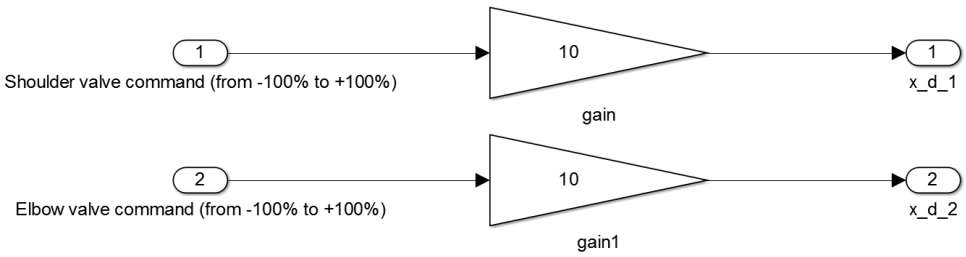

Figure A.13 The opening-to-voltage converters for valve commands in the Simulink model

Appendix 3.1.4 Actual spool position of the control valve

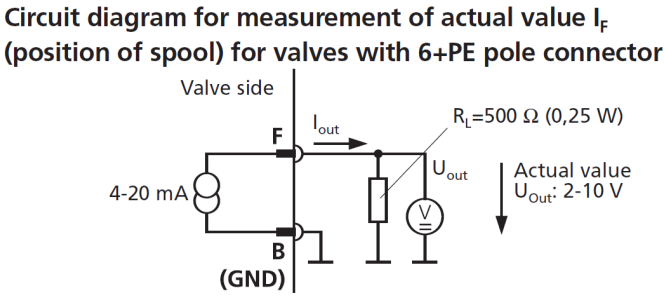

Figure A.14 The circuit diagram for measurement of actual spool position of D633 control valve (Moog, 2005)

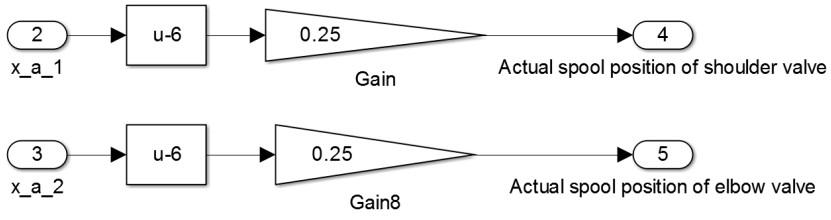

Figure A.15 The voltage-to-opening converters for two control valves in the Simulink model

Appendix 3.1.5 Relative encoder

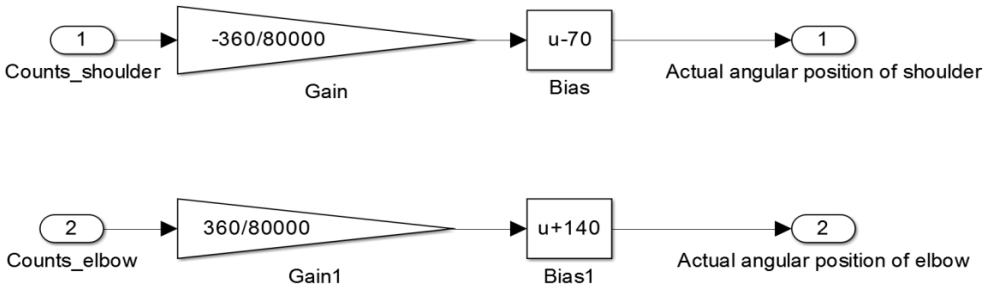

Figure A.16 The counts-to-position converter for two relative encoders in Simulink model

Appendix 3.1.6 Pressure transducer

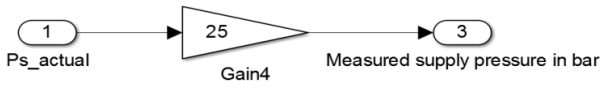

Figure A.17 The voltage-to-pressure converter for pressure transducer in Simulink model

Appendix 3.1.7 Load cell

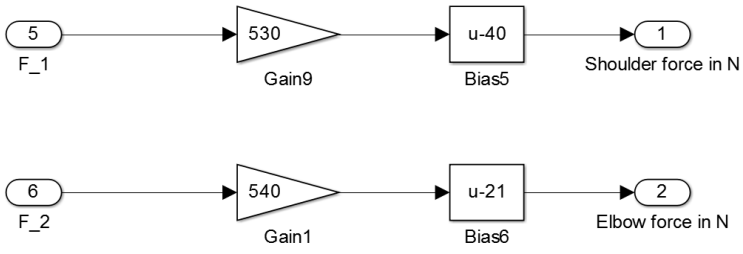

Figure A.18 The voltage-to-force converter for two load cells in Simulink model

Appendix 3.2 Pin arrangement of NI boards

Signal Name	Signal Description	Board	Pin Name	Corresponding Pin on Connector Block
ω_d	Motor speed command	1	AO 0 AO GND	22 55
x_{d_1}	Shoulder valve command	2	AO 0 AO GND	22 55
x_{d_2}	Elbow valve command	2	AO 1 AO GND	21 54
ω_actual	Actual motor speed	2	AI 4 AI GND	28 27
x_{a_1}	Actual opening of shoulder valve	2	AI 1 AI GND	33 32
x_{a_2}	Actual opening of elbow valve	2	AI 3 AI GND	30 29
angle_1	Actual angular position of shoulder joint	2	A: PFI 8 B: PFI 10 Z: PFI 9	37 45 3
angle_2	Actual angular position of elbow joint	2	A: PFI 3 B: PFI 11 Z: PFI 4	42 46 41
P_{S_actual}	Actual supply pressure	2	AI 0 AI GND	68 67
F_1	Actual actuation force of shoulder actuator	2	AI 5 AI GND	60 59
F_2	Actual actuation force of elbow actuator	2	AI 6 AI GND	25 24

Table A.1 The pin arrangement of NI boards